

**Effects of dilution on the Laminar Burning Characteristics of  
Oxy-Dodecane mixtures with and without Hydrogen blending  
and Oxy-Methane mixtures at elevated operating conditions**

*A Thesis submitted*

*in partial fulfilment for the degree of*

**Doctor of Philosophy**

*by*

**Rajesh N**



**Department of Aerospace Engineering**

**INDIAN INSTITUTE OF SPACE SCIENCE AND TECHNOLOGY**

**THIRUVANANTHAPURAM – 695547**

**August – 2023**



## CERTIFICATE

This is to certify that the thesis titled *Effects of dilution on the Laminar Burning Characteristics of Oxy-Dodecane mixtures with and without Hydrogen blending and Oxy-Methane mixtures at elevated operating conditions* submitted by **Rajesh N**, to the Indian Institute of Space Science and Technology, Thiruvananthapuram, in partial fulfilment for the award of the degree of **Doctor of Philosophy**, is a bonafide record of the original work carried out by him under my supervision. The contents of this thesis, in full or in parts, have not been submitted to any other Institute or University for the award of any degree or diploma.

**Dr. Prathap C**

Research Supervisor

Associate Professor

Department of Aerospace Engineering

**Dr. Deepu M**

Head of the Department

Department of Aerospace Engineering

IIST

**Place:** IIST, Thiruvananthapuram

**Date:** August 2023



## Declaration

I declare that this thesis titled *Effects of dilution on the Laminar Burning Characteristics of Oxy-Dodecane mixtures with and without Hydrogen blending and Oxy-Methane mixtures at elevated operating conditions* submitted in partial fulfilment for the award of the degree of **Doctor of Philosophy** is a record of the original work carried out by me under the supervision of **Dr. Prathap C** and has not formed the basis for the award of any degree, diploma, associateship, fellowship, or other titles in this or any other Institution or University of higher learning. In keeping with the ethical practice in reporting scientific information, due acknowledgments have been made wherever the findings of other have been cited.

**Place:** IIST, Thiruvananthapuram

**Date:** August 2023

**Rajesh N**

SC16D008



## Acknowledgments

I would like to express my sincere appreciation and gratitude to my mentor **Dr. Prathap C** for giving me the opportunity to work under his guidance. I am thankful for his invaluable support, advice, and encouragement throughout my research.

I am very thankful to all my doctoral committee members, Prof. Ravi M R (Mechanical Engineering, IIT Delhi), Prof. Sudarshan Kumar (Aerospace Engineering, IIT Bombay), Dr. Rajesh Sadanandan (Associate Professor, Aerospace Engineering, IIST), Dr. Deepu (DC chairman, Head, Aerospace, IIST), Dr. Aravind Vaidyanathan (former DC chairman) and Dr. Natarajan E (Associate Professor, Maths, IIST), for their valuable suggestions, insightful comments, and constructive criticism in each phase of my research work.

I also express my gratitude to the Director of IIST, the Dean of Academics, and the Dean of R&D for providing an excellent research ambiance during my tenure at IIST.

I would like to thank Mr. Dinesh D., Mr. Sathish Kumar, Mr. Prakash R S., Mr. Vinil, and Mr. Muhammed Rijas A. for all their instrumentation support for my research. A special thanks to Mr. Bipin Davidson for his enormous help with my experiments and personal care.

I express my thanks and wishes to my colleagues, Dr. Muniraja Tippa, Mr. Akash, Mr. Yashwant, Mr. Rishap, Ms. Shreya, and Ms. Aswathy, for their lab time, participation, and technical discussions. A special acknowledgment goes out to Ms. Risha Raju for her assistance and endless support at difficult times in the research journey.

I would also like to thank my parents, Mr. Natarajan & Mrs. Meenambal, for their unconditional love and constant encouragement. I am grateful to my sister, Dr. Bharathi Sathish, for her unwavering support and to a family friend, Ar. Vaibavasri, for her time and encouragement from afar.



## Abstract

N-Dodecane is an important representative in several surrogates of multicomponent fuels like gasoline and jet fuels. The choice of a surrogate fuel combination to estimate the combustion characteristics of a complex real fuel depends strongly on its individual component's physical, chemical, and combustion properties. Therefore, it is essential to have a precise reaction mechanism to predict the combustion characteristics, such as unstretched laminar burning velocity (LBV) and ignition delay times of the individual components of the surrogate fuel and the surrogate fuel itself. The combustion characteristics of (a) n-dodecane-air, (b) oxy-n-dodecane with diluents like  $N_2$ ,  $CO_2$ ,  $H_2O$ , and (c) n-dodecane- $H_2$ -air were less or not reported in the literature. The present work aims to fill the existing important gap. In this work, the unstretched LBV of n-dodecane at various operating conditions was measured using the freely expanding spherical flame (SPF) method. A new cuboidal combustion chamber (14.56 L) was constructed with 107 mm optical accesses on four sides. It had a dedicated heating system for elevated temperature experiments. Partial pressure method was used to prepare the combustible mixture inside the chamber. An electrical spark-ignition system was used to ignite the mixtures at the centre of the chamber. A high-speed shadowgraph system was used to image the spherical flame propagation. An in-house image-processing code was used to obtain the flame radius data from the flame images and subsequently the flame speed and flame stretch rate. Then, a non-linear stretch extrapolation scheme was used to find the unstretched flame speed, and finally, the unstretched LBV was estimated. The present rig was properly validated with the literature LBV data for  $CH_4$ -air and n-decane-air mixtures at different operating conditions. A freely propagating planar flame model in CHEMKIN was used to simulate the unstretched LBV using various reaction mechanisms.

Initially, the unstretched LBV and burned gas Markstein length of premixed n-dodecane-air mixtures at pressure = 1-4 bar, temperature = 400-450 K, and  $\phi = 0.8-1.4$ . The flame stability analysis of n-dodecane-air mixture at all the studied operating conditions quantified through burned gas Markstein length ( $L_b$ ) emphasized that a transition of stable to unstable flame occurred at  $\phi = 1.4$  due to thermo-diffusive effects.  $L_b$  was influenced significantly by an increase in pressure than temperature due to a substantial reduction in flame thickness. The comparison of measured unstretched LBV with available n-dodecane mechanisms indicated that JetSurF2.0, You et al., and PoliMi were the best candidates. Off-stoichiometric varieties of n-dodecane-air were more responsive to pressure and temperature

effects. Finally, the unstretched LBV of premixed n-dodecane-air mixtures increased/decreased with an initial temperature/pressure hike. Raise in initial temperature increased the flame temperature and improved the flame propagation rate. An increase in initial pressure amended the reaction rate but decreased the flame propagation rate due to the dominance of three-body reactions and increased unburned gas density.

The second objective here was to measure the LBV and  $L_b$  of oxy-n-dodecane mixtures having high-flame temperatures safely by adding a third-party inert species.  $(100-Z) \% (n\text{-C}_{12}\text{H}_{26} + (18.5 \text{ O}_2/\phi)) + Z\% (\text{N}_2/\text{CO}_2/\text{H}_2\text{O})$  mixtures were analysed at 400-450 K, 1-4 bar,  $\phi=0.6-1.4$ , and Z: (a)  $\text{N}_2=55-75\%$ , (b)  $\text{CO}_2/\text{H}_2\text{O} = 65\%$ .  $\text{N}_2$  diluted mixtures were subjected to predominant thermal effects, whereas  $\text{H}_2\text{O}/\text{CO}_2$  diluted mixtures were affected by all the real-time effects like thermal & chemical and thermo-diffusive effects. At 65% dilution, mixtures diluted with: (a)  $\text{N}_2$  had the highest LBV due to the high-flame temperature, (b)  $\text{CO}_2$  suppressed the LBV the most due to the thermal and chemical effects. Predicted LBV with You and JetsurF2.0 mechanisms showed excellent agreement with the present measurements. PoliMi's kinetic scheme always over-predicted the LBV in the rich mixtures. The diluted oxy-fuel mixtures generated stable flames with respect to thermo-diffusive effects at all the studied conditions. At a given thermodynamic condition, the flame's stability to the thermo-diffusive effects was the highest for mixtures diluted with steam, followed by  $\text{N}_2$  and  $\text{CO}_2$  due to their respective Lewis numbers. If the flame temperature attained was 2150 K or lower, the diluted oxy-n-dodecane mixtures at  $\phi=1.4$  were affected by thermo-diffusive instability. The sensitivity of the chain termination reaction  $\text{H} + \text{OH} + \text{M} \leftrightarrow \text{H}_2\text{O} + \text{M}$  showed a transition from negative to positive at 0%  $\text{N}_2$  case.

The effects of hydrogen addition on the premixed laminar burning characteristics of n-dodecane reacting in air was the third objective of the present research. Approximately, the unstretched LBV increased three times at off-stoichiometric and two times for stoichiometric mixtures, as the mole fraction of hydrogen increased from 0-40% by volume in n-dodecane. Further, the simulation using JetsurF2.0 and You et al. predicted the LBV satisfactorily within uncertainty limits at all operating conditions, and PoliMi-1410 prediction accuracy varies with the equivalence ratio. The n-dodecane/air mixtures were unstable at rich equivalence ratios due to the lower mass diffusivity of n-dodecane and  $Le < 1$ , in contrast,  $\text{H}_2$  blending transformed this unstable mixture to a stable mixture.  $\text{H}_2$  addition resulted in an earlier onset of hydrodynamic instability due to a reduction in the flame thickness. In addition, sensitivity analysis was performed to identify the key reactions responsible for the enhanced reactivity

associated with H<sub>2</sub> addition. Reaction pathway and emission analysis shows the significant reduction of CO<sub>2</sub>, and CO emissions.

The final objective of the current work was to investigate the dilution effect of steam, carbon dioxide, and nitrogen on the unstretched LBV and L<sub>b</sub> of premixed (100-Z) % (CH<sub>4</sub> + (2O<sub>2</sub>)/φ) +Z% (H<sub>2</sub>O/N<sub>2</sub> /CO<sub>2</sub>) mixtures at 300-453 K, 1-4 bar, equivalence ratio (φ)- 0.6-1.4, and Z was varied from 40-60% for steam and kept constant at 50% for CO<sub>2</sub>/N<sub>2</sub>. Present mixture formulation led to the comparison of the absolute dilution effect of each diluent at an identical mixture and thermodynamic conditions. The addition of 50% diluents significantly suppressed the flame propagation. It was the highest for CO<sub>2</sub> (87% as compared to no dilution) due to the simultaneous reduction in flame temperature and its kinetic effect, and it was followed by steam (69%) and N<sub>2</sub> (61%), and their suppression effect was primarily due to the reduction in the flame temperature. All the studied mixtures were stable to preferential diffusional instability as their: (a) Markstein length was positive and (b) the effective Lewis number of the mixtures were well higher than the critical Lewis number. Predicted LBV with GRIMech3.0 compared well with the experiments than FFCM-1. As the LBV increased beyond 150 cm/s, predicted LBV of both GRIMech3.0 and FFCM-1 showed significant deviation with the measurements.

*Keywords: Laminar burning velocity, Flame stability, hydrodynamic instability, n-dodecane, dilution, effective Lewis number, hydrogen blending, oxy-fuel combustion*



## Nomenclature

$S_u^0$	Laminar Burning Velocity (LBV), cm/s
$V_u$	Velocity of the unburned gas, cm/s
$V_b$	Velocity of the burned gases, cm/s
$K$	Flame stretch rate, $s^{-1}$
$r_f$	Instantaneous flame radius, mm
$L_b$	Burned gas Markstein length, mm
$S_b$	Stretched flame speed cm/s
$S_b^0$	Unstretched flame speed, cm/s
$Le$	Lewis number
$N_{fuel}$	Number of fuel moles
$p_{fuel}$	Partial pressure of fuel, bar
$V$	Volume of chamber, L
$R_u$	Universal gas constant, $J K^{-1}.mol^{-1}$
$MW$	Molar mass, g/mol
$V_{fuel}$	Volume of the fuel, ml
$T_u$	Unburned gas temperature, K
$p_u$	Unburned gas pressure, bar
$Z$	Diluent volume fraction
$U_g$	Displacement velocity, cm/s
$r_{fit}$	Circle fit radius, mm
$\Delta t$	Interframe time interval, s
$D_u$	Mass diffusivity $cm^2/s$
$c_{p,u}$	constant pressure specific heat capacity, J/ kg K
$T_b$	Adiabatic flame temperature, K
$E_a$	Activation energy
$Ze$	Zeldovich number
$Le_{eff}$	Effective Lewis number
$Le^*$	Critical Lewis number
$Le_E / Le_D$	excess/deficient reactant's Lewis number
$a_i$	Uncertainty of $i^{th}$ parameter

## Greek Symbols

$\phi$	Equivalence ratio
$\delta$	Characteristic flame thickness, mm
$\alpha$	Thermal diffusivity, $cm^2/s$
$\lambda$	Thermal conductivity, J/s cm K
$\sigma$	Density ratio, $\rho_u/\rho_b$
$\rho_u$	Density of the unburned gas, $kg/m^3$
$\rho_b$	Density of burned gas, $kg/m^3$



# Contents

Contents .....	ix
List of Tables .....	xv
List of Figures .....	xvi
Chapter 1 INTRODUCTION.....	1
1.1 General Introduction .....	1
1.2 Oxy-n-dodecane .....	1
1.3 H <sub>2</sub> -blending in n-dodecane.....	2
1.4 Basic Concepts .....	3
1.4.1 Combustion.....	3
1.4.2 Equivalence ratio .....	3
1.4.3 Equilibrium flame temperature.....	4
1.4.4 Laminar burning velocity .....	4
1.4.5 Flame stretch.....	5
1.4.6 Burned gas Markstein length.....	6
1.4.7 Instabilities in outwardly propagating spherical flames .....	7
1.5 Organisation of thesis.....	8
Chapter 2 Literature Review .....	10
2.1 Introduction .....	10
2.2 Laminar Burning velocity measurement methods .....	10
2.3 Outwardly spherical flame method in present work – it's choice and reasons.....	12
2.4 Liquid fuel evaporation strategies .....	12
2.4.1 Pre-vaporization of liquid fuel.....	13
2.4.2 Volume method .....	13
2.5 Surrogate component fuel: <i>n</i> -Dodecane.....	14
2.6 Oxy n-dodecane mixtures with EGR diluents.....	15

2.7 Hydrogen blended n-dodecane.....	16
2.8 Oxy-methane mixtures with EGR dilution.....	18
2.9 Conclusions of the literature survey.....	20
2.10 Objectives.....	21
Chapter 3 Experimental rig and Methodology.....	22
3.1 Combustion chamber.....	22
3.2 Leak test and Commissioning.....	24
3.3 Design Specifications.....	24
3.4 Design of subsystems.....	25
3.4.1 Gas Flow systems.....	25
3.4.2 Heating System.....	25
3.4.3 Liquid Fuel injection system.....	27
3.4.4 Ignition system.....	27
3.4.5 Imaging system.....	28
3.4.6 Data acquisition system.....	30
3.4.7 Triggering system.....	31
3.5 Experimental Procedure.....	31
3.5.1 Preparation of Gaseous mixtures.....	31
3.5.2 Preparation of combustible mixtures involving liquid fuels.....	33
3.5.3 Preparation of combustible mixtures without N <sub>2</sub> .....	35
3.6 Design of experiments.....	36
3.7 Methodology.....	36
3.7.1 Freely expanding spherical flame method (SPF).....	37
3.7.2 Data reduction procedure.....	38
3.7.3 Image processing.....	39
3.7.4 Procedure for the estimation of unstretched laminar flame speed.....	42
3.8 Flame global parameters.....	43

3.8.1 Flame thickness .....	43
3.8.2 Activation energy or Zeldovich Number .....	44
3.8.3 Analytical estimation of Markstein length .....	45
3.9 Thermo-diffusive instability.....	45
3.10 Hydrodynamic Instabilities .....	48
3.11 Uncertainty quantification.....	49
3.12 Summary .....	50
Chapter 4 Numerical Approach .....	51
4.1 Introduction - CHEMKIN .....	51
4.2 Gas-phase kinetics utility .....	52
4.3 Transport utility.....	52
4.4 Application solvers.....	54
4.4.1 PREMIX .....	55
4.5 Numerical solution method .....	56
4.6 Boundary conditions .....	58
4.7 Grid independence study.....	58
4.8 Reaction mechanisms.....	59
4.9 Sensitivity analysis.....	59
4.10 Reaction pathway analysis .....	60
Chapter 5 Test Rig Validation .....	61
5.1 Validation of experimental setup .....	61
5.2 Lower alkane without and with steam dilution .....	61
5.2.1 Elevated initial temperature and water evaporation .....	61
5.2.2 Validation of Markstein lengths of premixed CH <sub>4</sub> -air mixtures .....	63
5.3 Validation study with heavy hydrocarbon fuels.....	64
5.3.1 Unstretched LBV on premixed n-decane-air mixture .....	64
5.3.2 Validation of heavy hydrocarbon fuels on Markstein length .....	65

5.4 Repeatability.....	66
5.5 Summary .....	66
Chapter 6 Combustion characteristics of premixed n-Dodecane-air mixtures .....	67
6.1 Pressure - time evolution.....	68
6.2 Flame radius and flame speed variations .....	68
6.3 Nonlinear Flame speed behaviour.....	69
6.4 LBV Mechanism validation .....	70
6.5 Flame stability .....	72
6.6 LBV at elevated pressure .....	75
6.7 LBV at elevated temperatures .....	76
6.8 Temperature and pressure exponents .....	77
6.9 Sensitivity analysis.....	78
6.10 Hydrodynamic Instability.....	79
6.11 Summary .....	80
Chapter 7 Combustion characteristics of diluted premixed OXY n-dodecane mixtures.....	81
7.1 Pressure-time variation.....	82
7.2 Flame propagation history.....	83
7.3 Effect of N <sub>2</sub> addition on LBV .....	84
7.4 Effect of high flame temperature on LBV .....	85
7.5 Effect of N <sub>2</sub> addition on LBV at elevated pressures .....	87
7.6 Effect of N <sub>2</sub> addition on flame stability .....	88
7.7 Flame stability at different initial Temperatures/ pressures for 65%N <sub>2</sub> .....	90
7.8 Effect of different diluents on LBV of oxy-dodecane mixtures.....	91
7.9 Effective Lewis number .....	92
7.10 Analytical Burned gas Markstein length.....	93
7.11 Effect of different initial pressures on LBV for N <sub>2</sub> / H <sub>2</sub> O/ CO <sub>2</sub> .....	94
7.12 Flame global parameters .....	96

7.13 Sensitivity analysis.....	97
7.14 Pressure and different diluents effect on Markstein length.....	98
7.15 Reaction pathway analysis .....	99
7.16 Summary .....	104
Chapter 8 Combustion characteristics of Hydrogen Blended n-dodecane-air mixtures.....	105
8.1 Nonlinear flame stretch behavior .....	105
8.2 Effects of equivalence ratio on LBV .....	107
8.3 Effects of H <sub>2</sub> addition on LBV .....	108
8.4 Effects of initial pressure on LBV.....	109
8.5 Thermal and kinetic effects .....	110
8.6 Effects of hydrogen addition on Markstein length.....	111
8.7 Flame stability .....	112
8.8 Sensitivity analysis.....	114
8.9 Reaction pathways.....	117
8.10 Emission analysis .....	117
8.11 Summary .....	119
Chapter 9 Absolute EGR gas dilution effects on oxy-methane mixtures .....	121
9.1 Effects of Steam dilution on flame instability.....	122
9.2 Suppression effects of steam on LBV .....	123
9.3 Steam suppression effects on LBV at elevated pressures and temperatures.....	124
9.4 Effects of EGR diluents on flame stability.....	126
9.5 Effects of different diluents on LBV at a range of equivalence ratios.....	127
9.6 Effect of different diluents on LBV at elevated thermodynamic conditions .....	128
9.7 LBV correlation oxy-methane-steam mixtures .....	130
9.8 Summary .....	132
Chapter 10 Conclusions .....	133
10.1 n-dodecane-air mixtures.....	133

10.2 Oxy-n-dodecane mixtures .....	134
10.3 Hydrogen blended n-dodecane-air mixtures .....	135
10.4 Oxy-methane mixtures .....	136
10.5 The overall contribution of present work.....	137
10.6 Application potential of the present work .....	137
10.7 Future scope of the present work .....	138
References.....	139
Appendix -A: Ignition Discharge Energy Measurement .....	152
Appendix-B: Uncertainty Quantification.....	156
List of Publications .....	167

## List of Tables

Table 2.1. Summary of merits and demerits of stationary .....	10
Table 2.2. Summary of merits and demerits of propagating flames .....	11
Table 2.3. Literature data on laminar burning velocity data of n-dodecane + air mixtures.....	14
Table 3.1. Summary of final chamber design specifications .....	24
Table 3.2. Operating conditions of various mixtures.....	36
Table 3.3. Uncertainties averaged over equivalence ratio of LBV and $L_b$ for various mixtures .....	50
Table 4.1. Details of Chemical kinetic schemes used in the present work .....	59
Table 5.1. Summary of the operating conditions of validation experiments .....	61
Table 6.1. Operating conditions of n-dodecane-air mixtures .....	67
Table 6.2. Kinetic mechanism for validating LBV of n-dodecane-air mixtures .....	67
Table 6.3. List of Mechanisms and their deviation with measurements.....	71
Table 6.4. Flame stability data of premixed dodecane-air mixtures.....	73
Table 7.1. Summary of operating condition of diluted oxy n-dodecane mixtures .....	81
Table 7.2. Kinetic mechanism used for diluted oxy-n-dodecane mixtures.....	82
Table 7.3. Mixture and flame properties of 35% ( $C_{12}H_{26} + (18.5O_2)/\phi$ ) + 65% $N_2$ at 1-4 bar, 400-450K and $\phi = 1.0$ .....	89
Table 8.1. Operating boundary conditions of hydrogen blended n-dodecane-air mixtures...	105
Table 8.2. Kinetic schemes used for the hydrogen blended n-dodecane-air mixtures .....	105
Table 9.1. Summary of operating conditions of diluted oxy-methane mixtures .....	121
Table 9.2. List of chemical kinetic mechanisms used for diluted oxy-methane mixtures.....	122



## List of Figures

Figure 1.1. Planar flame propagating into the quiescent unburned fuel-air mixture at constant pressure .....	4
Figure 3.1. Final chamber design of (a) CAD model (b) sectional view (c) actual chamber ..	23
Figure 3.2. Graphical illustration of cartridge heater positions. ....	26
Figure 3.3. Images of the temperature controller and its electrical connection .....	26
Figure 3.4. Customized lengthy needle and gas-tight syringe .....	27
Figure 3.5. Ceramic electrode and externally triggerable ignition coil .....	28
Figure 3.6. The schematic and actual arrangement of the shadowgraph system .....	29
Figure 3.7. LabVIEW pressure and temperature measurement window .....	30
Figure 3.8. Synchronisation of different devices with a digital pulse generator and signals delay accuracy tested in an oscilloscope .....	31
Figure 3.9. The schematic and actual arrangement of the spherical flame test facility .....	32
Figure 3.10. Measured mixture uniform temperature and corresponding LabVIEW real-time measurement window .....	33
Figure 3.11. The absolute partial pressure variation during the mixture preparation stage.....	35
Figure 3.12. Graphical illustration of spherical flame propagation inside the cuboidal chamber and typical flame structure of stoichiometric methane/air mixture at 1 bar 300 K .....	37
Figure 3.13. The unsteady pressure evolution with time after the spark (left) of stoichiometric n-dodecane/air mixture at 1 bar 450 K. The zoomed version of the constant pressure zone (right) with upper and lower radius limits illustrated .....	39
Figure 3.14. The sequence of image processing procedures illustrated .....	41
Figure 3.15. Ignition and confinement effects of spherically propagating stoichiometric n-dodecane/air mixture at 1 bar 450 K.....	42
Figure 3.16. Comparison of different Lewis number models for n-dodecane/air mixture at 1 bar 425 K.....	47
Figure 3.17. Inception area of the spherical flame for cells.....	48
Figure 4.1. Structure of the CHEMKIN (PREMIX) Program .....	51
Figure 4.2. Profiles of reactant and products initial estimates .....	57
Figure 4.3. (a) LBV convergence with different grid points (b) convergence percentage of solution with different grid points.....	59

Figure 5.1. Experimental and computed unstretched laminar burning velocities as a function of the equivalence ratio for (a) Elevated temperature: CH <sub>4</sub> /air at 1 bar, 373 & 423 K and CH <sub>4</sub> /air/10%H <sub>2</sub> O mixtures at 1 bar and 373 K (b) Elevated pressure: CH <sub>4</sub> /air at 1 & 3 bar...	62
Figure 5.2. Variation of burned gas Markstein lengths of (a) CH <sub>4</sub> /air mixtures at 1 bar, 373 K and 423 K (b) CH <sub>4</sub> /air/10% steam at 1 bar 373 K. the measurements compared with [30]....	63
Figure 5.3. The comparison of measured unstretched laminar burning velocity of n-dodecane/air mixtures at 1 bar 400 K with existing literatures .....	64
Figure 5.4. Burned gas Markstein length of premixed n-decane-air mixtures at 1 bar, 400 K, and different equivalence ratios .....	65
Figure 5.5. Repeatability of unstretched laminar burning velocity for stoichiometric (a) CH <sub>4</sub> /air at 1 bar, 300 K and (b) n-Dodecane/air at 1 bar 425 K mixtures, for five different experiments .....	66
Figure 6.1. Variation of unsteady pressure after ignition as a function of time for different equivalence ratios of n-dodecane-air mixtures at 1 bar 450 K .....	68
Figure 6.2. Variation of flame radius and stretched flame speeds as a function of time of stoichiometric n-dodecane-air mixtures at 1bar and 450 K.....	69
Figure 6.3. Variation in the stretched flame speed of n-dodecane-air mixture with the flame stretch rate at 1bar, 425K, and $\phi = 0.8-1.2$ .....	70
Figure 6.4. Comparison of the measured unstretched LBV of n-dodecane/air mixtures with simulations and literature data at 1 bar and 400 K. solid/ dashed lines – detailed/ reduced mechanisms.....	70
Figure 6.5. Variation of burned gas Markstein length of n-dodecane/air mixtures at different (a)initial mixture temperature and (b) pressure .....	72
Figure 6.6. Variation of Lewis, critical Lewis number, and flame thickness as a function of equivalence ratio of dodecane/air mixtures at 425K, 1-4 bar .....	74
Figure 6.7. A predicted local equivalence ratio of premixed dodecane-air mixtures at $\phi = 1.4$ , 1bar, and 425 K using CHEMKIN .....	74
Figure 6.8. Measured unstretched LBV against equivalence ratio of premixed n-dodecane/air mixtures at 1-4 bar and 425 K. Filled, and open symbols represent present and Hui et al. [37] data and lines are corresponding numerical predictions of different mechanism.....	75
Figure 6.9. Measured unstretched LBV as a function of the equivalence ratio of premixed n-dodecane/air mixtures at 1 bar and 400-450K. Symbols and lines represent the present experimental and corresponding numerical predictions .....	76

Figure 6.10. (a) Temperature and (b) pressure exponents of n-dodecane/air mixtures as a function of equivalence ratio. The solid (JetsurF2.0), dashed (PoliMi), and dotted (You et al.) represent corresponding numerical predictions .....	77
Figure 6.11. Normalized sensitivity coefficient of important elementary reactions of n-dodecane/air mixtures at different initial pressure 1-4 bar and 425K, $\phi = 1.4$ .....	78
Figure 6.12. The variation of critical flame radius (filled symbols) and Peclet number (dashed lines) as a function of burned gas Markstein length of dodecane/air mixtures at 425 K, 1-4 bar .....	79
Figure 7.1. Pressure-time history of premixed (a) n-C <sub>12</sub> H <sub>26</sub> –air mixture (black solid line) and 35% (n-C <sub>12</sub> H <sub>26</sub> +(18.5/ $\phi$ ) O <sub>2</sub> ) + 65% N <sub>2</sub> T = 450 K, and $\phi = 1.2$ at (b) 2 bar (blue solid line) (c) 4 bar (red solid line) measured inside the chamber after spark ignition .....	83
Figure 7.2. Shadowgraph image of propagating spherical flame of 65% N <sub>2</sub> /H <sub>2</sub> O/CO <sub>2</sub> diluted premixed n-dodecane/O <sub>2</sub> mixtures at R ~ 30 mm, 450 K, 1 bar and $\phi = 1.0$ .....	83
Figure 7.3. The comparison of measured and computed laminar burning velocities of (100-Z) % (n-C <sub>12</sub> H <sub>26</sub> +(18.5O <sub>2</sub> / $\phi$ )) +Z% N <sub>2</sub> , Z = 55-75% at 1 bar 400 K. The symbols indicate the experiment and lines (Solid blue-JetsurF2.0, Dashed blue – You et al., and dashed red – PoliMi-1410.....	84
Figure 7.4. Normalized LBV, peak net heat release rate, and peak XO+OH+H vs. equilibrium flame temperature computed for the stoichiometric (100-Z) % (n-C <sub>12</sub> H <sub>26</sub> +18.5O <sub>2</sub> ) +Z% N <sub>2</sub> , Z = 0% (simulation), 55%, 65%, 75%, 78% (measurement with air) at 1 bar and 450 K .....	85
Figure 7.5. Normalized sensitivity coefficients of the most influencing elementary reactions on LBV of mixtures and operating conditions mentioned in Figure 7.4 were obtained using You et al.....	86
Figure 7.6. Comparison of unstretched LBV of 35%(n-C <sub>12</sub> H <sub>26</sub> +(18.5O <sub>2</sub> / $\phi$ )) +65%N <sub>2</sub> mixtures at 1-4 bar, 450 K. The different symbols indicate the experimental LBV, and lines (Solid line- JetsurF2.0, Dashed line – You et al., and dotted line – PoliMi-1410) represents the computed LBV.....	88
Figure 7.7. Variation of burned gas Markstein length with an equivalence ratio of (100-Z) % (n-C <sub>12</sub> H <sub>26</sub> +(18.5O <sub>2</sub> / $\phi$ )) +Z% N <sub>2</sub> , Z =55-75% mixtures at 1 bar 400 K .....	88
Figure 7.8. Variation of burned gas Markstein lengths for a different equivalence ratio of 35% (n-C <sub>12</sub> H <sub>26</sub> +(18.5 O <sub>2</sub> / $\phi$ )) + 65% N <sub>2</sub> mixtures at 1 bar, 400-450 K, and 1-4 bar at 450 K Effect of initial pressure on flame stability .....	90
Figure 7.9. Comparison of the unstretched laminar burning velocity of n-dodecane/O <sub>2</sub> mixtures burns in different diluent environments (N <sub>2</sub> , CO <sub>2</sub> , and H <sub>2</sub> O) at 1 bar 450 K. The symbols	

indicate the measurements and lines (Solid blue-Jetsurf2.0, Dashed blue – You et al., and dashed red – PoliMi-1410).....	91
Figure 7.10. The variation of effective and critical Lewis numbers of 35% (n-C <sub>12</sub> H <sub>26</sub> + (18.5O <sub>2</sub> /φ)) + 65% H <sub>2</sub> O/ N <sub>2</sub> / CO <sub>2</sub> mixtures at 1 bar and 450 K .....	93
Figure 7.11. Variation of experimental and analytical burned gas Markstein length as a function of equivalence ratio of n-dodecane/O <sub>2</sub> (a) with N <sub>2</sub> /CO <sub>2</sub> /H <sub>2</sub> O dilution (b) CO <sub>2</sub> dilution at 1-4 bar 450 K.....	94
Figure 7.12. Comparison of the unstretched laminar burning velocity of n-dodecane/O <sub>2</sub> mixtures burns with (a) 65% N <sub>2</sub> , (b) 65% H <sub>2</sub> O, and (c) 65% CO <sub>2</sub> diluents at different elevated pressures (1, 2, & 4 bar) and 450 K. The symbols (Filled-1 bar, open -2 bar, crossed-4 bar) denote the experimental and lines (Solid: Jetsurf2.0, dotted: You et al. and dashed: PoliMi-1410) denote predicted LBV.....	94
Figure 7.13. Pressure exponent (β) against equivalence ratio at 450 K, 1-4 bar, for 35% (n-C <sub>12</sub> H <sub>26</sub> + (18.5O <sub>2</sub> /φ)) + 65% N <sub>2</sub> / CO <sub>2</sub> / H <sub>2</sub> O and n-dodecane-air mixtures .....	95
Figure 7.14. Variation of Zel'dovich number Ze, the thermal expansion coefficient σ, the flame thickness δ, and thermal diffusivity α of 35% (n-C <sub>12</sub> H <sub>26</sub> + (18.5O <sub>2</sub> /φ)) + 65% N <sub>2</sub> / CO <sub>2</sub> / H <sub>2</sub> O flames at 450 K and 1 bar as a function of equivalence ratio .....	96
Figure 7.15. Sensitivity coefficients of 35% (n-C <sub>12</sub> H <sub>26</sub> + (18.5O <sub>2</sub> /φ)) + 65% N <sub>2</sub> / CO <sub>2</sub> / H <sub>2</sub> O mixtures at 1 and 4 bar, 450 K using Jetsurf2.0 detailed kinetic mechanism at (a) lean mixture φ = 0.6 and (b) rich mixture φ = 1.4.....	98
Figure 7.16. Experimental Burned gas Markstein lengths of Z% (n-C <sub>12</sub> H <sub>26</sub> + (18.5O <sub>2</sub> /φ)) + (1-Z) % H <sub>2</sub> O/ N <sub>2</sub> / CO <sub>2</sub> mixtures with EFT at 450 K, 1 bar & 4 bar and φ=0.8,1,1.4. Z=65% for CO <sub>2</sub> and H <sub>2</sub> O. Z=55-78.1% for N <sub>2</sub> . Also, at 78.1%N <sub>2</sub> , 400 K, and 425 K at φ=1.4 were also plotted. Red, black, & blue represents φ=0.8,1,1.4. Square and its variants represent 55-78.1%N <sub>2</sub> dilution. Shaded star and inverted triangles – 65%H <sub>2</sub> O and 65%CO <sub>2</sub> , Symbols without cross mark – 1 bar, Symbols with cross mark – 4 bar, respectively.....	99
Figure 7.17. Reaction pathway diagram for 35% (n-C <sub>12</sub> H <sub>26</sub> + (18.5O <sub>2</sub> /φ)) + 65% CO <sub>2</sub> diluted stoichiometric mixture at 450 K 1 bar .....	101
Figure 7.18. Reaction pathway diagram for 35% (n-C <sub>12</sub> H <sub>26</sub> + (18.5O <sub>2</sub> /φ)) + 65% H <sub>2</sub> O diluted stoichiometric mixture at 450 K 1 bar .....	102
Figure 7.19. Reaction pathway diagram for 35% (n-C <sub>12</sub> H <sub>26</sub> + (18.5O <sub>2</sub> /φ)) + 65% N <sub>2</sub> diluted stoichiometric mixture at 450 K 1 bar .....	103

Figure 8.1. Variation of stretched flame speed with the stretch rate of $\{(1-z) \% \text{ n-C}_{12}\text{H}_{26}+z\% \text{ H}_2\}$ /air mixtures, $z$ varies 0-40% at 1 bar 425 K (a) $\phi = 0.8$ (b) $\phi = 1.4$ . Symbols indicate the experimental data points used for extrapolation, dashed and solid lines represent the implied linear and nonlinear extrapolations schemes .....	106
Figure 8.2. The trend of extrapolation criteria $Ma_{\text{linear}}Ka_{\text{mid}}$ with an equivalence ratio of $\{(1-z) \% \text{ n-C}_{12}\text{H}_{26}+z\% \text{ H}_2\}$ /air mixtures, $z$ varies 0-40% at 1-4 bar 425 K. The two dashed lines represent the lower and upper limits of $-0.05 < Ma_{\text{linear}}Ka_{\text{mid}} < 0.15$ , as suggested by Wu et al. [126].....	107
Figure 8.3. Laminar burning velocity of $\{(1-z) \text{ n-C}_{12}\text{H}_{26}+z\% \text{ H}_2\}$ /air mixtures, $z$ varies 0-40% at 1 bar 425 K. Symbols and lines represent experimental and corresponding numerical simulation, respectively .....	108
Figure 8.4. Variation of Laminar burning velocity with $\text{H}_2$ fraction of $\{(1-z) \text{ n-C}_{12}\text{H}_{26}+z\% \text{ H}_2\}$ /air mixtures, $z$ varies 0-40% at (a)1 bar (b) 2 bar and (c) 4 bar and 425 K.....	108
Figure 8.5. Variation of Laminar burning velocity with $\text{H}_2$ fraction of (60% $\text{ n-C}_{12}\text{H}_{26}$ +40% $\text{H}_2$ )/air mixtures at 425 K, and (a)1 bar, (b) 2 bar, and (c) 4 bar .....	109
Figure 8.6. The normalized laminar burning velocity of $\{(1-z) \text{ n-C}_{12}\text{H}_{26}+z\% \text{ H}_2\}$ /air mixtures, $z$ , varies 0-40% as a function of hydrogen ratio for different normalized initial pressures...	110
Figure 8.7. Simulated mole fractions of key radicals and adiabatic flame temperature of stoichiometric $\{(1-z) \text{ n-C}_{12}\text{H}_{26}+z\% \text{ H}_2\}$ /air mixtures, $z$ varies 0-40% at bar 425 K.....	110
Figure 8.8. Measured burned gas Markstein length of (60% $\text{ n-C}_{12}\text{H}_{26}$ + 40% $\text{H}_2$ ) / air flames, at 1-4 bar 425 K as a function of (a) equivalence ratio, (b) Hydrogen ratio. An unstable region is highlighted with color .....	111
Figure 8.9. Shadowgraph images of spherically propagating (burning sequence of the flames of) $\{(1-z) \text{ n-C}_{12}\text{H}_{26}+z\% \text{ H}_2\}$ /air flames at $R = 30$ mm, $T_u = 425$ K, $P_u = 1-4$ bar, $\phi = 1.4$ , $X_{\text{H}_2} = 0-40\%$ .....	112
Figure 8.10. Variation of Zeldovich number $Ze$ , the thermal expansion coefficient $\sigma$ , the flame thickness $\delta$ , and the effective Lewis number of $\text{n-dodecane}/\text{H}_2/\text{air}$ flames as a function of equivalence ratio at 425 K. (a) at different initial pressures and $X_{\text{H}_2} = 20\%$ (b) at different $\text{H}_2$ ratio and 1 bar .....	114
Figure 8.11. The normalized sensitivity coefficient for the laminar burning velocity of $\{(1-z) \text{ n-C}_{12}\text{H}_{26}+z\% \text{ H}_2\}$ /air flames, $z$ varies 0-40% at 425 K and 1 bar (a) lean: $\phi = 0.8$ (b) stoichiometric: $\phi = 1.0$ and (c) rich: $\phi = 1.4$ .....	116
Figure 8.12. Normalized sensitivity coefficient of $\{(1-z) \text{ n-C}_{12}\text{H}_{26} + z\% \text{ H}_2\}$ /air flames, $z$ varies 0-40% at 425 K, 2-4 bar, and $\phi = 1.0$ .....	116

Figure 8.13. Reaction pathway diagram showing the carbon elemental flux change of n-dodecane/H <sub>2</sub> /air with (a) X <sub>H<sub>2</sub></sub> = 0% and (b) X <sub>H<sub>2</sub></sub> = 40% mixtures at $\phi = 1.4$ , at 450 K and 1 bar .....	118
Figure 8.14. Effect of H <sub>2</sub> addition of n-dodecane/H <sub>2</sub> /air mixtures on emissions (a) CO <sub>2</sub> and CO (b) NO <sub>x</sub> at 1 bar 425 K .....	119
Figure 9.1. Variation of burned gas Markstein length with equivalence ratio for different percentages of steam addition in the mixture at 1bar and 393 K (shaded symbols) 423 K (open symbols) obtained through nonlinear extrapolation method .....	122
Figure 9.2. Experimental (symbols) and computed (Solid and dotted lines) laminar burning velocities of CH <sub>4</sub> /O <sub>2</sub> / % Steam mixtures as a function of the equivalence ratio with various steam percentages at 1 bar 393 K (filled symbols) and 1bar 423 K (Open symbols). Dash lines represent laminar burning velocity data using the FFCM-1 mechanism, and the filled star symbol represents [43] data. The open star symbol indicates the present correlation prediction at the same operating condition .....	123
Figure 9.3. Experimental (symbols) and predicted (solid lines) laminar burning velocities of 50% (CH <sub>4</sub> + (2O <sub>2</sub> / $\phi$ ))+50% H <sub>2</sub> O mixtures at different equivalence ratios, 1-4 bar and 423 K. Continuous line – GRIMech3.0 dashed line- FFCM-1 and dark shaded star symbol represent [85] data. The open star symbol indicates the prediction using the present correlation at the same operating condition .....	124
Figure 9.4. Normalized sensitivity coefficients of top ten contributing elementary reactions of Stoichiometric 50% (CH <sub>4</sub> + (2O <sub>2</sub> / $\phi$ )) +50% H <sub>2</sub> O mixtures at initial pressures 1-4 bar and 423 K.....	125
Figure 9.5. Experimental (symbols) and predicted (solid lines) laminar burning velocities of 50% (CH <sub>4</sub> + (2O <sub>2</sub> / $\phi$ )) +50% H <sub>2</sub> O mixtures at different equivalence ratios, 1 bar and 393, 423, and 453 K. Continuous line – GRIMech3.0, dashed line- FFCM-1 .....	126
Figure 9.6. Variation in the burned gas Markstein length with an equivalence ratio of 50% (CH <sub>4</sub> + (2O <sub>2</sub> / $\phi$ )) +50% diluents at 1 bar and 423K .....	126
Figure 9.7. Variation in the effective/ critical Lewis number with an equivalence ratio of 50% (CH <sub>4</sub> + (2O <sub>2</sub> / $\phi$ )) +50% diluents at 1 bar and 423K.....	127
Figure 9.8. Experimental (symbols) and predicted (solid lines) unstretched LBV of 50% (CH <sub>4</sub> + (2O <sub>2</sub> / $\phi$ )) +50% diluents mixtures at different equivalence ratios at 1 bar and 423 K Continuous line – GRIMech3.0, dashed line- FFCM-1 and dotted line-modified GRIMech3.0 .....	128

Figure 9.9. (a) Variation in laminar burning velocities of 50% ( $\text{CH}_4 + (2\text{O}_2 / \phi)$ ) +50% diluents mixtures with initial temperatures and equivalence ratios at 1 bar. (b) Temperature exponent as a function of equivalence ratio. Continuous line – GRIMech3.0, dashed line- FFCM-1 ..... 129

Figure 9.10. (a) Variation in laminar burning velocities of 50% ( $\text{CH}_4 + (2\text{O}_2 / \phi)$ ) + 50% diluents" mixtures with an equivalence ratio at 423 K and 2 bar & 4 bar. (b): Pressure exponent as a function of equivalence ratio. Continuous line – GRIMech3.0, dashed line- FFCM-1 .130

Figure 9.11. Experimental (symbols) and computed (Solid and dotted lines) laminar burning velocities of  $(100-z) \% (\text{CH}_4+2\text{O}_2/\phi) +z\%\text{H}_2\text{O}$  where z was varied from 40-60% steam at different equivalence ratios, 1bar and 423 K. Continuous/dashed lines correspond to GRIMech3.0, and present correlation fits and filled star symbol represents [43] data. The open star symbol indicates the present correlation prediction at referred operating condition ..... 131



# CHAPTER 1

## INTRODUCTION

### 1.1 General Introduction

Air connectivity is today's buzzword to connect everyone in the world. The demand for aviation liquid fuel, a kerosene variant, continuously increases. Similarly, another kerosene variant is used in rockets too. Nearly 50% of the global oil demand caters to the transportation and aviation sectors [1]. The attractive advantages of the kerosene variants are their storability, high energy density, and shallow freezing point. It is comprised of hundreds of intermediate components. In most studies, the kerosene-based fuels are mimicked with a surrogate fuel comprising either n-Decane or n-Dodecane or a blend of two to three pure liquid fuels [2]. The purpose of “surrogate fuels” is to accurately reproduce the physical, transport, and combustion properties of real fuels using a mixture of fewer number of single component fuels. As lesser fuel components are involved in the surrogates, their fuel properties and combustion characteristics are accurately measured. Later, they are used for testing the detailed chemical kinetic models available for the real multicomponent fuel. Also, the simulation of a combustion application with a surrogate fuel requires shorter computational time. Several chemical kinetic models are available for lighter hydrocarbons and were tested thoroughly and reported in the literature.

To test and validate the existing chemical kinetic schemes of n-decane and n-dodecane, ignition delay time and LBV are often used [2–4]. As the existing LBV database on n-dodecane is limited, this work was dedicated to fill the gap, which helps in testing the chemical kinetic models accurately. This work does not involve in the findings of a new surrogate. Instead, the combustion characteristics, such as the laminar burning velocity, of one of the surrogate component species, n-dodecane, of a multicomponent liquid fuel, jet or kerosene fuel, is thoroughly investigated in this work.

### 1.2 Oxy-n-dodecane

Greenhouse gas emission causes global warming, and CO<sub>2</sub> is the primary contributor [5]. Reduction in CO<sub>2</sub> generation and its capture is the way forward to limit or negate its impact on the environment. Oxy-fuel combustion, as one of the key technologies, has received much attention in ground power generation [6] and as well as in space-relevant applications [7].

Allam cycle [8] is a futuristic closed thermodynamic cycle getting attention to reduce greenhouse gas emissions from power plants. Here the hydrocarbon fuel is burnt with pure oxygen in the presence of CO<sub>2</sub> at relatively higher pressures. After the expansion of the exhaust gases in the turbine, the CO<sub>2</sub> was captured and utilized back in the combustor. At present, technologies like EGR, oxygen enrichment, and in-cylinder water injection are utilized to improve the combustion and emission performance of internal combustion engines [9]. A novel development by Wu et al. [10] was that oxy-propane burnt in the presence of CO<sub>2</sub> in an IC engine, and along with in-cylinder water injection, to have zero NO<sub>x</sub> emissions together with better thermal efficiency in a SI engine. Yi [11] demonstrated the advantages of burning high water content fuels with pure oxygen in a swirl burner to cut down the energy intensive dewatering process of fuels to improve the thermal efficiency of the system. They tested with ethanol, 1-propanol, tert-butanol, glycerol (C<sub>3</sub>H<sub>8</sub>O<sub>3</sub>), and their blends to have a sustainable flame. The above discussion clearly mentioned that the new technologies seek to use oxy-fuel combustion diluted with CO<sub>2</sub>, water, etc. The design of these combustion applications demands combustion characteristics like laminar burning velocity. This is also addressed in this work.

### **1.3 H<sub>2</sub>-blending in n-dodecane**

In the past few decades, hydrogen has received much attention as a potential alternative to fossil fuel-based power generation. Researchers around the world advocate hydrogen use because it is environmentally safe and clean. Moreover, hydrogen has 2.7 times the energy per unit mass as compared to that of n-dodecane. Replacing fossil fuels with non-carbon fuels like hydrogen (H<sub>2</sub>) or NH<sub>3</sub> is an important step to achieve the reduction of greenhouse gas emissions and global warming effects. Burning pure H<sub>2</sub> or NH<sub>3</sub> in existing combustion units involves many practical challenges due to its chemical structure. Hydrogen is a zero-carbon energy source, lightweight (2 g/mole) and has a high calorific value of 120 – 140 MJ/kg – roughly two to three times higher than that of hydrocarbon fuels (44-50 MJ/kg). The combustion product of hydrogen reacting with air/ oxygen is water vapor (H<sub>2</sub>O), environmental friendly one, which is an attractive characteristic that makes it a superior fuel compared to that of hydrocarbon fuels. However, hydrogen is not yet a feasible option for practical applications due to high risk of leaks, low-ignition energy (0.017 mJ), high flammability (4% -75% by volume), laminar burning velocity of ~ 3 m/s at equivalence ratio 1.8 and consequential risk of explosion. These risks can be minimized by blending hydrogen with hydrocarbons, results in a blended fuel with enhanced combustion characteristics. In the automobile sector, hydrogen blending increases the hydroxyl radical, and the combustion process accelerated. Also, peak heat release rate and

cylinder pressure increases, ignition delay, and combustion duration decreases. Additionally, with hydrogen blending increases, the knock resistance is enhanced because hydrogen has a high knock resistance and octane number. Therefore, to gain the merits of non-carbon fuels, blending them with the base fuels is the achievable intermediate step. Commercial aviation and industrial gas turbine engines are operated at lean heavy hydrocarbons-air mixtures to have high thermal efficiency and low NO<sub>x</sub> emissions [12]. The major issues associated with lean heavy hydrocarbon-air combustion at high pressures are the narrow flammability limits, local flame quenching due to the low LBV, ignition difficulties, and the slow diffusivity of heavy fuels resulted in thermo-diffusional instabilities. One of the effective options to overcome most of the above-mentioned challenges is by blending highly reactive hydrogen with slow reactive heavy hydrocarbons. The advantage of blending the lighter hydrogen with a heavy hydrocarbon was essentially due to its high reactivity, faster diffusivity, wider flammability limit, and low minimum ignition energy [13]. H<sub>2</sub> blending enhances the overall mixture diffusivity, which results in improved flame stability [14]. n-dodecane is one of the important high-volume components (~ 35%) in many surrogates of practical fuels [15].

## **1.4 Basic Concepts**

The fundamental combustion concepts related to the current study are discussed below.

### **1.4.1 Combustion**

Combustion is a rapid oxidation process of a fuel that generates heat, or both heat and light [16]. As the present work measures the LBV, only gaseous combustible mixtures are considered. Based on the state of mixedness, the combustion is classified as premixed or non-premixed. In premixed combustion, the fuel and the oxidizer are mixed to the molecular level, whereas in the non-premixed case, the fuel and the oxidizer meet and react at the reaction zone. As the LBV is a characteristic of a premixed gaseous combustible mixture, this work involves only premixed combustion. Flames can also be either laminar or turbulent based on the flow conditions. The focus of this study is only on the laminar, premixed gaseous combustion.

### **1.4.2 Equivalence ratio**

Equivalence ratio ( $\phi$ ) is a non-dimensional variable to characterize the composition of a premixed combustion mixture. It is defined as the ratio of stoichiometric oxidizer to fuel to the actual oxidizer to fuel ratio as

$$\phi = \frac{\left(\frac{\text{oxidizer}}{\text{fuel}}\right)_{\text{Stoichiometric}}}{\left(\frac{\text{oxidizer}}{\text{fuel}}\right)_{\text{Actual}}} \quad 1.1$$

In this definition, both the oxidizer to fuel ratio should have the same units, and they can be either volume or mass. If  $\phi$  equals unity, it is called a stoichiometric mixture;  $\phi < 1$  refers to a fuel-lean mixture, and  $\phi > 1$  refers to a fuel-rich mixture.

### 1.4.3 Equilibrium flame temperature

The temperature of flame or products is an essential intensive thermodynamic property of the combustion process. It is a crucial variable in the design of a combustion application. It is necessary to provide adequate residence time to the combustion process, assumed to be adiabatic with the surroundings, to generate products at equilibrium composition and temperature. The equilibrium composition and temperature of the products are estimated for a given set of reactants considering the equivalence ratio, initial pressure, initial temperature, and prescribed/ expected product species. These are achieved by minimizing the Gibbs free energy approach and solving the energy equation. In this work, the equilibrium composition and the temperature are estimated using the equilibrium model in ANSYS CHEMKIN software [17].

### 1.4.4 Laminar burning velocity

Unstretched adiabatic laminar burning velocity (LBV or  $S_u^0$ ) of a premixed combustible mixture is defined as the relative velocity of unburned reactants propagating normal to the adiabatic planar flame front, as shown in Figure 1.1. It is a measure of the mixture's reactivity, diffusivity, and exothermicity and depends primarily on equivalence ratio, the temperature of the unburned mixture, and the pressure. It is a critical parameter in calculating and assessing complex phenomena like ignition, quenching, flashback, flame stabilization, etc.

It is one of the standard parameters used for validating and updating the existing and new chemical kinetic schemes.

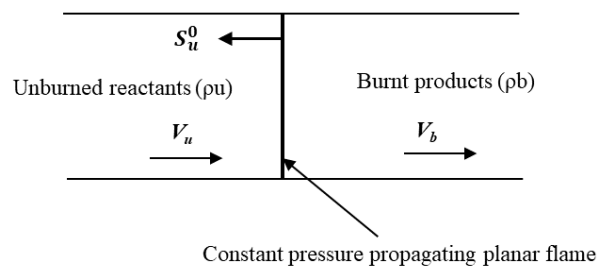


Figure 1.1. Planar flame propagating into the quiescent unburned fuel-air mixture at constant pressure

Figure 1.1 shows the sketch of a one-dimensional, adiabatic planar flame propagating normal to the quiescent unburned gas fuel-air mixture at constant pressure condition. Both the unburned reactants and burned products are assumed to be at different thermodynamic states demarcated by the flame front. The burnt products move away from the flame at a velocity of  $V_b$ . With respect to the laboratory coordinates, the planar flame propagates into the unburned gas mixture at a velocity of  $S_u^0$  from the point of ignition and is called unstretched, adiabatic, laminar burning velocity. With reference to the flame coordinates, the upstream unburned mixture flows into the flame and gets transformed into products at a velocity of  $V_u$ , then the LBV of the planar flame propagating normal to the quiescent mixture at constant pressure conditions is the same as that of the unburned gas velocity which is shown in

$$S_u^0 = V_u \quad 1.2$$

Applying the conservation of mass across the constant pressure planar flame having a cross-sectional area,  $A_f$ , yields

$$\rho_u S_u^0 = \rho_u V_u = \rho_b V_b \quad 1.3$$

where  $\rho_u$  is the density of the unburned gases,  $S_u^0$  is the one-dimensional, adiabatic laminar burning velocity,  $V_u$  is the velocity of the unburned gases,  $\rho_b$  is the density of burned gases, and  $V_b$  is the velocity of the burned gases.

### 1.4.5 Flame stretch

Flame stretch is the manifestation of the combined effects of flow non-uniformity, flame curvature, and flame motion [18]. A general definition of stretch at any point on a flame surface involves the rate of change of the area of an infinitesimal element of the flame surface, as follows:

$$K = \frac{1}{A} \frac{dA}{dt} s^{-1} \quad 1.4$$

where  $A$  is the area of an infinitesimal element on the flame surface. The above simple expression contains all the factors that contribute to the influence of stretch. Another more detailed and generalized expression reported by Law and Sung [19] which is applicable to all flame configurations is,

$$K = \{\nabla_t \cdot v_t + (V \cdot n)(\nabla \cdot n)\}_s \quad 1.5$$

Where  $\nabla_t$  and  $v_t$  are the tangential components of  $\nabla$  and  $v$  evaluated at the surface, and  $n$  is the unit normal vector of the surface, pointing in the direction of the unburned gas. The first term on the right-hand side of Eq. 1.5. represents the effect of flow non-uniformity through  $v$ ,

while the second term represents the effects of flame propagation/ motion through  $V$  and flame curvature through  $\nabla \cdot n$ . Freely expanding spherical flames are also classified as positively stretched flames as the flame is convex to the reactants and concave to the products. The spherical flame focusses the chemical energy into it and defocusses the thermal energy out of it. The stretch rate Eq. (1.6) of an expanding spherical flame is

$$K = \frac{2}{r_f} \frac{dr_f}{dt} \quad 1.6$$

Where  $r_f$  is the instantaneous flame radius and  $\frac{dr_f}{dt}$  is the flame speed with respect to laboratory coordinates. In Eq. 1.6, the first term  $\left(\frac{2}{r_f}\right)$  represents the curvature of the spherical flame, and the second term  $\left(\frac{dr_f}{dt}\right)$  represents the flame motion.

#### 1.4.6 Burned gas Markstein length

Burned gas Markstein length,  $L_b$ , addresses the sensitivity of the stretched laminar flame speed (speed of the flame with respect to the laboratory coordinates) to the flame stretch and thermo-diffusional effects in the weak stretch regime ( $Ka \ll 1$ ). Karlovitz number ( $Ka$ ) is defined as the ratio of the characteristic reaction time to the characteristic stretch time.  $L_b$  is independent of flame stretch rate.  $L_b$  depends only on the composition of unburned gas mixtures.  $L_b$  is calculated for weakly stretched flames with reference to either burned or unburned gas using a linear or nonlinear relationship between flame speed and flame stretch rate. The linear relation to finding  $L_b$  is shown in Eq. 1.7.

$$S_b = S_b^0 - L_b K \quad 1.7$$

The negative slope of Eq. 1.7 is  $L_b$ . If the value of  $L_b$  is positive, then it results in stable flames with respect to thermo-diffusional effects. If the value of  $L_b$  is negative, then it probably anchors (a) a stable flame – if the deficient reactant is not the fastest diffusive species, (b) an unstable flame – if the deficient reactant is more diffusive, it will alter the local equivalence ratio, and the propagation rate which resulted in instability due to the thermo-diffusional effects. From the literature as well as from the present work, it was observed that unstable spherical flames have large cracks on the surface during the propagation, whereas the stable flames were smooth without any irregularities on the flame surface.  $L_b$  strongly depends on the Lewis number (ratio of thermal diffusivity to the mass diffusivity of the mixture) of the mixture.

The discussion on the non-linear correlations available to find the  $L_b$  is reported in section 3.7.4. The ratio of burned gas Markstein length to the flame thickness is called the Markstein

number. It is a non-dimensional quantity. The flame thickness can be estimated in different ways. One way is to estimate from the flame's temperature profile. The temperature profile of the flame was predicted using a freely propagating planar flame model. Other methods are to estimate the flame thickness as a ratio of laminar burning velocity to thermal diffusivity or mass diffusivity. Mass diffusivity has multiple definitions, such as (a) binary diffusivity of a deficient reactant to a bulk species, (b) mixture mass diffusivity, and (c) multi-component diffusivity. Based on the choice of the flame thickness definition, the Markstein number can have multiple values. To avoid uncertainty, in the present work, only the fundamental burned gas Markstein length data were presented at all the studied operating conditions.

#### **1.4.7 Instabilities in outwardly propagating spherical flames**

In general, there are four modes of flame instabilities observed in outwardly propagating spherical flames: ignition, thermo-diffusive instability, hydrodynamic instability, and buoyancy-induced instability.

Ignition instability: Flame is highly disturbed from its inception till the full development, even when it is initiated using the minimum ignition energy. Outwardly propagating spherical flame is considered to be fully developed when the ratio of the flame thickness to the instantaneous flame radius is well less than unity. The effects of ignition can be visualized from the flame images, that the flame shape is not a regular sphere. As the flame grows, the transient effects of ignition die down, and the flame attains a smooth aspherical shape with reference to the point of ignition. In the present study, ignition-related instabilities are minimized or avoided by keeping the ignition energy as close to the mixture's minimum ignition energy. Also, the images having flame that were affected by ignition effects were not considered in the data reduction procedure by fixing an appropriate lower radius limit of 8 mm.

The second mechanism of flame instability is called thermo-diffusive instability. It is the mechanism of major interest in turbulent flame research due to its capability to enhance or retard the distortion of flame surfaces in the laminar flamelet regime. Thermo-diffusive instability is caused by the preferential diffusion of heat and mass, and hence it is governed by the Lewis number. If the  $Le > 1$ , preferential diffusion of heat dominates over mass in the flame, and hence, an increase in the stretch rate results in more heat loss from the reaction zone to the preheat zone, and it reduces the reaction rate and always results in stable flames. For mixtures having  $Le = 1$ , the effect of the flame stretch rate on the combustion characteristics is less as the preferential diffusion effects are absent. For the mixtures that have  $Le < 1$ , the preferential

diffusion effect of mass will dominate over the heat, which affects the local equivalence ratio, and possibly results in unstable flame, as explained in section 6.5.

Hydrodynamic instability arises as the low-density flame propagates into a high-density reactant. Its onset was easily identified from the sudden occurrence of small cells uniformly over the entire flame surface. This instability was observed at larger flame diameters for all the studied mixtures. The magnitude of the radius at which the hydrodynamic instability onsets differs with operating conditions. A flame that was unstable to thermo-diffusional effects preponed the onset of hydrodynamic instability. This was also studied and reported in this work.

Buoyancy induced instabilities are due to the acceleration of the heavier fluid into the lighter fluid, producing an unstable flame due to the effects of gravity. This type of instability generally occurs near flammability limits where the LBV is lesser than 18 cm/s. This effect can be visualized if the center of the flame transcends upwards from the geometrical center of the chamber. In the present work, buoyancy-induced instabilities are not considered, as the near-limit flames were not investigated.

## **1.5 Organisation of thesis**

The content of the thesis is organised into ten chapters. In addition to the above, a few appendices are also added to further explain the presented content.

*Chapter-1: Introduction.* This chapter outlines the general background and motivation behind the present objectives of the work. Later, the necessary fundamental combustion concepts pertinent to the current work are discussed, followed by the organization of the thesis.

*Chapter-2: Literature review.* The present work dealt with the four different mixture compositions of n-dodecane and methane fuels. A detailed literature review on the laminar flame characteristics relevant to the present objectives are presented and summarized. The research gaps are carefully identified, and the specific objectives are framed out and discussed.

*Chapter-3: Test rig development and experimental procedures.* The design of the test facility, along with its subsystems are concisely discussed in this chapter. Also, the experimental procedure, as well as post processing methodology of the experimental data, are presented.

*Chapter-4: Numerical approach.* The flame models used for the prediction of the unstretched laminar burning velocity, flame global properties, sensitivity analysis, and reaction pathway background theories are documented.

*Chapter-5: Test rig validation.* The validation results of the new test facility are presented independently for the gaseous and liquid fuels at various thermodynamic conditions.

*Chapter-6: Study-1: n-dodecane/air mixtures.* The results and discussion on laminar burning velocity and flame stabilities of n-dodecane reacting with air at elevated pressure and temperature and different equivalence ratios are presented.

*Chapter-7: Study-2: n-dodecane/O<sub>2</sub>/diluent mixtures.* The LBV and flame stability of oxy-n-dodecane mixtures diluted with different diluents at different thermodynamic and mixture conditions are presented in this chapter.

*Chapter-8: Study-3: n-dodecane/air with H<sub>2</sub> blending.* The effect of blending H<sub>2</sub> to n-dodecane and its effect on LBV and burned gas Markstein lengths at various operating conditions were reported in this chapter.

*Chapter-9: Study-4: CH<sub>4</sub>/O<sub>2</sub> with EGR diluents.* The absolute effect of individual EGR diluents, such as CO<sub>2</sub>/H<sub>2</sub>O/N<sub>2</sub>, on the LBV and flame stability due to thermo-diffusive effects, were discussed in this chapter.

*Chapter-10: Conclusions.* The comprehensive conclusion obtained from all the present studied objectives are reported. The future scope of this work is also presented.

*References:* All the referred sources in the above-discussed chapters are consolidated.



# CHAPTER 2

## LITERATURE REVIEW

### 2.1 Introduction

In this chapter, the different burning velocity measurement methods, along with their merits and demerits, are briefly discussed. The reasons for the choice of outwardly propagating spherical flame measurement method in the present work were provided. Subsequently, a literature review on the laminar burning velocity and flame stability of n-dodecane and methane reacting with (a) air and (b) artificial air with a higher mole fraction of oxygen is presented. Later, literature on the effect of the addition of (c) diluents like  $N_2/H_2O/CO_2$  in oxy- $CH_4$  and oxy-n- $C_{12}H_{26}$ , and (d) finally, the effect of hydrogen blending to n- $C_{12}H_{26}$  are also discussed. Ultimately, the possible research gaps were identified, and the specific objectives of the present work were chalked out.

### 2.2 Laminar Burning velocity measurement methods

There are various experimental techniques available to measure the laminar burning velocity, which can be categorized as stationary flame methods and propagating flame methods. In the stationary flame method, there are different ways to anchor a stationary flame. They are: (a) conical flames anchored at the exit of tubes/ orifices/ nozzles, (b) stagnation flames (counter-flow flame method), and burner stabilized flat flames (heat flux method) [20],[21],[22,23]. One of the chief propagating flame methods is the outwardly propagating spherical flame method. This method suits both the faster and slower combustible mixtures. This method facilitates LBV measurement at higher initial pressures and initial temperatures with high accuracy. The Table 2.2 and Table 2.2. briefly summarise the merits and demerits of each flame type in detail.

Table 2.1. Summary of merits and demerits of stationary

Method	Flame configuration	Advantage	Disadvantages
Stationary Flames	Conical flame anchored at the exit of a cylindrical/ orifice/ nozzle burner [20]	<ul style="list-style-type: none"> <li>• Traditional and Inexpensive method</li> <li>• Easy to use and simple data reduction procedures involved.</li> </ul>	<ul style="list-style-type: none"> <li>○ Flame anchoring challenges</li> <li>○ Strong curvature effect</li> <li>○ Difficult to quantify the stretch effects</li> <li>○ flame tip opening, polyhedral flames are challenges [24].</li> <li>○ Heat loss to the burner</li> </ul>

	Counter flow flame [21]	<ul style="list-style-type: none"> <li>• Generally adiabatic due to symmetry.</li> <li>• The stretch effects can be quantified, and unstretched LBV can be estimated.</li> </ul>	<ul style="list-style-type: none"> <li>○ Flame stabilization problem at high pressures due to heat loss to nozzle [25].</li> <li>○ Detecting flame at high pressure/small flame thickness is difficult with laser diagnostic techniques.</li> <li>○ Limited to low LBV and mid-range of operating pressures.</li> </ul>
	Flat flame burner method or Heat flux method [22]	<ul style="list-style-type: none"> <li>• Relatively simple and does not need a complicated diagnostic.</li> <li>• It's free of flame stretch effects.</li> </ul>	<ul style="list-style-type: none"> <li>○ The complicated design of burner plate [26].</li> <li>○ Applicable for mixtures with low LBV.</li> <li>○ The rig gets cumbersome for elevated initial pressures.</li> </ul>

Table 2.2. Summary of merits and demerits of propagating flames

Method	Flame configuration	Advantage	Disadvantages
Propagating flames	Cylindrical tube method [27]	<ul style="list-style-type: none"> <li>• Quite a simple method where a freely propagating planar flame was established inside a circular/rectangular tube containing a quiescent combustible mixture</li> </ul>	<ul style="list-style-type: none"> <li>○ Flame-to-wall interaction is unavoidable.</li> <li>○ Difficult to anchor a planar flame.</li> </ul>
	Soap bubble method [28]	<ul style="list-style-type: none"> <li>• The combustible mixture is filled inside a soap bubble and carefully ignite. During the flame propagation, both the flame and the enlargement of the soap bubble were recorded, and LBV was estimated.</li> <li>• Simple method.</li> </ul>	<ul style="list-style-type: none"> <li>○ Contamination of the combustible mixture by the moisture on the bubble surface.</li> <li>○ Soap bubble surface distortion during flame propagation</li> <li>○ Limited to a small range of initial pressure/temperature.</li> </ul>
	Spherically expanding flame [29]	<ul style="list-style-type: none"> <li>• LBV is measured from radius – time data.</li> <li>• Flame stretch effects were properly quantified, and unstretched LBV was estimated.</li> </ul>	<ul style="list-style-type: none"> <li>○ The rig is expensive. An involved data reduction procedure</li> <li>○ Flame instabilities at higher pressures [30].</li> <li>○ Lengthy experimental procedures,</li> </ul>

		<ul style="list-style-type: none"> <li>• Thermo-diffusional and hydrodynamic Flame stabilities were measured.</li> <li>• No need of first-hand information on the LBV of the mixtures to be investigated.</li> <li>• It can be utilized for fast/ slow mixtures and a wide range of initial pressure and temperatures.</li> </ul>	especially at high initial temperatures.
--	--	---	--

### **2.3 Outwardly spherical flame method in present work – it's choice and reasons**

The present work was aimed to measure the laminar burning velocities and burned gas Markstein lengths of fast-burning oxy-fuel mixtures in the presence of diluents, as well as slow-burning fuel-air mixtures too at temperatures ranging from 300-450 K, and initial pressures ranging from 1-4 bar. Based on the above discussion of different flame configurations, the outwardly propagating spherical flame method was the most appropriate method for the present objectives. An inherent additional feature of this method was its ability to quantify thermo-diffusional stability through burned gas Markstein length and hydrodynamic instability through a critical Peclet number. Standard combustion codes are available to simulate the one-dimensional spherical flames with different chemical kinetic schemes too. Hence, the outwardly propagating spherical flame method was chosen in the present work.

### **2.4 Liquid fuel evaporation strategies**

The preparation of a premixed gaseous combustible mixture that involved liquid hydrocarbon fuels was a challenge. First, the liquid fuel needed to be vaporized at a higher temperature well above its saturation temperature at a given pressure. The combustion rig that held the vaporized liquid fuel should also be at a higher temperature to prevent its condensation. The same procedure is applicable for the dilution studies with water too. But the challenges compounded if it was a heavy hydrocarbon fuel such as n-dodecane. The mole fraction of a heavy hydrocarbon and its associated partial pressure in a combustible mixture was quite small, So the uncertainty of the measured LBV strongly depends on the accuracy of the measurement. Researchers [31–33] reported two techniques, such as (a) Pre-vaporization of liquid fuel, (b)

volume method, to prepare a premixed combustible gas mixture that involved liquid fuels or dilution with the water at a given equivalence ratio, initial pressure, and initial temperature. This section discusses both techniques briefly.

### **2.4.1 Pre-vaporization of liquid fuel**

Metghalchi et al. [32] used the pre-vaporization of liquid fuel method in their study. In this method, fuel vapours of liquid fuel were generated in a vaporization chamber, and then it was transferred to the heated combustion rig, where the LBV was measured through a heated feed tube according to its partial pressure. After filling the fuel vapours, the oxidizer was later filled according to the partial pressure method, and the requisite combustible mixture was prepared in the chamber. Farrell and co-workers [31] also followed a similar approach. They improved the design of the vaporization chamber by adding a stirrer to prepare fuel vapours involving multiple liquid fuels. The merit of this method was that it was independent of the volume of the combustion rig. The demerits were it needed an additional vaporization chamber, feed pipes, and control valves.

### **2.4.2 Volume method**

In this method, a known volume of liquid fuel was directly injected into the combustion chamber and allowed to vaporize [33]. Hence, the fuel vapours were generated directly in the combustion chamber itself. It did not need a separate vaporization chamber and the associated feed systems. The accurate volume of the combustion chamber was quite essential to estimate the quantity of liquid fuel to be injected. Usually, the combustion chamber was heated to the required initial temperature and evacuated. Its absolute pressure before the liquid fuel injection was noted down. Then the liquid fuel was injected and allowed to vaporize. The chamber pressure increased till the complete vaporization of the liquid fuel. The final chamber pressure after the fuel vaporization was also noted down. The net increase in the chamber pressure due to the injection of the liquid fuel had to match the desired partial pressure of the fuel. In this work also, the volume method was used.

The number of fuel moles required at a given equivalence ratio, initial pressure, and the temperature was determined from the volume of the combustion chamber, partial pressure of the fuel, and the initial temperature using the equation of state as shown below:

$$N_{fuel} = \frac{p_{fuel}V}{R_u T} \quad 2.1$$

where  $N_{fuel}$ ,  $p_{fuel}$ ,  $V$ ,  $R_u$ , and  $T$  are the number of fuel moles, partial pressure of fuel, the volume of chamber, and the initial temperature of the mixture, respectively. And the volume of the liquid fuel was determined as

$$V_{fuel} = \frac{N_{fuel}MW}{\rho_{fuel}} \quad 2.2$$

Where  $V_{fuel}$ ,  $MW$ , and  $\rho$  are the volume, molar mass, and density of fuel, respectively. In this method, the decomposition of liquid fuel was eliminated by maintaining the bottom wall temperature of the combustion chamber well below the pyrolysis temperature of the liquid fuel.

## 2.5 Surrogate component fuel: *n*-Dodecane

The merits of *n*-dodecane and the requirement to study its combustion characteristics were briefed in the introduction section 1.2. In this chapter, the literature review on the unstretched/ stretched laminar burning velocity and the burned gas Markstein length of *n*-dodecane fuel reacting with air or oxygen was carried out. Table 2.3 summarizes the available literature LBV data of premixed *n*-dodecane-air mixtures. The limited data presented in the table essentially pointed out the experimental challenges involved with the heavy liquids.

Table 2.3. Literature data on laminar burning velocity data of *n*-dodecane + air mixtures

Reference	Method	$T_u$ (K)	$\phi$	Pressure	Extrapolation
Kumar et al. [34]	Counter flow	400, 470	0.7-1.4	1 bar	Linear
Ji et al. [35,36]	Counter flow	403	0.7-1.5	1 atm	Linear/ Nonlinear
Hui et al. [37]	Counter flow	400	0.7-1.4	1–3 atm	Linear/ Nonlinear
Ritcher [38]	Bunsen	473	0.7-1.8	0.1- 0.6 MPa	NA
Dortz et al. [39]	Spherical	400	0.7-1.4	0.1MPa	Nonlinear

Kumar and his co-workers [34] measured the LBV of *n*-decane/ *n*-dodecane and a kerosene surrogate reacting with air using a counter-flow twin flame method equipped with particle image velocimetry. Their measured LBV agreed well with Dryer mechanism predictions than JetsurF0.2. Ji et al. [35,36] measured the unstretched LBV (linear/ nonlinear scheme) and extinction strain rates of premixed *n*-dodecane/air, JP-7 /air, and JP-8 /air using the counter-flow/ stagnation flame method. They also reported a newly developed chemical kinetic scheme. Their measured LBV showed a good agreement with their own kinetic scheme as well as with JetsurF0.2 at all their investigated conditions. Ji et al. [36] investigated the effect of the cracking of *n*-dodecane on its LBV using a Bunsen flame method at 1 atm and 403 K. Dodecane cracked at higher temperatures and broke down into smaller fragments. To crack

dodecane, they heated it to 653 K and subsequently cooled it down to 398 K. Interestingly, the LBV of cracked dodecane-air mixtures was relatively higher than the uncracked dodecane. The cracking process resulted in the production of sub species like  $H_2$  and  $C_2H_4$  along with dodecane, which enhanced the enthalpy of the cracked fuel and resulted in higher LBV. Hui et al. [37] measured the unstretched LBV of several hydrocarbons ( $C_5$ - $C_{12}$ ) and jet fuel ( $C_{10.17}H_{19.91}$ )-air mixtures at 1-3 bar and 400 K using counter-flow flame and digital particle image velocimetry method. Their measurements matched well with the predictions using Naik et al. [40] mechanism as compared to that of JetsurF2.0 [41]. Ritcher et al. [38] used the Bunsen burner method to measure the LBV of the premixed n-dodecane/ air mixtures at  $p=0.1$  to 0.6 MPa and  $T=473$  K. Their data matched well with the Kumar et al. [34] measurements, and the deviation was within  $\pm 6.14\%$ . Recently, Dortz et al. [39] used the spherical flame method to measure the LBV of commercial kerosene and its pure components, and n-dodecane's LBV makes a better agreement with the JetsurF2.0 mechanism at atmospheric pressure.

The preceding discussion outlined that the study on the combustion characteristics of premixed n-dodecane-air mixtures such as LBV is quite few, irrespective of its prominent presence in many commercial liquid fuels and many surrogates, as mentioned in the introduction section. The common challenges in investigating the combustion characteristics of the n-dodecane are its low vapour pressure and high boiling point (65 mbar at 400 K and 370 mbar at 450 K). Even with the limited available data outlined in Table 2.3, none had estimated burned gas Markstein length ( $L_b$ ), which is considered one of the vital stability parameters to quantify the stretch and thermo-diffusive effects. Therefore, in the present work, one of the objectives was targeted to bridge the gap and measure the unstretched LBV and the burned gas Markstein length of the premixed n-dodecane-air mixtures at  $p=1$ - 4 bar,  $T=400$ -450K using freely expanding spherical flame method. All measurements were simulated using contemporary chemical kinetic schemes to predict LBV, and the same was compared to examine the prediction accuracy at higher pressures with the present measurements.

## 2.6 Oxy n-dodecane mixtures with EGR diluents

The benefit of burning fuels in pure oxygen was discussed in the introduction section 1.2. A brief analysis from a detailed literature review on the existing LBV data of oxy-fuel mixtures is as follows. Cai et al. [42] studied the effect of oxygen enrichment on the unstretched LBV and burned gas Markstein lengths of  $CH_4 + ((2(zO_2 + (1-z)N_2))/\phi)$  mixtures at elevated pressures using expanding spherical flame method and  $O_2$  in the air was varied from 21% to 60% at 353

K. Mazas et al. [43] measured the LBV of methane-air mixtures diluted with steam at 1 bar and 373 K using the conical flame method. Khan et al. [44] investigated the dilution effect of N<sub>2</sub>/CO<sub>2</sub> on the LBV of (100-Z) % (CH<sub>4</sub>+(2O<sub>2</sub>/φ)) +Z%(N<sub>2</sub>/CO<sub>2</sub>) and varied Z as 50-70%/ 30-50% mixtures at 1 bar, 300 K. They mentioned that the simulated LBV using the GRIMech3.0 were well under-predicted as compared to the experiments, and with the help of sensitivity analysis, they modified the kinetic parameters of the key elementary reactions in the GRIMech3.0, which improved the accuracy in the predictions.

The above discussion clearly indicated that (a) the oxy-fuel studies are available only for low alkane fuels, (b) No oxygen enrichment or pure oxy combustion studies are available for heavy alkanes like n-dodecane, irrespective of their predominant presence in commercial fuels like kerosene and Jet fuel, and it is one of the important components in the surrogate fuels of kerosene and Jet fuels. To bridge this important gap, the second objective of the present work was to measure the unstretched LBV and burned gas Markstein length of premixed n-dodecane-pure oxygen mixtures in the presence of third-party gaseous diluents like N<sub>2</sub>/CO<sub>2</sub>/H<sub>2</sub>O at elevated temperatures and pressures. The mixture was prepared by following the novel mixture-diluent approach proposed by Prathap et al. [45], which allowed to investigate and compare the effects of different diluents on the combustion characteristics at a given set of initial conditions. Unstretched LBV at all experimental conditions were predicted using CHEMKIN with different contemporary reaction mechanisms, and their accuracy were tested by comparing it with the present measurements.

## 2.7 Hydrogen blended n-dodecane

The introduction section explained the importance of the addition of H<sub>2</sub> to the existing conventional hydrocarbon fuels to increase its LBV, widen the flammability limit, and reduce the minimum ignition energy. This section discusses the literature review on the LBV of hydrocarbon fuels blended with H<sub>2</sub>. Significant research had been carried out to understand the effect of H<sub>2</sub> blending on the combustion characteristics of alkenes [46–50], alcohol [51,52], ethers [53,54], syngas [55–57], NH<sub>3</sub> [58–62], liquid hydrocarbon fuels [63–68]. Recent review articles [14,69–72] were also available on the effects of H<sub>2</sub> blending with conventional fuels. There are plenty of literatures available for studies on H<sub>2</sub> blended IC engines [73–78]. Okafor et al. [47] studied the effect of H<sub>2</sub> addition on lean CH<sub>4</sub>/air mixtures using the spherically propagating flame method at 1-5 bar, 350 K, and H<sub>2</sub> was varied from 0 to 100%. They reported that hydrodynamic instabilities occurred earlier and were enhanced with an increase of H<sub>2</sub>

fraction in the mixture, and Markstein length transitioned from positive to negative at elevated pressures of CH<sub>4</sub>/H<sub>2</sub>/air mixtures due to the thermo-diffusive effects. Berwal et al. [50] investigated the effect of H<sub>2</sub> addition to CH<sub>4</sub>/air mixtures using an externally heated diverging channel method at elevated temperatures of 300 – 650 K, atmospheric pressure, and mole fraction of H<sub>2</sub> in the mixture varied from 0 to 50% by volume. They reported that the LBV and temperature exponent of CH<sub>4</sub>/H<sub>2</sub>/air mixtures at elevated temperatures enhanced the LBV due to the H<sub>2</sub> addition. Xiao et al. [51] measured the LBV and Markstein length of the methanol/air mixture with 0-100% H<sub>2</sub> blending at 1 bar, 375 K using the spherically propagating flame method. They concluded that H<sub>2</sub> addition enhanced the LBV due to the enhancement of the radical pool, and the magnitude of Markstein length increased for the mixture having greater than 40% H<sub>2</sub> due to the strong diffusivity of the added hydrogen. Yu et al. [53] reported the LBV of dimethyl ether/H<sub>2</sub>/air mixtures at atmospheric pressure and temperature. They varied the mole fraction of H<sub>2</sub> from 0 to 100%. Their study revealed that above/ below a critical equivalence ratio ( $\phi^* = 1.3$ ), the magnitude of the Markstein length increased/ decreased with an increase in the mole fraction of H<sub>2</sub>. Zhang et al. [57] and Li et al. [62] studied the effect of H<sub>2</sub> addition on NH<sub>3</sub>/ air flames at 0.5-2 bar, 298 K, with 0 to 100% H<sub>2</sub> variation in the mixture. They reported that the cellular instabilities occurred at the lean mixtures due to the combined effect of thermo-diffusive and hydrodynamic instabilities. Comandini et al. [66] investigated the effect of H<sub>2</sub> addition on LBV and Markstein length of n-heptane/air flames with 0 to 50% H<sub>2</sub> at 1 bar, 294 K, using the spherically propagating flame method. Their results showed that a 10% increase in the LBV was observed for 50% H<sub>2</sub> addition due to an increase in the mole fraction of radicals in the flame. Also, a slight decrement in the magnitude of Markstein lengths were observed at lean mixtures with H<sub>2</sub> addition, and interestingly, there was no effect of H<sub>2</sub> addition in the rich mixtures. Xu et al. [64] measured the effect of the addition of H<sub>2</sub> on the LBV of n-decane-air mixtures using propagating Spherical flames at 1 - 2 bar and 470 K. The H<sub>2</sub> was varied from 0 to 50% in the mixture. They found that the LBV increased linearly with the addition of H<sub>2</sub>. At elevated pressures, with an increment of H<sub>2</sub> in the lean mixtures, the flames were more susceptible to instability. Recently, Akram et al. [67] numerically studied the effect of H<sub>2</sub> addition on the emission characteristics with the co-flow 2-D flame model. They found that H<sub>2</sub> addition diminished the production rate of CH<sub>3</sub>O and CH<sub>2</sub>O species, and hence, the mole fraction of CO<sub>2</sub> was reduced in the products. No study is available on the effect of the addition of H<sub>2</sub> on the LBV and burned gas Markstein length of n-dodecane-air mixtures. So, the third objective of the present work was to investigate the combustion characteristics of n-dodecane blended with hydrogen at different operating conditions. This study was quite

interesting as it involved the dual chemistry (lighter and highly reactive hydrogen and denser and slow-reacting heavy hydrocarbon) effect on the LBV, flame stability, and emission analysis. The hydrogen was added to n-dodecane in different mole fractions, the binary fuel mixture was burnt in the air, and their combustion characteristics were studied using a spherical flame method. Unstretched laminar burning velocity and burned gas Markstein length were measured at elevated pressures and different equivalence ratios. Later all the flame global parameters were estimated and discussed in detail for this binary fuel. The LBV measurement were compared with the predictions obtained with different detailed chemical mechanisms.

## 2.8 Oxy-methane mixtures with EGR dilution

The combustion characteristics of heavy hydrocarbons are a strong function of smaller species ( $C_0$ - $C_4$ ), and methane is one of the crucial species present in large quantities in natural gas. Methane is also used in hydrogen production through methane reformer plants. Natural gas/methane is extremely used in the ground power station under various Exhaust Gas Recirculation (EGR) diluent fractions. Important EGR diluents are  $CO_2$ ,  $H_2O$  and  $N_2$ . Steam was an independent diluent usually added to various combustible mixtures like hydrogen [79], syngas [80], and iso-octane [81] in order to reduce thermal  $NO_x$  emissions. The importance of oxy-fuel combustion at diluted conditions was detailed in the introduction section. It provides higher flame temperature, wider flammability limits, and wider flame stability limits too. A short summary of the existing research data on the addition of steam and other diluents and their respective effect on the combustion characteristics of the methane-oxidizer mixture is as follows.

Galmiche et al. [82] measured the independent effects of  $CO_2$ /  $N_2$ / steam/ He/ Ar on the LBV of  $(100-Z)\%(CH_4+4.76Air)+Z\%(N_2/CO_2/H_2O/Ar/He)$  at stoichiometric condition,  $Z= 0-30\%$ , 0.1 MPa and 393 K using freely expanding spherical flame method. They registered that at a constant percentage of diluent, the LBV was lowest in the following order  $CO_2$ / steam/ Ar/  $N_2$ / He. They performed simulations using fictitious species and reported that  $CO_2$  has the highest suppression effect due to both thermal (The addition of a diluent lead to a reduction in the chemical energy, flame temperature, and transport properties, and then it is addressed as thermal effect) and chemical effects (If the added diluent also participated in the reaction kinetics that may change the reaction paths and also the reaction rate, and it is addressed as a chemical effect [43]) whereas other diluents have only thermal effects. Mazas et al. [43] measured the LBV of methane-air mixtures diluted with steam at 1 bar and 373 K using the

conical flame method. Their study (i) increased the dilution fraction of steam and (ii) enhanced the mole fraction of O<sub>2</sub> in the air and studied its impact on the LBV. They found that the LBV decreased/ increased quasi-linearly with an increase in the mole fractions of steam/ O<sub>2</sub> due to the thermal effect. Boushaki et al. [83] investigated the dilution effect of the steam on the methane-air flames at 300-330 K and 1 bar by using a slot burner. They varied the steam content by changing the relative humidity from 0-100% at a given temperature. The LBV decreased linearly with an increase in the steam mole fraction. Albin et al. [84] measured the laminar/ turbulent burning velocities of methane-air mixtures represented by (100-Z)%(CH<sub>4</sub>+4.76/φ Air)+Z%H<sub>2</sub>O using both Bunsen and V-flame methods at 400, 480 K, 1 bar, steam dilution, Z was varied from 0-20% and φ=0.6-1.3. Recently, Cano et al. [85] investigated the effect of steam addition on the LBV of the stoichiometric methane-air mixtures using the spherically propagating flame method at 300-473 K and 1-5 bar. Their mixture composition is (100-Z)%(CH<sub>4</sub>+ΩO<sub>2</sub>+(1-Ω) N<sub>2</sub>)+Z%H<sub>2</sub>O as and they varied the mole fraction of O<sub>2</sub> in the air, Ω, from 0.21 to 1 and the mole fraction of the steam, Z, from 0-0.2. This study also provided the LBV and the L<sub>b</sub> for the premixed methane-oxygen mixtures with the steam dilution up to 70% at only stoichiometric mixture condition, 1-5 bar and 473 K. They reported that the steam addition resulted in both the chemical (weak) and thermal effects. They also mentioned that the weak chemical effect diminished with an increase in the initial pressure. Khan et al. [44] investigated the dilution effect of N<sub>2</sub>/ CO<sub>2</sub> on the LBV of oxy-methane mixtures at 1 bar and 300K. They represented the combustible mixture as (100-Z)% (CH<sub>4</sub> +  $\frac{2}{\phi}$  O<sub>2</sub>) + Z%(N<sub>2</sub>/CO<sub>2</sub>) and varied Z as 50-70%/ 30-50%. They reported that the simulated LBV using the GRIMech3.0 were well under predicted as compared with that of the experiments and with the help of sensitivity analysis, they modified the kinetic parameters of the key elementary reactions in the GRIMech3.0 which improved the accuracy in the predictions. Burned gas Markstein length remained positive for all of their investigated mixtures.

The oxy-methane reviews clearly stated that most of the research reported on the dilution with the steam in literature were mainly focused on: (a) lower mole fractions of steam, (b) studied with methane-air mixtures resulted in the presence of both N<sub>2</sub> and steam simultaneously which posed challenges in quantifying the independent dilution effect of steam, (c) quite a few measurements were performed with burner rigs which did not quantify the thermo-diffusive effects, (d) some studies were based on simulations only [86–89]. Also, it is hard to find studies on the LBV/ flame stability of premixed oxy-CH<sub>4</sub> mixtures other than Khan et al. [44] that too at atmospheric conditions. Hence, in this work, the independent effects arising due to the

addition of steam/ CO<sub>2</sub>/ N<sub>2</sub> on the laminar burning velocity and burned gas Markstein length of premixed methane- oxygen mixtures were performed at different: (i) dilution fractions of each diluent, (ii) equivalence ratios, (iii) elevated pressures and temperatures.

## 2.9 Conclusions of the literature survey

The foregoing literature review suggested that the outwardly propagating spherical flame method was one of the accurate methods for the measurement of LBV of fast/ slow burning mixtures at higher initial pressures and temperatures. It allows for the quantification of flame stretch effects along with the thermo-diffusive effects of the measured real flames and provides a methodology to find the unstretched LBV and the burned gas Markstein length. The extensive literature survey conducted in the present work clearly showed that the laminar burning velocity and the flame stability of lower alkane gaseous fuels burnt in conventional air at different operating conditions were abundantly available. On the other hand, the experimental data on unstretched LBV and burned gas Markstein length of premixed n-dodecane-air mixtures at elevated thermodynamic condition is scarce in the literature due to the measurement challenges. Also, there are no oxy combustion studies reported on heavy hydrocarbon liquid fuels till date. In addition, the effect of dilution with nitrogen, carbon dioxide, and argon of only lower alkane fuels burned under oxygen-enriched air conditions with various dilution levels at different operating conditions had also been studied. The important takeaways of the present literature review were that: (a) the requirement of accurate LBV and Markstein length data for premixed n-dodecane-air flames at elevated pressure and temperatures to validate the existing chemical kinetic mechanisms, (b) there is no study available on the independent dilution effects of all the major EGR gases on the LBV and flame stability, even for lower alkanes, (c) Also, it is hard to find studies on the LBV/ flame stability of premixed oxy-CH<sub>4</sub> mixtures at elevated thermodynamic conditions. On the other hand, for oxy-fuel combustion, information on heavy hydrocarbon fuel (n-decane/n-dodecane) was completely missing in the literature, irrespective of its prominent presence in many commercial fuels, due to the stiff challenges involved in their measurements. For liquid fuel vaporization, the direct injection strategy promises accuracy with less experimental implementations.

## 2.10 Objectives

The objectives of the present research are listed below:

1. To develop a new test facility to measure the unstretched LBV of both gaseous and liquid fuels reacting with air or with oxygen at diluted conditions using a freely expanding spherical flame method at high initial temperatures & pressures along with uncertainty analysis.
2. To study the effect of initial temperature and initial pressure on the LBV and flame stability of premixed n-dodecane-air mixtures at wide-range equivalence ratios.
3. To measure the unstretched LBV and burned gas Markstein length of premixed oxy-n-dodecane (higher alkane) and oxy-methane (lower alkane) mixtures diluted with different EGR gases.
  - Dilution with N<sub>2</sub> decreases the flame temperature and LBV, which allows the safe handling of high-temperature N<sub>2</sub>-diluted Oxy-hydrocarbon mixtures without compromising the structural integrity of the rig.
  - Dilution with steam/ CO<sub>2</sub> brings in all real-time effects like thermal-diffusion, radiation, and chemical effects.
4. To investigate the unstretched LBV and flame stability of n-dodecane blended with different proportions of H<sub>2</sub> at elevated pressures.
5. To predict the unstretched LBV using a freely propagating planar flame model in CHEMKIN for all the experiments using contemporary chemical kinetic schemes.

# CHAPTER 3

## EXPERIMENTAL RIG AND METHODOLOGY

The design of the experimental rig, various associated subsystems, experimental operating conditions, experimental procedure, post-processing methodologies, and experimental uncertainty quantification procedures are discussed in this chapter.

### 3.1 Combustion chamber

Based on the detailed literature study (section 2.2) on different flame configurations, outwardly expanding spherical flame was chosen in the present research. Therefore, to generate spherical flames experimentally in a confined environment, a constant volume combustion chamber was required. The combustible mixture was prepared inside the chamber mostly by the partial pressure method. The mixture was ignited at the centre of the chamber to initiate a spherical flame. Then, the spherical flame propagates from the centre towards the wall till the complete consumption of the combustible mixture. During the flame propagation, the pressure inside the chamber increases due to the energy release by the flame. During the initial consumption of 1-2% of the volume of the reactants in the chamber, the chamber pressure nearly remains close to that of the initial pressure, and this duration of flame propagation was called the pre-pressure period or constant pressure regime of the constant volume combustion chamber. In this method, the flames propagating in this duration was imaged and processed to find the LBV. Hence, the design of the chamber assumes much important. The larger the volume of the chamber, the longer will be the pre-pressure period, which allows to record of flame images with a larger radius, which provides a very accurate LBV. In the present work, a cuboidal combustion chamber was chosen, as shown in Figure 3.1. The choice of this cuboidal shape, a non-spherical one, was due to the following reasons: (a) heating cartridges can be easily inserted into the chamber walls for heating the chamber, which is essential for combustible mixtures involving liquid fuels, (b) flat surfaces of the combustion chamber provides easy access to an optical window, and all the inlet, exhaust, instrumentation ports, (c) insulation of the external surface of the combustion chamber is easy. The inner volume of the cuboidal chamber in the present work was  $215 \times 215 \times 315 \text{ mm}^3$ . The chamber was fitted with top and bottom flanges having a thickness of 50mm, respectively. The geometrical inner volume of the chamber was 14.56 L. The flanges were fastened to the chamber through sixteen M16 bolts on each side. To prevent the leak between the flange and the chamber, a square-

shaped endless silicon O-ring (ISG Elastomers, India) having a thickness of 8 mm was used. The combustion chamber has four circular optical accesses to visualize the flame propagation. The optical windows were mounted to the chamber with the help of circular flanges, having 8 numbers of M10 bolts on each side, as shown in Figure 3.1. An endless O ring having 6mm thickness was used between the optical window and the optical access to avoid the leak. To avoid glass to metal contact, the optical access region was sealed with 3 mm high-temperature gaskets (Novapress, Frenzelit). Figure 3.1 shows the complete and sectional CAD models of the chamber, as well as the actual fabricated chamber.

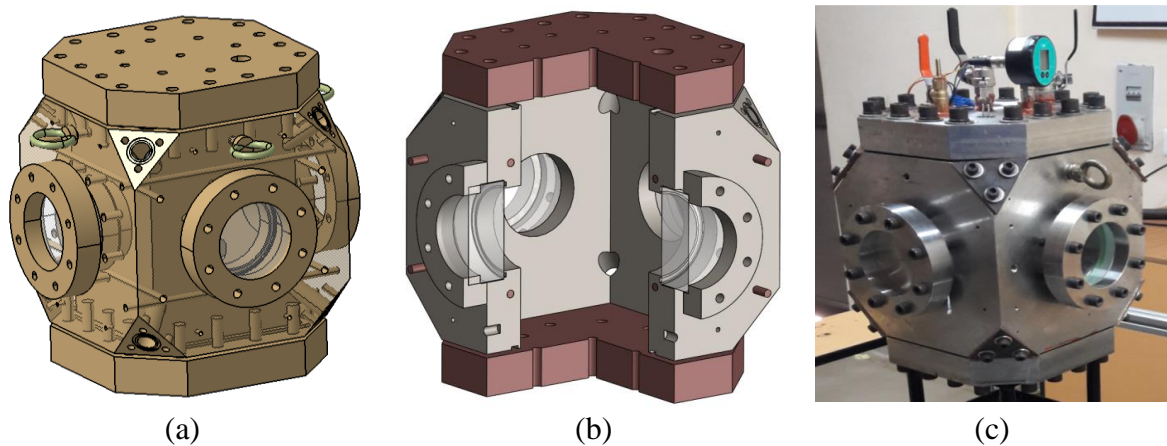


Figure 3.1. Final chamber design of (a) CAD model (b) sectional view (c) actual chamber

The maximum diameter of the sphere that just fits into the vessel is 215 mm. Therefore, a spherical flame can propagate up to a radius of 107.5 mm before it impinges on the wall. Taylor et al. [90] mentioned that after ignition, during 1-2% of the chamber volume, the pressure remains constant. Out of the 107.5mm wall radius, the data reduction radius range of 8-20 mm falls less than 1% of the chamber volume, and hence the constant pressure assumption was justified. Burke et al. [91] reported that a non-spherical combustion chamber could result in flame elongation on the longer side of the chamber as compared to its shorter side, and it will affect the accuracy in the measurement of LBV. They also pointed out that those effects were negligible if the flame radius used for the calculation of burning velocity exceeds 0.3 times the radius of the combustion chamber. In the present work, a cuboidal combustion chamber is used, and the range of flame radius used for the estimation of LBV was 8-20 mm only, and it was well within the 0.3 times that of one half of the shorter side of the cuboid of 107.5 mm. hence, the choice of the cuboidal chamber with an inner volume of 14.5 litres in the present work will result in the accurate measurement of unstretched LBV. The top and bottom flanges have eight different 1/2" BSP threaded ports to facilitate the mounting of different instruments and gas

inlet/ exhaust. Also, the top flange has a dedicated port to aid the flush mounting of the unsteady pressure sensor to measure the unsteady pressure evolution during the combustion event.

### 3.2 Leak test and Commissioning

After the fabrication, the combustion chamber was assembled with optical windows and undergone a hydraulic and pneumatic test at Proof Test Lab, LPSC Valiamala. The chamber with the optical windows was hydraulic tested till 100 bar for a duration of 15 min. The optical windows withstood the pressure. There was no leakage observed during the hydraulic test. Again, the pneumatic test was conducted till 50 bar for an hour to identify any possible leakages. No leakage was identified. The chamber was evacuated till 1 mbar, and it was kept at low pressure for almost 12 hours. There was no change in the chamber pressure. All these tests validated the design and its leak prevention strategies.

### 3.3 Design Specifications

Below Table 3.1 shows the key design specifications of the developed combustion chamber.

Table 3.1. Summary of final chamber design specifications

Sl. No.	Design parameter	Value
1	Design Pressure	100 bar
2	Temperature	500 K
3	Chamber Material	SS-304
4	Exact Inner volume	15.65 L (including crevices)
5	Inner & Outer shape	Cuboidal
6	Inner dimensions	215 × 215 × 315 mm <sup>3</sup>
7	Outer dimension	315 × 315 × 315 mm <sup>3</sup>
8	Wall thickness	50 mm
9	Weight	~200 kg
10	Clear aperture	107 mm
11	Number of optical accesses	4
12	Optical window material	Fused Quartz
13	Diameter of instrument holes	1/2" BSP
14	No. of flange bolts	16 (M16) on top & bottom (each) 8 (M12) on optical flanges (each)
15	Sealing	O-rings, Gaskets, and Septum
16	Temperature limitation of seals	230°C (503 K)
17	Number of access ports	18
18	Ignition electrodes	Vertically aligned
19	Cartridge heater port diameter	10 mm
20	No. of Cartridge ports	8

## 3.4 Design of subsystems

The present work demands following customized subsystems to carry out the experiments. The need, design, and functionality of each subsystem was clearly explained below:

### 3.4.1 Gas Flow systems

The gas flow system consists of dedicated feed lines for the (a) evacuation of the chamber, (b) filling of various gases in the chamber during the mixture preparation, and (c) purging of the product gases from the chamber after the experiments. Since the main combustion chamber undergoes heating, these flow lines need additional attention at their connection joints with the chamber.

**Evacuation system:** The evacuation feed line connected the chamber to the vacuum pump (HHV Pumps: 12 m<sup>3</sup>/hr). The feedline connection is comprised of leak-free fittings to generate the desired vacuum inside the chamber. Galvanized Iron (GI) tubes were used as the feedlines.

**Filling System:** The purpose of this system was to fill the high-purity fresh gases from the respective gas cylinders to the chamber through dedicated feedlines and control valves. The present work used a partial pressure method to prepare the combustible mixture.

**Purging system:** A separate metallic feedline was used for ventilating the hot product gases after the combustion event. The same feedline was used during the purging of the chamber too before and after the experiments. It is essential to release the hot product gases immediately, else the water vapour in the products undergo condensation and get deposited on the optical windows.

### 3.4.2 Heating System

Experiments involving liquid n-dodecane and steam at ambient conditions demanded the pre-vaporization of the liquid n-dodecane and water to achieve a homogeneous combustible mixture prior to the ignition. In the present work, the vaporization of the fuel was attained by heating the combustion chamber. To heat the chamber, a heating system was used. It consisted of eight split-type heating cartridges (Elmec Speciality heaters) having a diameter of 10 mm and a length of 300 mm. The heating cartridges (1 kW each) were positioned inside all the walls symmetrically to obtain a homogeneous temperature field inside the vessel as well as the mixture, as shown in Figure 3.2. A custom-designed microprocessor-based independent PID controller (Figure 3.3: A. G. Enterprises, load capacity of 2 kW each) was used to independently control the temperature of each cartridge based on the feedback of the gas

temperature. The entire circumference of the top and bottom flanges were heated separately with silicone tape heaters (Fusion Solutions, power density: 1 W/cm<sup>2</sup>). Ceramic fiber sheets (Shree ceramic fiber Pvt. Ltd, 1260 C, Thermal conductivity 0.12 W/m K) having a thickness of 5 mm were used to wrap all the flow lines and the entire outer surface of the chamber to prevent heat loss and hence, avoid the condensation of fuel vapour during the experiments.

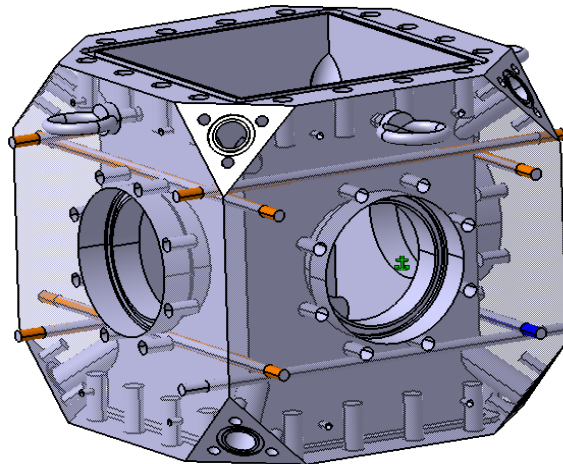


Figure 3.2. Graphical illustration of cartridge heater positions.

The main objective of the heating system was to have a steady and uniform temperature field inside the chamber to perform the experiment at the desired initial temperatures. To aid the heating process, four type-K sheathed thermocouples were inserted inside the chamber.



Figure 3.3. Images of the temperature controller and its electrical connection

### 3.4.3 Liquid Fuel injection system



Figure 3.4. Customized lengthy needle and gas-tight syringe

As mentioned in section 2.4.2, the volume method was followed in the present work to prepare the combustible mixture involving liquid fuel in the chamber. The liquid fuel was directly injected into the chamber using a 5 ml Gas-tight syringe (Hamilton-1005 TTL series) along with a 300 mm long needle (Hamilton), Shown in Figure 3.4. The long needle ensured that the liquid was injected at the centre of the chamber, which prevented the scattering of liquid fuel due to the low pressure inside the chamber.

### 3.4.4 Ignition system

In the present work, a spark ignition system was used to ignite the combustible mixture at the centre of the chamber. The custom-designed electrodes system (S & S advance ceramics) resembled a spark plug, typically used in petrol engines. It consisted of stainless-steel housing with ceramic sleeves, and thin SS rods were inserted and glued at the axis of the ceramic sleeves in order to electrically insulate it from the chamber. The surface of contact between the electrode, ceramic sleeve, and steel housing was coated with Inconel and later glazed to prevent leaks at high pressures and temperatures. The electrodes were 2 mm in diameter and 240 mm in length. The electrodes with pointed ends were carefully aligned in the vertical direction at the axis of the combustion chamber, and they faced each other in opposite directions at the centre of the chamber. The gap between the electrodes was adjustable from 0.5-3 mm. One of the electrodes was connected to an ignition coil (TVS Stick coil) which can be triggered externally, and the other one was electrically grounded. The length of the ceramic housing around the electrode was 40 mm which prevented the jumping of the spark to the chamber walls and provided a spark only at the centre of the chamber. Using a trigger pulse, a spark was

generated between the two electrodes to ignite the combustible mixture. In order to minimize the flame instability arising due to the highly transient spark ignition process, the deposited ignition energy typically matched that of the minimum ignition energy of the combustible mixture at all the measured conditions. Figure 3.5. shows the actual image of the high-temperature ceramic housing with an electrode (grounded one) and externally triggerable spark ignition stick coil.

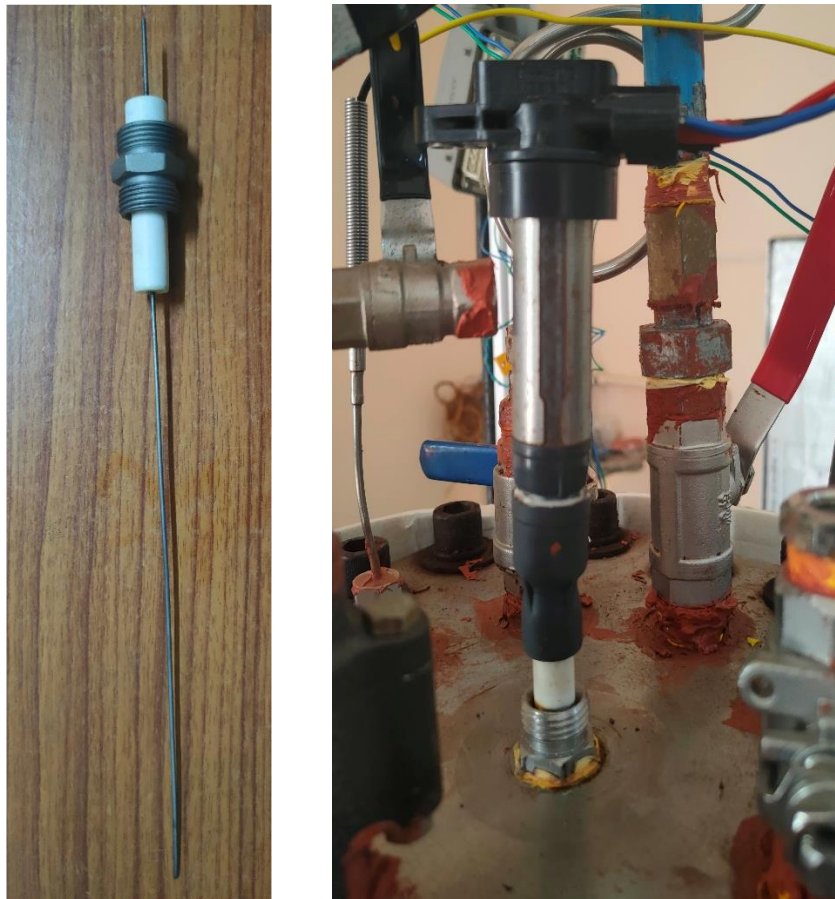


Figure 3.5. Ceramic electrode and externally triggerable ignition coil

### 3.4.5 Imaging system

To view and record the flame propagation inside the chamber, a high-speed z-type shadowgraph imaging method was used along with a high-speed camera (Phantom-V1210). The images were captured with a resolution of  $512 \times 512$  pixels with a framing rate between 10,000 to 17,000 frames per second based on the operating conditions. The schematic of a light source, mirrors, lens, camera, and its actual arrangements are shown in Figure 3.6. The light source is a 100 W LED chip (Luminus: CBT-140-WCS-L16-UA123) with a cooling fan arrangement that provides a sharp and intense beam of white light. A pinhole placed in front of the light source acts as a point light source. The light diverges from the pinhole and focused

on a spherical concave mirror (M1) of 6-inch diameter and 60-inch focal length, which generated a cylindrical collimated beam of light. The collimated light beam passed through the chamber to a second mirror (M2) placed behind the chamber. The 2<sup>nd</sup> mirror converges the beam to a planar mirror which reflected the light and focused onto the high-speed camera. The planar mirror was used to keep-off the high-speed camera from the hot chamber.

The light source, spherical concave mirrors, and flat mirror were aligned in a z configuration. The angle between the line of the axis of the light source and mirror is around 13° and it was kept the same as that of the angle between the line of the axis of the mirror and flat mirror to cancel out the aberrations arising due to the off-axis effect.

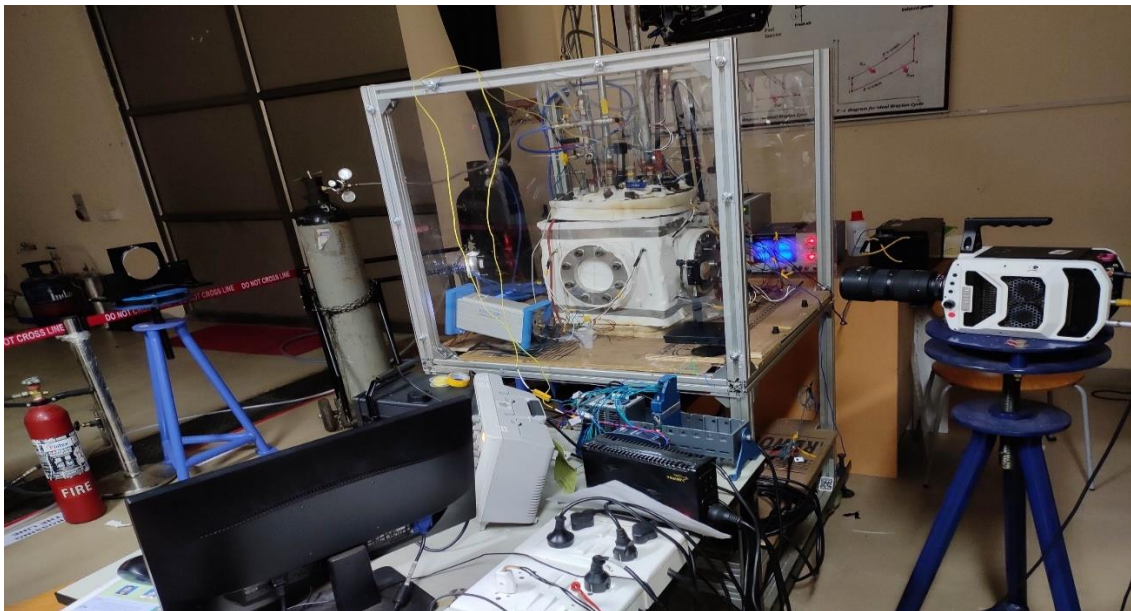
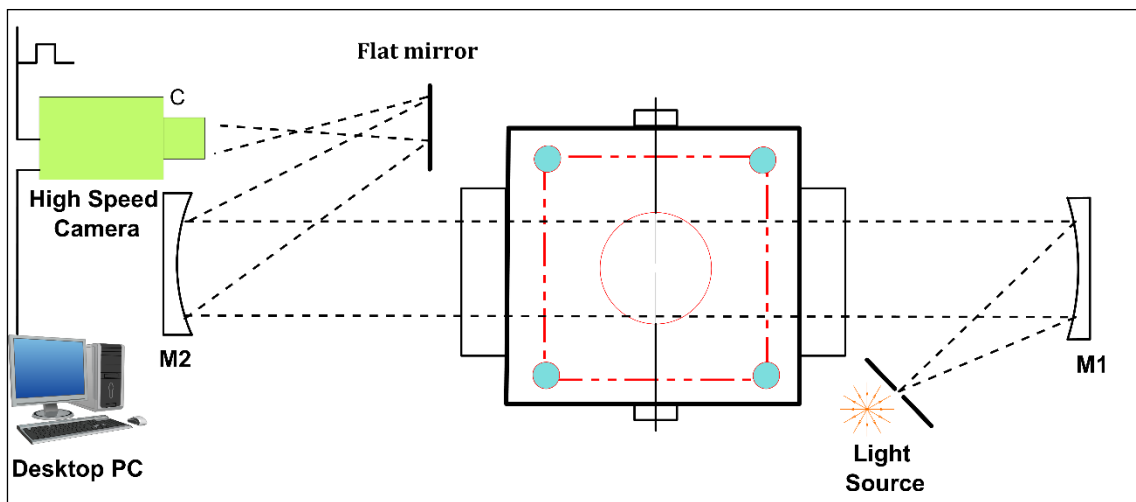


Figure 3.6. The schematic and actual arrangement of the shadowgraph system

The vertical and horizontal alignments of the optical paths and axis alignment of the optical beam and chamber was systematically verified using standard heights placed closed to the

optical windows on the two sides of the combustion chamber, which aligned with the optical beam. After the alignment, only one of the standard height was imaged in the camera. Then, the camera was focussed on the electrodes. The camera was set to external trigger mode so that it starts capturing the images only upon receiving a trigger signal. The diameter of the optical window was 127 mm. After fixing it into the chamber, the clear aperture was 107 mm.

### 3.4.6 Data acquisition system

The combustion chamber is equipped with pressure and temperature sensors to aid in the mixture preparation and to track the temperature and combustion events. One of the pressure sensors used was a piezoelectric unsteady pressure sensor (Kistler 7061B with a sensitivity of  $-80.0 \text{ pC/bar}$ ) designed explicitly for high-pressure combustion application, along with a charge amplifier (Kistler-5018B). This sensor was flush mounted to the top flange of the chamber, and it was used to measure the unsteady pressure rise during the combustion event. Its measurement range was from 0 to 250 bar. It generated a charge output. The charge amplifier converted the charge into voltage signals and amplified it to a level that was recordable in an oscilloscope. Another type of pressure sensor was the piezo-resistive type, which was used for preparing the combustible mixture in the chamber using the partial pressure method.

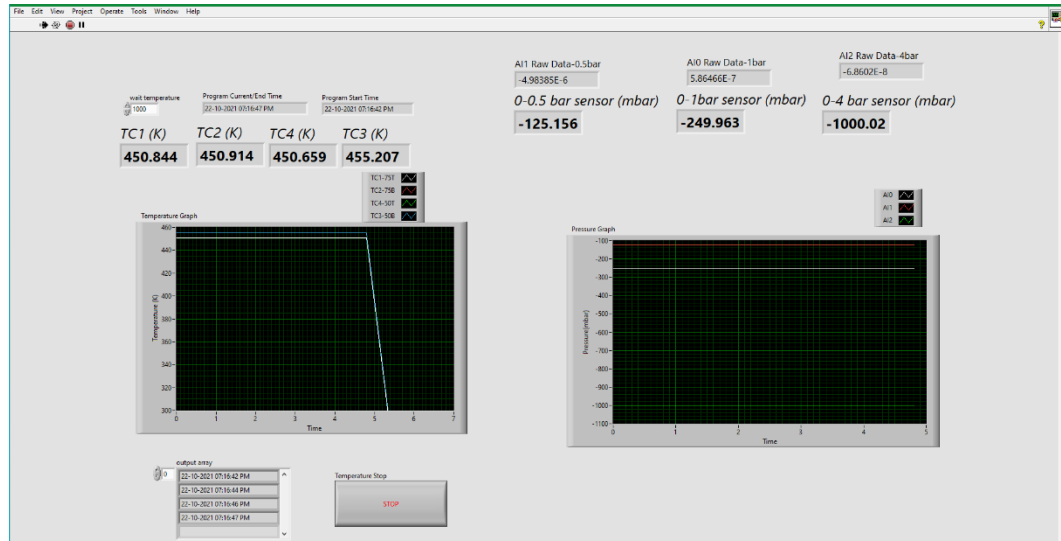


Figure 3.7. LabVIEW pressure and temperature measurement window

Therefore, three different ranges of absolute pressure transducers (0-0.5 bar & 0-1 bar with  $\pm 0.25\%$  FSL and 0-4 bar with  $\pm 0.1\%$  FSL) were used to minimize the uncertainty in equivalence ratio (less than 2%) in measurements. Four K-type thermocouples were used to measure the temperature of the mixture inside the chamber at different locations. The partial pressure and temperature variation inside the chamber was recorded in the LabVIEW using

NIcRIO 9035 with NI 9214 (Temperature) and NI-9203 (pressure), and the typical measurement window is shown in Figure 3.7.

### 3.4.7 Triggering system

The purpose of the triggering system was to synchronise the ignition, image acquisition, and data acquisition systems during the combustion event. The spark ignition coil, high-speed camera, and oscilloscope were connected to a digital pulse generator (BNC-577). A manual command to the pulse generator provides three different TTL Signals with 5 V to trigger all the above-mentioned devices simultaneously. Figure 3.8 shows the synchronisation arrangement of three devices with the three channels of the pulse generator. Before the synchronization, the properties of generated signals, like delay and pulse width, were tested in an oscilloscope.



Figure 3.8. Synchronisation of different devices with a digital pulse generator and signals delay accuracy tested in an oscilloscope

## 3.5 Experimental Procedure

The earlier section explained in detail about the rig and the instruments used for the measurement of LBV. In this section, the procedure for performing the experiments was discussed. Figure 3.9 shows the schematic and actual final arrangements of various subsystems along with the combustion chamber.

### 3.5.1 Preparation of Gaseous mixtures

For all the ambient temperature experiments, the chamber was thoroughly purged with dry air for 15 minutes and evacuated to a pressure of 1 mbar. The combustible mixture was

prepared using the partial-pressures method. First, the gas with the lowest partial pressure was filled, and later other gases were filled based on the ascending order of their partial pressures.

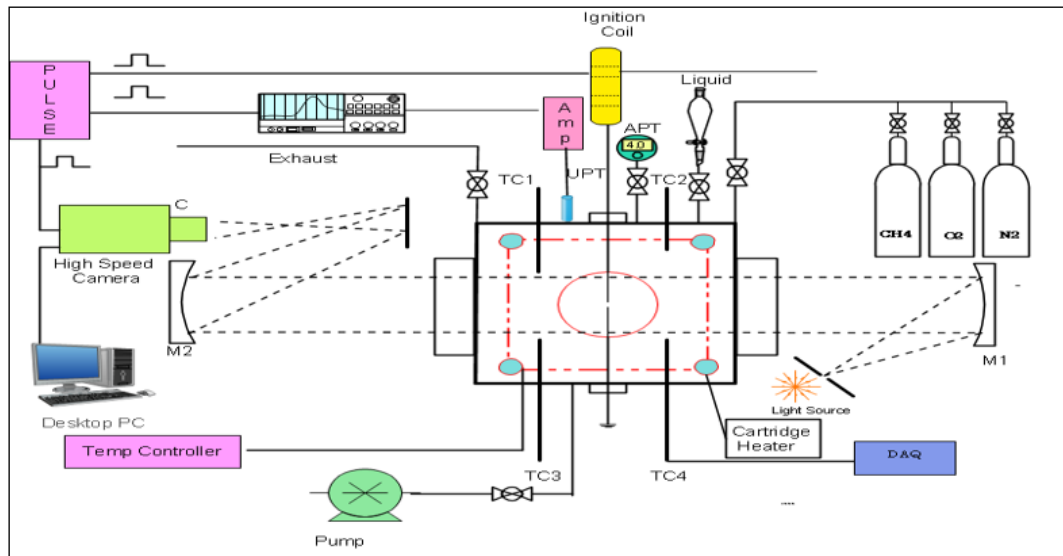


Figure 3.9. The schematic and actual arrangement of the spherical flame test facility

In the present work, the ultra-high pure gases such as CH<sub>4</sub> (99.9997%), O<sub>2</sub> (99.997%), N<sub>2</sub> (99.9995%), CO<sub>2</sub> (99.9995%) [Bhoruka gases private limited] were used. After filling, the chamber was left undisturbed for three minutes to attain a quiescent combustible mixture inside the chamber. The duration was obtained after multiple trails. At ambient temperature conditions, the duration of the whole experiment was shorter, and hence, three minutes were provided after the filling.

At the elevated temperature experiments, the procedure was as follows: the chamber was purged thoroughly with air, evacuated, and filled with nitrogen at 2 bar to avoid the moisture present in the air. To attain an initial temperature of 450 K, first, the temperature of all the

cartridges were set to 325 K using the master controller. Once the gas temperature reached the set value, a new set value was entered, which was 25 K higher than the previous one, and it was recurred till the attainment of the desired initial temperature. The gradual increase of the

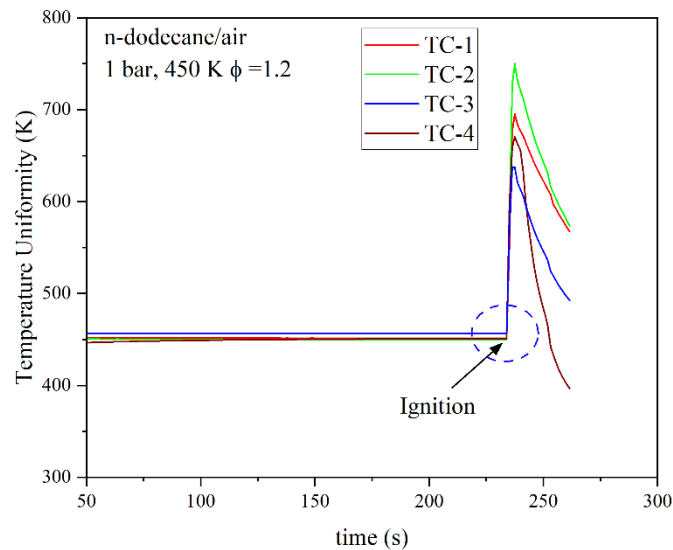


Figure 3.10. Measured mixture uniform temperature and corresponding LabVIEW real-time measurement window

system temperature was essential to have a steady and uniform temperature distribution of gases inside the chamber. As mentioned earlier, the inner chamber had four K-type sheathed thermocouples mounted at different locations to measure the gas temperature. Figure 3.10 shows the measured temperature distribution of all the thermocouples with time. The temperature measured by all four thermocouples were very close to each other, and the variation was within the measurement error, which indicated that a steady and uniform temperature distribution was achieved inside the chamber. The duration of the heating process spanned from 4 hours to 6 hours based on the magnitude of the initial temperature. Once the desired temperature was attained, the  $N_2$  in the chamber was removed, and the chamber was evacuated to 1 mbar. Then, the combustible mixture was prepared by following the partial pressures method and left undisturbed for three minutes to obtain a quiescent mixture. Here too, longer duration trials had been performed, but it did not have any influence on the LBV, and hence, three minutes was chosen for all the elevated temperature conditions.

### 3.5.2 Preparation of combustible mixtures involving liquid fuels

As the LBV was measured for a gaseous combustible mixture, to measure the LBV of liquid fuels, they needed to be vaporized and mixed with the oxidizer. They needed to be retained in the gaseous phase till the end of combustion. As mentioned in the literature review

section 2.4, in this work, the liquid fuel was directly injected into the chamber and allowed to vaporize. The volume of the n-dodecane (purity – 99%, Merck & Co.) or water (de-ionized) to be injected during an experiment needed accurate information on the inner volume of the combustion chamber. Hence, the entire chamber was filled with water, including its crevices and the volume was calculated to be 15.65 L  $\pm$ 25 mL. For a given set of initial operating conditions, the volume of n-dodecane or water to be injected was estimated. For proper vaporization and retaining the liquid fuel in the gaseous phase, the mixture needed to be maintained at an initial temperature above the boiling point of the liquid for a given partial pressure of the liquid. For the initial temperature of 425 K, the saturation vapour pressure of n-dodecane is about 168 mbar, which corresponds to the fuel partial pressure for a n-dodecane/air mixture that needs to be operated at  $\phi = 1.4$  and an initial pressure of 10.7 bar. For n-dodecane/air mixture of  $\phi = 1.4$  with 425 K, fuel condensation would occur when initial pressure increased beyond 10.7 bar. Therefore, all the elevated pressure experiments (1-4 bar) were performed at 425 K, which was well away from the saturation conditions. So, the initial temperature of the n-dodecane was fixed at 400-450 K for initial pressures of 1 bar-4 bar. This temperature was well below the pyrolysis temperature of n-dodecane, which is reported as 750 K or higher in [92]. The chamber was heated by filling N<sub>2</sub>, as explained in the previous paragraph, and after attaining the required initial temperature, it was evacuated. Even though the present initial temperatures were well below the pyrolysis temperature of the n-dodecane, the inner side of the bottom flange temperature was measured as one of the thermocouples were mounted close to it. Now, the estimated volume of the liquid was collected in the syringe, which had a long needle, as explained in section 3.4.3, and was injected slowly into the chamber. The long needle of the syringe ensured that the fuel entered all the way into the chamber, away from its walls. After the liquid fuel injection, the liquid started vaporizing, and the absolute pressure of the chamber increased. The net increase in the absolute pressure of the chamber, after and before the fuel injection, matched with the desired partial pressure of the liquid fuel, which ensured the complete vaporization of the liquid fuel.

For demonstration, the 35% (n-C<sub>12</sub>H<sub>26</sub>+18.5O<sub>2</sub>) + 65%N<sub>2</sub> mixture at  $\phi=1.4$ , 1 bar, and 450 K was considered. The partial pressures of the respective species were:  $p_{n-C_{12}H_{26}} = 25$  mbar,  $p_{O_2} = 325$  mbar, and  $p_{N_2} = 650$  mbar. Now, the heated chamber at 450 K was evacuated to 1 mbar. At this condition, an equivalent volume of liquid n-dodecane was injected into the chamber to attain the desired partial pressure and allowed to evaporate. During the evaporation of the n-dodecane, the absolute pressure of the chamber increased. At the end of fuel evaporation, the

absolute pressure of the chamber was 26 mbar (1 mbar + 25 mbar), and it remained constant, as shown in Figure 3.11. Once the chamber attained a steady estimated partial pressure of the liquid, the complete vaporization of the liquid was confirmed.

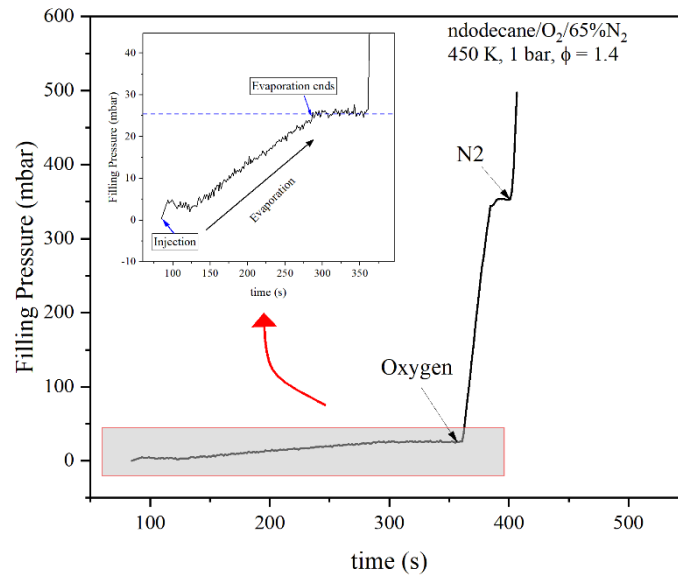


Figure 3.11. The absolute partial pressure variation during the mixture preparation stage.

Other gaseous species were then filled into the chamber based on the values of the respective partial pressures in ascending order. During the purging of  $N_2$  from the chamber, followed by the evacuation processes, the temperature measured inside the chamber showed a minor reduction, but it was recovered back to the desired initial temperature after the completion of filling of the combustible mixture, as it was observed from the temperature measurements.

### 3.5.3 Preparation of combustible mixtures without $N_2$

In the present work, the following mixtures,  $(100-Z) \% (\text{Fuel}+(\text{O}_2/\phi)) + Z\% (\text{CO}_2/\text{H}_2\text{O})$ , were investigated. The speciality of the above mixture was that it did not involve any nitrogen. For such mixtures, the following procedure was adopted, and it was applicable for all initial temperatures and liquid/ gaseous fuels. Initially, the chamber was purged with dry air. Then, it was evacuated till 1 mbar. Now, the partial pressure of  $N_2$  in the chamber was  $7.9e-4$  bar. Then, the chamber was filled with pure oxygen till 0.5 bar, and the mole fraction of  $N_2$  in the chamber was  $1.58e-3$ . Then, the chamber was again evacuated to 0.001 bar, and the partial pressure of  $N_2$  in the mixture was  $1.58e-6$  bar or 0.158 Pa. Then, the gas species needed to prepare the mixture was filled in ascending order based on their partial pressures. For example, the chamber was filled with a non-nitrogen combustible mixture till 1 bar. Now, the mole fraction

of N<sub>2</sub> in the mixture was 1.58e-6, which was quite negligible, and hence, the mixture was considered to be free of nitrogen. After this procedure, the combustible mixture was prepared based on the above-said methods meant for gaseous mixtures or mixtures that involve liquid fuels.

The abovementioned sections clearly discussed the methodology to prepare a quiescent combustible mixture for a given equivalence ratio, initial pressure, and initial temperature. Then, the combustible mixture was ignited at the centre of the chamber using the spark ignition system with the lowest possible ignition energy [93]. A delay pulse generator was used to synchronize the spark ignition, high-speed imaging, and pressure-time acquisition. From the onset of ignition and the associated flame propagation was recorded in a high-speed camera. Also, the unsteady pressure-time history measured by the unsteady pressure sensor and amplified by a charge amplifier was recorded in an oscilloscope. At the end of combustion, the chamber was immediately purged with the dry compressed air to remove the residuals of product gas and bring the chamber temperature back to its operating conditions.

### 3.6 Design of experiments

Table 3.2. Operating conditions of various mixtures

Fuel/oxidizer	Initial conditions			Diluents (% , by vol.)			Blending
	P (bar)	T (K)	$\phi$	CO <sub>2</sub>	H <sub>2</sub> O	N <sub>2</sub>	H <sub>2</sub>
Dodecane/air	1, 2, 4	400 - 450	0.8 - 1.4	-	-	-	-
Dodecane/O <sub>2</sub>	1, 2, 4	400 - 450	0.6 - 1.4	65	65	55, 65, 75	-
(Dodecane+H <sub>2</sub> )/air	1, 2, 4	425	0.8 - 1.4	-	-	-	0 - 40
Methane/O <sub>2</sub>	1, 2, 4	393 - 453	0.6 - 1.4	50	40, 50, 60	50	-

To meet all the objectives, the gas mixtures listed in Table 3.2 were investigated. All the experiments were carried out with an adequate number of repetitions, and the average value was reported.

### 3.7 Methodology

In this section, the necessary spherical flame theory, data reduction, and image processing procedures, laminar burning velocity and burned gas Markstein length formulations, different extrapolation schemes, various Lewis number correlations adapted for different mixtures, and finally, experimental operating procedures for both gaseous and liquid fuel mixtures are presented in detail.

### 3.7.1 Freely expanding spherical flame method (SPF)

The earlier section explained in detail regarding the present new combustion rig to measure the LBV using the SPF method. In this method, the combustible mixture was prepared in a constant volume chamber, and the same was ignited at the centre of the chamber using an electrical spark. A spherical flame was formed at the centre, and it outwardly propagates, as illustrated in Figure 3.12. As mentioned earlier, the pressure of the chamber remained constant during the consumption of 1-2% of the volume of the reactants in the chamber. After that, the pressure of the chamber rises, and it attained a peak value as the reactants were completely consumed.

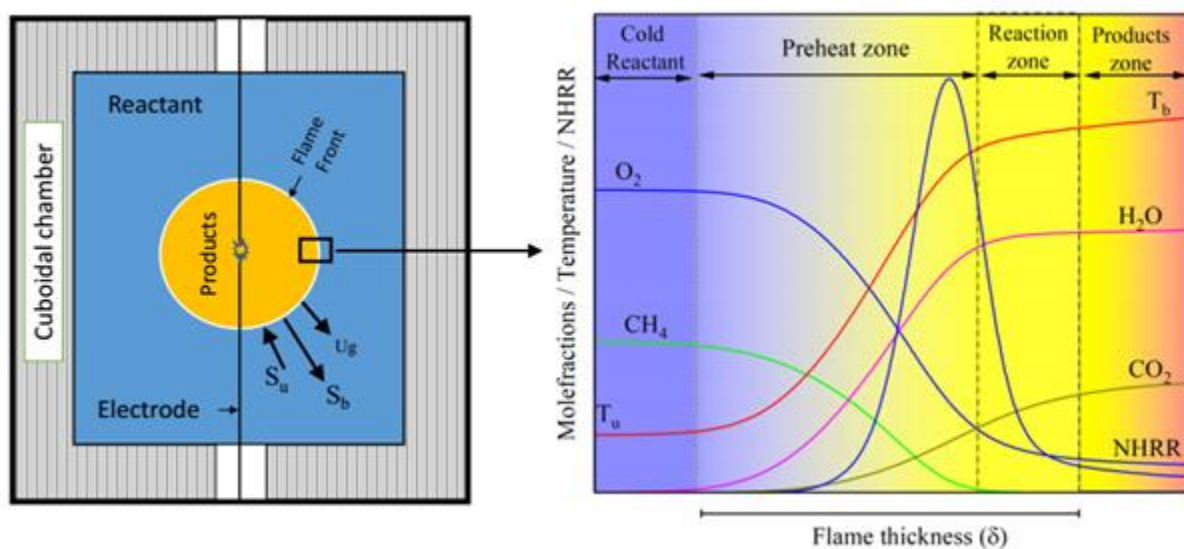


Figure 3.12. Graphical illustration of spherical flame propagation inside the cuboidal chamber and typical flame structure of stoichiometric methane/air mixture at 1 bar 300 K

In this work, the flame propagation event was imaged during the pre-pressure period, and it was processed to find the unstretched LBV. From this point onwards, the discussion was with respect to the constant pressure of outwardly spherical flames only. As the pressure remained constant, the flame separated the products from the reactants, as shown in Figure 3.12. The structure of a laminar flame is also shown in Figure 3.12, where the presence of large gradients in temperature, mole fraction, and net heat release rate (NHRR) intimated that the transport phenomena was quite important over there. The flame consisted of a thick preheat zone and a reaction zone. The reactants are heated in the preheat zone by means of heat diffusion from the reaction zone, and its temperature is raised. The preheated reactant transformed into products in the reaction zone, with a large amount of heat release, and the products leave the reaction zone at the equilibrium flame temperature. The heat release rate

was confined within the narrow reaction zone, which strongly depended on the flame temperature.

With respect to the laboratory coordinates, the burned gas products are expanding, or the flame is propagating into unburned gases at a velocity,  $S_b$ , and is called laminar flame speed. Unburned gases adjacent to the flame front was pushed away by the flame due to the expansion of the burnt products at a velocity of  $U_g$ . The unburned reactants got transformed into products at a velocity of  $S_u$ , which is called laminar burning velocity, and it is the relative velocity of the flame with respect to the unburned gases. The laminar burning velocity of the constant pressure spherically propagating flame can be expressed as

$$S_u = S_b - U_g \quad 3.1$$

The above equation is independent of the thermodynamic properties of reactants or products, and it needs only the information of laminar flame speed,  $S_b$ , and  $U_g$ , and unburned gas velocity with respect to laboratory coordinates. But the challenge here is that in a propagating spherical flame method, it is very difficult to measure the  $U_g$ , due to the available short span of time. Only Balusamy et al. [94] and their co-workers had measured the  $U_g$  using a two-dimensional particle image velocimetry technique and had reported the laminar burning velocity based on Eq. 3.1. PIV needed seeding particles to be added to the unburned gases, which will result in additional uncertainty in the measurement of LBV. For high-speed mixtures, this method becomes more complicated. Hence, in the present work, the LBV was estimated by applying the continuity equation at the infinitesimal flame surface as follows:

$$\rho_u S_u^0 = \rho_b S_b^0 \quad 3.2$$

where  $S_u^0$  denotes the unstretched LBV,  $S_b^0$  denotes the unstretched laminar flame speed,  $\rho_u$  represents the density of reactants obtained from the known composition and thermodynamic conditions of reactants, and  $\rho_b$  corresponds to the burned gas density estimated by assuming burned gases to be at the equilibrium condition. The estimation of unstretched LBV using Eq. 3.2 is the standard methodology, as mentioned in Law et al.[95], Egolfopoulos et al. [96] and Faeth et al.[97].

### 3.7.2 Data reduction procedure

In this section, the procedure involved in the estimation of unstretched LBV and burned gas Markstein length from the raw experimental data is explained in detail. At the end of each successful experiment involving a combustible mixture at a prescribed initial pressure, initial temperature, and equivalence ratio resulted in the acquisition of the following data: (a)

unsteady pressure time history, (b) video of the flame propagation event. The post-processing starts with the identification of the constant pressure period from the measured pressure-time history. In the present work, the constant pressure combustion regime was considered to be within a 1-2% rise of the initial chamber pressure. Figure 3.13 shows the typical unsteady pressure history recorded during the combustion event of stoichiometric n-dodecane/air mixture at 1 bar and 450 K. The noise in the measured unsteady raw pressure data was essentially due to the high sensitivity of the unsteady pressure sensor. Use of any digital filters will remove the noise. As the pressure-time data was not used for the estimation of LBV, no filters were applied. The peak pressure measured at the end of combustion was 6.02 bar. The equilibrium pressure was also estimated using a constant volume combustion model in CHEMKIN for the corresponding condition and was 6.49 bar. The deviation between the measured peak pressure to that of the equilibrium values was 7.24%, and it was essentially due to the energy losses from the flame to the chamber walls. The close agreement confirmed the accurateness of the present mixture preparation methodology. A similar observation was also presented by Keshavamurthy et al. [24] for a wide-range of methane-air mixtures.

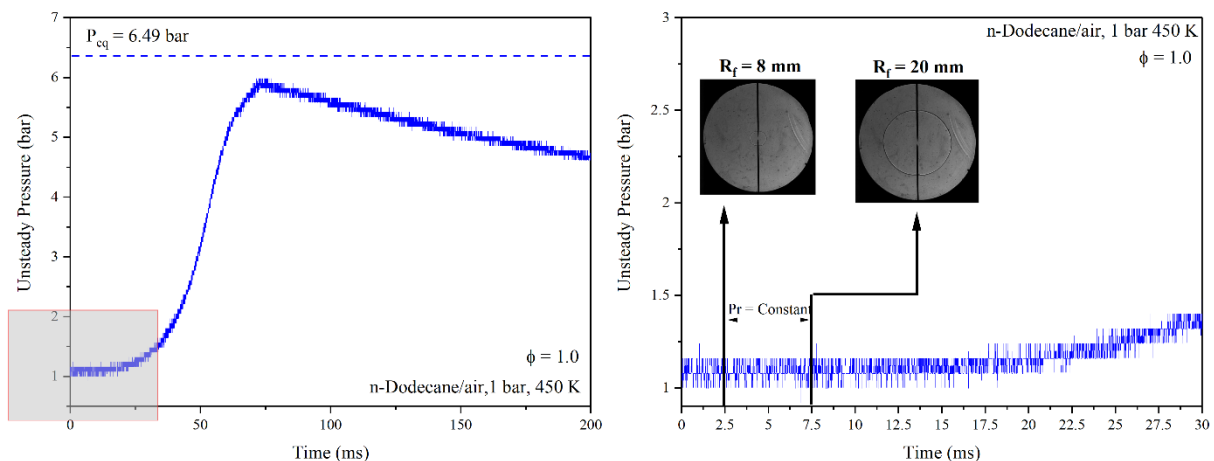


Figure 3.13. The unsteady pressure evolution with time after the spark (left) of stoichiometric n-dodecane/air mixture at 1 bar 450 K. The zoomed version of the constant pressure zone (right) with upper and lower radius limits illustrated

### 3.7.3 Image processing

The images recorded from the high-speed camera were processed using an in-house MATLAB program to extract the flame radii. The canny edge detection function available in MATLAB [98] was used to find the edges of flame, optical access, etc. Only the smooth flames recorded in the pre-pressure period was considered. Initially, an image without any flame (background) was processed using the code to find the circular edge of the optical access, and

later its diameter was estimated in terms of pixels. From the information of the known diameter of the optical access (107 mm), a calibration factor to convert the pixels into the respective physical distance was estimated. Then, standard heights having width and height of 10 mm and 20 mm was placed on the flange of the optical window, and it was imaged independently. Then it was processed using the developed code, and their dimensions were estimated and checked against the known distances to verify the accuracy of the estimated calibration factor in estimating the smaller distances, as the present work used flame radii in the range of 8 mm-20 mm. Next, the background image was subtracted from all the images having smooth spherical flames to remove other edges that are of no interest, such as the electrode and window opening, from the image. After the subtraction, the image contained only the flame, and it was referred to as the foreground image. Then, its edge was identified. There were minor disturbances observed on the flame edge close to the electrodes, and hence, to avoid such effects on the LBV, 0-5° segment near the electrodes were omitted. The geometric centre of this edge was then found for a given foreground image, and the radius (in terms of pixels) of each point on the edge, excluding the 0-5° segment near the electrodes, was found. This radii information was used to determine the optimum radius of the flame at that instance of time by optimizing using an objective function, *fmincon*, in MATLAB. The objective function was:

$$objective = \sqrt{\sum_{i=1}^n (r_i(t) - r_{fit}(t))^2} \quad 3.3$$

Where  $r_i$  is the radius of the flame edge and  $r_{fit}$  is the fit radius obtained through the circle fit method, and  $k$  is the number of points considered for circle fit. Figure 3.14 shows the sequence of image processing operations to find the flame edge without the regime close to the electrodes and its flame radius. The same procedure was extended to all the eligible images recorded for a given experiment.

The previous section explained the procedure for finding the flame radius from the recorded flame image. For a given experiment, the flame radii were estimated from all the eligible flame images along with their absolute time stamp with respect to the onset of ignition. The flame radius-time were used to calculate the stretched flame speed,  $S_b$ , by the first-order derivative using the finite-difference of the two consecutive instantaneous flame radii as

$$S_b = \frac{dr_f}{dt} = \frac{r_{f2} - r_{f1}}{t_2 - t_1} \quad 3.4$$

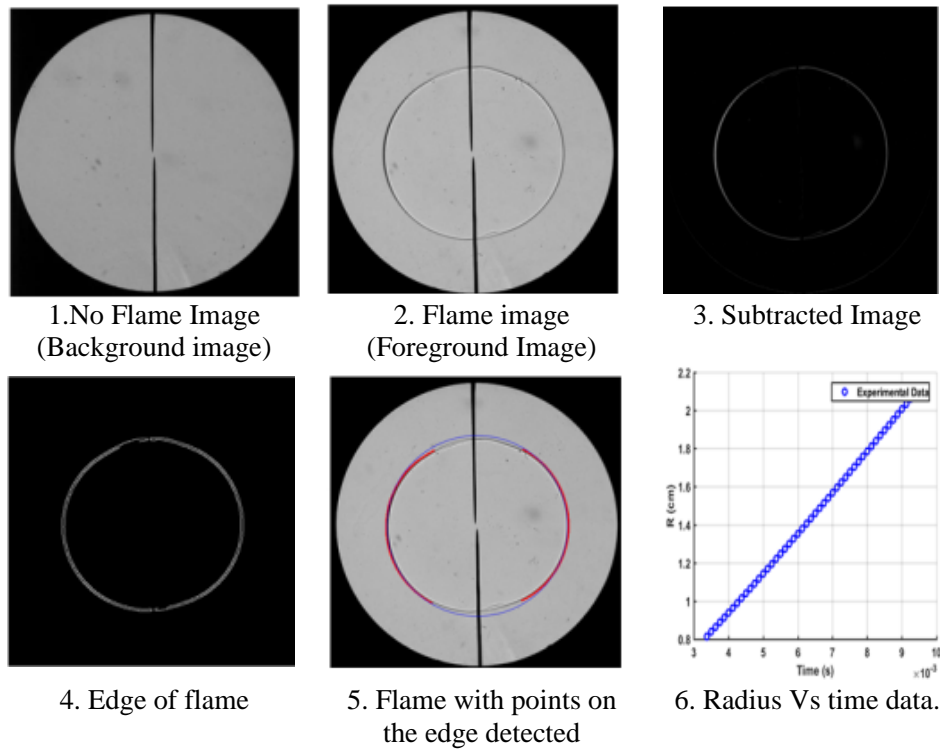


Figure 3.14. The sequence of image processing procedures illustrated

where  $r_{f1}$ ,  $r_{f2}$  are the flame radius at time  $t_1$ ,  $t_2 = t_1 + \Delta t$  where  $\Delta t = (\text{frames of camera/s})^{-1}$ . The occurrence of scatter in the data was due to the numerical differentiation of the raw data was corrected by using the LOWESS algorithm in MATLAB.

The area of the expanding spherical flame was affected by the unsteadiness and curvature, and it is called flame stretch. It was quantified by flame stretch rate,

$$K = \frac{2}{r_f} \frac{dr_f}{dt} \quad 3.5$$

Figure 3.15 shows the stretched flame speed against the flame stretch rate of stoichiometric n-dodecane/air mixtures at 1 bar, 425 K. The open circle in the figure refers to the data extracted from all the eligible flame images. The observation of Figure 3.15 indicated that immediately after the onset of the ignition, the flames in the radius range of 3-8 mm were largely affected by strong stretch effects ( $700\text{-}600 \text{ s}^{-1}$ ), and their stretched flame speed showed a strong non-linear relation towards the flame stretch rate. The reason was that the ratio  $(\delta/r_f)$  of flame thickness ( $\delta$ ) to the flame radius ( $r_f$ ) was higher, indicating the presence of active transport effects as well as the flames were not fully developed. Then, in the radius range of 8-20 mm, which corresponded to a flame stretch rate of  $600\text{-}200 \text{ s}^{-1}$ , the stretched flame speed well-behaved towards the stretch effects as shown in the figure as the flames in the regime

were fully developed spherical flames with lower values of  $(\delta/r_f)$  and that too away from the ignition transient effects. Beyond the flame radius of 20 mm, again, the flame speed showed strong non-linear effects, and this was essentially due to confinement effects. For a given experiment, the range of data chosen for the extrapolation was achieved by plotting the data similar to that of Figure 3.15 to ensure that the data was free of ignition transients and confinement effects. Figure 3.15, the data chosen for finding the unstretched laminar flame speed is marked in red-filled circles. The same procedure was followed during the post-processing of experimental data. Also, linear and nonlinear extrapolation fits are presented for the non-unity Lewis number mixture, and its significance for the present mixture is discussed in chapters 6-9.

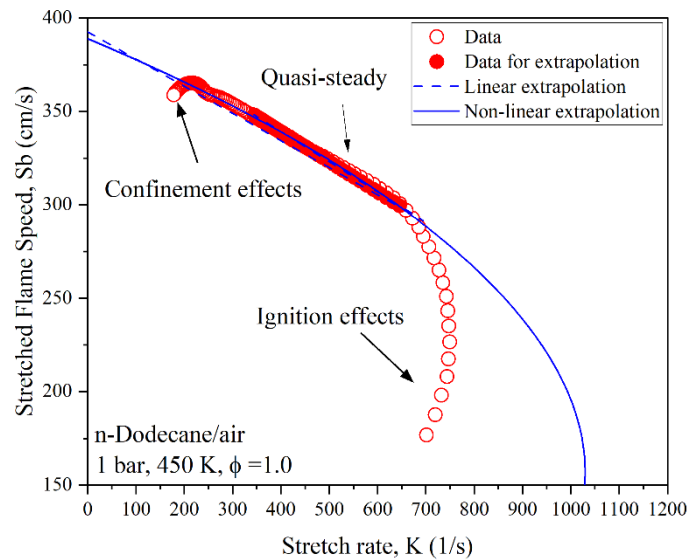


Figure 3.15. Ignition and confinement effects of spherically propagating stoichiometric n-dodecane/air mixture at 1 bar 450 K

### 3.7.4 Procedure for the estimation of unstretched laminar flame speed

The above section explained the procedure to obtain the stretched flame speed as a function of a finite stretch rate. Now, to find the unstretched flame speed,  $S_b^0$ , the obtained stretched flame speed needed to be extrapolated to zero stretch rate or infinite flame radius. The present studied mixtures had a non-unity Lewis number,  $Le$ , due to the significant differences in the mass diffusivity of  $O_2$  and n-dodecane. Hence, non-linear extrapolation models were used over the linear model. The current work utilized the two non-linear models (a) Eq. 3.6 proposed by Kelly and Bechtold [99] addressed as nonlinear expansion (NE), and (b) Eq. 3.7 reported by Kelly and Law [100], addressed as Quasi nonlinear scheme (NQ) to estimate the unstretched

flame speed,  $S_b^0$ . The nonlinear extrapolation scheme (NE) uses radii and stretched flame speed, whereas NQ scheme uses stretched flame speed and stretch data to obtain the unstretched flame speed ( $S_b^0$ ) and burned gas Markstein lengths ( $L_b$ ). As explained in the foregoing sections, flame radii in the range of 8 – 20 mm was used for the extrapolation to avoid ignition transient, and confinement effects.

$$\frac{S_b}{S_b^0} \left( 1 + \frac{2L_b}{r_f} + \frac{4L_b^2}{r_f^2} + \frac{16L_b^3}{3r_f^3} + O^4 \left( \frac{L_b}{r_f} \right) \right) = 1 \quad 3.6$$

$$\left( \frac{S_b}{S_b^0} \right)^2 \ln \left( \frac{S_b}{S_b^0} \right)^2 = -2 \frac{L_b K}{S_b^0} \quad 3.7$$

Finally, the unstretched laminar burning velocity  $S_u^0$  was obtained by multiplying the unstretched flame speed with the density ratio (burned/unburned), and the burned gases were assumed to be in equilibrium, and it was estimated using equilibrium calculation.

$$S_u^0 = S_b^0 \left( \frac{\rho_b^0}{\rho_u} \right) \quad 3.8$$

where  $\rho_u$  is the density of the reactants and  $\rho_b^0$  is the density of products.

## 3.8 Flame global parameters

The following important flame global parameters that are frequently used in effective Lewis number correlations are estimated for different mixtures and discussed in the results and discussion section, therefore, their definition and formulation are provided here.

### 3.8.1 Flame thickness

There are two procedures available to estimate flame thickness. The first method was based on the transport and combustion properties of the reactants, as shown in equation 3.9:

$$\delta = \frac{\alpha}{S_u^0} \text{ or } \delta = \frac{D_u}{S_u^0} \quad 3.9$$

$$\alpha = \frac{\lambda}{\rho_u c_{p,u}} \quad 3.10$$

Equation 3.9 uses thermal diffusivity,  $\alpha$ , or mass diffusivity,  $D_u$ , of the mixture and unstretched LBV ( $S_u^0$ ) to find the flame thickness. The thermal diffusivity of the mixture was estimated by Eq. 3.10. It depends on the thermal conductivity ( $\lambda$ ) and constant pressure specific heat capacity ( $c_{p,u}$ ) of the unburned gas mixture. But the mass diffusivity of the reactant mixture has multiple

definitions, such as (a) binary diffusivity of a deficient reactant to a bulk species, (b) mixture diffusivity, and (c) multi-component diffusivity. Based on the choice of the thermal or one of the variants of mass diffusivity results in multiple values of flame thickness. Also, Eq.3.9 is a function of the LBV, which prevents the independent nature of the flame thickness in characterizing the flame behaviour [101].

Therefore, due to the concerns stated above, in the present work, flame thickness was estimated by using Eq. 3.11.

$$\delta = \frac{T_b - T_u}{\left(\frac{dT}{dx}\right)_{max}} \quad 3.11$$

It needs the temperature profile of the flame, which was obtained from the freely propagating planar flame simulations in CHEMKIN. From the temperature profile, the equilibrium flame temperature and the maximum temperature gradient was estimated, and then the flame thickness was estimated.

### 3.8.2 Activation energy or Zeldovich Number

The activation energy ( $E_a$ ) represents the sensitivity of the LBV to the variation in the flame temperature, and it was expressed in Eq. 3.12, which is also called as the activation temperature. The activation temperature is the negative slope of  $\ln(\rho_u S_u^0)$  vs  $1/T_b$  plot. For plotting purposes,  $\ln(\rho_u S_u^0)$  and  $1/T_b$  was obtained for the mixture at a given pressure, temperature, and at slightly different equivalence ratios other than its initial value. A dimensionless form of activation energy is designated as the Zeldovich number (Eq. 3.13),

$$\frac{E_a}{R_u} = -2 \left[ \frac{\partial [\ln(\rho_u S_u^0)]}{\partial (1/T_b)} \right] \quad 3.12$$

$$Ze = \frac{E_a(T_b - T_u)}{R_u T_b^2} \quad 3.13$$

Where  $\rho_u, S_u^0$  are the unburned mixture density and LBV.  $T_b$  denotes the equilibrium flame temperature,  $T_u$  refers to the temperature of the unburned gas mixture, and  $R_u$  is the universal gas constant.

### 3.8.3 Analytical estimation of Markstein length

Burned gas Markstein length,  $L_b$ , represents the sensitivity of the flame propagation speed to the stretch rate. In one of the previous sections, the estimation of  $L_b$  from measurements was deliberated. Now, in this section, the existing procedure reported in the literature to find  $L_b$  analytically is described. Bechtold and Matalon [102] provided an analytical expression (Eq. 3.14) to estimate the  $L_b$  as a function of density ratio  $\sigma$ , the effective Lewis number of the mixture,  $Le_{eff}$ , and Zeldovich number,  $Ze$ .

$$L = \delta[\alpha - (\sigma - 1)\gamma_1/\sigma] \quad 3.14$$

$$\alpha = \gamma_1 + \frac{1}{2} Ze (Le_{eff} - 1)\gamma_2 \quad 3.15$$

$$\gamma_1 = \frac{2\sigma}{\sqrt{\sigma} + 1} \quad 3.16$$

$$\gamma_2 = \frac{4}{\sigma - 1} \left\{ \sqrt{\sigma} - 1 - \ln \left[ \frac{1}{2} (\sqrt{\sigma} + 1) \right] \right\} \quad 3.17$$

with  $L = L_b/\sigma$ ,  $\delta$  is the flame thickness using Eq. 3.11,  $Ze$  is the Zeldovich number using Eq. 3.13, and  $Le_{eff}$  is the weighted average of the Lewis numbers of the deficient and excess reactants.

## 3.9 Thermo-diffusive instability

The distinct feature of the outwardly propagating spherical flame method was that it provides an quantitative information on the flame stability with respect to thermo-diffusive effects in terms of burned gas Markstein length. It quantifies the response of the flame to the stretch effects. A combustible mixture is stable/ unstable to thermo-diffusive effects if the  $L_b$  was positive/ negative. As  $L_b$  quantifies the thermo-diffusive effects, it is a strong function of the Lewis number of the combustible mixture. If a flame was stable/ unstable with respect to the thermo-diffusive effects, then the Lewis number of the combustible mixture will be greater/ lesser than the unity or critical Lewis number ( $Le^*$ ). Lewis number ( $Le$ ) is a ratio of the thermal diffusivity ( $\alpha$ ) of the mixture to the binary mass diffusivity ( $D_{ij}$ ), where  $i/j$  represents the deficient/ bulk species.

$$Le = \frac{\alpha}{D_{ij}} = \frac{\lambda}{\rho_u c_p D_{ij}} \quad 3.18$$

Where  $\lambda$ ,  $\rho$ , and  $c_p$  were thermal conductivity, density, and specific heat capacity of the reactants. It indicates the stability of the flame towards an imbalance in thermal and mass diffusional effects. The general definition of Lewis number with respect to the binary mass

diffusivity of deficient reactant into the bulk species lacks in the estimation of the flame transition from stable to unstable due to the following reasons, (a) identification of the deficient reactant to estimate the binary mass diffusion coefficient was quite challenging, especially for mixtures involving heavy hydrocarbon fuel as the mole fraction of the fuel will be always smaller as compared to other species, hence it is ambiguous, (b) it is easily applicable for single fuel, than for multicomponent fuels as a complication arises in finding the suitable representative species, (c) many intermediate species emerge in the preheat zone and influence the Lewis number with their different diffusivities, which was not accounted in the estimated Lewis number. To overcome these challenges, researchers had defined effective Lewis number ( $Le_{eff}$ ). It is a kind of mixing rule which includes the contribution from most of the relevant species in the mixture.  $Le_{eff}$  correlations developed for binary fuel mixtures were accurate enough to find the transition of Markstein length from positive to negative[103,104]. In the present work for oxy-fuel mixtures (n-dodecane/O<sub>2</sub> and methane/O<sub>2</sub>) effective Lewis number proposed by Addabbo et al. [105] (Eq. 3.19) was used, and for the hydrogen blended n-dodecane diffusion dominated mixtures, diffusion model suggested by Dinkelacker et al. [106] (Eq. 3.20) was adopted.

(a) Effective Lewis number (Addabbo et al. [105]) for oxy-fuel-diluent mixtures

$$Le_{eff} = 1 + \frac{(Le_E - 1) + (Le_D - 1)A}{1 + A} \quad 3.19$$

where  $Le_E / Le_D$  are excess/deficient reactant's Lewis number.  $A = 1 + Ze (\Phi - 1)$  is a measure of mixture strength, and  $\Phi$  is defined as the ratio of the mass of excess-to-deficient reactants in the fresh mixture relative to their stoichiometric ratio, and  $Ze$  is the Zeldovich number.

(b) Diffusion Model (Dinkelacker et al.[106]) for hydrogen blended n-dodecane/air mixtures

Diffusion model based on an effective molecular diffusivity of the fuel components  $D_{eff}$

$$\frac{1}{Le_{eff}} = \frac{D_{eff}}{\alpha} \quad 3.20$$

where,  $D_{eff} = x_{C_{12}H_{26}} D_{C_{12}H_{26}} + x_{H_2} D_{H_2}$  with  $x_i$  being the volumetric fractions of the fuel mixture, and  $\alpha = \lambda / \rho_u C_p$  is the thermal diffusivity of the mixture,  $\lambda$  = mixture averaged thermal conductivity,  $\rho_u$  is the unburned mixture density, and  $C_p$  = specific heat of the mixture.

Researchers [Matalon [102], Chen [107], and Law et al. [108]] had calculated the Lewis number by following asymptotic analysis, which involved burned gas Markstein length too. In the present work, one of such variations presented by Beckett and Matalon [102] was used to estimate the Lewis number of premixed n-dodecane-air mixtures. It was called the BM model [102] in this work, and it is as follows:

BM model estimates  $Le$  as a function of experimental burned gas Markstein length.

$$Le = 1 + \left[ \frac{L_b}{\delta} - \frac{2}{\sqrt{\sigma} + 1} \right] \left[ \frac{2Ze}{\sigma - 1} \left\{ \sqrt{\sigma} - 1 - \ln\left(\frac{1}{2}(\sqrt{\sigma} + 1)\right) \right\} \right]^{-1} \quad 3.21$$

where  $L_b$  and  $\delta$  are the burned gas Markstein length from measurements and laminar flame thickness from the predicted temperature profile.  $\sigma$  is the ratio of unburned to burned gas densities, and  $Ze$  is the Zeldovich number.

Critical Lewis number ( $Le^*$ ) was calculated using Eq. 3.22 according to [109],

$$Le^* = 1 - \frac{1}{Ze} \quad 3.22$$

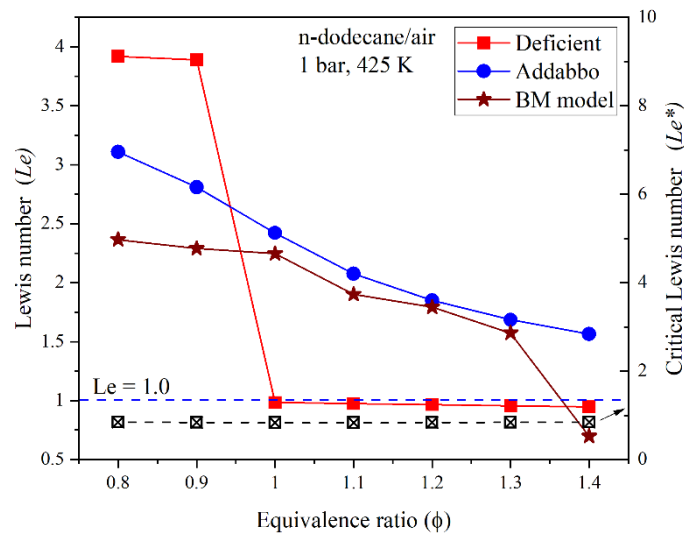


Figure 3.16. Comparison of different Lewis number models for n-dodecane/air mixture at 1 bar 425 K

Figure 3.16 shows the capability of different Lewis number formulations in the prediction of transitions at  $\phi = 1.4$  and the shifts when the equivalence ratio increasing from lean to rich. The deficient reactant model shows a sudden jump; the effective Lewis number model shows a smooth transition but failed to predict the thermo-diffusive instability. The BM model shows the accurate prediction of transition and  $Le < Le^*$  for unstable flames. This suggests that it is

difficult to determine the most accurate Lewis number definition, which is valid for all mixtures and all operating conditions.

### 3.10 Hydrodynamic Instabilities

The critical radius was the radius of the spherical flame where the flame started developing uniform cells on the surface in a significant amount. Quantification by earlier researchers was based on visual inspection. The present work estimated the radius using a MATLAB program based on cell identification criteria rather than visual inspection. For calculating the critical radius, the intensity of the pixels in a rectangular inspection area of 69920 pixels (two rectangles of size  $190 \times 184$  to omit electrodes) within the diameter of the optical access window was monitored, as shown in Figure 3.17.

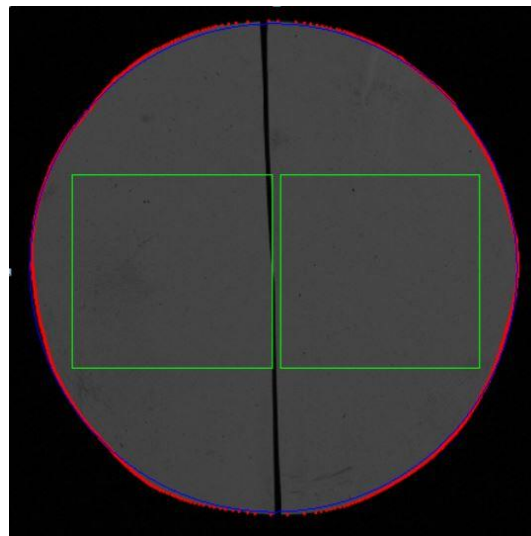


Figure 3.17. Inception area of the spherical flame for cells

The developed criteria: 1) Image corresponding to the maximum change in the average intensity to the base image without the flame, 2) The maximum value of the second-order time derivative of intensity should occur within 0.1% of the frame rate after attaining a peak value of first-order time intensity and 3) The instant corresponding to drop below 85% of the average intensity of at least 0.14% of the total number of pixels (equal to  $\sim 50$  pixels, this value can be adjusted with intensity and tailored as per the requirement). All the criteria were verified and sequenced based on robustness and accuracy.

The resilience of a flame to hydrodynamic instability was directly proportional to its laminar flame thickness ( $\delta$ ). Here, the necessary data of flame thickness was computed for different mixtures from the respective temperature profiles predicted using CHEMIN. The critical radius

( $R_{cr}$ ) was normalized with the flame thickness to calculate the critical Peclet number ( $P_{cr}$ ) to categorize the instabilities. Thermal expansion ratio ( $\sigma$ ) was obtained from burned and unburned gas mixture densities, and this parameter provided information about the density jump across the flame. The coefficient of self-acceleration ( $\alpha$ ) was obtained by fitting the radius-time data in the equation,  $R = R_0 + Ct^\alpha$ , where  $R_0$  (referred to as virtual origin),  $C$  (constant) and  $\alpha$  were the fitting parameters.

### 3.11 Uncertainty quantification

The uncertainty involved in the measurement of unstretched LBV and burned gas Markstein length by using the outwardly propagating spherical flame method was quantified statistically based on the propagation of uncertainty method proposed by Xiouris et al.[110]. In this method, the uncertainty was estimated by considering all the parameters relevant to measurements, data processing, and data interpretation. Based on this method, the total uncertainty involved in the measurement of laminar burning velocity ( $a_{S_u^0}$ ) will be discretized into two stages (i) mixture preparation and (ii) Post-processing. The uncertainty of each stage was evaluated separately and subsequently combined to provide an accurate estimate of the total uncertainty in the reported  $S_u^0$  and  $L_b$ .

The general expression for uncertainty from all parameters (such as mixture preparation, initial temperature, pressure, etc.)  $Q$  to the function  $F = F(Q_1, Q_2, \dots, Q_M)$ , with  $M$  being the number of parameters involved, is:

$$a_F^2 = \sum_{i=1}^M \left( \frac{\partial F}{\partial Q_i} \right)^2 a_i^2 + \sum_{i=1}^M \sum_{i=1, j \neq i}^M \left( \frac{\partial F}{\partial Q_i} \right) \left( \frac{\partial F}{\partial Q_j} \right) a_{ij} \quad 3.23$$

Where  $a_i$  is the uncertainty of each parameter,  $Q_i$ ,  $a_{ij}$  are the correlation coefficient between parameters  $Q_i$  and  $Q_j$ , and  $a_F$  the final propagated uncertainty of  $F$ . The detailed uncertainty procedures are explained with sample calculations reported in Appendix B. The uncertainty of LBV and  $L_b$  for each and every operating condition is different. The absolute value of each operating point is represented in the figures in the results section. For presenting the data in a readable fashion, the uncertainties of LBV and  $L_b$  were averaged over equivalence ratio for a given temperature and pressure. From the estimated averaged values of different pressures and temperatures of a given fuel-oxidizer mixture, the minimum and maximum values were estimated and presented in Table 3.3.

Table 3.3. Uncertainties averaged over equivalence ratio of LBV and  $L_b$  for various mixtures

Study	Mixtures	Uncertainty range (%)	
		LBV	Markstein length
Study-1	n-dodecane-air	$\pm 5.87 - 6.03$	$\pm 6.27 - 9.28$
Study-2	n-dodecane-O <sub>2</sub> -diluent	$\pm 5.81 - 6.45$	$\pm 7.64 - 8.95$
Study-3	(n-dodecane+H <sub>2</sub> )-air	$\pm 4.8 - 8.69$	$\pm 7.8 - 13.2$
Study-4	Methane-O <sub>2</sub> -diluent	$\pm 4.83 - 6.93$	$\pm 6.48 - 9.42$

### 3.12 Summary

A test facility for performing spherical flame experiments was developed, and the necessary subsystem are customized. The strategy for data reduction and image processing was finalized, and an in-house code was developed for (a) image processing, (b) nonlinear extrapolation schemes, (c) uncertainty quantification, (d) hydrodynamic instability, (e) LabVIEW program for data acquisitions. Various Lewis number correlations were identified for specific mixtures, and the procedure to determine unstretched LBV and burned gas Markstein lengths are concluded. Also, different flame global parameters such as flame thickness, activation energy, and Zeldovich number formulations are discussed.



# CHAPTER 4

## NUMERICAL APPROACH

### 4.1 Introduction - CHEMKIN

CHEMKIN is a software to solve complex chemical kinetics problems for various industrial applications, including combustion and chemical processing. The software was originally developed by Sandia National Laboratory, and has been continuously developed and improved by Reaction Design, recently CHEMKIN was procured by ANSYS Inc.

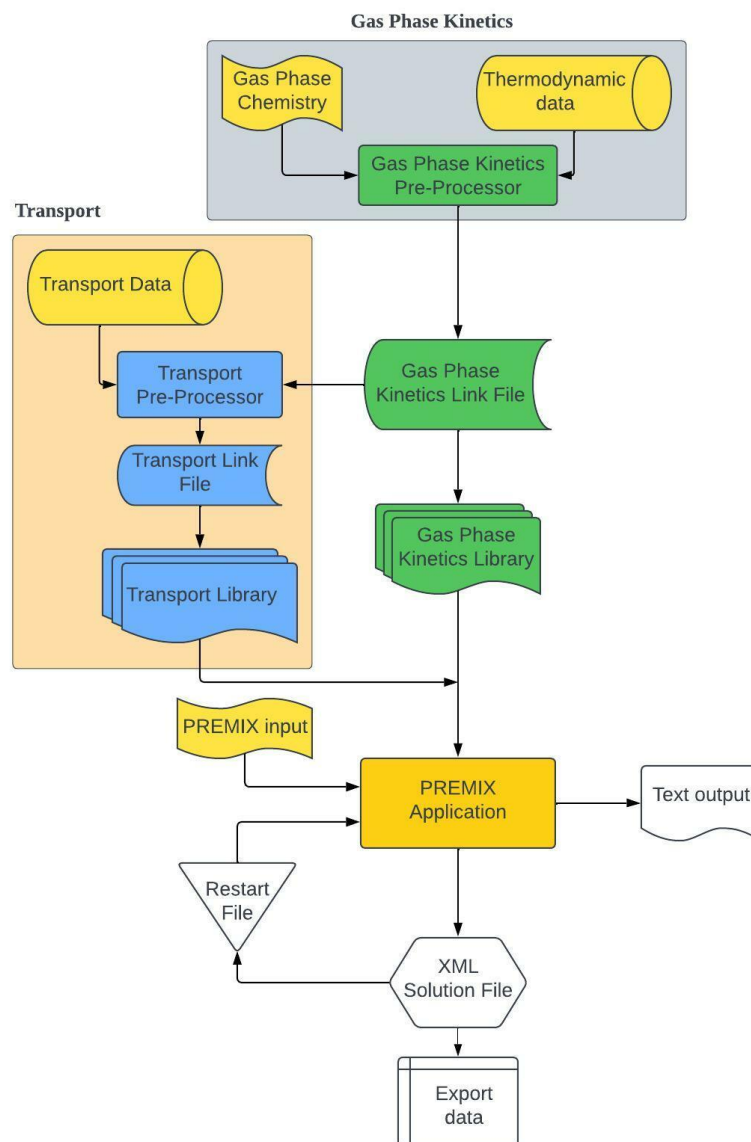


Figure 4.1. Structure of the CHEMKIN (PREMIX) Program

CHEMKIN is a highly structural program with several sub-programs, including Gas-Phase Kinetics, Transport, Surface Kinetics, Application solver, and Graphical Post-Processor. The workflow diagram of the CHEMKIN is shown in Figure 4.1. In this section, all the equations and figures are cited from CHEMKIN manuals [111].

## 4.2 Gas-phase kinetics utility

In Gas-Phase Kinetic, Gas-Phase Kinetic Pre-processor reads a symbolic description of a reaction mechanism from the chemical kinetics input data file and then extracts the needed thermodynamic data from the Thermodynamic database for each species involved in the reactions. The input file specifies the elements, species, and the elementary reactions in detailed chemical reaction mechanism.

The Thermodynamic Database is a large data file which contains the polynomial coefficients of thermodynamic properties: specific heat at constant pressure, enthalpy, and entropy, of each species as follows.

$$\text{Specific heat at constant pressure } \frac{c_{pi}^0}{R} = \sum_{k=1}^5 a_{ki} T_i^{k-1} \frac{c_{pi}^0}{R} = \sum_{k=1}^5 a_{ki} T_i^{k-1} \quad 4.1$$

$$\text{Enthalpy } \frac{h_i^0}{RT_i} = \sum_{k=1}^5 \frac{a_{ki}}{k} T_i^{k-1} + \frac{a_{6i}}{T_i} \quad 4.2$$

$$\text{Entropy } \frac{s_i^0}{R} = a_{1i} \ln T_i \sum_{k=2}^5 \frac{a_{ki}}{k-2} T_i^{k-1} + a_{7i} \quad 4.3$$

The users can optionally specify the thermodynamic data of any species in an input file to override or supplement the database information.

Once the Gas-Phase Kinetic Pre-processor is executed, the information from Thermodynamic Database and user-specified chemical kinetics input is stored in the Gas-Phase Kinetics Linking file. The Linking file is subsequently accessed by subroutines in Gas-Phase Kinetics Subroutine Library to complete the information on the equation of state, thermodynamic properties, and production rate. The Gas-Phase Kinetics Linking File is also required to execute Transport Pre-processor and needed in Gas-Phase Kinetics Subroutine Library.

## 4.3 Transport utility

In the reaction flow, the chemical species production and destruction is often balanced by a transport due to convection or diffusion. The transport properties play a key role in determining the gas state in laminar premixed and diffusion flames. Transport utility computes the molecular transport of species, momentum, and energy in a multi-component gaseous mixture

and requires the evaluation of diffusion coefficient, viscosities, thermal conductivities, and thermal diffusion coefficients. There are two kinds of methods to solve transport properties: multicomponent and mixture-averaged methods. For the mixture-averaged formula, the diffusion velocity  $V_i$  is assumed as

$$V_i = v_i + w_i + V_c \quad 4.4$$

Where  $v_i$  is the ordinary diffusion velocity and is given in Curtiss-Hirschfelder approximation by

$$v_i = -D_{im} \frac{1}{X_i} \frac{dX_i}{dx} \quad 4.5$$

Where  $X_i$  is the mole fraction and where the mixture-averaged diffusion coefficient  $D_{im}$  is given explicitly in terms of the binary diffusion coefficients.

$$D_{im} = \frac{1 - Y_i}{\sum_{j \neq i}^I \frac{X_j}{D_{ij}}} \quad 4.6$$

A non-zero thermal diffusion velocity is included only for the low molecular weight species H, H<sub>2</sub>, and He. The thermal diffusion velocity is given as

$$w_i = \frac{D_{im} \Theta_i}{X_i} \frac{1}{T} \frac{dT}{d\chi} \quad 4.7$$

Where  $\Theta_i$  is the thermal diffusion ratio.

The correction velocity,  $V_c$ , which is a function of distance,  $x$ , is included to insure that the mass-averaged diffusion velocity of all species in the mixture is zero, as shown below:

$$\sum_{i=1}^I Y_i V_i = 0 \quad 4.8$$

On the other hand, for the multi-component method, the diffusion velocity is defined as

$$V_i = v_i + w_i \quad 4.9$$

The correction velocity,  $V_c$  is not required in the multi-component method.

And the ordinary diffusion velocity is given as:

$$v_i = \frac{1}{X_i \bar{W}} \sum_{j \neq i}^I W_j D_{k,j} d_j \quad 4.10$$

Where  $\bar{W}$  is the mean molar mass,  $W_j$  is the molar mass of species  $j$ , and  $d_j$  is defined as:

$$d_j = \nabla X_i + (X_i - Y_i) \frac{1}{P} \nabla P \quad 4.11$$

The thermal diffusion velocity is given as

$$w_i = \frac{D_i^T}{\rho Y_i T} \nabla T \quad 4.12$$

Where  $D_i^T$  is the thermal diffusion coefficient for  $i^{th}$  species.

The multi-component methods have several important advantages over the relatively simpler mixture averaged methods. The multi-component methods have a better accuracy. The mixture-average methods can predict accurately on some special cases, such as in a binary mixture or in the diffusion of trace amounts of species into a nearly pure species. On the other hand, mixture-average methods have an advantage to save the computational time comparing to multi-component methods due to its simplicity. In the transport utility, Transport Pre-processor computes the polynomial representations of the temperature-dependent viscosities, thermal conductivities, and binary diffusion coefficients of each species involved in the reaction from transport property database and gas phase kinetics subroutine library. The polynomial fitting for these transport properties are given as

$$\text{Viscosity} \quad \ln \eta_i = \sum_{k=1}^K a_{k,i} (\ln T)^{k-1} \quad 4.13$$

$$\text{Thermal conductivity} \quad \ln \lambda_i = \sum_{k=1}^K b_{k,i} (\ln T)^{k-1} \quad 4.14$$

$$\text{Binary Diffusion Coefficient} \quad \ln \mathcal{D}_{ij} = \sum_{k=1}^K a_{k,ij} (\ln T)^{k-1} \quad 4.15$$

By default, Transport uses third-order polynomial fits ( $K=4$ ), and the fitting errors are well within one percent.

Similar to Gas-Phase Kinetic Pre-processor, users can specify the transport property data in an input file to override or supplement the transport database. The transport pre-processor produces a linking file which is needed in the transport subroutine library, which will evaluate the mixture properties for the Application solvers.

## 4.4 Application solvers

Users specify the Application Solvers for their own applications. The Application Solvers include EQUIL, OPPDIF, PLUG, PREMIX, SHOCK, and SURFTHERM. The Application Solvers call the appropriate subroutines from Gas-Phase Kinetics and /or transport Subroutine or Surface Kinetics Libraries depending on the applications solvers for the simulations of chemical characteristics in different applications.

#### 4.4.1 PREMIX

In the present work, the unstretched flame characteristics were simulated using PREMIX, a steady, one-dimensional, laminar premixed flame code of Kee et al. [112] available in CHEMKIN. PREMIX is a FORTRAN program that computes the flame characteristics that included species mole fraction, temperature profiles, and laminar flame speed for steady burner stabilized and freely propagating premixed laminar flames using finite-rate chemistry and molecular transport.

In the PREMIX code, users specify either Burner-stabilized flame or Flame-speed Calculation models. The burner-stabilized flame model is one of the most commonly used model for analysing species profiles in the flame experiments, where the mass flow rate through the burner is known. The users have two options for this model: one where the temperature is known and another in which the temperature profile is determined by the energy conservation equation. In the case where the temperature profile is known, only the species transport is solved. In most of the experimental setup, there would be significant heat losses to the external environment, which are of unknown or questionable origin and thus are difficult to model. The chemistry strongly depends on temperature, so the chemical kinetics behaviour can be accurately simulated knowing the temperature profile in a flame. The flame speed calculation model involves a freely propagating flame. This configuration is used to determine the characteristic flame speed of the gas mixture at specified system pressure and inlet temperature. In this model, the temperature was computed from the energy equation. Flame speed depends on the thermal energy transport, and predicting the temperature distribution is an integral part of the flame speed calculation.

In order to formulate the governing equations, the following assumptions were made: no body forces, zero bulk velocity, no Dufour effect, no viscous dissipation, ideal gas behaviour of the mixture, and a constant pressure. The final form of the governing equations in the PREMIX flame code is as follows [112],

$$\dot{M} = \rho u A \quad 4.16$$

$$\dot{M} \frac{dT}{dx} - \frac{1}{C_p} \frac{d}{dx} \left( \lambda A \frac{dT}{dx} \right) + \frac{A}{C_p} \sum_{i=1}^N \rho Y_i V_i C_{pi} \frac{dT}{dx} + \frac{A}{C_p} \sum_{i=1}^N h_i \dot{w}_i = 0 \quad 4.17$$

$$\dot{M} \frac{dY_i}{dx} - \frac{d}{dx} (\rho A Y_i V_i) - A \dot{w}_i = 0 \quad 4.18$$

$$\rho = \frac{p\bar{W}}{R_u T} \quad 4.19$$

The net production rate of each species  $\dot{w}_i$  results from a competition between the chemical reactions involving that species. Each reaction proceeds according to the law of mass action, and the coefficients of the forward reaction rate is given in the modified Arrhenius form,

$$k_f = AT^\beta \exp\left(\frac{-E_A}{RT}\right) \quad 4.20$$

PREMIX reads the user input, which defines the flame condition, and puts any other needed parameters in a keyword format from the input file. The users have to specify three valuables: either pressure or density, temperature, and either a mass fraction, mole fraction, or molar concentration, to describe the state of a gas mixture. The PREMIX computes the flame properties and produces printed output, and saves the solution in an XML solution file. The solution file may be used as an initial estimate to compute the properties of a new flame condition, which may decrease the iteration time of the new computation.

## 4.5 Numerical solution method

The numerical solution procedure involves the application of finite difference approximations to the partial differential equations of the boundary value problem to obtain a system of algebraic equations. To start the iteration of the 1-D steady state freely propagating flame model, an initial estimate of the solution is required. The general form of this estimate is shown in Figure 4.2. On the reactant side of the reaction zone, the reactant species profiles are flat at the reactant values. On the product side, the product species are flat at the estimated product species. While the intermediate species profiles are estimated using a Gaussian profile that peaks in the centre of the reaction zone. The peak heights of major intermediate species, the centre zone, and the reaction zone width are specified in the input file.

Starting from the initial approximation on a small number of mesh points, new mesh points are added adaptively in the regions where the solution or its gradients change rapidly. The approximation on the finer mesh are obtained by interpolating the solution on a previous mesh. This procedure continues to add more number of grids or meshes until the number of mesh resulted in a converged solution that satisfied all the boundary conditions. The system of algebraic equations is solved for the solution vector by the damped modified Newton algorithm

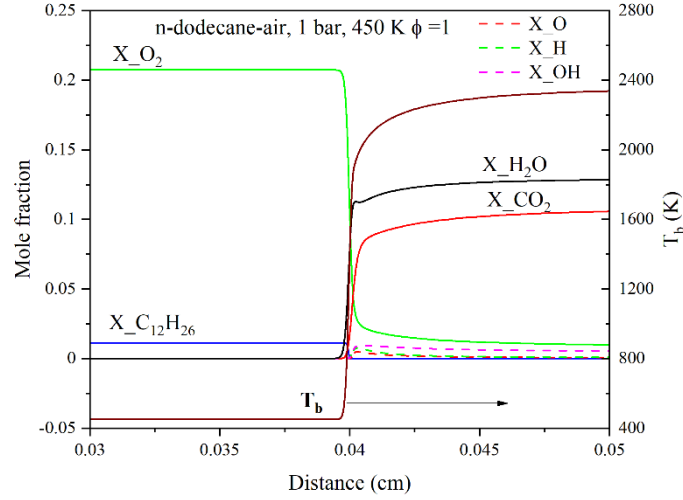


Figure 4.2. Profiles of reactant and products initial estimates

in TWOPNT. The approximated solution vectors defined as  $\phi$  are substituted into residual vectors defined as  $F(\phi)$  composed of the energy and species, and continuity equations. CHEMKIN solves the vector  $\phi$  that satisfies.

$$F(\phi) = 0 \quad 4.21$$

and the solution vector for this is given as,

$$\phi = (T_1, Y_{1,1}, \dots, Y_{K,1}, \dot{M}_1, \dots, T_J, Y_{1,J}, \dots, Y_{K,J}, \dot{M}_J)^T \quad 4.22$$

With the sufficiently good approximation  $\phi^{(0)}$  of the solution, Newton's method produces a sequence  $\phi^{(n)}$  that converges to the solution of the nonlinear equations ( $\phi$ ). Newton's method can be expressed as

$$\phi^{(n+1)} = \phi^{(n)} - \left( \frac{\partial F}{\partial \phi} \right)_{\phi^{(n)}}^{-1} F(\phi^{(n)}) \quad 4.23$$

The Jacobian matrices  $\frac{\partial F}{\partial \phi}$  is replaced by  $J^{(n)}$  defined as

$$J_{i,j} \approx \frac{F_i(\phi_j + \delta) - F_i(\phi_j)}{\delta} \quad 4.24$$

And the full step from  $\phi^{(n)}$  to  $\phi^{(n+1)}$  may be cut short by a damping parameter  $\lambda^{(n)}$  where  $0 < \lambda^{(n)} \leq 1$ , then the iteration becomes

$$\phi^{(n+1)} = \phi^{(n)} - \lambda(J^{(n)})^{-1} F(\phi^{(n)}) \quad 4.25$$

If the damped modified Newton algorithm fails to converge, the solution estimate is conditioned by integration over time. This provides a new starting point for the Newton

algorithm that is closer to the solution, and this is more likely to be in the domain of convergence for Newton's method.

## 4.6 Boundary conditions

Unburned gas side or cold boundary: Temperature and mass-flux fractions are specified

Burnt side or hot boundary:

Temperature and mass flux fraction gradients are zero, i.e.,

$$\frac{dT}{dx} = \frac{dY_k}{dx} = 0, \quad 4.26$$

where  $K = 1, 2, \dots, K_g$  and  $K_g$  is the number of species.

For freely propagating adiabatic flame simulations, mass consumption rate,  $\dot{M}$  is an eigen value and is determined as part of the solution. It requires an additional boundary condition. So, the flame location is specified in terms of known temperature, and it is fixed at a point. The selection of this point is to insure that the temperature and species gradients “nearly” vanish at the cold boundary. If this condition is not met, then the resultant burning velocity will be low because of some heat loss through the cold boundary. These boundary conditions are sufficient for the prediction of the burning velocity.

## 4.7 Grid independence study

The computation started with a coarse mesh with the grid adaptation parameters as GRAD0.5 and CURV0.5 of computational domain length varied from -2 cm to 10 cm. Then, the GRAD and CURV were systematically decreased, as shown in the table reported in Figure 4.3(a). Reduction in the values of GRAD and CURV lower than 0.01 and 0.1 did not show any change in the solution, which could be observed from the residues plotted in Figure 4.3(b). Therefore, the grid refinement was achieved at a GRAD=0.01 and CURV=0.1, and hence, the same parameters were applied for all operating conditions. It is important to mention that we had tested the grid independency for other diluents too, and the same values of GRAD=0.01 and CURV=0.1 worked fine there too.

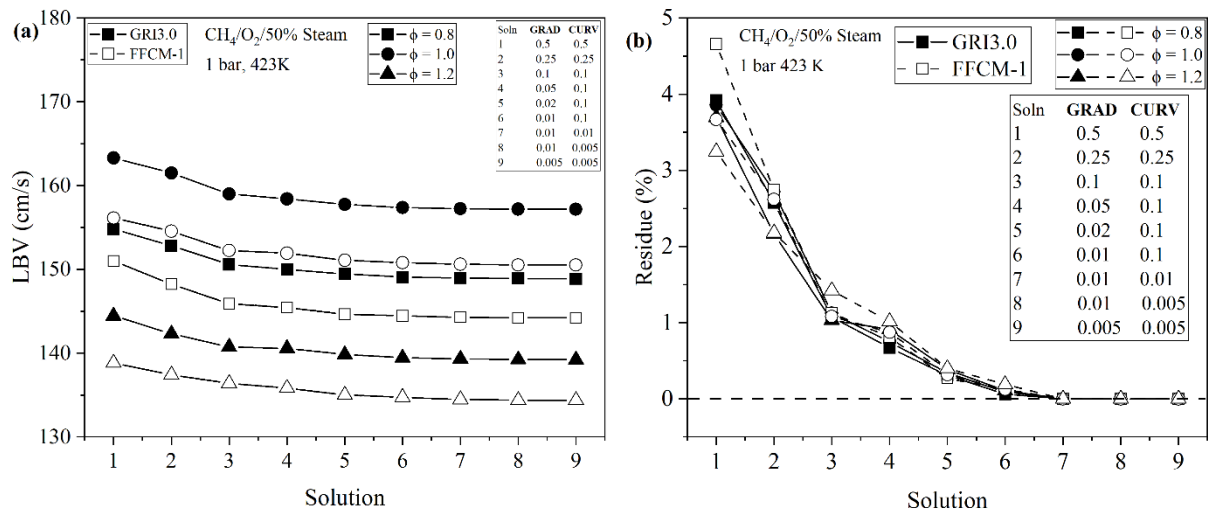


Figure 4.3. (a) LBV convergence with different grid points (b) convergence percentage of solution with different grid points

## 4.8 Reaction mechanisms

Table 4.1. Details of Chemical kinetic schemes used in the present work

Mixtures	Mechanism name	Species	Reactions
Methane/ $\text{O}_2$ /air/diluents	GRIMech 3.0 [113]	53	325
	FFCM-1 [114]	36	291
Dodecane/ $\text{O}_2$ /air/diluents/ $\text{H}_2$	JetsurF2.0 [41]	348	2163
	You et al. [115]	175	1318
	PoliMi-1410 [116]	130	2323
	Naik et al. [40]	597	3854
	Krithika et al. [117]	225	1509
	LLNL [118]	65	363

The chemical kinetic mechanisms reported in Table 4.1 were utilized in the present work to determine various parameters such as equilibrium flame temperature, unstretched laminar burning velocity, density ratio, temperature profiles, mixture thermal conductivity, specific heat capacity, and thermal diffusivities of all the investigated combustible mixtures.

## 4.9 Sensitivity analysis

Sensitivity analysis provides a quantitative understanding of how the solution of a problem depends on the various parameters present in the respective problem. In this work, sensitivity

analysis helped to identify the most dominant elementary reactions in a given reaction mechanism. It is also used to generate shorter or reduced reaction mechanisms from the existing detailed reaction mechanism. In CHEMKIN, the first-order sensitivity coefficients of the gas temperature, species fractions, and flow rate with respect to the reaction rate coefficients are considered.

A set of model parameters  $\alpha$  are added to the solution variables in the governing equations, and the residual vector is modified as

$$F(\Phi(\alpha); \alpha) \quad 4.26$$

In CHEMKIN, the  $\alpha$  represents the pre-exponential “A-factors” in the Arrhenius reaction-rate expressions. By differentiating the equation with respect to  $\alpha$ , a matrix equation for the sensitivity coefficients are given as

$$\left. \frac{\partial F}{\partial \Phi} \frac{\partial \Phi}{\partial \alpha} \right|_F + \frac{\partial F}{\partial \alpha} = 0 \quad 4.27$$

Where the matrix  $\frac{\partial F}{\partial \Phi}$  is the Jacobian of the original system and  $\frac{\partial F}{\partial \alpha}$  is the matrix of partial derivatives of  $F$  with respect to the parameters. The sensitivity coefficients are defined as  $\frac{\partial \Phi}{\partial \alpha}$ . This matrix contains quantitative information on how each reaction rate coefficient affects the temperature, species profiles, and flow rate of flame.

## 4.10 Reaction pathway analysis

The reaction pathway diagram is the graphical representation of the rate of production and consumption of major and minor species involved in a complex reaction mechanism. The thickness of the arrow lines is governed by the strength of elemental flux to highlight the importance of a reaction path. The reaction pathway for the carbon element flux was estimated using Cantera software [119] that was available in the python package [120]. Graphviz tool [121] was also used. Jetsurf2.0 [41] mechanism was used in the reaction pathway analysis. A threshold value equal to 5% of the largest elemental flux is chosen to simplify the complex combustion behaviour of the mixture. From the pathways, it is observed that the combustion chemistry of heavy hydrocarbon n-dodecane ( $nC_{12}H_{26}$ ) mainly depends on smaller species like  $C_1$ - $C_4$ , and it was discussed in detail in the results chapter.

# CHAPTER 5

## TEST RIG VALIDATION

### 5.1 Validation of experimental setup

The newly developed test facility was validated at different operating conditions. The fuels considered were CH<sub>4</sub>, a representative of lighter hydrocarbon, and n-decane, a representative of a heavier liquid hydrocarbon mixture. The oxidizer considered was dry air. Its composition was 21%O<sub>2</sub> and 79%N<sub>2</sub> by volume. They were tested at different initial temperatures, initial pressures, and with steam dilution too. All the operating conditions of the validation experiments are presented in Table 5.1. The measured unstretched LBV and burned gas Markstein lengths from these experiments were compared with the existing literature. Important results from the validation results are presented in this section.

Table 5.1. Summary of the operating conditions of validation experiments

Lighter hydrocarbon without and with steam dilution					
Cases	Mixtures	T (K)	p (bar)	$\phi$	Condition
1	CH <sub>4</sub> - air	300	1	0.8, 1.0, 1.2	Atmospheric pressure
2	CH <sub>4</sub> - air	373	1	0.8, 0.9, 1, 1.1, 1.2	Elevated temperature
3	CH <sub>4</sub> - air	423	1	0.8, 1.0, 1.2	Elevated temperature
4	(CH <sub>4</sub> - air)/10% steam	373	1	0.8, 0.9, 1, 1.1, 1.2	Steam evaporation
5	CH <sub>4</sub> - air	300	3	0.8, 1.0, 1.2	Elevated pressure
Heavy hydrocarbon mixture					
6	n-Decane - air	425	1	0.8, 0.9, 1, 1.1, 1.2, 1.3, 1.4	Liquid fuel

### 5.2 Lower alkane without and with steam dilution

Validation of lighter and small hydrocarbon CH<sub>4</sub>-air-steam mixtures under different operating conditions were tested, and the measurements of unstretched LBV and Markstein lengths are discussed below.

#### 5.2.1 Elevated initial temperature and water evaporation

The present study involved the vaporization of a liquid medium such as water for steam dilution studies and n-dodecane liquid fuel. To keep them in the gas phase, the chamber and mixture needed to be heated, as mentioned in section 3.4.2, to facilitate the measurement of

unstretched LBV. To check the mixture preparation in the present test facility at elevated temperatures, the unstretched LBV of premixed methane-air mixtures was measured at 373 K & 423 K, 1 bar, and  $\phi = 0.8$ –1.2. A nonlinear NE model (Eq. 3.6) was used to find the unstretched LBV and  $L_b$ . All the operating conditions were simulated in a freely propagating planar flame model to find the unstretched LBV using GRIMech3.0 and FFCM-1 reaction mechanisms. Figure 5.1(a) shows the unstretched LBV obtained from the present experiments and simulations, along with the Duva et al. [30] data. Present data showed an excellent agreement with that of Duva et al. [30], and the deviation was in the range of  $\pm 0.7\%$  to  $\pm 4.3\%$  and was well within the measurement uncertainty. The simulated LBV data of methane-air mixtures with GRIMech3.0 matched with that of measurements at all studied conditions, whereas the LBV predicted with FFCM-1 showed discrepancies with the measurements at stoichiometric and rich mixture conditions.

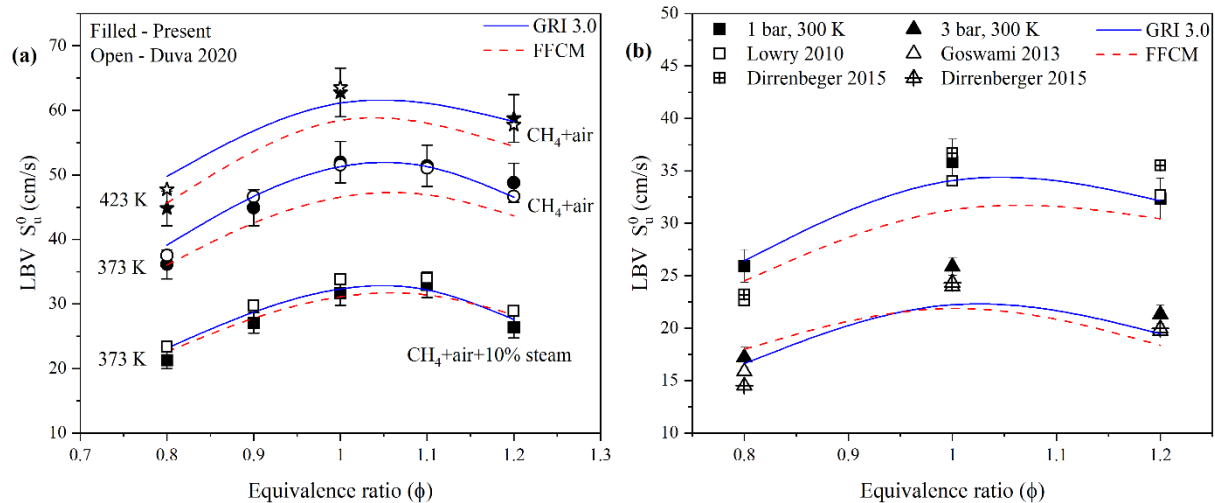


Figure 5.1. Experimental and computed unstretched laminar burning velocities as a function of the equivalence ratio for (a) Elevated temperature:  $CH_4$ /air at 1 bar, 373 & 423 K and  $CH_4$ /air/10%  $H_2O$  mixtures at 1 bar and 373 K (b) Elevated pressure:  $CH_4$ /air at 1 & 3 bar

To verify the present vaporization procedure involving steam and the mixture preparation, additional experiments were performed with 90% ( $CH_4+4.76/\phi$  Air) + 10%  $H_2O$  mixture at 1 bar, 373 K, and different equivalence ratios. The mixture was prepared by following the experimental procedure reported in section 3.5. The obtained unstretched LBV is shown in Figure 5.1(a), along with the [30] data. There was a good agreement between them. At 10% steam dilution, the predicted LBV from both the GRIMech3.0 and FFCM-1 models matched well with the measurements. The deviations of the present data from those of the literature and simulated data were well within the experimental uncertainties. Hence, the rig was successfully validated for studies related to elevated temperatures and steam dilution.

To validate the new rig at elevated pressures, the unstretched LBV of premixed methane-air mixtures was measured at initial pressures of 1 and 3 bar, 300K, and  $\phi=0.8, 1.0, 1.2$ . The measured LBV was compared with the recent literature data [22,122,123] and shown in Figure 5.1(b), along with the respective numerical predictions using GRIMech3.0 and FFCM. The present measurement is in good agreement with the literature, and there is a little discrepancy with the simulation at elevated pressures. Here too, at elevated pressure conditions, the present new facility worked excellently, and hence, it was validated.

### 5.2.2 Validation of Markstein lengths of premixed CH<sub>4</sub>-air mixtures

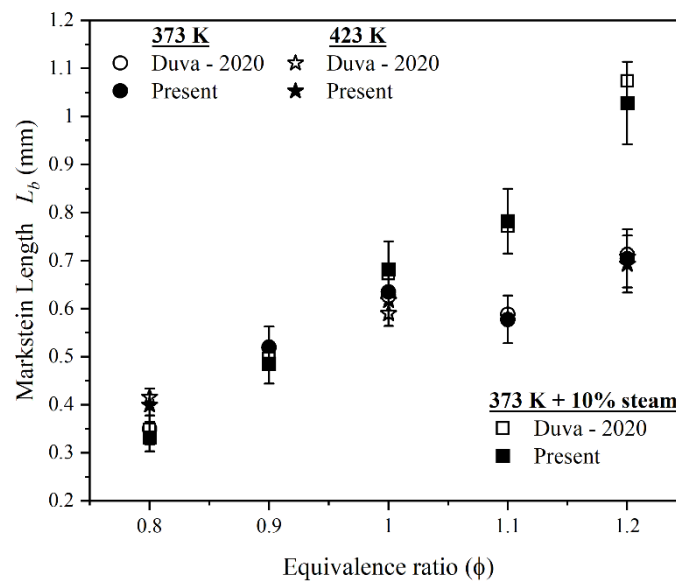


Figure 5.2. Variation of burned gas Markstein lengths of (a) CH<sub>4</sub>/air mixtures at 1 bar, 373 K and 423 K (b) CH<sub>4</sub>/air/10% steam at 1 bar 373 K. the measurements compared with [30]

Another widely used experimental parameter is the burned gas Markstein length, which addresses the effect of flame stretch and thermos-diffusive effects on the LBV. Although its value highly depends on many parameters, such as the radius range, and the choice of extrapolation scheme, the  $L_b$  obtained from present measurements were compared with Duva et al. [30], who also measured it using the spherical flame method. Figure 5.2 shows the variation in the burned gas Markstein lengths of premixed CH<sub>4</sub>-air mixtures at 373 and 423 K and 90% (CH<sub>4</sub>+4.76/ $\phi$  Air) +10% H<sub>2</sub>O mixtures at 373 K and 1 bar. The present measurement agreed well with Duva et al. [30] in terms of the sign and magnitude of burned gas Markstein length well within the experimental uncertainties.

## 5.3 Validation study with heavy hydrocarbon fuels

As the present study intended to find the unstretched LBV of n-dodecane reacting in air and oxygen mixtures, another widely used heavy liquid hydrocarbon, n-decane, was chosen for validation experiments for which the unstretched LBV and burned gas Markstein length data were available in the literature. Unfortunately, for n-dodecane, only unstretched LBV was reported in the literature but not the Markstein length data. Hence, the n-decane was chosen for the validation experiments. The boiling point of n-decane was 447.5 K at 1 bar. In the present work, the partial pressures of n-decane was in the range of (10 –19 mbar), and the respective saturation temperature was 340-352 K. Hence, the initial temperature was kept at 400 K. The premixed combustible mixture of n-decane-air mixture was prepared by following the strategy mentioned in the methodology section. The unstretched LBV of premixed n-decane-air mixtures at 1 bar, 400 K, and  $\phi=0.8-1.4$  was measured.

### 5.3.1 Unstretched LBV on premixed n-decane-air mixture

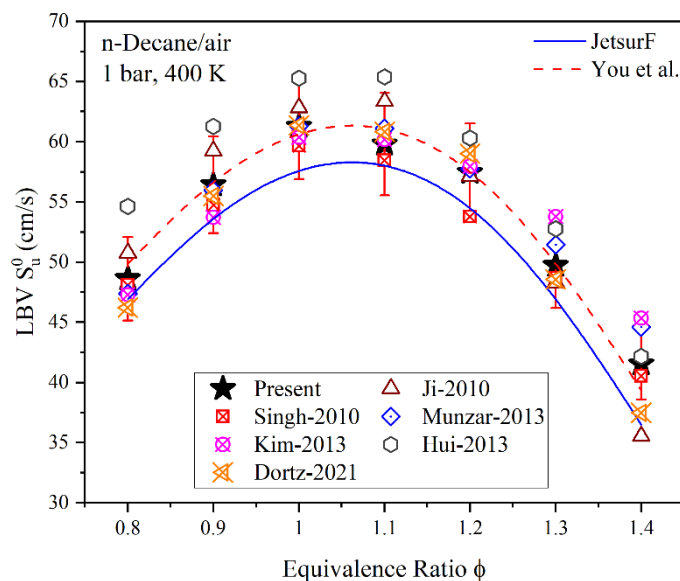


Figure 5.3. The comparison of measured unstretched laminar burning velocity of n-dodecane/air mixtures at 1 bar 400 K with existing literatures

Figure 5.3 shows the variation of measured unstretched LBV with the equivalence ratio of the premixed n-decane-air mixture at 1 bar and 400K. The present measurements were compared with the literature data [33,36,37,39,124,125]. The LBV reported in the literature was using different measurement methods such as the counter-flow flame method, stagnation flame method, and outwardly propagating spherical flame method. It is observed that the

present experimental LBV (filled star) shows an excellent agreement with the literature data [33,39,124] that was measured using the spherical flame method. Present data was on the lower side as compared with the data measured with counter flow flames [36,37] and stagnation flames [125] as these methods had inherent uncertainties such as the presence of seeding particles in the combustible mixture, smaller planar flame, etc. The fuel-rich mixtures exhibited more scatter because of the choice of different extrapolation schemes, as these mixtures have a non-unity Lewis number. The present LBV aligned with the You et al. [115] mechanism prediction, whereas JetsurF2.0 [41] was slightly under-predicted at all equivalence ratios.

### 5.3.2 Validation of heavy hydrocarbon fuels on Markstein length

Unlike methane-air mixtures, the n-decane-air mixture was very sensitive to the stretch and thermo-diffusive effects due to the huge disparity in the mass diffusivity of n-decane and oxygen species. The burned gas Markstein length was estimated using the nonlinear extrapolation model (Eq. 3.6).

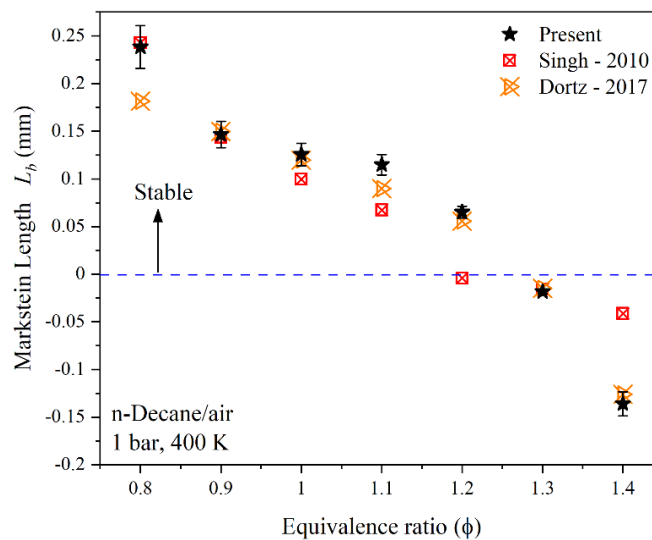


Figure 5.4. Burned gas Markstein length of premixed n-decane-air mixtures at 1 bar, 400 K, and different equivalence ratios

Figure 5.4 shows the measured  $L_b$  as a function of the equivalence ratio for n-decane-air mixtures. At  $\phi \geq 1.3$ , the  $L_b$  shows a transition from a positive to a negative value indicating that these mixtures were unstable to thermo-diffusive effects. The magnitudes and the transition all matched well with Dortz et al. [39] data which also was obtained using SPF method.  $L_b$  data of Singh et al. [33] was obtained using SPF method with a higher upper radius (30 mm), and their values were slightly off with the present measurements.

## 5.4 Repeatability

To verify the repeatability of the present experimental setup, five different experiments were conducted for a stoichiometric (a) methane-air mixture at 1 bar and 300 K and (b) n-dodecane-air mixture at 1 bar and 425 K. The unstretched LBV was calculated and plotted in Figure 5.5.

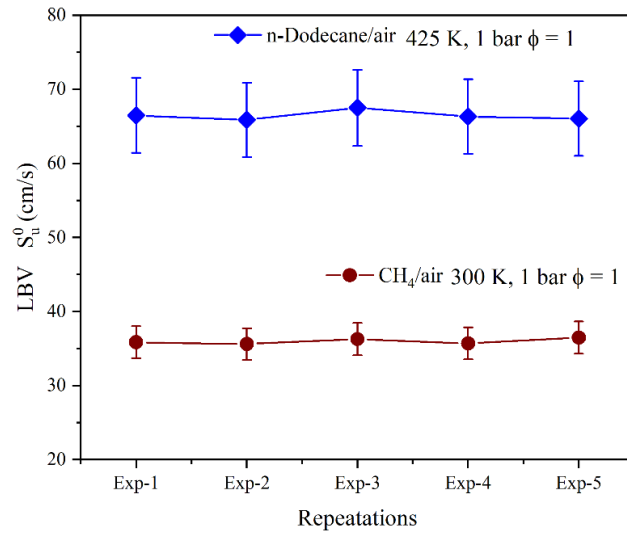


Figure 5.5. Repeatability of unstretched laminar burning velocity for stoichiometric (a) CH<sub>4</sub>/air at 1 bar, 300 K and (b) n-Dodecane/air at 1 bar 425 K mixtures, for five different experiments

The experimental uncertainties in the calculation of the unstretched LBV were  $\pm 6.03\%$  and  $\pm 7.64\%$  for methane and n-dodecane mixtures, respectively. The observation in Figure 5.5 indicated that the experimental unstretched LBV of all the experiments fall within the experimental uncertainty limits, and it is clear that the present experimental setup shows excellent repeatability.

## 5.5 Summary

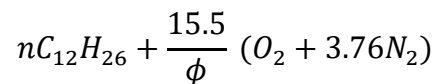
Six different sets of experiments were performed to validate the present new experimental facility and its post-processing procedures at different: initial temperatures and initial pressures. Both the unstretched LBV and burned gas Markstein length measured from the present work showed a very good agreement with the literature data. The repeatability of the present rig was also demonstrated.

# CHAPTER 6

## COMBUSTION CHARACTERISTICS OF PREMIXED N- DODECANE-AIR MIXTURES

As mentioned in the introduction, n-dodecane is one of the important surrogate species of kerosene fuel [2]. To test and validate the existing chemical kinetic schemes of n-dodecane, ignition delay and LBV are often used [2–4]. It is important to understand the response of a flame to stretch and thermo-diffusional effects and to obtain the unstretched LBV. In the present work, the burned gas Markstein length and unstretched LBV of n-dodecane reacting with air was measured and simulated. Important results and the associated inferences are discussed in this chapter.

### Mixture formulation



### Operating conditions

Table 6.1. Operating conditions of n-dodecane-air mixtures

n-dodecane-air	1 bar	400 K	$\phi$ : 0.8 – 1.4	7
		425 K	$\phi$ : 0.8 – 1.4	7
		450 K	$\phi$ : 0.8 – 1.4	7
	425 K	2 bar	$\phi$ : 0.8 – 1.4	7
		4 bar	$\phi$ : 0.8 – 1.4	7
	Total number of experiments			

### Chemical kinetic mechanism

Table 6.2. Kinetic mechanism for validating LBV of n-dodecane-air mixtures

Name of the Mechanism	Number of Species	Number of reactions
JetsurF2.0 [41]	348	2163
PoliMi-1410 [116]	130	2323
You et al. [115]	175	1318
Naik et al. [40]	597	3854
Krithika [117]	225	1509
LLNL [118]	65	363

## 6.1 Pressure - time evolution

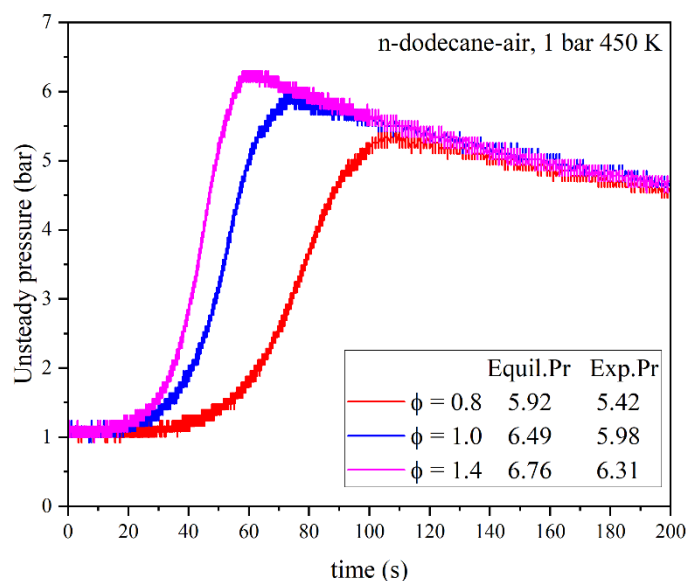


Figure 6.1. Variation of unsteady pressure after ignition as a function of time for different equivalence ratios of n-dodecane-air mixtures at 1 bar 450 K

Figure 6.1 depicts the variation of unsteady pressure-time history measured inside the chamber for three different equivalence ratios of n-dodecane-air mixtures at 1 bar and 450 K. The post-combustion pressure initially remained constant for a brief duration as the generated products were not sufficient enough to compress the reactants and to raise the pressure. After the pre-pressure duration, it started increasing rapidly and attained a peak. After the peak, it decreased due to the completion of combustion and heat transfer from the gases to the chamber walls. The measured peak pressures were very close to the estimated equilibrium pressure, which corroborated the complete combustion of the reactant mixture, and the minor deviation (average of 7.65%) was due to the heat transfer from the gases to the chamber walls. The constant pressure zone was quite essential in this work as the flames imaged during that period alone were analysed to estimate LBV.

## 6.2 Flame radius and flame speed variations

Figure 6.2 shows the expected linear variation of the flame front radius with time for stoichiometric n-dodecane-air mixtures at 1 bar and 450 K. The predefined radius limits ( $R_{fl}:0.8$ -  $R_{fu}:2.0$  cm, filled circles) was used to avoid the ignition and confinement related perturbations. Figure 6.2 also shows the variation of raw and smoothed flame speeds with time for the same mixtures. The stretched flame speed was calculated as first-order derivative using the finite difference of two consecutive flame radii with respect to time Eq. 3.4. The obtained

stretched flame speed was slightly scattered (red line) due to the use of numerical differentiation, and a smoothing algorithm LOWESS (locally weighted scatterplot smoothing) with a smoothing factor of 0.35 was used to remove the oscillations.

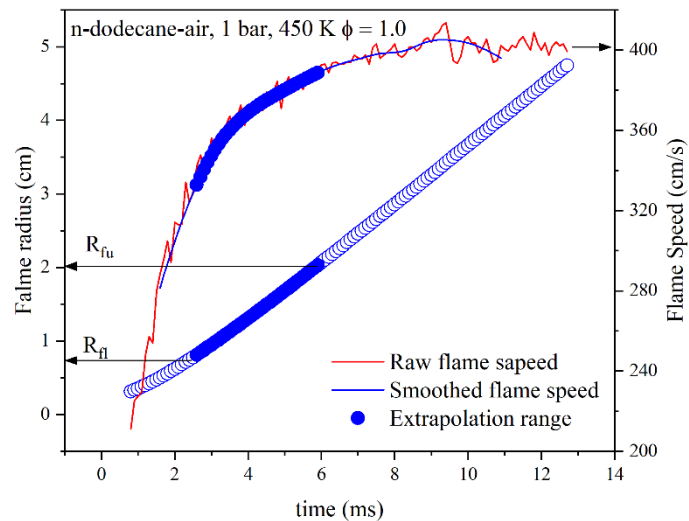


Figure 6.2. Variation of flame radius and stretched flame speeds as a function of time of stoichiometric n-dodecane-air mixtures at 1 bar and 450 K

In the smooth stretched flame speed (blue line), only an 8-20 mm radius range of smoothed flame speeds (filled circles on the blue line) was only used for nonlinear extrapolation to estimate unstretched LBV and burned gas Markstein length.

### 6.3 Nonlinear Flame speed behaviour

Figure 6.3 depicts the behaviour of flame speed with the stretch rate of premixed n-dodecane-air mixtures at 1 bar and 425 K. Different linear, and nonlinear extrapolation schemes were fitted to address its nonlinear nature, as shown in Figure 6.3. The linear extrapolation scheme overestimated the unstretched flame speed by 2.91%/ 0.49%/ 4.27% of 0.8/ 1/ 1.2 mixtures compared to LBV obtained with NE at identical operating conditions, respectively, with better goodness of fit.

Nonlinear effects were quite strong for mixtures having non-unity  $Le$ . For the present mixtures, Lewis numbers were estimated as the ratio of the thermal diffusivity of the mixture to the mass diffusivity of deficient reactant to bulk inert. Off-stoichiometric mixtures had non-unity Lewis numbers ( $Le = 3.9$  for  $\phi = 0.8$  and  $0.9$  for  $\phi = 1.4$ ), resulted in the non-linear variation of stretched flame speed with stretch rate. Therefore, nonlinear extrapolation schemes provided better results than the linear scheme. Among the nonlinear extrapolation schemes, NE performed better than NQ for n-dodecane in terms of (1) better goodness of fit and (2) being

less sensitive to the radius range chosen for extrapolation. Additionally, Wu et al. [126] suggested that the product of the Markstein number and Karlovitz number should be as  $-0.05 < MaKa < 0.15$  to reduce the extrapolation uncertainty, In the present work, the  $MaKa$  value is between  $-0.03 < MaKa < 0.13$ . Therefore, all the LBV data reported in this study were obtained with a nonlinear expansion scheme, NE [99].

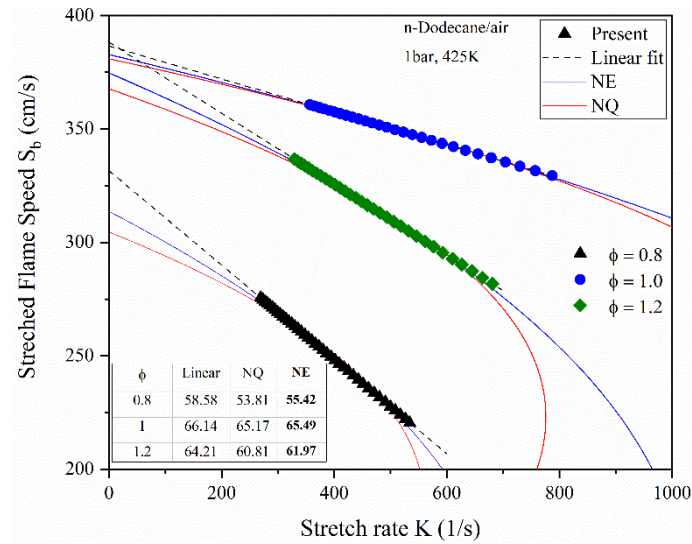


Figure 6.3. Variation in the stretched flame speed of n-dodecane-air mixture with the flame stretch rate at 1bar, 425K, and  $\phi = 0.8-1.2$

## 6.4 LBV Mechanism validation

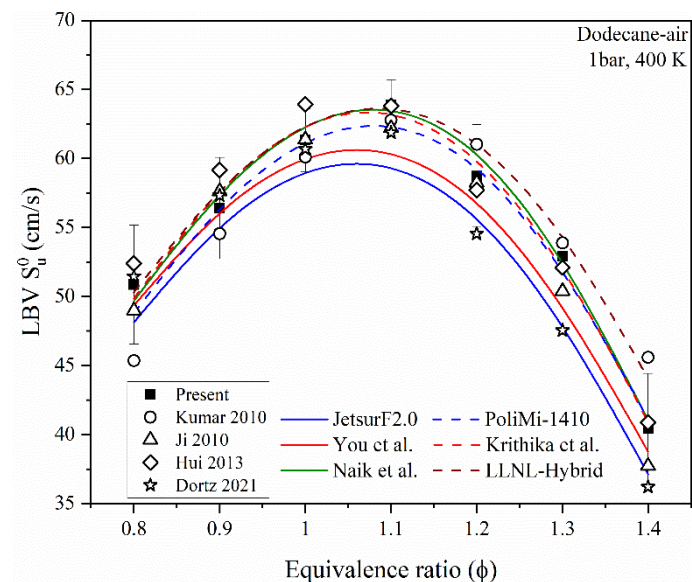


Figure 6.4. Comparison of the measured unstretched LBV of n-dodecane/air mixtures with simulations and literature data at 1 bar and 400 K. solid/ dashed lines – detailed/ reduced mechanisms

Figure 6.4 shows the variation of measured unstretched LBV of premixed n-dodecane-air mixtures with equivalence ratio at 1 bar and  $400 \pm 3$  K, along with the literature data. LBV peaked at  $\phi=1.1$  due to higher flame temperature. Present measurements showed better agreement with the literature data predominantly obtained with the counter-flow flame method. Scattering within the reported counter-flow flame data was observed at off-stoichiometric conditions, as shown in Figure 6.4. The possible reason for the uncertainty in the counter-flow flame could be the presence of seeding particles in the combustible mixture while measuring the velocity profile of the reacting flow field, intensive post-processing involved in PIV, the presence of a small region of planar flame, and the choice of the reference velocity [25]. The present result precisely matched with the recent work of Dortz et al. [39] up to  $\phi = 1.0$ , but quite a bit of deviation was observed at rich mixture conditions, and it was essentially due to their choice of NQ extrapolation scheme, which typically underperforms at rich mixtures having  $Le < 1$  [100,126]. An important objective was to test the existing kinetic schemes; all measurements were simulated using different kinetic schemes presented in Figure 6.4. Table 6.3 shows the percentage deviation of predictions with respect to the measurements at 1 bar, 4 bar, and 425 K.

Table 6.3. List of Mechanisms and their deviation with measurements

n-Dodecane/air, 425K								
Name of the Mechanism	Number of Species	Number of reactions	LBV Deviation (in %)					
			1 bar			4 bar		
			$\phi = 0.8$ (55.42 cm/s)	$\phi = 1.0$ (65.49 cm/s)	$\phi = 1.4$ (44.00 cm/s)	$\phi = 0.8$ (35.03 cm/s)	$\phi = 1.0$ (45.59 cm/s)	$\phi = 1.4$ (23.26 cm/s)
JetsurF2.0 [41]	348	2163	3.15	0.57	5.00	2.62	4.84	4.43
PoliMi [116]	130	2323	1.46	4.59	7.78	8.05	7.65	27.92
Youet al.[115]	175	1318	0.63	2.30	2.71	10.59	6.34	17.98
Naik at al.[40]	597	3854	0.40	6.50	4.08	12.33	12.00	27.62
Krithika [117]	225	1509	0.58	6.38	4.59	13.53	15.02	32.99
LLNL[118]	65	363	1.48	6.27	12.64	11.55	10.43	33.93

Predicted LBV with the detailed mechanism of JetsurF2.0 [41] and You et al. [115] showed a good agreement with the present measurements at 1 bar. The next best was a reduced mechanism, PoliMi-1410 [116]. As shown in Table 6.3, at 4 bar other than JetsurF2.0, predicted LBV with other mechanisms showed large deviation at all the studied conditions, especially poor predictions at rich mixtures. Based on Table 6.3, JetsurF2.0, You et al., and

PoliMi-1410 were considered for the comparison of experimental results further for all other operating conditions.

## 6.5 Flame stability

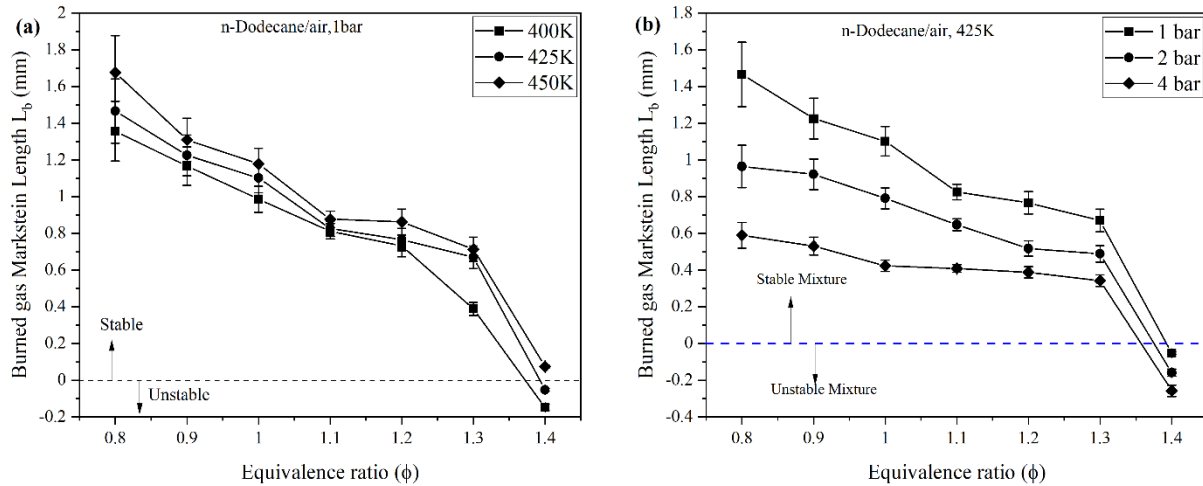


Figure 6.5. Variation of burned gas Markstein length of n-dodecane/air mixtures at different (a) initial mixture temperature and (b) pressure

Burned gas Markstein length,  $L_b$ , quantifies the sensitivity of the flame to flame stretch and thermo-diffusional effects. It is positive/ negative for the stable/ unstable flames with respect to thermo-diffusional effects. Its variation with the equivalence ratio of premixed n-dodecane and air mixtures at 1 bar and 400–450 K was displayed in Figure 6.5 (a). The current interest was to locate the onset of instability due to the thermo-diffusional effects; the equivalence ratio was limited from 0.8 to 1.4. Extending the measurements after  $\phi=1.4$ , resulted in relatively slower flames affected by buoyancy at elevated pressures. Figure 6.5 indicates that  $L_b$  remained positive for most of the studied cases vindicating that the n-dodecane-air mixture remained stable to thermo-diffusional effects. At  $\phi = 1.4$  and  $T < 450$  K,  $L_b$  of n-dodecane-air mixtures were negative, and they were unstable to thermo-diffusional effects due to the occurrence of thicker (thickness = 0.4-0.6 mm) and slower (reaction time  $\approx 1$  ms) flames. These slow flames were affected by stretch and thermo-diffusional effects for a longer duration (stretch time  $\approx 2.8$ -5 ms). All these effects resulted in an unstable flame. As the initial temperature increased to 450 K at  $\phi=1.4$  as shown in Figure 6.5(a), the transition of  $L_b$  from negative to positive occurred, indicating that an increase in temperature has further widened the flame stability limits due to an increase in the mixture's thermal diffusivity. To support the new findings, effective  $Le$  (Eq. 3.21) and critical  $Le$  (Eq. 3.22) numbers were estimated. Effective/ critical  $Le$  formulation reported by different researchers were attempted, and

unfortunately, the estimated values did not agree with the measurements. Finally, the expression provided by Matalon et al. [102] accurately predicted the transition as it involved  $L_b$  values. For the mixtures having negative  $L_b$ , the effective  $Le$  was less than the critical  $Le$ . As shown in Figure 6.5(a), the magnitude of the  $L_b$  has not significantly changed with the range of initial temperatures investigated in the present work due to a slight decrement in the flame thickness (Figure 6.6) and  $Ka \left( K \delta / S_u^0 \right)$ , as shown in Table 6.4. Hence, it is suggested to maintain initial temperatures at or above 450 K to avoid unstable flames at rich mixture conditions.

Figure 6.5(b) shows the  $L_b$  as a function of equivalence ratio at different initial pressures and 425 K. Except at  $\phi=1.4$ ,  $L_b$  remained positive for mixtures at other equivalence ratios and elevated pressures. At  $\phi=1.4$ , the studied mixtures showed a transition from stable ( $L_b > 0$ ) to unstable ( $L_b < 0$ ) conditions towards the thermo-diffusional effects. Effective/ critical  $Le$  of these mixtures is shown in Figure 6.6. As mentioned earlier, for all the unstable mixtures,  $Le_{eff} < Le^*$  supported preferential diffusion instability. An increase in initial pressure decreased the magnitude of  $L_b$  substantially at all the conditions. Flame thickness estimated from the simulated temperature profile are displayed in Figure 6.6, and it reduced significantly with an increment in the initial pressure due to an increase in reaction rate. Table 6.4 shows the kinetic and stretch response times of all the unstable mixtures along with their ratios as Karlovitz number. As pressure increased, thinner flames were generated with smaller  $Ka$  (less responsive to stretch), and therefore,  $L_b$  also decreased. Another caution was that the  $L_b$  may undergo transition at higher pressures and result in unstable flames. All the reported unstable mixtures resulted in slowly propagating thicker flames that responded hefty to the stretch effects.

Table 6.4. Flame stability data of premixed dodecane-air mixtures

P	T	$\phi$	$\delta$	LBV	K ( $s^{-1}$ )		$\tau_r$	$\tau_s$ (ms)		Ka		$L_b$
					Max	Min		ms	Min	Max	Max	
bar	K		mm	cm/s								(mm)
1	400	1.4	0.45	40.4	607	243	1.11	1.65	4.12	0.67	0.27	-0.147
1	425	1.4	0.43	44	352	201	0.97	2.84	4.98	0.34	0.20	-0.051
2	425	1.4	0.25	38.5	403	196	0.66	2.48	5.09	0.27	0.13	-0.158
4	425	1.4	0.16	23.3	306	136	0.68	3.27	7.36	0.21	0.09	-0.257

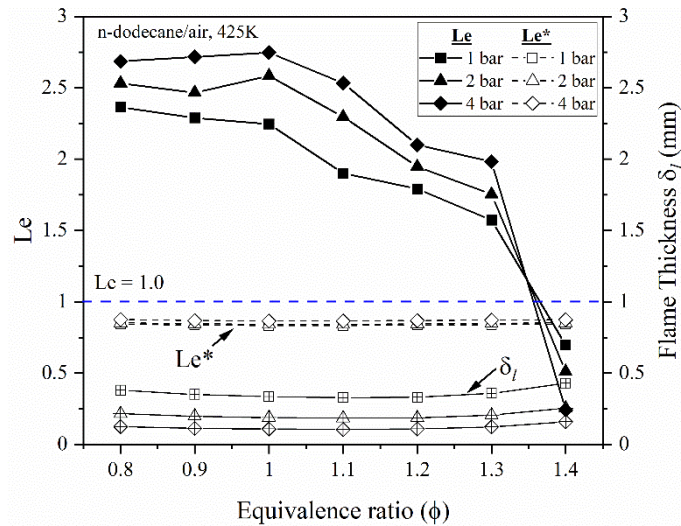


Figure 6.6. Variation of Lewis, critical Lewis number, and flame thickness as a function of equivalence ratio of dodecane/air mixtures at 425K, 1-4 bar

To further understand the cause of the unstable flames, the flame structure estimated using the PREMIX model in CHEMKIN is plotted in Figure 6.7 at  $\phi=0.8$  & 1.4, 425 K, and 4 bar. The flame structure comprised of net heat release rate, equilibrium flame temperature, and the local equivalence ratio. It showed that the of  $O_2$  preferential diffused from the preheat zone to the reaction zone, which resulted in the local equivalence ratio estimated with respect to reactants shot till 1.63 in the preheat zone than the global equivalence ratio of 1.4. The main reason was that at richer mixtures,  $O_2$  was the deficient reactant, and it was highly diffusive compared to n-dodecane and nitrogen.

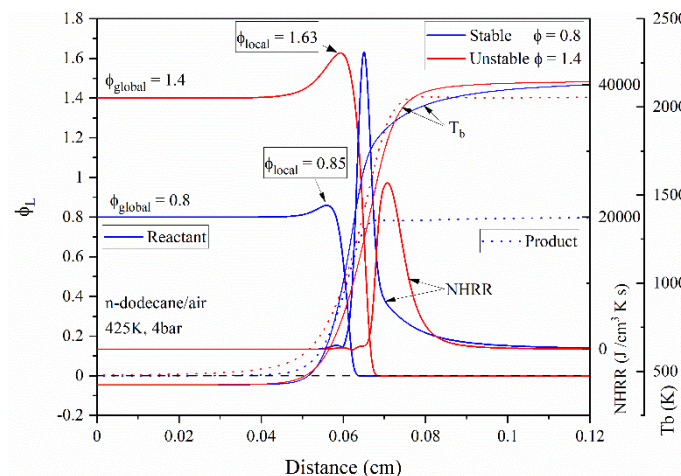


Figure 6.7. A predicted local equivalence ratio of premixed dodecane-air mixtures at  $\phi = 1.4$ , 1 bar, and 425 K using CHEMKIN

A closer look at the corresponding decrease in the local equivalence ratio with respect to the products was 1.35. Predominant diffusion of  $O_2$  in larger quantities resulted in preferential diffusion instability at  $\phi = 1.4$ . At  $\phi = 0.8$  also, a minor preferential diffusion effect could be seen as the local  $\phi$  increased till 0.85. This was expected as the diffusivity of  $O_2$  was higher than that of n-dodecane.

## 6.6 LBV at elevated pressure

The measured and predicted unstretched LBV of premixed n-dodecane-air mixtures at different equivalence ratios, different initial pressures, and 425 K are displayed in Figure 6.8. The peak value of LBV was observed at  $\phi=1.1$  at all pressures. At  $\phi=1.1$ , the value of LBV was 66.63 cm/s at 1 bar, and as the pressure raised to 4 bar, the LBV decreased by 30% to 47.82 cm/s as compared to atmospheric conditions. LBV decreased with an increase in the initial pressure was due to an increase in the (a) density of the mixture and (b) prominence of third body reactions. Irrespective of the decrease in the LBV, the mass consumption rate of the mixture increased with pressure due to an increase in the density of the reactant mixture [19]. LBV reported by

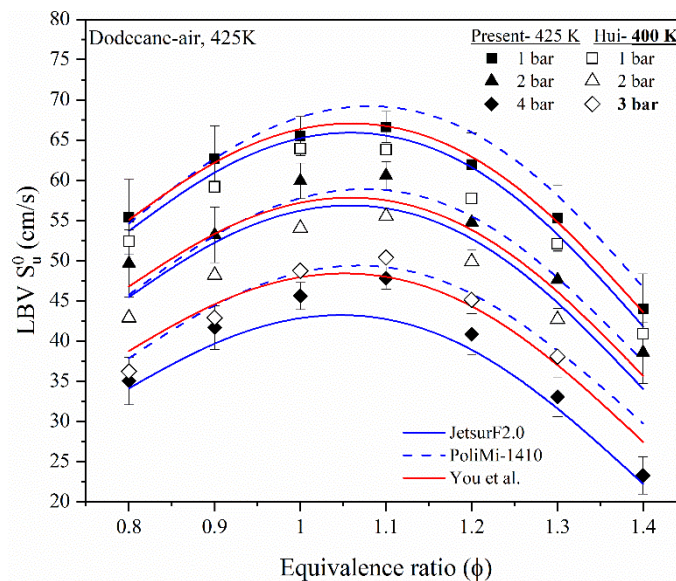


Figure 6.8. Measured unstretched LBV against equivalence ratio of premixed n-dodecane/air mixtures at 1-4 bar and 425 K. Filled, and open symbols represent present and Hui et al. [37] data and lines are corresponding numerical predictions of different mechanism

Hui et al. [37] at 400 K and different pressures was the closest match available in the literature to compare it with the present LBV data measured at elevated pressures, and hence, it was also plotted in Figure 6.8 and followed the trend of present data. Figure 6.8 also shows the

comparison of current measurements with the predictions obtained with different reaction mechanisms such as PoliMi-1410 [116], Jetsurf2.0 [41], and You et al. [115] using CHEMKIN. The deviation was evident within the predicted LBV by the three different reaction mechanisms. The predicted LBV of Jetsurf2.0 and You et al. mechanisms showed better agreement with most of the measurements within the experimental uncertainty. Albeit, the reduced PoliMi-1410 mechanism shows larger discrepancies ( $> 25\%$ ) with present rich mixtures at elevated pressures.

## 6.7 LBV at elevated temperatures

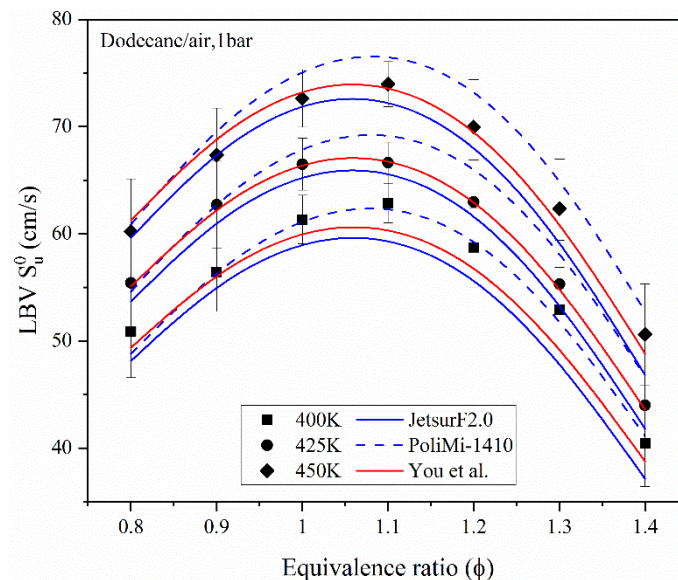


Figure 6.9. Measured unstretched LBV as a function of the equivalence ratio of premixed n-dodecane/air mixtures at 1 bar and 400-450K. Symbols and lines represent the present experimental and corresponding numerical predictions

The measured/ predicted unstretched LBV of premixed n-dodecane-air mixtures and its response to equivalence ratio and initial temperature at 1 bar is shown in Figure 6.9. As the initial temperature hiked, the flame temperature and the mixture's diffusivity increased, resulting in a gain in the values of LBV. Among the predictions with the three mechanisms, Jetsurf2.0 formed the lower bound, and the other two were predicted in the higher bound. The present measurement shows good agreement with all the mechanisms at most conditions within the experimental uncertainty. A maximum scatter of 10.73%/ 8.71%/ 5.81% were observed with PoliMi/ Jetsurf/ You et al. prediction compared with present measurements.

## 6.8 Temperature and pressure exponents

Figure 6.10 (a) shows the temperature exponents of the measurements and simulations at three different operating pressures and temperatures as the equivalence ratio varied from 0.8 to 1.4.

A power-law,  $S_{u, T_u, 1\text{bar}}^o = S_{u, 0}^o \left( \frac{T_u}{T_{u0}} \right)^\alpha$  where  $T_u$  is the initial temperature,  $T_{u0}$  is 400 K,  $S_{u, T_u, 1\text{bar}}^o$  is

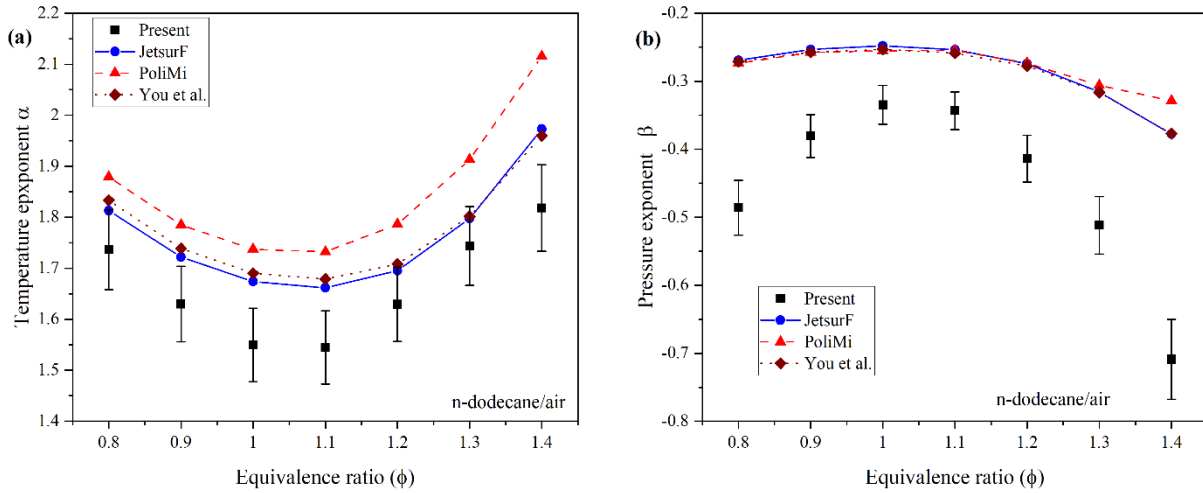


Figure 6.10. (a) Temperature and (b) pressure exponents of n-dodecane/air mixtures as a function of equivalence ratio. The solid (Jetsurf2.0), dashed (PoliMi), and dotted (You et al.) represent corresponding numerical predictions

the unstretched LBV at  $T_u$  & 1 bar,  $S_{u,0}^o$  is the unstretched LBV at 400 K & 1 bar, and  $\alpha$  is the temperature exponent, was fitted to the measured/ predicted unstretched LBV to find the temperature exponent at each equivalence ratio, respectively. Similarly, temperature exponents were estimated for the simulated LBV too. The temperature sensitivity of LBV estimated from measurements was the lowest as equated with simulations. Excluding the magnitude, the trend of variation of  $\alpha$  in both the measurements and simulations showed an excellent agreement.

Using a global reaction [16], the Boltzmann energy factor  $\exp\left(\frac{-E_A}{R_u T}\right)$  Where  $E_A/R_u$  - activation Temperature and  $T$  - equilibrium flame temperature was calculated, and as expected, it conformed to the trend displayed in Figure 6.10 (a), and hence, the LBV sensitivity to initial temperature was strongly dependent on equilibrium product temperature and the reaction rate.

Figure 6.10 (b) shows the pressure exponent ( $\beta$ ) obtained from  $S_{u, 400\text{K}, p}^o = S_{u, 0}^o \left( \frac{p}{p_o} \right)^\beta$  where  $p$  is initial pressure,  $p_o = 1$  bar,  $S_{u, 400\text{K}, p}^o$  is the unstretched LBV measured at 400 K and  $p$ , and its variation with equivalence ratio. The exponents estimated from the measurements displayed

more sensitivity than the simulations. Kinetic schemes need to be optimized. The increase in LBV sensitivity with a hike in pressure is discussed in the next section.

## 6.9 Sensitivity analysis

To find out the key elementary reactions that influence the LBV at different pressures, a normalized A-factor sensitivity was analyzed and reported. Figure 6.11 shows the normalized sensitivity coefficients of the dominant elementary reactions of three different mechanisms used to predict LBV of n-dodecane-air mixtures at  $\phi = 1.4$  and  $p=1-4$  bar. The top eight elementary reactions that had the highest magnitude of sensitivity coefficients of the JetsurF2.0 [41] reaction mechanism are reported in the figure. Then the normalized sensitivity coefficient of these eight reactions were identified from You et al. [115] and PoliMi-1410 [116] and are also included in the figure. An earlier study [36] mentioned that the propagation rate of n-dodecane-air flames was pretty sensitive to the oxidation chemistry of smaller species, which can be corroborated with Figure 6.11 too. The normalized sensitivity coefficients of the chain branching reactions R1 and R3 increased with an increase in the initial pressure. Similar to other hydrocarbon/air flames, R1 has the largest positive sensitivity coefficient for the n-dodecane/air mixtures, and its coefficient is much higher than those of other elementary reactions. The most sensitive reactions (R5-R8) that suppressed the LBV were the chain-termination reactions, such as  $H + OH + M = H_2O + M$  and  $HCO + H = CO + H_2$ , as they compete with R1-R4. Three-body reactions were chiefly dominating at the elevated pressure, altered the reaction path, and reduced the radical production; therefore, LBV decreased with pressure increase.

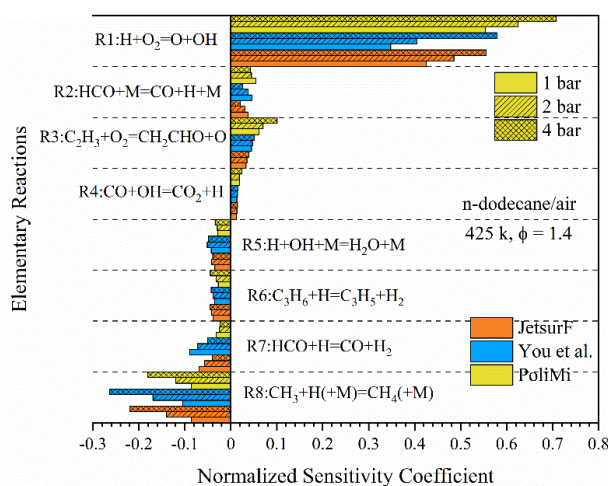


Figure 6.11. Normalized sensitivity coefficient of important elementary reactions of n-dodecane/air mixtures at different initial pressure 1-4 bar and 425K,  $\phi = 1.4$

## 6.10 Hydrodynamic Instability

All expanding spherical flames generated at the centre of an enclosure experience hydrodynamic instability (HI) due to the density jump across the flame irrespective of the fuel-oxidizer mixtures. The sudden formation of uniform small cells on the entire flame surface was an indicator of the onset of HI. Its onset is strongly dependent on the preferential diffusional stability of a mixture [127]. In the present work, an in-house image processing code developed

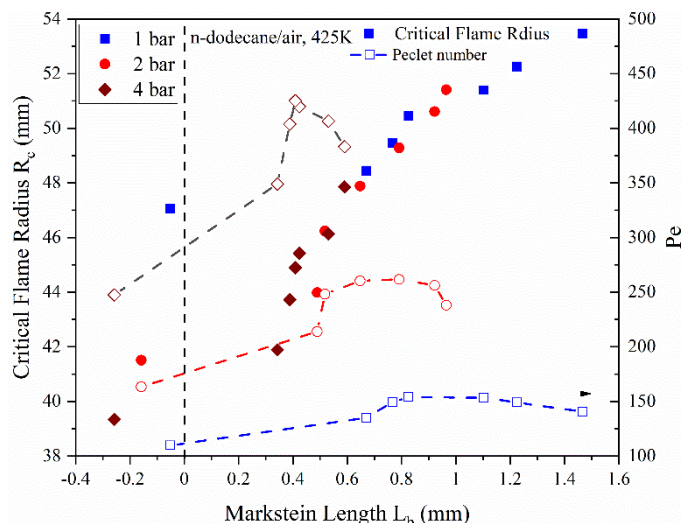


Figure 6.12. The variation of critical flame radius (filled symbols) and Peclet number (dashed lines) as a function of burned gas Markstein length of dodecane/air mixtures at 425 K, 1-4 bar

MATLAB was used to find the critical flame radius corresponding to the onset of HI to avoid human error, unlike in the literature, where the critical flame radius was estimated manually. As the present work involved slowly diffusive n-dodecane, information on the onset of HI becomes quite essential. Figure 6.12 presents the critical flame radius and Peclet number and their variation with  $L_b$  of n-dodecane-air mixtures at  $p=1-4$  bar and  $T=425$  K. The data were sorted in ascending order based only on their  $L_b$  without considering any other operating conditions. As the magnitude of  $L_b$  increased from negative to higher positive values, the onset of HI was delayed significantly, which clearly mentioned that diffusional effects balanced the effects of gas expansion across the flame and the associated perturbations. At the critical radius: (a) the chamber pressure was slightly higher than the initial pressure, (b) the flame radius was significantly larger as compared to its thickness, (c) the reaction and the diffusion time were shortened, resulting in HI.

## 6.11 Summary

The important conclusions are summarized below:

1. This study investigated the LBV and stability aspects of premixed n-dodecane-air mixtures at  $p=1-4$  bar,  $T = 400-450$  K, and equivalence ratio = 0.8-1.4 using expanding spherical flame method and 1D planar flame simulations.
2. LBV of n-dodecane/air mixtures increased with an increase in the initial temperature due to a hike in the flame temperature and mixture diffusivity. LBV decreased with an increase in initial pressure due to higher mixture density and dominance of third-body reactions obtained from sensitivity analysis.
3. Three detailed and three reduced mechanisms were tested. Out of which, two detailed and one reduced mechanism showed better comparison with the measurements within the experimental uncertainties.
4. Measured  $L_b$  showed that rich mixtures at  $\phi=1.4$  and at all temperatures and pressures other than 450 K were negative, indicating an unstable mixture due to preferential diffusion effects. The estimated effective  $Le$  of an unstable flame was less than the critical  $Le$  and corroborated well with the measurements.
5. The onset of hydrodynamic instability was estimated from all experiments. The critical flame radius increased with an increase in  $L_b$ , and a preferentially stable mixture delayed the onset of HI.

# CHAPTER 7

## COMBUSTION CHARACTERISTICS OF DILUTED PREMIXED OXY N-DODECANE MIXTURES

As discussed in the introduction in section 1.2, oxy-fuel combustion results in high flame temperature. The combustion characteristics of such high-flame temperature mixtures were not reported in the literature. Pure oxy-fuel combustion results in a flame temperature of ~3000 K, and the post-combustion pressure in a constant volume chamber was also quite higher. The LBV were in the range of ~3 m/s. Dealing with high-speed mixtures with high post-combustion pressure and temperature poses challenges to the structural integrity of the experimental rig. In this work, the oxy-fuel mixtures were diluted with a third-party diluent species, and the combustible mixture,  $(100-Z) \% (n-C_{12}H_{26} + (18.5 O_2/\phi)) + Z\% (N_2/CO_2/H_2O)$ , was prepared by following mixture diluent approach [45] where the diluent species is not a function of equivalence ratio. The equilibrium flame temperatures of the above mixtures were in the range of 2100 to 2800 K. The choice of three diluents were for the following reasons: (1)  $N_2$  – thermal effect, no chemical effect, and radiation, and it does not promote differential diffusion [44]. It helps to understand the high-temperature oxy-n-dodecane mixtures safely, (2)  $H_2O$  &  $CO_2$  –has both thermal and kinetic effects, radiation effects, and less-strong differential diffusion effects. Other degrees of freedom varied were the mole fraction of the diluent species in the combustible mixture, initial pressure, initial temperature, and equivalence ratio, and their effects on unstretched LBV and  $L_b$  were studied. Parallely, for all the experimental conditions, simulations were performed using 1D freely propagating flame model to estimate the unstretched LBV using different reaction schemes. All the important results are discussed in this section.

### Operating conditions

Table 7.1. Summary of operating condition of diluted oxy n-dodecane mixtures

Mixtures	Dilution (%)	P (bar)	T(K)	$\phi$	#
$(100-Z) \% (n-C_{12}H_{26} + (18.5 O_2/\phi)) + Z\% N_2$	55, 65, 75	1	400 - 450	0.6-1.4	45
	65	2	450	0.6-1.4	5
	65	4	450	0.6-1.4	5

35% (n-C <sub>12</sub> H <sub>26</sub> + (18.5O <sub>2</sub> /φ)) + 65% CO <sub>2</sub> /H <sub>2</sub> O	65	1,2,4	450	0.6-1.4	15+15
Total number of experiments					85

## Chemical kinetic mechanisms

Table 7.2. Kinetic mechanism used for diluted oxy-n-dodecane mixtures

Name of the Mechanism	Number of Species	Number of reactions
JetsurF2.0[41]	348	2163
PoliMi [116]	130	2323
You et al.[115]	175	1318

## 7.1 Pressure-time variation

Figure 7.1 shows the comparison of measured post-combustion pressure of oxy-n-dodecane mixture diluted with 65%N<sub>2</sub> at 2 and 4 bar and n-dodecane-air mixture at 1 bar. It is absolutely clear that in the case of oxy-combustion, the pressure time trace had sharp pressure gradients with intense fluctuations during the flame propagation close to the chamber walls due to strong turbulence and the associated increase in the consumption rate. Another possible reason could be the autoignition during the end of the combustion due to the faster propagation rate, higher flame temperature, etc., as reported in [128]. The sharp pressure peak with intense fluctuation were consistently reproduced in the repeatability experiments too. When the flame impinges on the chamber walls and the optical windows, it generated a knocking sound. The magnitude of peak pressure (>35 bar) was higher than the estimated equilibrium pressure due to the faster propagation rates and the associated turbulence generated inside the chamber. The same figure displayed the pressure history of n-dodecane-air mixture where the peak pressures were close to the equilibrium pressure, and the pressure gradients were gradual. Due to the above-mentioned reasons, the experiments were limited to an initial pressure of 4 bar only.

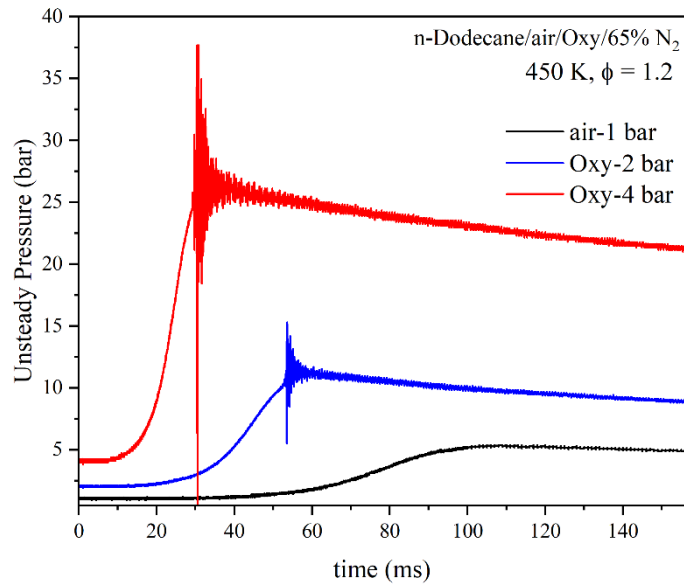


Figure 7.1. Pressure-time history of premixed (a) n-C<sub>12</sub>H<sub>26</sub> –air mixture (black solid line) and 35% (n-C<sub>12</sub>H<sub>26</sub>+ (18.5/φ) O<sub>2</sub>) + 65% N<sub>2</sub> T = 450 K, and φ = 1.2 at (b) 2 bar (blue solid line) (c) 4 bar (red solid line) measured inside the chamber after spark ignition

## 7.2 Flame propagation history

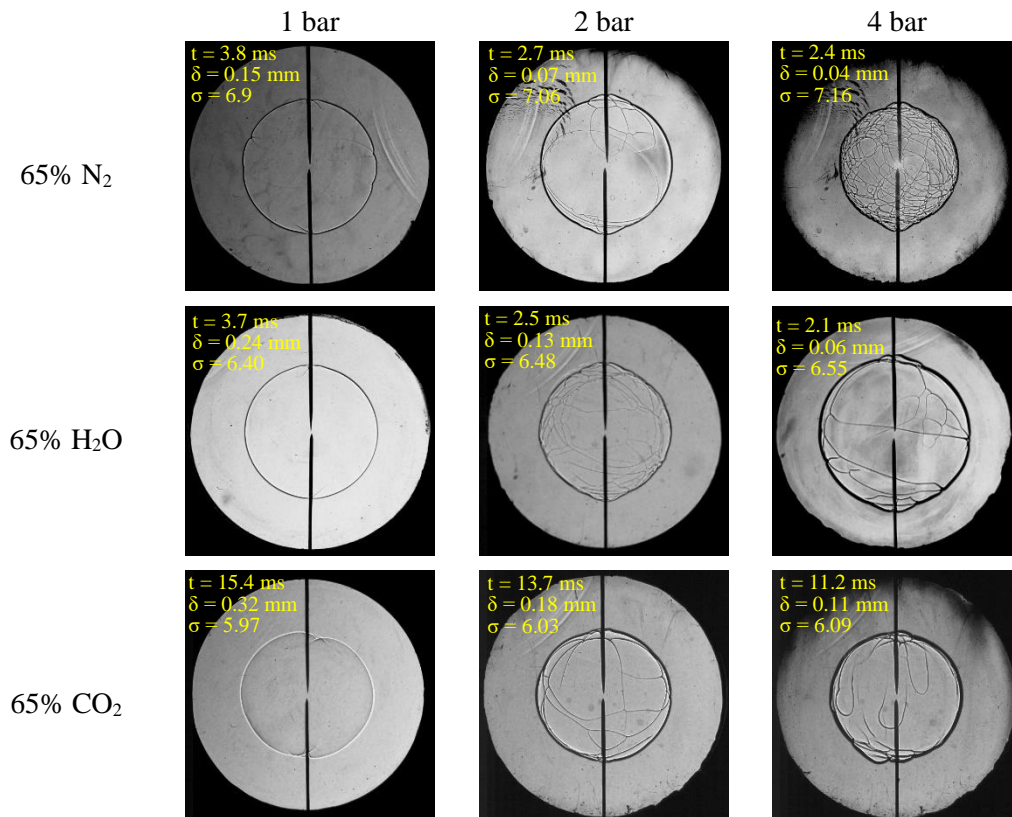


Figure 7.2. Shadowgraph image of propagating spherical flame of 65% N<sub>2</sub>/H<sub>2</sub>O/CO<sub>2</sub> diluted premixed n-dodecane/O<sub>2</sub> mixtures at R ~ 30 mm, 450 K, 1 bar and φ = 1.0

Figure 7.2 shows a sequence of shadowgraph images of spherical flames of 65%  $N_2/H_2O/CO_2$  diluted n-dodecane/ $O_2$  mixtures at  $R \sim 30$  mm, 450 K, 1 bar, and  $\phi = 1.0$ . Even though the radius range of 8-20 mm was only used while estimating the LBV, the images were presented at a radius of 30 mm in order to display all the instabilities encountered in this work. At an initial pressure of 1 bar, all the flames were smooth irrespective of the diluent species. At  $p=2$  bar, cracks started appearing on the flame surface at all the reported conditions due to stretch effects. At  $p=4$  bar, small and uniform cells were present on the flame surface for  $N_2$  dilution, which indicated the onset of hydrodynamic instability due to the occurrence of the thinnest flames and the increase in the density ratio across the flame among all the report conditions. For  $H_2O$  and  $CO_2$  dilution, only cracks due to stretch effects was observed, and hydrodynamic instability had not initiated due to thicker flames even at a higher initial pressure. From the present experience, the onset of hydrodynamic instability was quite earlier for richer mixtures at all operating conditions, as they were subjected to thermo-diffusive effects (Lewis number less than the critical Lewis number) too. The flame images considered in the present extrapolation analysis (radius range from 8 to 20 mm) to estimate unstretched LBV and Markstein length were completely smooth and wrinkle-free at all operating conditions.

### 7.3 Effect of $N_2$ addition on LBV

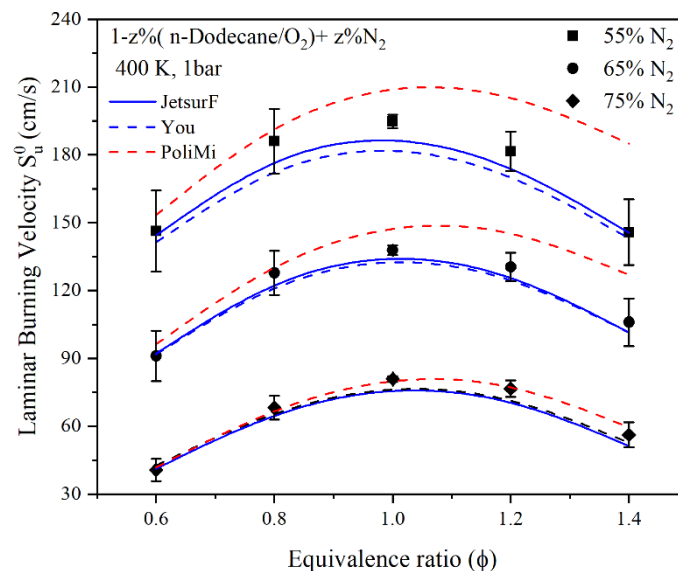


Figure 7.3. The comparison of measured and computed laminar burning velocities of  $(100-Z) \% (n-C_{12}H_{26}+(18.5O_2/\phi)) + Z\% N_2$ ,  $Z = 55-75\%$  at 1 bar 400 K. The symbols indicate the experiment and lines (Solid blue-Jetsurf2.0, Dashed blue – You et al., and dashed red – PoliMi-1410)

Figure 7.3 shows the measured and predicted unstretched LBV of premixed oxy-n-dodecane mixture in the presence of different mole fractions of  $N_2$  at 1 bar, 400 K. The figure

also showed that the length of error bars of LBV was different at each operating condition as estimated by the methodology followed as that of Xiouris et al. [110], and it was essentially due to the contribution of mixture uncertainty, and it was reported in detail in Appendix-B. The peak value of LBV was obtained at  $\phi=1.0$  for all the studied conditions due to the occurrence of the highest net heat release rate and the mole fraction of H+OH+O ( $X_{O+OH+H}$ ) even though the flame temperature peaked at  $\phi=1.1$ . Similar observations on LBV peaking at  $\phi=1.0$  were reported by Prathap and co-workers [44] for the oxy-CH<sub>4</sub> mixtures diluted with third-party inert species. Additional simulations were also performed for oxy-CH<sub>4</sub> and oxy-n-dodecane mixtures, and interestingly, the LBV peaked at  $\phi=1$  for those cases too. Hence, the occurrence of LBV at  $\phi=1$  was a characteristic of oxy-CH<sub>4</sub>/n-dodecane mixtures independent of initial pressure (Figure 7.6)/ temperature and the presence of a third-party diluent species (Figure 7.9 & Figure 7.12) that does not vary with the equivalence ratio. The LBV increased by nearly three times, as the  $X_{N_2}$  reduced from 75%-55%, due to an increase in the chemical energy and temperature, and it was quantified in the next section. Predicted LBV with JetsurF2.0 [41] and You et al. [115] mechanisms showed excellent agreement with the measurements, and the deviation was well within the experimental uncertainties. PoliMi-1410 [116] showed a key difference with the measurements, especially for richer mixtures.

## 7.4 Effect of high flame temperature on LBV

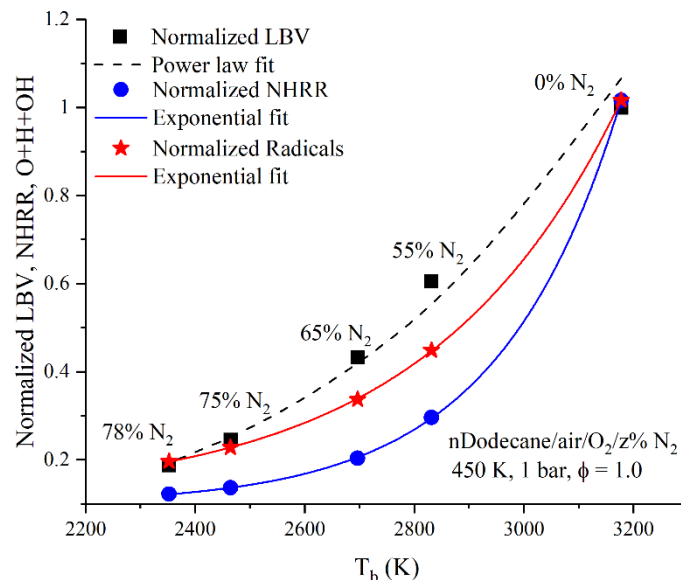


Figure 7.4. Normalized LBV, peak net heat release rate, and peak XO+OH+H vs. equilibrium flame temperature computed for the stoichiometric (100-Z) % (n-C<sub>12</sub>H<sub>26</sub>+18.5O<sub>2</sub>) +Z% N<sub>2</sub>, Z = 0% (simulation), 55%, 65%, 75%, 78% (measurement with air) at 1 bar and 450 K

One of the objectives was to measure the LBV of high-temperature oxy-n-dodecane flames by adding a third-party diluent  $N_2$  so that it can be measured safely using SPF method. Experiments were conducted for the stoichiometric mixture of the oxy-n-dodecane mixtures diluted with  $N_2$ : 55%, 65%, 75%, 78.1% (corresponds to n-dodecane-air experiment [129]), at 1 bar, and 450 K. For better comparison, the unstretched LBV of pure oxy-n-dodecane mixtures without any dilution was predicted using PREMIX at the same operating conditions. At the abovementioned conditions, the peak value of the net heat release rate and the peak value of the mole fraction of  $H+OH+O$  were predicted using the 1D planar flames with You et al. [115]. All the parameters estimated with different levels of  $N_2$  dilution were normalized with the respective parameters of the oxy-n-dodecane mixture and are displayed in Figure 7.4 as a function of the equilibrium flame temperature (EFT). The corresponding mole fraction of  $N_2$  ( $X_{N_2}$ ) in the mixture was also labeled near each dataset. The peak values of NHRR and the  $X_{O+OH+H}$  increased exponentially with an increase in the EFT (achieved by decreasing the % $N_2$ ). But, the normalized LBV followed a power-law distribution with the EFT (obtained by increasing the % $N_2$ ) as it also depends on the thermal diffusivity of the mixture. Thermal diffusivity of the mixture with 0% $N_2$  was the smallest, and it increased with the addition of  $N_2$ , and between 55-78.1% $N_2$ , it was in the range of 0.29-0.42  $cm^2/s$ . The  $R^2$  value of all the curve fits was greater than 99%. To get more information on the high-temperature flames on kinetics, sensitivity analysis was performed. To find out the key elementary reactions that influence the LBV at different % $N_2$ , a normalized A-factor sensitivity was analyzed and reported in Figure 7.5.

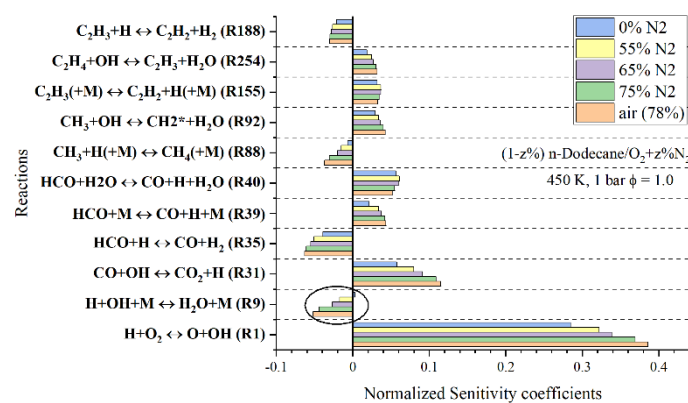


Figure 7.5. Normalized sensitivity coefficients of the most influencing elementary reactions on LBV of mixtures and operating conditions mentioned in Figure 7.4 were obtained using You et al.

An interesting observation of Figure 7.5 was that the trends of all the most influential reactions were the same as that of n-dodecane-air, irrespective of a substantial variation in the flame

temperature except for one reaction (R9). As expected,  $\text{H}+\text{O}_2 \leftrightarrow \text{O}+\text{OH}$  and  $\text{CO}+\text{OH} \leftrightarrow \text{CO}_2+\text{H}$  promoted LBV, and their sensitivities decreased with an increase in the flame temperature or reduction in %N<sub>2</sub> in the mixture essentially due to a hike in the mole fraction of the respective species due to the reduction in the  $X_{\text{N}_2}$  in the mixture. Similarly, the other reported influential reactions with positive sensitivities also varied in the same trend. Influential termination reactions were  $\text{HCO}+\text{H} \leftrightarrow \text{CO}+\text{H}_2$ ,  $\text{C}_2\text{H}_3+\text{H} \leftrightarrow \text{C}_2\text{H}_2+\text{H}_2$  and they had negative sensitivities as expected, and its sensitivities decreased with an increase in EFT. The sensitivity of the chain termination reaction  $\text{H}+\text{OH}+\text{M} \leftrightarrow \text{H}_2\text{O}+\text{M}$  showed a crossover from negative to positive at 0%N<sub>2</sub> case. Hence, an increase in the reaction rates of the important elementary reactions significantly augmented the LBV of nitrogen-diluted oxy-n-C<sub>12</sub>H<sub>26</sub> mixtures with an increase in EFT or a decrease in  $X_{\text{N}_2}$  in the mixture.

## 7.5 Effect of N<sub>2</sub> addition on LBV at elevated pressures

Figure 7.6 displays the effect of initial pressure on the LBV at different equivalence ratios for oxy-n-dodecane mixtures diluted with  $X_{\text{N}_2}=65\%$ . The measurements were limited to 4 bar only, as the measured post-combustion pressure showed a very strong gradient for these oxy-n-dodecane mixtures, even in the presence of 65% dilution. The peak pressures were always higher than the respective equilibrium pressures, and the pressure-time traces had strong fluctuations close to the peak value. Higher initial pressures greater than 4 bar may be possible only in the dual chambers for these quite fast-burning mixtures. The stoichiometric mixture was more reactive, and it was similar to Figure 7.3, and the same reasons will apply here too. As expected, the LBV decreased with a rise in the initial pressure. Flame temperature variation due to an increase in the initial pressure (1-4 bar) was 100 K ( $T_b$ : 2691/1 bar, 2748/2 bar, 2799/4 bar at  $\phi = 1$ ), and it was small. Thermal and mass diffusivities of the mixture decreased considerably as the initial pressure hiked. The flame became a lot thinner as the  $p_i$  hiked due to an increase in the reaction rates. The occurrence of thin flames in a denser mixture with slow diffusivities, along with the enhanced activity of three body termination reactions, were responsible for the LBV reduction. At most of the conditions reported in Figure 7.6, the simulated LBV using: (a) You et al. [115] mechanism agreed well with the measurements, (b) JetsurF2.0/ PoliMi-1410 mechanisms were lower/ higher than the measurements, and the deviations were higher than the experimental uncertainties.

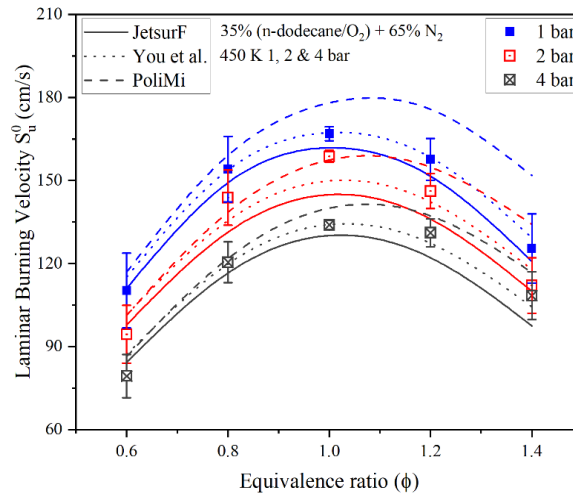


Figure 7.6. Comparison of unstretched LBV of 35%(n-C<sub>12</sub>H<sub>26</sub>+(18.5O<sub>2</sub>/φ)) +65%N<sub>2</sub> mixtures at 1-4 bar, 450 K. The different symbols indicate the experimental LBV, and lines (Solid line- Jetsurf2.0, Dashed line – You et al., and dotted line – PoliMi-1410) represents the computed LBV

### 7.6 Effect of N<sub>2</sub> addition on flame stability

Figure 7.7 shows the burned gas Markstein length obtained using the NE extrapolation scheme for all N<sub>2</sub>-diluted oxy-n-dodecane mixtures at 400 K, 1 bar, and different equivalence ratios. The reported Markstein lengths were positive, indicating that the flames were stable to preferential diffusion effects.

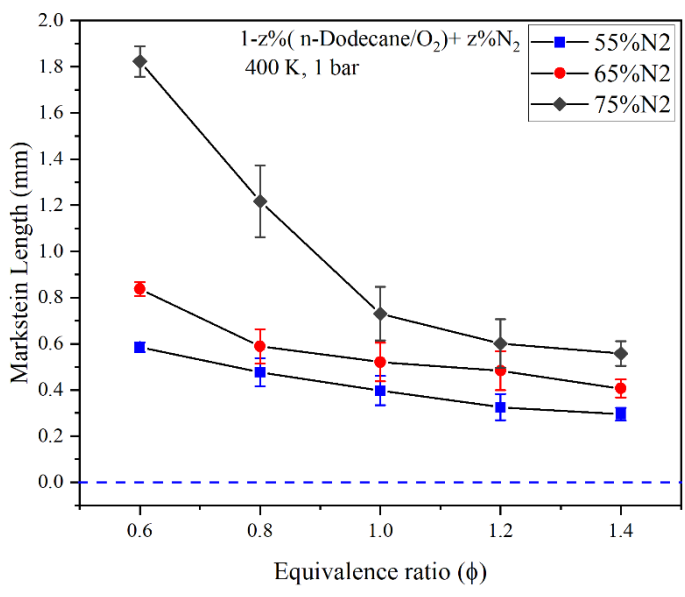


Figure 7.7. Variation of burned gas Markstein length with an equivalence ratio of (100-Z) % (n-C<sub>12</sub>H<sub>26</sub>+(18.5O<sub>2</sub>/φ) +Z% N<sub>2</sub>, Z =55-75% mixtures at 1 bar 400 K

The estimated effective Lewis number  $Le_{eff}$  (Eq.3.18) were in the range of 3.29 (lean) –1.55 (rich) and were greater than the critical Lewis number,  $Le^*$  (Eq.3.22). Table 7.3 shows all the essential properties of reactants & flame, along with the flame thickness and unstretched LBV at stoichiometric condition.

Table 7.3. Mixture and flame properties of 35% ( $C_{12}H_{26} + (18.5O_2)/\phi$ ) + 65%  $N_2$  at 1-4 bar, 400-450K and  $\phi = 1.0$

T (K)	p (bar)	% $N_2$	$\alpha$ ( $cm^2/s$ )	$T_b$ (K)	$K^{-1}_{max}$ (ms)	$K^{-1}_{min}$ (ms)	$L_b$ (mm)	$Le_{eff}$	$\delta$ (mm)	$S_u^o$ (cm/s)	$t_{reaction}$ (ms)
400	1	55	0.292	2822	0.411	0.907	0.398	2.58	0.133	194.81	0.068
400	1	65	0.307	2685	0.397	0.907	0.521	2.37	0.175	137.87	0.127
400	1	75	0.323	2447	0.486	0.876	0.730	2.28	0.275	80.89	0.340
425	1	65	0.339	2691	0.397	0.907	0.602	2.33	0.173	159.04	0.109
450	1	65	0.372	2697	0.486	0.876	0.714	2.30	0.156	166.89	0.094
450	2	65	0.185	2748	0.381	0.922	0.355	2.30	0.076	158.67	0.048
450	4	65	0.093	2799	0.471	1.078	0.329	2.30	0.041	133.98	0.030

The sensitivity of the flame to the stretch effects increased with a hike in the  $X_{N_2}$  from 55% to 75% in Figure 7.7 due to an increase in the: (1) duration of the flame's response to stretch, & (2) reaction times as reported in Table 7.3 Leaner mixtures were very sensitive due to lower flame temperature, thicker flame, larger thermal diffusivity, longer duration of exposure to stretch effects in association with the preferential diffusional effects, but as the deficient reactant n-dodecane was not the highly reactive species, the  $L_b$  remained positive and increased. But in richer mixtures, the presence of differential diffusion effects had a completely different effect as  $O_2$  was the deficient reactant (with respect to the equivalence ratio only because magnitude wise mole fraction of n-dodecane was the smallest), and it was more diffusive, and hence, the local equivalence ratio was less richer at the flame front than the global equivalence ratio (which tried to decrease  $L_b$ ) in richer mixtures that had altered its response, even though it had all the other effects similar to that of lean mixtures.

## 7.7 Flame stability at different initial Temperatures/ pressures for 65%N<sub>2</sub>

Figure 7.8 shows the effects of initial temperature/ pressure on the thermo-diffusive stability of the 35% (n-C<sub>12</sub>H<sub>26</sub> + (18.5O<sub>2</sub>)/ $\phi$ ) + 65% N<sub>2</sub> mixtures at different equivalence ratios. At 65% N<sub>2</sub> dilution, a hike in the initial temperature of the oxy-n-dodecane mixtures leads to an increase in  $L_b$ , indicating that the mixtures become more stable to thermo-diffusive effects. As shown in

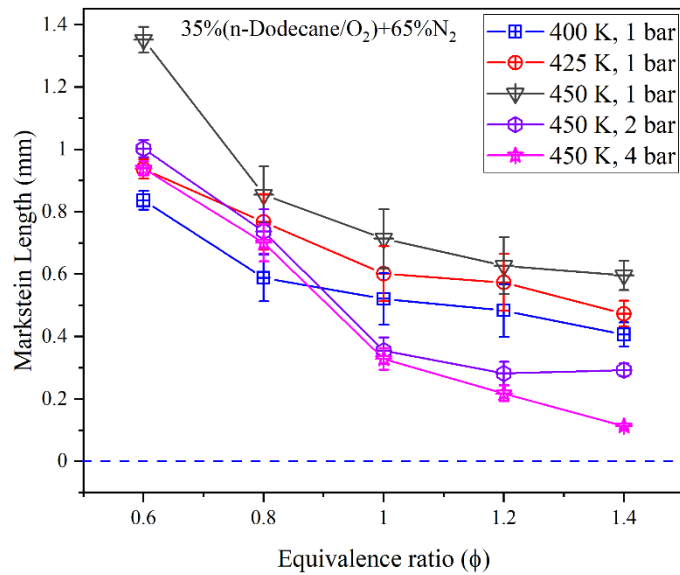


Figure 7.8. Variation of burned gas Markstein lengths for a different equivalence ratio of 35% (n-C<sub>12</sub>H<sub>26</sub>+(18.5 O<sub>2</sub>/ $\phi$ )) + 65% N<sub>2</sub> mixtures at 1 bar, 400-450 K, and 1-4 bar at 450 K Effect of initial pressure on flame stability

Table 7.3, with an increase in the initial temperature: (a) the heat diffusivities of the mixture enhanced, (b) the flame temperature increased, (c) the flame thickness decreased marginally, resulted in more stable flames. As explained in 7.6, slow/ fast reactive deficient reactant n-dodecane/ O<sub>2</sub> in lean/ rich mixtures resulted in larger/ smaller variations in the magnitudes of  $L_b$  with the increase in initial temperature. The same figure shows the variation of  $L_b$  at  $p_i = 1-4$  bar.  $L_b$  values decreased with an increase in pressure at a given equivalence ratio due to the occurrence of thin flames with reduced diffusivities.

An important observation was that an increase in the initial temperature too, resulted in thinner flames, but these flames were more stable, indicated by a hike in the value of  $L_b$  essentially due to an increase in the mixture heat diffusivities. At 4 bar, and 450 K, the  $L_b$  of the mixture at  $\phi = 1.4$  was close to zero, indicating that it was neutral to thermo-diffusive effects, but may be with a further increase in the pressure, the transition may occur.

## 7.8 Effect of different diluents on LBV of oxy-dodecane mixtures

After the detailed study on the high-temperature oxy-dodecane flames diluted with  $N_2$ , the response of oxy-n-dodecane flames in the presence of  $CO_2/H_2O$  was also studied as these mixtures have all the real-time effects like thermal & kinetic effects and thermo-diffusive effects. This is the first time in the literature an independent effect of important diluents like  $N_2$ ,  $CO_2$ , and  $H_2O$  on the LBV of 35% (n- $C_{12}H_{26} + (18.5O_2/\phi)$ ) + 65% diluent is reported in Figure 7.9 at  $\phi=0.6-1.4$ , 1 bar, and 450 K.

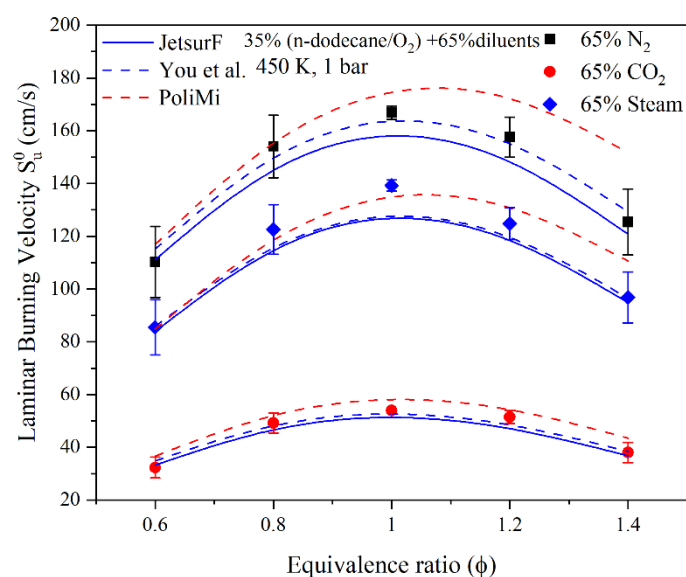


Figure 7.9. Comparison of the unstretched laminar burning velocity of n-dodecane/ $O_2$  mixtures burns in different diluent environments ( $N_2$ ,  $CO_2$ , and  $H_2O$ ) at 1 bar 450 K. The symbols indicate the measurements and lines (Solid blue-Jetsurf2.0, Dashed blue – You et al., and dashed red – PoliMi-1410)

The chemical energy of all the combustible mixtures reported in Figure 7.9 was kept constant, and irrespective of it, a change in the diluent in the order of  $N_2$ ,  $H_2O$ , and  $CO_2$  resulted in a significant reduction in the LBV largely to a strong reduction in the flame temperature (due to an increase in mixture heat capacities), and the respective variation in the mixture diffusivities too. Another notable observation was that the steam-diluted mixtures had a lower flame temperature, but higher mixture diffusivities as compared to  $N_2$  diluted mixtures but still, the LBV being lesser for steam dilution as compared to  $N_2$  dilution indicating the dominant effect of flame temperature.

The prominent LBV reduction by CO<sub>2</sub> over other diluents was due to its active participation in the reaction pathway by enhancing chain breaking elementary reactions, which had been well documented in the literature [44]. The standard procedure of replacing the actual diluent with a fictitious diluent to demarcate the thermal and chemical effect of the added diluents on the LBV was also simulated. The overall decrease in the LBV due to the addition of 65% N<sub>2</sub>/ H<sub>2</sub>O/ CO<sub>2</sub> as compared to an undiluted mixture was 60%/ 68%/ 87%. The contribution to the overall suppression by: the thermal effect was 96%/ 93%/ 67%, and the chemical effect was 4%/ 7%/ 33%. Here too, the simulated LBV agreed well with the measurements in the following order: You et al.[115], JetSurF2.0 [41], and PoliMi-1410 [116].

As present mixtures contained CO<sub>2</sub> & steam, the radiation effects may become important. The unstretched LBV of present mixtures were in the range of 40 cm/s- 233 cm/s except two mixtures whose LBV were less than 25 cm/s. The largest flame diameter considered for the estimation of unstretched LBV was 40 mm only. Yu et al. [130] and Xie et al.[131] mentioned that radiation effects become significant for slow flames having LBV less than 26 cm/s. The presence of CO<sub>2</sub> result in reabsorption which will further reduce the loss due to radiation [132]. Zhang et al. [133] reported that radiation effects influenced the minimum ignition energy at the very limits of flammable mixture. As the present mixture were fast and well away from flammability limits, radiation effects were neglected. Additional efforts were carried out to quantify the radiation effects using freely propagating planar flame model in CANTERA which had two radiation models such as Optical Thin model and gray gas approximation with absorption model of the above mentioned mixtures that had larger mole fraction of CO<sub>2</sub> and H<sub>2</sub>O. Unfortunately, the results obtained from those simulations were not accurate, and hence, it was not presented in this thesis.

## 7.9 Effective Lewis number

The Lewis number (Le) is the ratio of the mixture thermal diffusivity ( $\alpha$ ), and the mass diffusivity ( $D_m$ ) of the deficient species (i) into the mixture (m) can also be used for the identification of the onset of preferential diffusional instability if its value is less than the critical Lewis number respectively.  $Le_{eff}$  (Eq. 3.19) was chosen over  $Le_{deficient}$  (Eq. 3.18) as it agreed well with the present stability study. Figure 7.10 compares the effective Lewis numbers of n-dodecane/O<sub>2</sub> mixtures diluted with 65% N<sub>2</sub>/H<sub>2</sub>O/CO<sub>2</sub> at 1 bar and 450 K. Among all diluents, the steam diluted mixtures show a higher effective Lewis number due to its better diffusivity nature than other diluents.

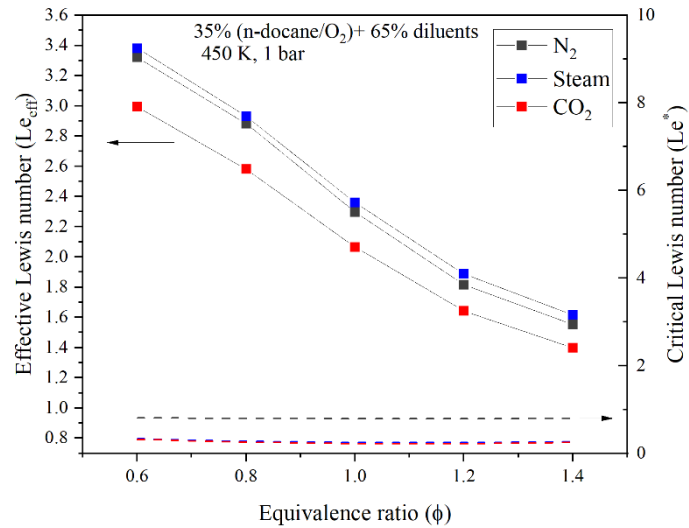


Figure 7.10. The variation of effective and critical Lewis numbers of 35% ( $nC_{12}H_{26} + (18.5O_2/\phi)$ ) + 65%  $H_2O/ N_2/ CO_2$  mixtures at 1 bar and 450 K

For all the studied operating conditions, irrespective of the equivalence ratio, the  $Le_{eff} > Le^*$  which indicated that all the mixtures were stable against preferential diffusion instability, and steam diluted mixtures were more stable towards thermos-diffusive effects than other diluents. Therefore, all the studied mixtures in the oxy-n-dodecane category are stable flames with respect to thermo-diffusional effects at all the operating pressure conditions.

## 7.10 Analytical Burned gas Markstein length

As mentioned earlier, burned gas Markstein length represents the sensitivity of the flame propagation speed on the stretch rate. Bechtold and Matalon [102] provided an explicit expression (Eq.3.14) for  $L_b$  as a function of density ratio, the effective Lewis number of the mixture, and the global activation energy of the chemical reaction. Experimental and analytical values of burned gas Markstein length are presented in Figure 7.11 as a function of equivalence ratio for all diluents at 1 bar 450 K and elevated pressure for  $CO_2$  diluted mixtures.  $L_b$  decreases with the equivalence ratio for all the diluents for both analytical and experimental results. The evolution is very similar, although the analytical values are slightly fluctuating and under-predicted than the measurements. In the present work,  $Le_{eff} > 1$  for all equivalence ratio as well as all the diluents, it can be concluded that oxy-combustion flames are negligibly affected by flame stretch rates, and flame become stable at all operating conditions due to high stretch rates at oxy-combustion. Similarly, the expression predicts the burned gas Markstein lengths closer to the measurements at elevated pressure conditions, for clarity only the  $CO_2$  mixture comparison is presented here.

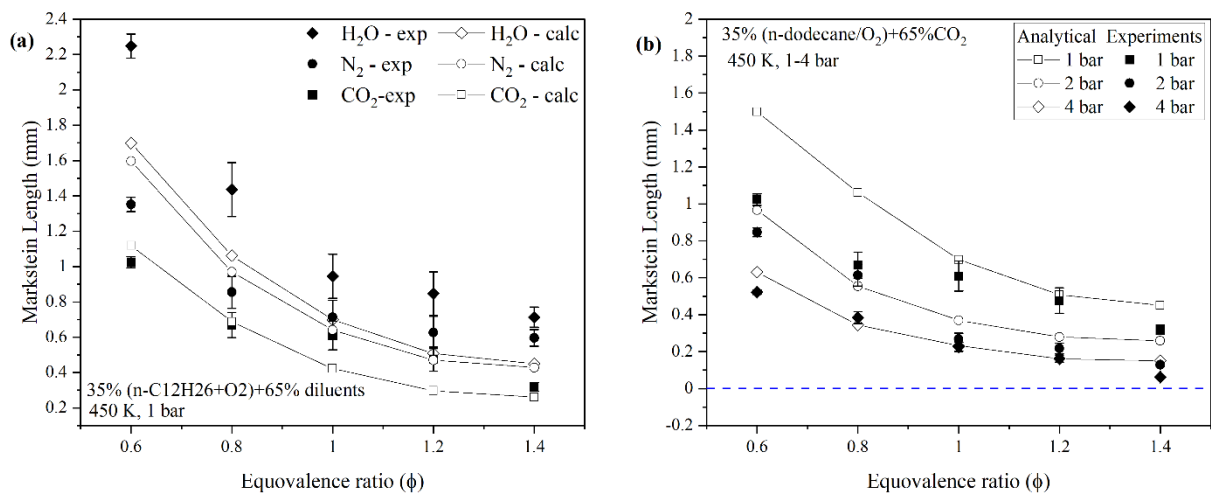


Figure 7.11. Variation of experimental and analytical burned gas Markstein length as a function of equivalence ratio of n-dodecane/O<sub>2</sub> (a) with N<sub>2</sub>/CO<sub>2</sub>/H<sub>2</sub>O dilution (b) CO<sub>2</sub> dilution at 1-4 bar 450 K

## 7.11 Effect of different initial pressures on LBV for N<sub>2</sub>/ H<sub>2</sub>O/ CO<sub>2</sub>

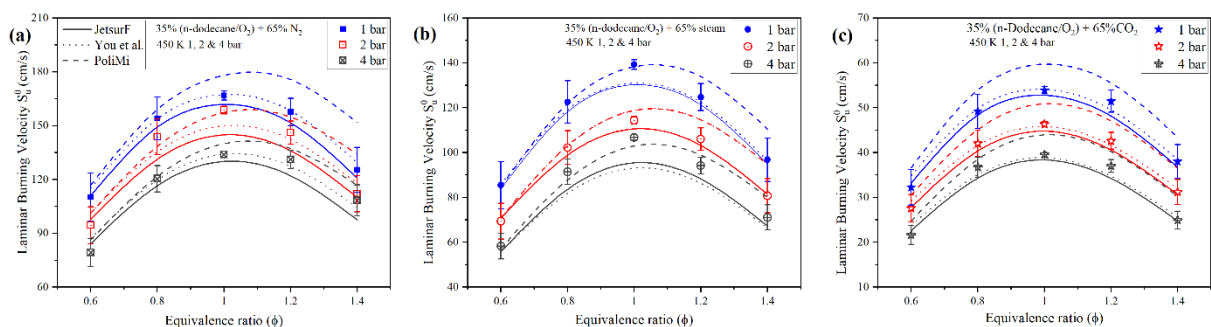


Figure 7.12. Comparison of the unstretched laminar burning velocity of n-dodecane/O<sub>2</sub> mixtures burns with (a) 65% N<sub>2</sub>, (b) 65% H<sub>2</sub>O, and (c) 65% CO<sub>2</sub> diluents at different elevated pressures (1, 2, & 4 bar) and 450 K. The symbols (Filled-1 bar, open -2 bar, crossed-4 bar) denote the experimental and lines (Solid: JetsurF2.0, dotted: You et al. and dashed: PoliMi-1410) denote predicted LBV

Figure 7.12 indicated that the unstretched LBV at a given initial pressure was the highest for the mixture diluted with N<sub>2</sub> and followed by H<sub>2</sub>O and CO<sub>2</sub>, similar to that of Figure 7.9. Even at higher pressures, the LBV peaked at  $\phi=1$ . It also shows that the unstretched LBV monotonically decreased with an increase in the initial pressure for all the diluents. It was essentially due to an increase in the density of the unburned mixture and the dominance of chain termination reactions. In the pressure range investigated, the inhibiting reactions  $H + O_2 + M \rightarrow HO_2 + M$  and  $H + OH + M \rightarrow HO_2 + M$  were enhanced as initial pressure increased, which reduced the H atom concentration and competed with the chain branching reaction

producing free radicals O and OH:  $H + O_2 \rightarrow OH + O$ . A retarding effect is therefore imposed on the overall progress of the reaction with increasing pressure. The effect of the increase in pressure on the LBV and the associated reaction kinetics is further discussed in section 6.9. You et al. [115] had been efficient in predicting the behavior of LBV at all pressures and as well as for the  $N_2$  and  $CO_2$  diluted mixtures, but it underpredicted the LBV of steam diluted mixtures. JetsurF2.0 [41] was accurate for estimating LBV at lower pressure but consistently underpredicted at higher pressure for all the diluents. Except for steam mixtures, PoliMi-1410 always overpredicted for  $CO_2$  and  $N_2$  diluted mixtures, especially at  $\phi = 1.4$ , the predicted values significantly deviated till 30% for  $N_2$  dilution at 4 bar, 450 K, and needed attention to improve its performance. Effect of pressure on Markstein lengths.

Figure 7.13 shows the pressure exponent ( $\beta$ ) at each equivalence ratio estimated from the power law,  $S_{u,450K,p}^o = S_{u,450K,1bar}^o \left(\frac{p}{p_o}\right)^\beta$  where  $p$  is the initial pressure,  $p_o = 1$  bar,  $S_{u,450K,p}^o$  is the unstretched LBV measured at 450 K and  $p$  of the respective equivalence ratio of each diluent. For better comparison, the values of  $\beta$  of n-dodecane-air obtained at 425 K [129] are also plotted in Figure 7.13. The effect of the high-flame temperature of the oxy-n-dodecane mixtures diluted with different inert species was quite visible in the figure.

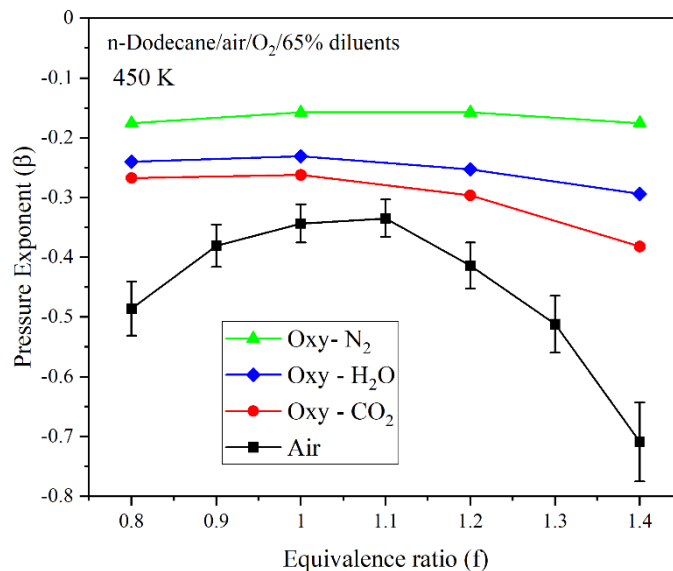


Figure 7.13. Pressure exponent ( $\beta$ ) against equivalence ratio at 450 K, 1-4 bar, for 35% ( $n-C_{12}H_{26} + (18.5O_2/\phi)$ ) + 65%  $N_2/CO_2/H_2O$  and n-dodecane-air mixtures

The  $N_2$  diluted mixtures had the highest flame temperature and LBV, and its  $\beta$  was less than -0.2 for all the equivalence ratios that showed its least sensitivity to the pressure. For  $H_2O$  and  $CO_2$  diluted mixtures, the flame temperature and LBV was lower than the  $N_2$  diluted mixtures,

and hence, the sensitivity of LBV to initial pressure increased. As expected, the negative values of n-dodecane-air mixture were the highest, and for this mixture, the equivalence ratio had also a strong effect. The reason could be that as the flame temperature decreased, the reaction time increased, and the slow termination or third body reactions dominated and increased the sensitivity of LBV to the initial pressure.

## 7.12 Flame global parameters

Thermal Flame thickness  $\delta$ , (Eq. 3.11), Zeldovich number  $Ze$  (Eq. 3.13), thermal diffusivity  $\alpha$  (Eq. 3.10), and expansion ratio  $\sigma = \rho_u / \rho_b$  where  $\rho_b$  and  $\rho_u$  are the density of burned and unburned gases, respectively, was numerically calculated using CHEMKIN with You et al. chemical kinetic mechanism.

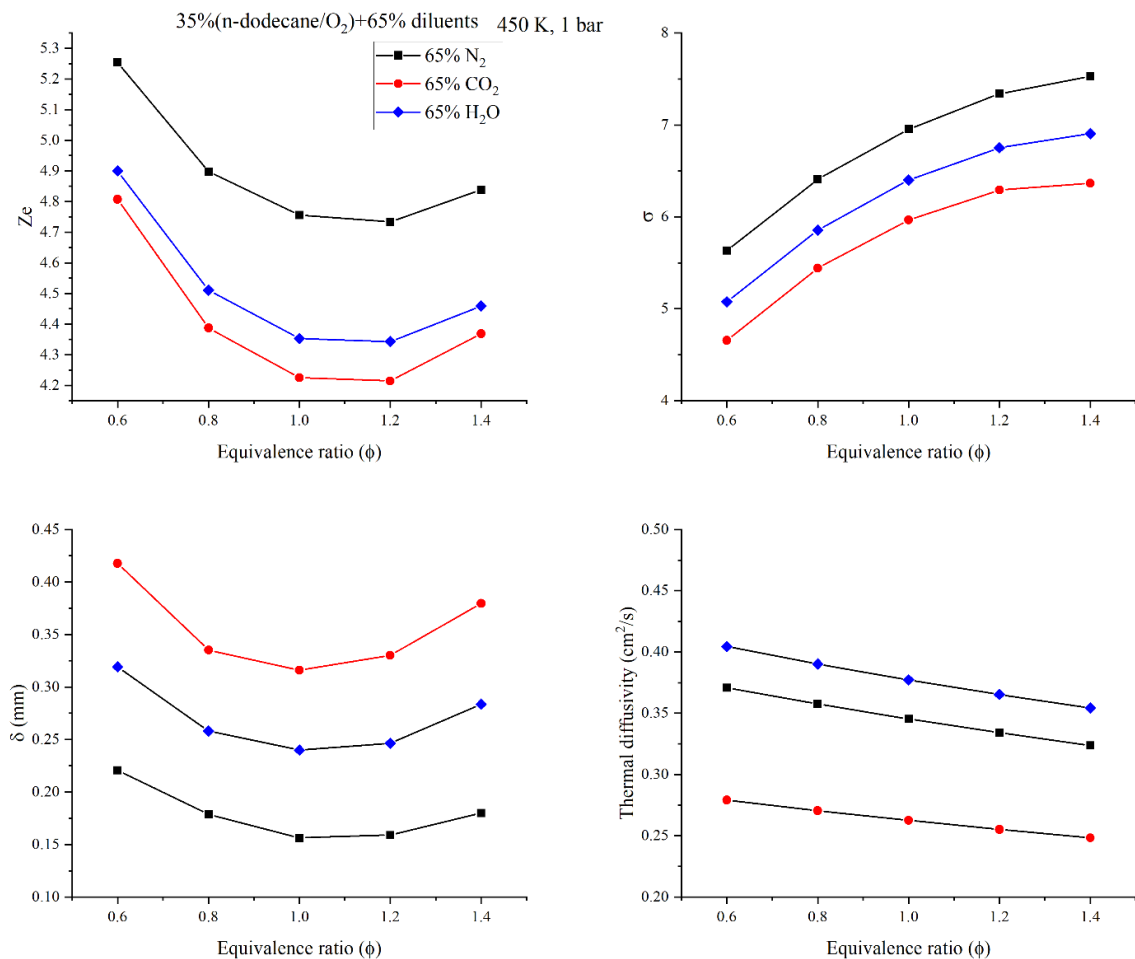


Figure 7.14. Variation of Zel'dovich number  $Ze$ , the thermal expansion coefficient  $\sigma$ , the flame thickness  $\delta$ , and thermal diffusivity  $\alpha$  of 35% (n-C<sub>12</sub>H<sub>26</sub> + (18.5O<sub>2</sub>/ $\phi$ )) + 65% N<sub>2</sub>/ CO<sub>2</sub>/ H<sub>2</sub>O flames at 450 K and 1 bar as a function of equivalence ratio

Figure 7.14 shows the variation of the flame global parameters, i.e.,  $Ze$ ,  $\sigma$ ,  $\delta$ , and  $\alpha$  for  $n\text{-C}_{12}\text{H}_{26}/\text{O}_2/\text{N}_2/\text{CO}_2/\text{H}_2\text{O}$  flames at 450 K and 1 bar as a function of equivalence ratio. The addition of  $\text{CO}_2$  with dodecane/ $\text{O}_2$  mixtures reduces the global activation energy, and hence Zeldovich number is less for  $\text{CO}_2$  diluted mixture than  $\text{H}_2\text{O}$  and  $\text{N}_2$  diluents. For all equivalence ratios,  $\text{N}_2$  diluted mixture has high values of the Zeldovich number and that of  $\text{H}_2\text{O}$  and  $\text{CO}_2$ . Similar to  $Ze$ , the thermal expansion ratio of  $\text{N}_2$  diluted mixtures has high values than  $\text{CO}_2$  and  $\text{H}_2\text{O}$  due to flame temperature. The flame thickness of  $\text{CO}_2$  diluted flame was the largest among all the studied diluents due to the low flame temperature and thermal diffusivities. In contrast, the thermal diffusivity and the effective Lewis number (in Figure 7.10) of steam diluted  $n\text{-dodecane}/\text{O}_2$  mixtures was the highest, which resulted in thermo-diffusional stable flame as it had the higher value of  $L_b$  as shown in Figure 7.8.

### 7.13 Sensitivity analysis

To further understand the influence of added different diluents flame chemistry on LBVs at normal and elevated pressures, sensitivity analysis was carried out for the diluted oxy  $n\text{-dodecane}$  flames. Figure 7.15 shows the normalized sensitivity coefficients of LBV on reaction rates of the most influencing top 10 elementary reactions of three different diluents at lean and rich equivalence ratios of 35% ( $n\text{-C}_{12}\text{H}_{26} + (18.5\text{O}_2/\phi)$ ) + 65%  $\text{H}_2\text{O}/\text{N}_2/\text{CO}_2$  mixtures at 1 and 4 bar, 450 K using You et al. mechanism. This analysis showed that all the diluted oxy  $n\text{-dodecane}$  flame propagation were quite sensitive to the kinetics of intermediate species of  $\text{C}_0\text{-C}_4$ , which corroborates with [134]. The chain branching reaction,  $\text{H} + \text{O}_2 = \text{O} + \text{OH}$  (R1), is the most important reaction for all equivalence ratios and increases from lean to rich, which helped to break the heavier molecules at faster rates along with H radicals generated through H-abstraction reactions. The reaction that competes with R1 will reduce the mole fraction of the H radical and the LBV. It was observed that, the reactions  $\text{CO} + \text{OH} \leftrightarrow \text{CO}_2 + \text{H}$ ,  $\text{H} + \text{O}_2 (+\text{M}) \leftrightarrow \text{HO}_2(+\text{M})$ , and  $\text{HO}_2 + \text{OH} \leftrightarrow \text{H}_2\text{O} + \text{O}_2$  were more influential at  $\phi = 0.6$ . The sensitivity of  $\text{H} + \text{O}_2 \leftrightarrow \text{O} + \text{OH}$ ,  $\text{CH}_3 + \text{H} (+\text{M}) \leftrightarrow \text{CH}_4(+\text{M})$  and  $\text{H} + \text{OH} + \text{M} \leftrightarrow \text{H}_2\text{O} + \text{M}$  were quite dominant for rich mixtures. Hence, the flame chemistry of oxy  $n\text{-dodecane}$  flames showed a larger variation between lean and rich mixtures. The added diluents altered the flame temperature and the third body efficiencies [135], and hence it considerably affected the reaction kinetics which were reflected in the change in the sensitivities of the chain termination reactions like  $\text{H} + \text{O}_2(+\text{M}) \leftrightarrow \text{HO}_2(+\text{M})$ ,  $\text{H} + \text{OH} + \text{M} \leftrightarrow \text{H}_2\text{O} + \text{M}$  and  $\text{CH}_3 + \text{H} \leftrightarrow \text{CH}_4(+\text{M})$ . The sensitivities of reactions R1, R2, R5, and R7 were enhanced as the increased pressure varied from 1 to 4 bar. The critical inhibiting reactions at 4 bar were R5, R6, R7, and R8 for both  $\text{H}_2\text{O}$  and  $\text{CO}_2$  dilution, which

were largely responsible for the reduction in the LBV of the respective mixtures. At 4 bar too, the effect of lean and rich equivalence ratios on the reaction kinetics was quite evident as R5 was the most dominant termination reaction at lean condition, whereas R7 dominated at rich conditions.

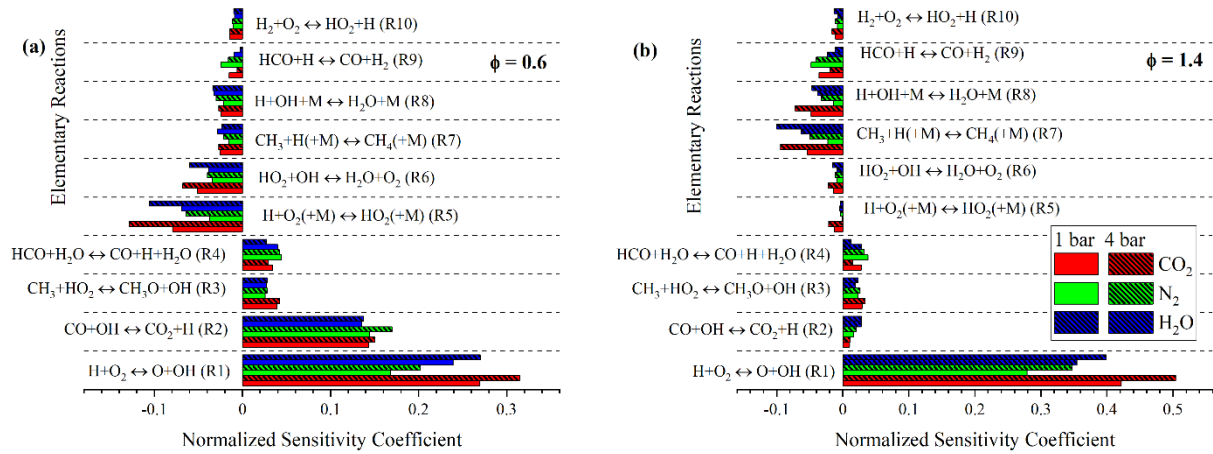


Figure 7.15. Sensitivity coefficients of 35% (n-C<sub>12</sub>H<sub>26</sub> + (18.5O<sub>2</sub>/φ)) + 65% N<sub>2</sub>/CO<sub>2</sub>/H<sub>2</sub>O mixtures at 1 and 4 bar, 450 K using JetsurF2.0 detailed kinetic mechanism at (a) lean mixture φ = 0.6 and (b) rich mixture φ = 1.4

## 7.14 Pressure and different diluents effect on Markstein length

Figure 7.16 is a comprehensive thermo-diffusive stability plot that shows the  $L_b$  of oxy-n-dodecane diluted with 65% N<sub>2</sub>/H<sub>2</sub>O/CO<sub>2</sub> and its response to equilibrium flame temperature (EFT) at φ=0.8,1,1.4, 450 K, and p=1, 4 bar. EFT was obtained during the LBV simulations. For the sake of completeness,  $L_b$  of air (mole fraction of N<sub>2</sub> = 78.11%) reported in [129] at φ=1.4, 400 K (1 bar), and 425 K (1, 4 bar) with negative  $L_b$  values are also included in Figure 7.16. In the present work, the  $L_b$  was always positive at all the studied conditions (65% dilution), essentially due to the higher flame temperature, i.e., lesser flame residence time, of oxy-mixtures. The  $L_b$  of the mixture diluted with 65% H<sub>2</sub>O was always higher than the 65% N<sub>2</sub> and 65% CO<sub>2</sub> due to the higher mixture thermal diffusivity and the associated Lewis number, even though its flame temperature was slightly lesser than the N<sub>2</sub> diluted mixtures. The slowest flames were generated by 65% CO<sub>2</sub> diluted mixtures at 4 bar as compared to 65% N<sub>2</sub> and 65% H<sub>2</sub>O had the  $L_b$  values close to zero, signalling that they were stable and less sensitive to the stretch and thermo-diffusive effects. As the 65% CO<sub>2</sub> mixtures at 4 bar were on the verge of transition from stable to unstable limits, maybe with further increase in the initial pressure, the  $L_b$  may become negative due to thermo-diffusive effects.

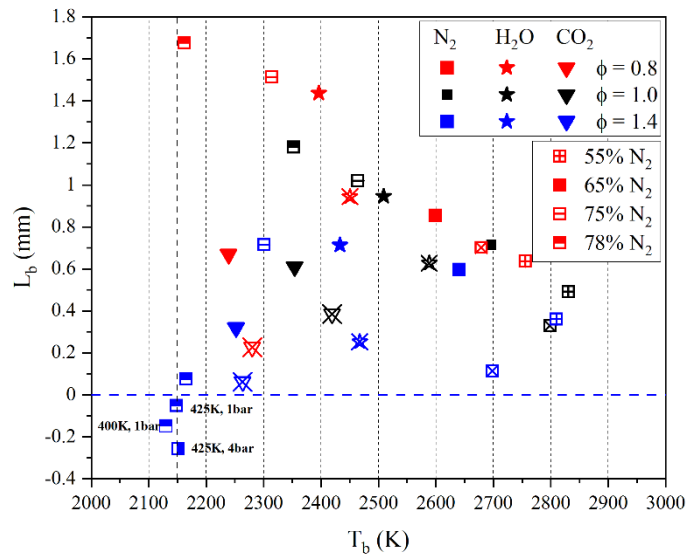


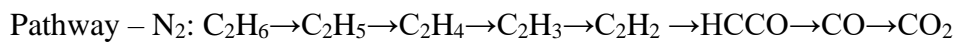
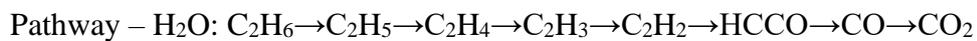
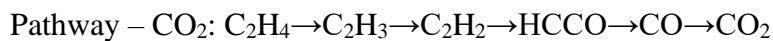
Figure 7.16. Experimental Burned gas Markstein lengths of  $Z\%$  ( $n\text{-C}_{12}\text{H}_{26} + (18.5\text{O}_2/\phi)$ ) +  $(1-Z)\%$   $\text{H}_2\text{O}/\text{N}_2/\text{CO}_2$  mixtures with EFT at 450 K, 1 bar & 4 bar and  $\phi=0.8,1,1.4$ .  $Z=65\%$  for  $\text{CO}_2$  and  $\text{H}_2\text{O}$ .  $Z=55\text{-}78.1\%$  for  $\text{N}_2$ . Also, at 78.1% $\text{N}_2$ , 400 K, and 425 K at  $\phi=1.4$  were also plotted. Red, black, & blue represents  $\phi=0.8,1,1.4$ . Square and its variants represent 55-78.1% $\text{N}_2$  dilution. Shaded star and inverted triangles – 65% $\text{H}_2\text{O}$  and 65% $\text{CO}_2$ , Symbols without cross mark – 1 bar, Symbols with cross mark – 4 bar, respectively

The  $L_b$  values of mixtures diluted with 55% to 78.11% $\text{N}_2$  indicated that: (a) at lean mixtures, the increase in % $\text{N}_2$  in the mixture increased the thermal diffusivity and resulted in a hike in  $L_b$  at a given pressure, (b) at rich mixtures, the preferential diffusion of  $\text{O}_2$  dominated over the thermal diffusivity, and as the flame temperature attained 2150 K or lower resulted in unstable flames with respect to preferential diffusion of mass over heat diffusion. The above discussion clearly brought out the important advantage of having high-temperature oxy-n-dodecane mixtures in combustion applications as it offers better thermo-diffusive flame stability even in the presence of heavier inert species like  $\text{CO}_2$ . This is good news for the upcoming combustion applications that shall be using oxy-fuel mixtures diluted with  $\text{CO}_2$ , and later its capture too, to reduce the greenhouse emissions.

## 7.15 Reaction pathway analysis

The reaction pathway diagrams of high-temperature, premixed oxy-n-dodecane diluted with (a) 65%  $\text{CO}_2$  [Figure 7.17], (b) 65%  $\text{H}_2\text{O}$  [Figure 7.18], and (c) 65%  $\text{N}_2$  [Figure 7.19] mixtures at  $\phi = 1.0$  respectively at a mixture temperature of 450 K and 1 bar pressure are presented. The reaction pathway diagram is the graphical representation of the rate of production and

consumption of major and minor species involved in a complex reaction mechanism. The thickness of the arrow lines is governed by the strength of elemental flux to highlight the importance of a reaction path. The reaction pathway for the carbon element flux is formulated with a threshold value equal to 5% of the largest elemental flux is chosen to gain more insight into the combustion behaviour of the mixture. From the pathways, it is observed that the combustion chemistry of heavy hydrocarbon n-dodecane ( $nC_{12}H_{26}$ ) strongly depends on smaller species like  $C_1$ - $C_4$ . The major reaction pathways for the consumption of carbon observed were:



The major pathways of premixed diluted mixtures of oxy-n-dodecane with different diluents ( $CO_2/H_2O/N_2$ ) have not changed significantly. But the conversion rate of  $C_2H_2 \rightarrow HCCO$  increased up to 56% for  $H_2O$  diluted mixture than  $N_2$  and  $CO_2$ . A notable variation was observed in the minor species pathways with respect to the diluents.

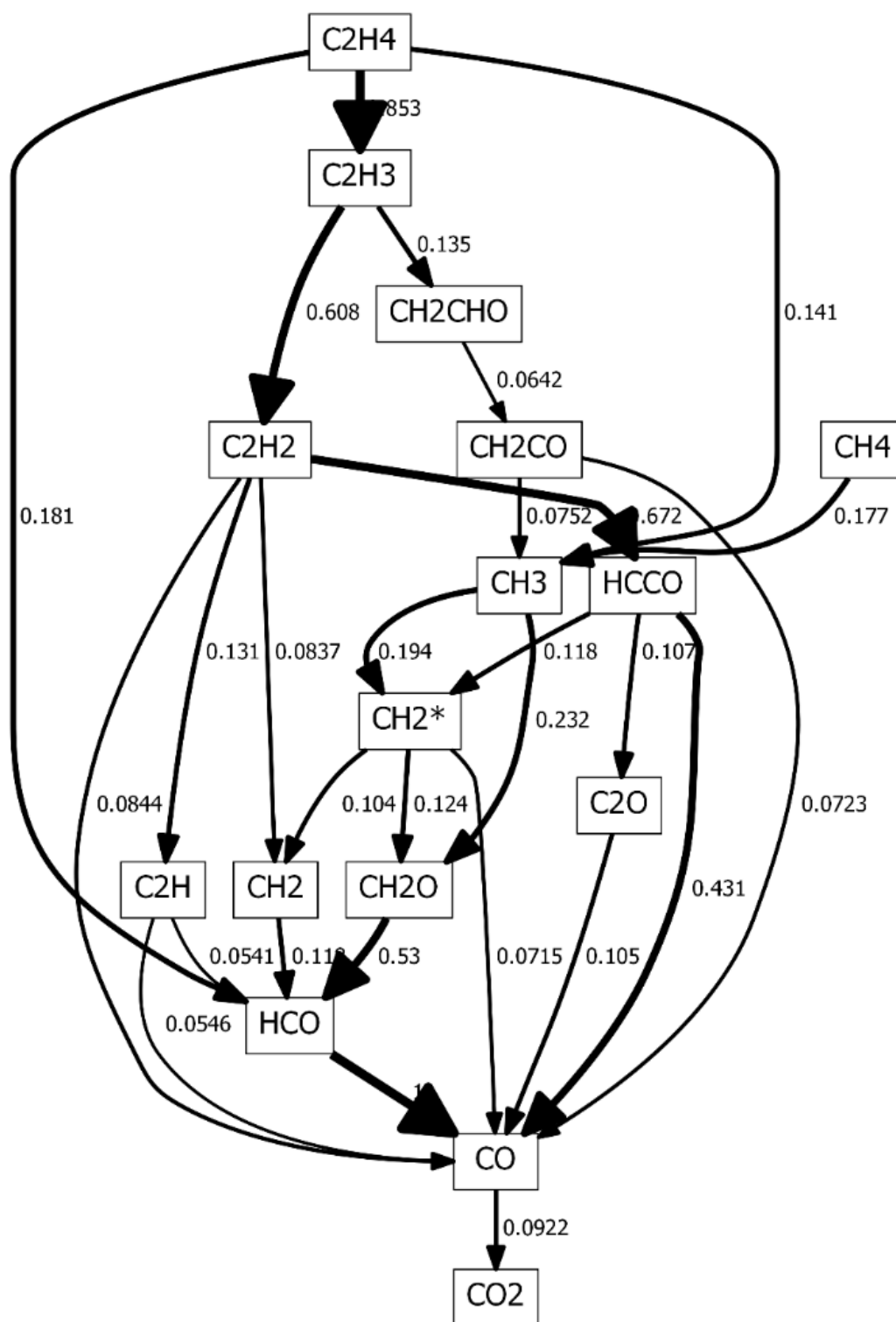


Figure 7.17. Reaction pathway diagram for 35% (n-C<sub>12</sub>H<sub>26</sub> + (18.5O<sub>2</sub>/φ)) + 65% CO<sub>2</sub> diluted stoichiometric mixture at 450 K 1 bar

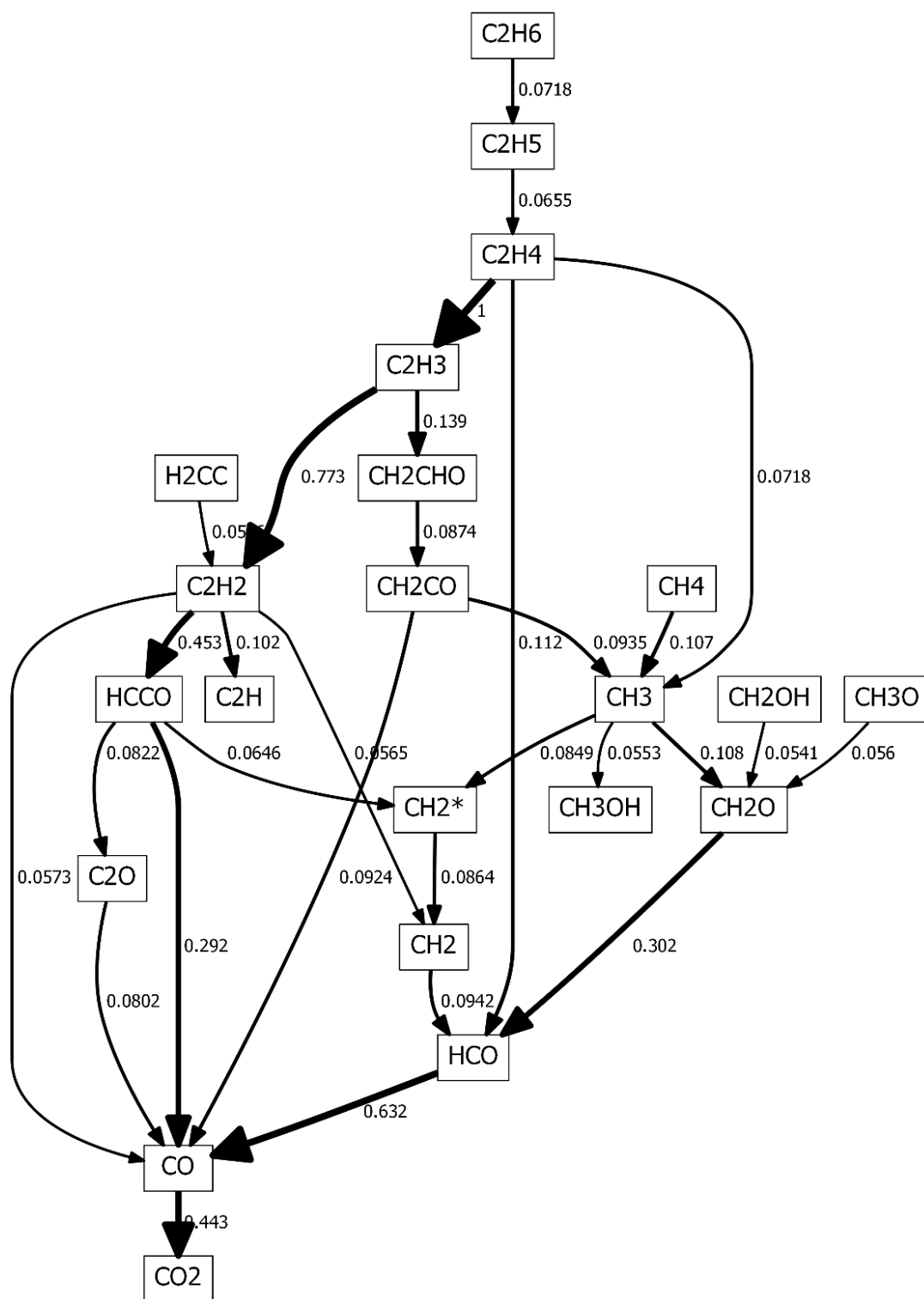


Figure 7.18. Reaction pathway diagram for 35% (n-C<sub>12</sub>H<sub>26</sub> + (18.5O<sub>2</sub>/φ)) + 65% H<sub>2</sub>O diluted stoichiometric mixture at 450 K 1 bar

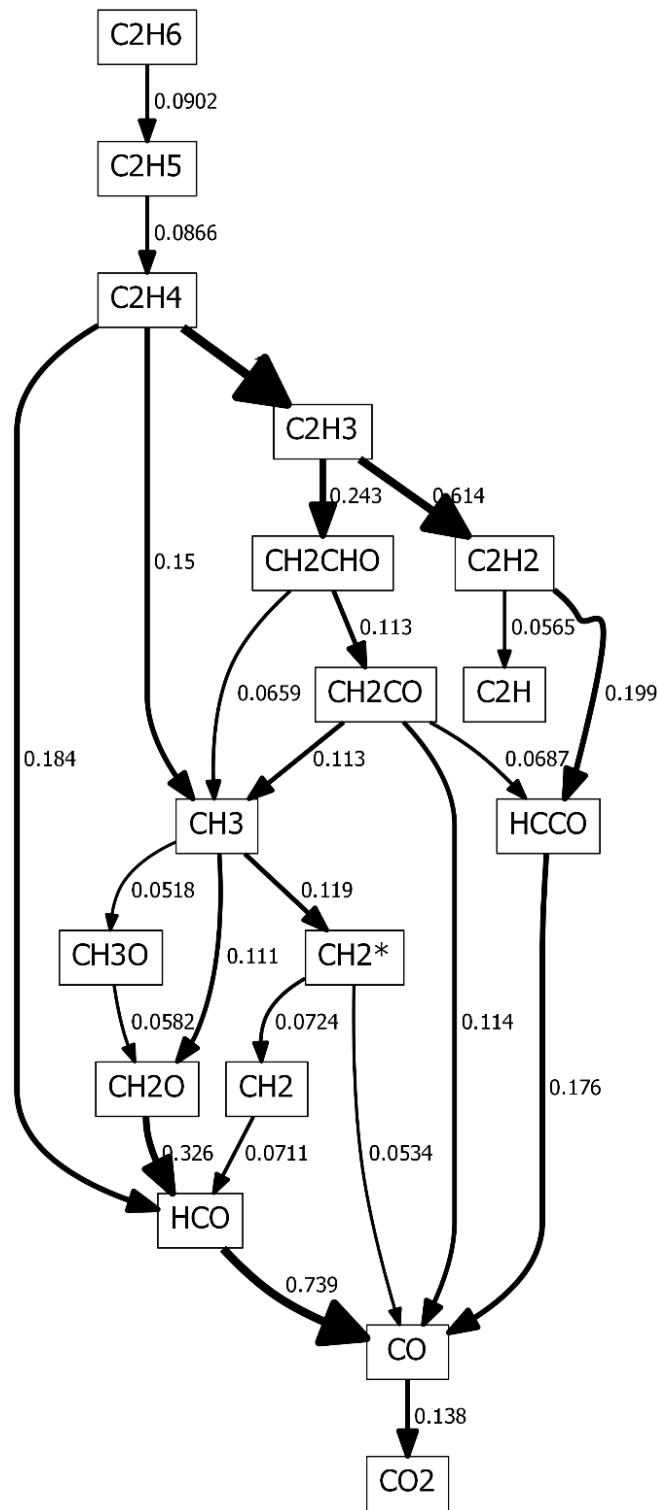


Figure 7.19. Reaction pathway diagram for 35% (n-C<sub>12</sub>H<sub>26</sub> + (18.5O<sub>2</sub>/φ)) + 65% N<sub>2</sub> diluted stoichiometric mixture at 450 K 1 bar

## 7.16 Summary

The mixtures considered in this work were  $(100-Z) \% (n-C_{12}H_{26} + (18.5O_2/\phi)) + Z\%$  ( $N_2/CO_2/H_2O$ ) mixtures at 400-450 K, 1-4 bar,  $\phi=0.6-1.4$ , and  $Z$  varied for (a)  $N_2=55-75\%$ , (b)  $CO_2/H_2O = 65\%$ . Planar flame simulations were performed with You, JetSurF2.0, and PoliMi-1410 mechanisms. Important interferences were:

1. At 55%  $N_2$  dilution, a peak value of 233 cm/s was measured at the stoichiometric condition at 450 K and 1 bar. With the increase in  $N_2$  mole fraction, the LBV decreased linearly.
2. At 65% dilution, 450 K,  $\phi=0.6-1.4$ , the overall decrease in the LBV due to the addition of  $N_2/H_2O/CO_2$ , as compared to an undiluted mixture was 60%/ 68%/ 87%, which was due to thermal effect: 96%/ 93%/ 67%, and chemical effect: 4%/ 7%/ 33%.
3. The estimated pressure exponents showed that the high-temperature oxy-n-dodecane flames, even in the presence of dilution, were less sensitive to initial pressure as compared to n-dodecane-air mixtures.
4. Simulated LBV with You et al. and JetsurF2.0 mechanisms matched well with the measurements at most of the conditions within the measurement uncertainties. But the predictions with PoliMi-1410 were well away from the predictions, especially in the rich mixture conditions.
5. In the  $N_2$  dilution study, at 75%  $N_2$  dilution, 400 K, 1 bar,  $\phi = 0.6$ , the highest positive value of  $L_b$  of 1.8 was observed due to higher thermal diffusivity and longer reaction time, and the deficient reactant, n- $C_{12}H_{26}$  is not the fast-diffusing species.
6. At a given mole fraction of diluent, initial pressure/temperature, and equivalence ratio, the steam diluted mixtures anchored the most stable flames towards the thermo-diffusive effects owing to higher thermal diffusivity and the associated  $Le$  number.
7. Irrespective of the diluents, all the studied mixtures were stable to thermo-diffusive effects even at rich conditions where the deficient species  $O_2$  had the highest reactivity and at higher initial pressures provided that the flame temperature was greater than or equal to 2150 K for the oxy-n-dodecane combustion.

# CHAPTER 8

## COMBUSTION CHARACTERISTICS OF HYDROGEN BLENDED N-DODECANE-AIR MIXTURES

In this section, the measured values of unstretched LBV and burned gas Markstein length of the premixed  $\{(1 - Z)\% nC_{12}H_{26} + Z\% H_2\} + \frac{18.5}{\phi} (O_2 + 3.76N_2)$  mixtures were presented. The investigated operating conditions are presented in Table 8.1. This chapter provided the valuable information on the combustion characteristics and flame stability with respect to the thermos-diffusive effects of a binary fuel that comprised of a highly diffusive and reactive  $H_2$  and a slowly diffusive and less reactive  $nC_{12}H_{26}$ .

### Operating conditions

Table 8.1. Operating boundary conditions of hydrogen blended n-dodecane-air mixtures

Mixtures	Blending z (%)	T (K)	p (bar)	$\phi$	#
$\{(1-z) n-C_{12}H_{26}+z\% H_2\} + \text{air}$	0	425	1, 2, 4	0.8-1.4	21
	20		1, 2, 4	0.8-1.4	21
	40		1, 2, 4	0.8-1.4	21
Total number of experiments					63

### Chemical kinetic mechanism

Table 8.2. Kinetic schemes used for the hydrogen blended n-dodecane-air mixtures

Name of the Mechanism	Number of Species	Number of reactions
JetsurF2.0[41]	348	2163
PoliMi [116]	130	2323
You et al.[115]	175	1318

## 8.1 Nonlinear flame stretch behavior

Figure 8.1 depicts the measured stretched flame speed and its variation with the flame stretch rate of n-dodecane and n-dodecane- $H_2$  mixtures reacting in the air at (a) lean and (b) rich conditions. N-dodecane mixtures had a strong nonunity Lewis number of 3.2 at  $\phi = 0.8$  and  $Le$

= 0.9 at  $\phi = 1.4$ . Due to this wide disparity in the  $Le$ , and on top of it, the  $H_2$  was also added, and, hence, the selection of the extrapolation schemes was assumed crucial in finding the unstretched flame speed and later the unstretched LBV. In the present work, two extrapolation schemes were used: (a) nonlinear [99], which is applicable for a wide range of  $Le$ , and (b) linear [19]. Plots (2a) and (2b) compared the effect of the choice of the linear and non-linear schemes on the estimated unstretched flame speed of the heavy n-dodecane blended without or with  $H_2$ . To quantify the accuracy of the schemes, the predicted unstretched LBV

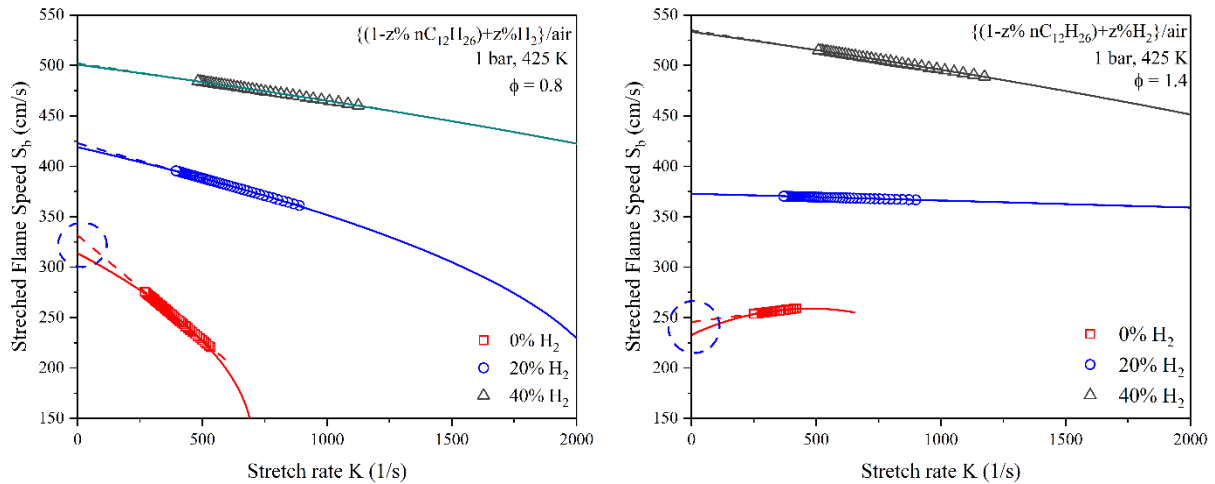


Figure 8.1. Variation of stretched flame speed with the stretch rate of  $\{(1-z)\% \text{ nC}_{12}\text{H}_{26} + z\% \text{ H}_2\}$ /air mixtures,  $z$  varies 0-40% at 1 bar 425 K (a)  $\phi = 0.8$  (b)  $\phi = 1.4$ . Symbols indicate the experimental data points used for extrapolation, dashed and solid lines represent the implied linear and nonlinear extrapolations schemes

using CHEMKIN and JetSurf was used. A relative difference ( $\epsilon$ ) parameter was defined as  $\epsilon = \frac{S_{u,mea}^o - S_{u,simu}^o}{S_{u,mea}^o}$ , where  $S_{u,mea}^o$  corresponds to unstretched LBV obtained with linear/ nonlinear extrapolation schemes, and  $S_{u,simu}^o$  represents unstretched LBV from a 1D planar flame model with JetSURF. The estimated  $\epsilon$  of n-dodecane-air mixtures was smaller for the values obtained with the nonlinear scheme as compared with the linear scheme, and they were:  $\phi = 0.8$ :  $\epsilon_L = 9.31\%$  to  $\epsilon_{NL} = 3.04\%$  and  $\phi = 1.4$ :  $\epsilon_L = 4.52\%$  to  $\epsilon_{NL} = 2.28\%$ . However, for the  $H_2$  blended mixtures, this discrepancy further diminished due to the balancing act provided by the contrasting diffusive characteristics of hydrogen (fast) and n-dodecane (slow).

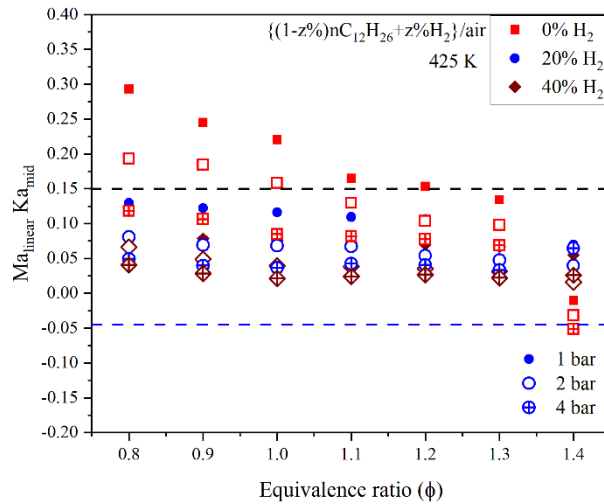


Figure 8.2. The trend of extrapolation criteria  $Ma_{linear}Ka_{mid}$  with an equivalence ratio of  $\{(1-z) \% nC_{12}H_{26}+z\%H_2\}/air$  mixtures,  $z$  varies 0-40% at 1-4 bar 425 K. The two dashed lines represent the lower and upper limits of  $-0.05 < Ma_{linear}Ka_{mid} < 0.15$ , as suggested by Wu et al. [126]

To further validate that the range of  $S_b$  chosen for the extrapolation was well within the weakly stretched regime, Wu et al. [126] recommended that the product of Markstein number ( $Ma$ ) and Karlovitz ( $Ka$ ) should be between  $-0.05$  to  $0.15$  to minimize the uncertainty involved in the extrapolation. Here too, the product of  $Ma$  and  $Ka$  was estimated, and its change with equivalence ratio was displayed in Figure 8.2 for all the present experiments.

## 8.2 Effects of equivalence ratio on LBV

Figure 8.3 depicts the measured and simulated LBV of n-dodecane without and with H<sub>2</sub> at 1 bar, 425 K, and  $\phi = 0.8 - 1.4$ . The addition of hydrogen in n-dodecane had considerably increased the LBV of the fuel mixture. The maximum LBV occurred at  $\phi = 1.1$ , and it was nearly independent of the mole fraction of H<sub>2</sub> ( $X_{H_2}$ ) in n-dodecane. The remarkable effect of H<sub>2</sub> addition was visible at  $\phi = 1.2$ , where the LBV was 54.76 cm/s at 0% H<sub>2</sub>, and it increased to 119.73 cm/s (120% increase) with the addition of 40% H<sub>2</sub> in n-dodecane. At other mixture ratios, too, as the  $X_{H_2}$  in n-dodecane hiked to 40%, the LBV was 1.7 ( $\phi = 0.8$ ) / 2.3 ( $\phi = 1.4$ ) times higher as compared to the pure n-dodecane case. Adding H<sub>2</sub> with a base fuel enhanced the combustion characteristics of the base fuel in the following ways: [14] a) a linear increment in the transport properties caused by the high mobility of H<sub>2</sub>, b) the kinetic effect enhanced strongly due to the fast reactivity of the H<sub>2</sub>, and (c) a minor increment in the equilibrium flame temperature (EFT). With the present n-dodecane-H<sub>2</sub> mixtures too, the EFT increased by only 20 K even at 40% H<sub>2</sub> addition in the n-dodecane, and hence, its effect is insignificant. Hence, the LBV increment was linked directly to the enhancement in the chemical kinetics due to the

addition of H<sub>2</sub>, and it corroborated well with the literature [62,64]. The predicted LBV using detailed mechanisms such as Jetsurf2.0 and You et al. accorded well with the measurements, and their variation was well within the measurement errors. But, the reduced mechanism, PoliMi-1410, over/ under predicted the LBV of the rich/ lean mixtures of unblended/ H<sub>2</sub> blended mixtures.

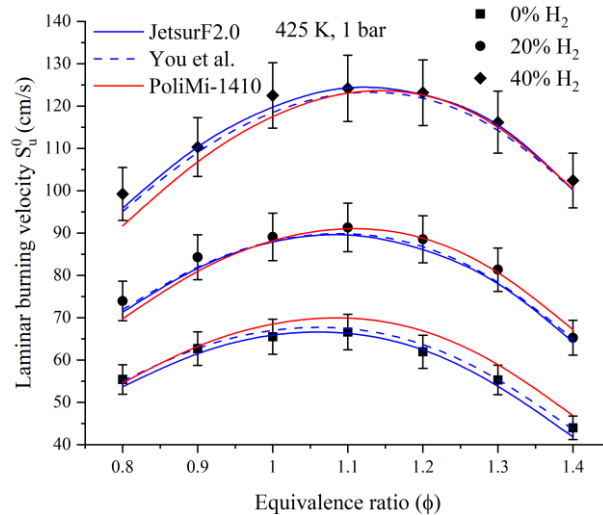


Figure 8.3. Laminar burning velocity of  $\{(1-z) \text{ n-C}_{12}\text{H}_{26} + z\% \text{ H}_2\}$ /air mixtures,  $z$  varies 0-40% at 1 bar 425 K. Symbols and lines represent experimental and corresponding numerical simulation, respectively

### 8.3 Effects of H<sub>2</sub> addition on LBV

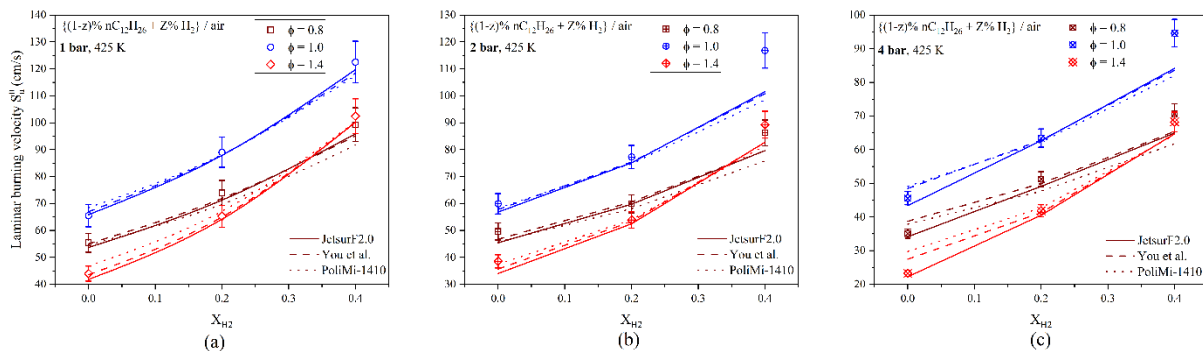


Figure 8.4. Variation of Laminar burning velocity with H<sub>2</sub> fraction of  $\{(1-z) \text{ n-C}_{12}\text{H}_{26} + z\% \text{ H}_2\}$ /air mixtures,  $z$  varies 0-40% at (a)1 bar (b) 2 bar and (c) 4 bar and 425 K

Figure 8.4 (a-c) shows the variation in the unstretched LBV with the mole fraction of H<sub>2</sub> in the binary  $\{(1-z) \text{ n-dodecane} + z\% \text{ H}_2\}$  fuel mixture reacting with air,  $z$  varied 0-40% at 1 – 4 bar, 425 k, and  $\phi=0.8, 1, 1.4$ . It was observed that, for lean and stoichiometric mixtures, the LBV hiked linearly with a raise in the  $X_{\text{H}_2}$ , irrespective of initial pressures. A moderate nonlinear increment occurred at  $\phi = 1.4$  when the  $X_{\text{H}_2}$  increased from 0 to 40% due to the strong coupling

of kinetic and mass & thermal diffusional effects of H<sub>2</sub> and n-dodecane. Also, the maximum increments in LBV happened at  $\phi = 1.4$  (132%/1 bar and 193% / 4 bar) due to the conversion of maximum chemical energy and heat release rate.

## 8.4 Effects of initial pressure on LBV

Figure 8.5 depicts the variation of the experimental and numerical LBV with an equivalence ratio of 60% n-C<sub>12</sub>H<sub>26</sub>+40% H<sub>2</sub> reacting in air at 1-4 bar and 425 K. The LBV of the binary mixture peaked at  $\phi=1.1$  independent of initial pressure, and it was identical to that of n-dodecane case, which highlighted that the combustion characteristics of the binary mixture was still commanded by n-dodecane. As expected, Figure 8.5 b & c showed the reduction in the LBV of the binary fuel mixture with an upraise in the initial pressure, and this trend was similar to that of pure single fuel cases too. An increase in its unburned gas density was the reason: (a) for the reduction in the LBV with an increase in pressure and (b) an increase in the mass burning flux. Also, the dominance of slow, third-body reactions at higher pressures was also an additional factor in the reduction of LBV. Figure 8.5 b & c inform that at higher initial pressures and higher mole fractions of H<sub>2</sub>, the widely recognised Jetsurf2.0 and PoliMi kinetic models failed to predict the LBV accurately and exhibited a significant deviation of 15.33% at  $\phi = 1.0$ , 4 bar, and  $X_{H2} = 40\%$

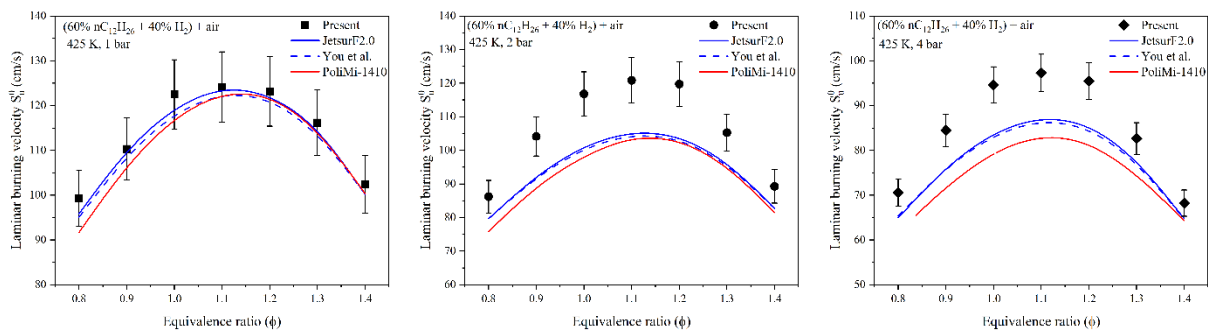


Figure 8.5. Variation of Laminar burning velocity with H<sub>2</sub> fraction of (60% n-C<sub>12</sub>H<sub>26</sub> +40% H<sub>2</sub>)/air mixtures at 425 K, and (a)1 bar, (b) 2 bar, and (c) 4 bar

Figure 8.6 To display the sensitiveness of LBV to initial pressure, a normalized LBV,  $S_u^*$ , was defined as  $S_u^* = S_u/S_{u0}$  where the  $S_u$  was the unstretched LBV of the stoichiometric mixture at a given initial pressure, and  $S_{u0}$  refers to unstretched LBV at  $\phi = 1.0$ ,  $P_u = 1$  bar ( $P_{u0}$ ) and 425 K. Figure 8.6 shows the measured  $S_u^*$  and its variation with  $X_{H2}$  at different normalized initial pressures,  $P_u^* = P_u/P_{u0}$ . The result showed that the effect of pressure on LBV is strongly dependent on  $X_{H2}$ . At higher  $X_{H2}$ , the magnitude of  $S_u^*$  reduction significantly decreased with

an increase in pressure. This was due to a decrease in the mole fraction of  $\text{CO}_2$  in the products and the associated reduction in the third body reactions.

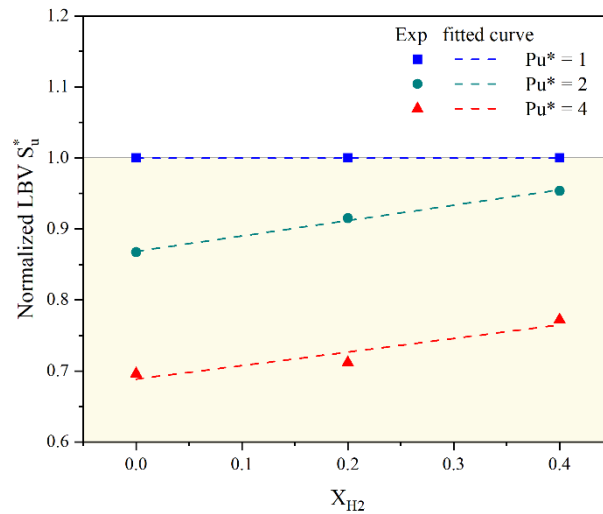


Figure 8.6. The normalized laminar burning velocity of  $\{(1-z) \text{n-C}_{12}\text{H}_{26} + z\% \text{H}_2\}/\text{air}$  mixtures,  $z$ , varies 0-40% as a function of hydrogen ratio for different normalized initial pressures

## 8.5 Thermal and kinetic effects

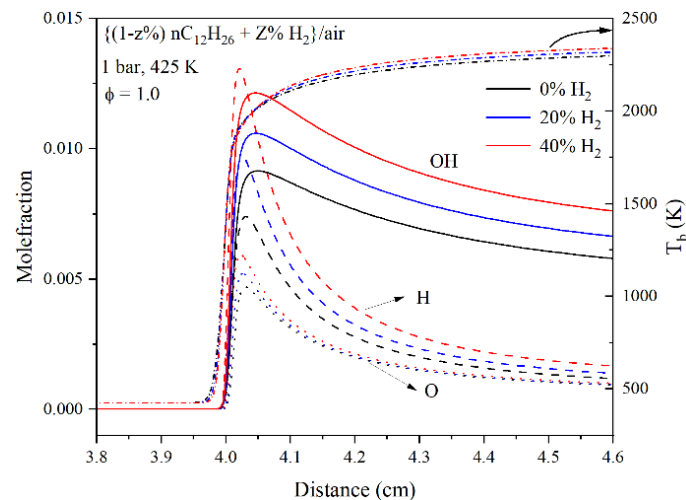


Figure 8.7. Simulated mole fractions of key radicals and adiabatic flame temperature of stoichiometric  $\{(1-z) \text{n-C}_{12}\text{H}_{26} + z\% \text{H}_2\}/\text{air}$  mixtures,  $z$  varies 0-40% at bar 425 K

The effect of the  $\text{H}_2$  addition on the oxidation chemistry of the n-dodecane can also be assessed via a relative increase in the mole fraction of H, O, and OH radical in the active radical pool, as it will increase the LBV too. Figure 8.7 shows the spatial distribution of mole fraction of species H, O, and OH and equilibrium flame temperature at different  $\text{H}_2$  mole fractions in n-dodecane reacting with air at  $\phi = 1.0$ , 1 bar, and 425 K. The mole fraction of H, O, and OH hiked as the mole fraction of  $\text{H}_2$  in n-dodecane increased, which indicated a strong kinetic

effect. On the other side, even the addition of 40% H<sub>2</sub> in n-dodecane increased the T<sub>b</sub> to around 20 K only. The above discussion clearly pointed to the fact that the significant increment of LBV of the binary mixture was essentially due to the enhanced kinetic effect due to the addition of H<sub>2</sub> than the thermal effect.

## 8.6 Effects of hydrogen addition on Markstein length

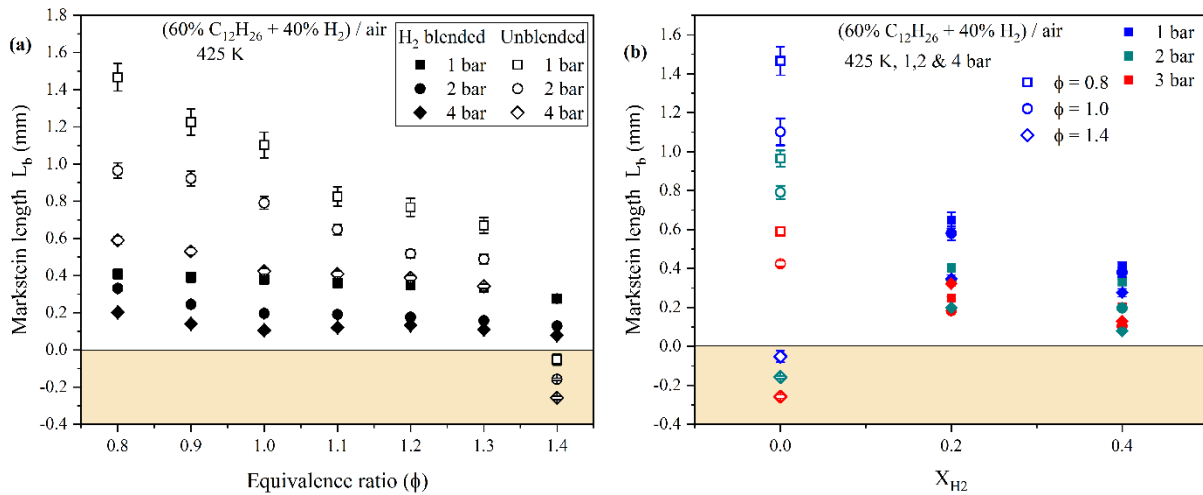


Figure 8.8. Measured burned gas Markstein length of (60% n-C<sub>12</sub>H<sub>26</sub>+ 40% H<sub>2</sub>) / air flames, at 1-4 bar 425 K as a function of (a) equivalence ratio, (b) Hydrogen ratio. An unstable region is highlighted with color

Burned gas Markstein length ( $L_b$ ) was estimated using Eq. 3.6. Figure 8.8 shows the measured  $L_b$  of the premixed 60% n-dodecane+ 40% H<sub>2</sub>-air mixture at 1-4 bar, 425 K, and different (a) equivalence ratios, and (b) hydrogen fraction. Figure 8.8 (a) shows that the  $L_b$  of the binary mixture did not show a marked change with equivalence ratio, which contrasted to the behavior of long-chain hydrocarbons [66] at all the studied initial pressures. The same figure shows that the response of the unblended n-dodecane-air mixtures to the stretch effects was quite strong at all the equivalence ratios. Also, the flame transitioned from stable to unstable at  $\phi = 1.4$  for n-dodecane-air mixtures whose  $Le < 1$  at p=1-4 bar, and this was essentially due to the slower diffusion of n-dodecane and the associated change in the local equivalence ratio. The H<sub>2</sub> blending enhanced the stability of the binary mixture towards the stretch effects. It was quite visible at  $\phi=1.4$ , where it prevented the transition of stable to unstable flames. The addition of H<sub>2</sub> increased the  $Le$  number above the critical limit due to its high mobility and reduced the magnitude of  $L_b$ , which indicated the weak response of flame to stretch effects on LBV, and an earlier onset of hydrodynamic instabilities were observed [136,137]. Figure 8.8 (b) shows that  $L_b$  decreased non-monotonically with an increase in the mole fraction of hydrogen at  $\phi=0.8-$

1.4. Here too, the magnitude of  $L_b$  showed a little change with equivalence ratio at a given pressure mainly due to a constant Lewis number. Further, the  $L_b$  decreased with an increase in the initial pressure for all the blended/ unblended mixtures, as expected, due to a hike in the thermal expansion ratio. One encouraging observation was that the addition of  $H_2$  reduced the destabilizing effect of stretch and thermo-diffusional effects, but  $L_b$  was close to the transition limit at  $X_{H_2}=40\%$ . The above results were corroborated with the estimated effective Lewis numbers at all the operating conditions and are presented in Figure 8.10.

## 8.7 Flame stability

Figure 8.9 shows the shadowgraph images of spherical flames stabilized with  $nC_{12}H_{26}/H_2/air$  mixtures at  $R \approx 30$  mm,  $T_u = 425$  K,  $P_u = 1-4$  bar,  $\phi = 1.4$ , and  $X_{H_2} = 0-0.4$ . Increasing the initial pressure of the unblended n-dodecane-air mixture (Row-1 of Figure 8.9) whose  $Le < 1$  resulted in large cracks and wrinkles on the flame, indicating the declining flame stability due to the stretch and thermo-diffusive (deficient reactant  $O_2$  had the higher mass diffusivity) effects.

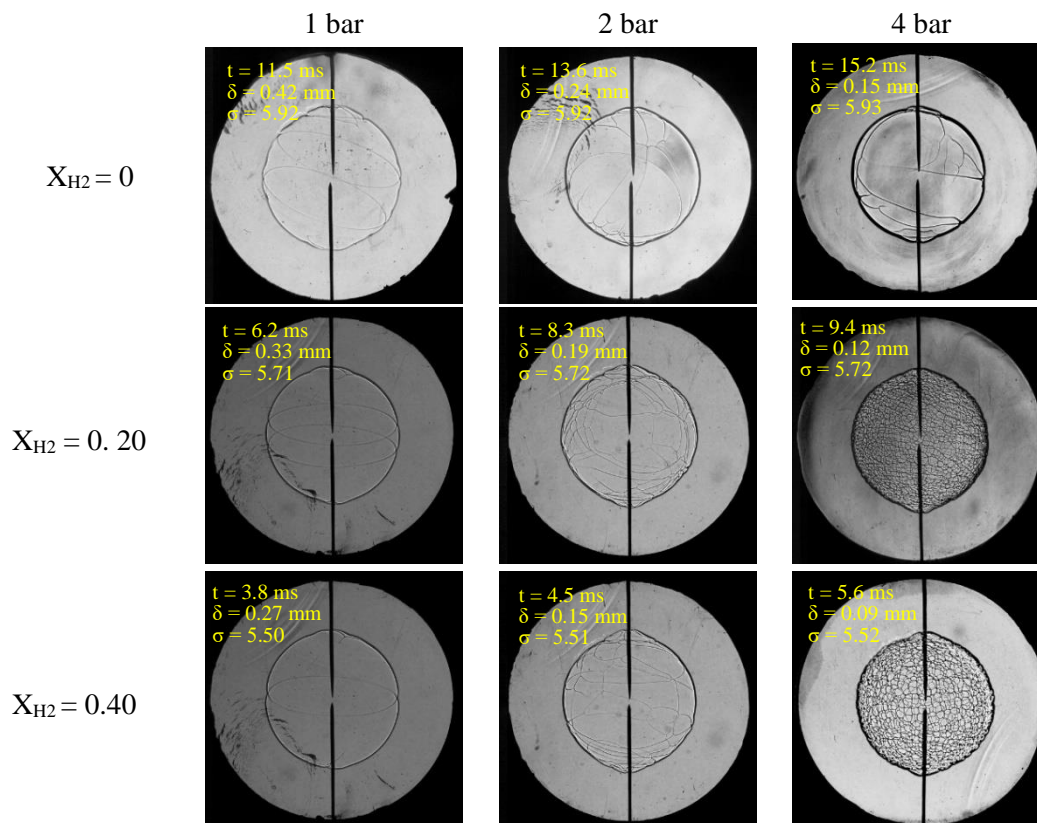


Figure 8.9. Shadowgraph images of spherically propagating (burning sequence of the flames of)  $\{(1-z)nC_{12}H_{26}+z\% H_2\}/air$  flames at  $R = 30$  mm,  $T_u = 425$  K,  $P_u = 1-4$  bar,  $\phi = 1.4$ ,  $X_{H_2} = 0-40\%$ .

The interesting aspect was that even though the n-dodecane-air at 425 K, 4 bar, &  $\phi = 1.4$  was affected by thermo-diffusional effects (represented by negative  $L_b$  as shown in Figure 8.8), but it still had not been affected by the hydrodynamic instability (appearance of small and uniform cells on the entire flame surface) even at  $R \approx 30$  mm. Addition of  $H_2$  to n-dodecane enhanced the diffusional characteristics of the mixture, and resulted in thinner flames. Thinner flames were less susceptible to flame stretch and thermo-diffusional effects, which could be corroborated with the smaller magnitudes of  $L_b$ , as shown in Figure 8.8. But it resulted in an earlier onset of hydrodynamic instability at elevated pressures, as shown in Figure 8.9 (columns 2 & 3), as compared to the unblended mixtures, as both the hydrogen addition and pressure rise had together significantly reduced the flame thickness. The images were displayed to show the onset of different types of instabilities, and the flames with instabilities were never considered while estimating the LBV.

Figure 8.10 presents the different global flame properties of the premixed binary fuel (n-dodecane/ $H_2$ )-air flames and its dependence on equivalence ratio at 425 K,  $X_{H_2} = 0-40\%$ , and  $p=1-4$  bar. Zeldovich number ( $Ze$ ) is a non-dimensional global activation energy, and it represents the sensitivity of chemical reaction to the flame temperature. Figure 8.10 shows that the variation of the Zeldovich number with equivalence ratio was exactly opposite to the trend of LBV with  $\phi$  as shown in Figure 8.3 & 8.5. It showed that  $Ze$  increased with a hike in the initial pressure was due to an increase in the mass burning flux ( $\rho_u S_u^0$ ), and a subsequent increase in the global activation energy,  $E_a = -2R \left[ \frac{\partial(\ln \rho_u S_u^0)}{\partial(1/T_b)} \right]_p$ . As  $X_{H_2}$  increased in n-dodecane, the Zeldovich number decreased, due to an enhancement in the global reaction rate [64]. The flame thickness decreased with either an increase in  $H_2$  (due to an increase in the transport properties and reaction rate) or with, an increase in the initial pressure (due to an increase in the reactant's density, number of collisions, and collision rate) or both. The effective Lewis number (Eq. 3.20) decreased with an increase in the initial pressure due to a reduction in the thermal and mass diffusivities. It varied non-monotonically with the addition of  $H_2$  (0 to 40%) in n-dodecane as the rate of increase in the mass diffusivity ( $D_{eff}$ ) of the combustible mixture was higher as compared to that of thermal diffusivity, and consequently,  $Le_{eff}$  decreased with  $H_2$  fraction. The effective Lewis number is less than the critical  $Le$  at  $\phi = 1.4$  but greater than it for all  $\phi < 1.4$ , indicated that the thermo-diffusive instability destabilized the flame at rich mixtures (as the deficient reactant  $O_2$  had the highest diffusivity), but

generated stable flame at lean mixtures (as the deficient reactant  $n\text{-C}_{12}\text{H}_{26}$  had the lowest diffusivity).

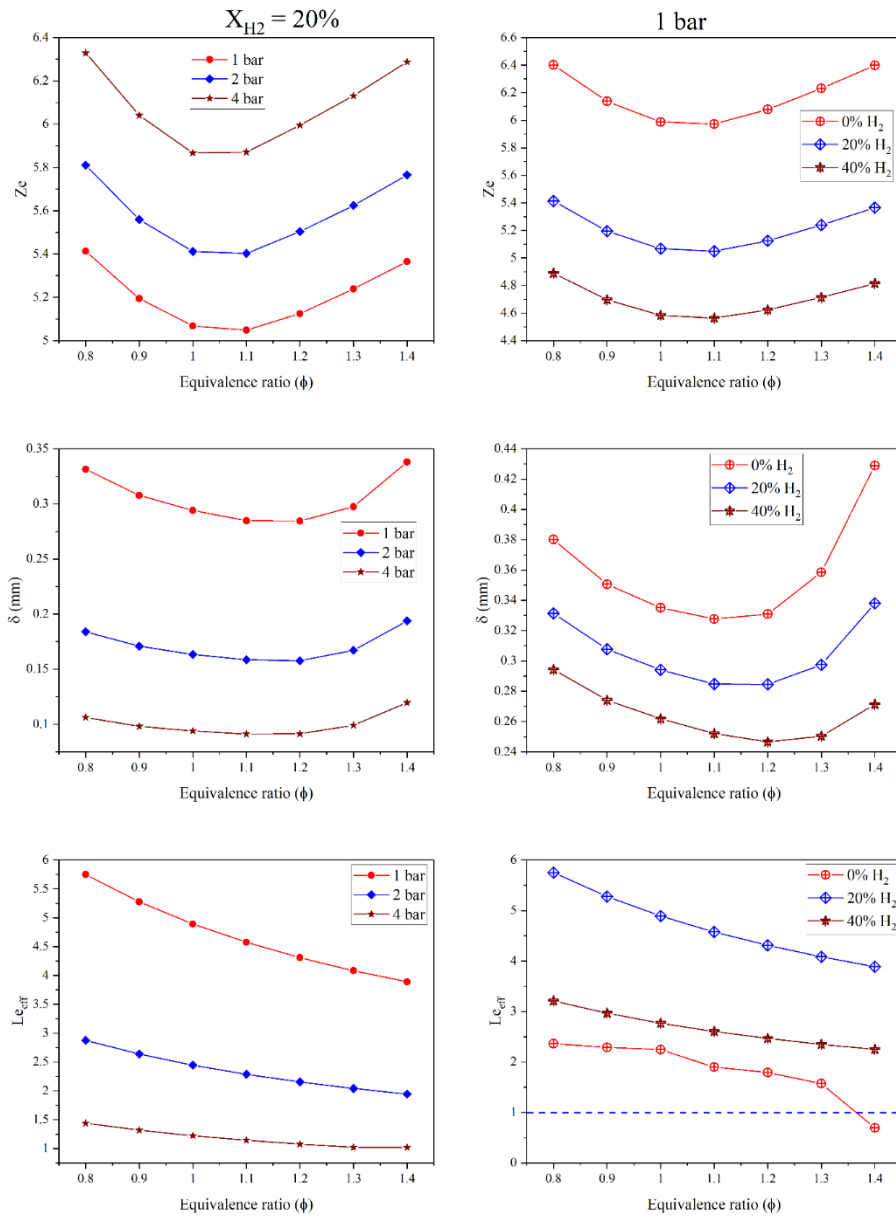


Figure 8.10. Variation of Zeldovich number  $Z_c$ , the thermal expansion coefficient  $\sigma$ , the flame thickness  $\delta$ , and the effective Lewis number of  $n$ -dodecane/ $\text{H}_2$ /air flames as a function of equivalence ratio at 425 K. (a) at different initial pressures and  $X_{\text{H}_2} = 20\%$  (b) at different  $\text{H}_2$  ratio and 1 bar

## 8.8 Sensitivity analysis

A sensitivity analysis was performed to analyse the impact of  $\text{H}_2$  blending on the chemical kinetics and its sequential effect on LBV. The  $A$ -factor of reaction  $k$  was estimated from CHEMKIN [17] and JetsurF2.0 chemical kinetic mechanism. The top 15 elementary reactions which have a significant impact on LBV are plotted in Figure 8.11 for lean, stoichiometric, and

rich mixtures of (n-dodecane/H<sub>2</sub>)-fuel mixtures reacting with air at various levels of H<sub>2</sub> addition and 1 bar 425 K. An elementary reaction which has a positive value of normalized sensitivity coefficient enhanced the LBV, and vice-versa for an elementary reaction that has a negative value of normalized sensitivity coefficient. It can be observed that reactions involving H radicals were the most sensitive one, and its sensitivity further scaled up with an addition of H<sub>2</sub>. The chain branching reaction, H+O<sub>2</sub> = O+OH (R1), was the most important reaction at all equivalence ratios and mole fraction of H<sub>2</sub> in n-dodecane. The products of reaction R1 were O and OH radicals. These radicals attacked the heavier molecules to hydrocarbon radicals at faster rates. Any reaction which competes with R1 will reduce the overall reactivity and hence, the LBV. H and OH radicals are dominant in lean mixtures, but H is more dominant in rich mixtures than OH, as was observed in the sensitivity plot itself from the reactions R27, R9, and R3. It was noticed that with an increase in the H<sub>2</sub> mole fraction in n-dodecane, the reaction R1 becomes more significant, as its sensitivity increased with the addition of H<sub>2</sub> independent of the equivalence ratio. This observation is in line with the findings of Comandini et al.[66].

When the mole fraction of H<sub>2</sub> in the n-dodecane was increased from 0 to 40%, the sensitivity of R1 increased significantly only for the lean and the stoichiometric mixtures, however, in the rich mixture, its sensitivity showed a minor increment due to the availability of higher mole fraction H radicals which helped in breaking the HC. The reaction CO+OH = CO<sub>2</sub>+H (R27) was the second highest sensitive reaction for the premixed n-dodecane/H<sub>2</sub> mixtures reacting with air. Its sensitivity decreased with a hike in the H<sub>2</sub> mole fraction in the n-dodecane, which clearly indicated that the kinetics and the reaction path-way of the binary mixture was dominated by the presence of H<sub>2</sub> than the HC(n-dodecane) at lean and stoichiometric mixtures, however, R27 is insignificant at rich mixtures due to the competition between H<sub>2</sub> and HC combustion chemistry. The chain termination reaction CH<sub>3</sub>+H(+M) = CH<sub>4</sub>(+M) (R84) shows the influence of a smaller HC species in the reaction pathway of a heavier n-dodecane, and as expected, its sensitivity increased with H<sub>2</sub> addition for lean stoichiometric mixtures, but at rich mixtures, the sensitivity decreased due to the dominance of HC combustion. The negative sensitivity reaction of H+O<sub>2</sub>(+M) = HO<sub>2</sub>(+M) (R12) coefficient significantly increased only on lean mixture due to the availability of excess oxygen. The sensitivity of chain branching O+H<sub>2</sub> = H+OH (R2) and chain propagation OH+H<sub>2</sub> = H+H<sub>2</sub>O (R3) reactions increased appreciably with the addition of H<sub>2</sub> in n-dodecane, and the dominance of these two reactions were the evidence for the shift in the oxidation chemistry from HC pathway to H<sub>2</sub> pathway at high H<sub>2</sub> addition levels (40%). The positive sensitivity of R2 and R3

at lean and stoichiometric mixtures indicated the dominance of H<sub>2</sub> chemistry, and it changed their sign from positive to negative (coefficient reversal) for rich mixtures as these reactions competed for the O and OH radicals with HC combustion chemistry reactions-those with positive sensitivity coefficients in Figure 8.11 (c).

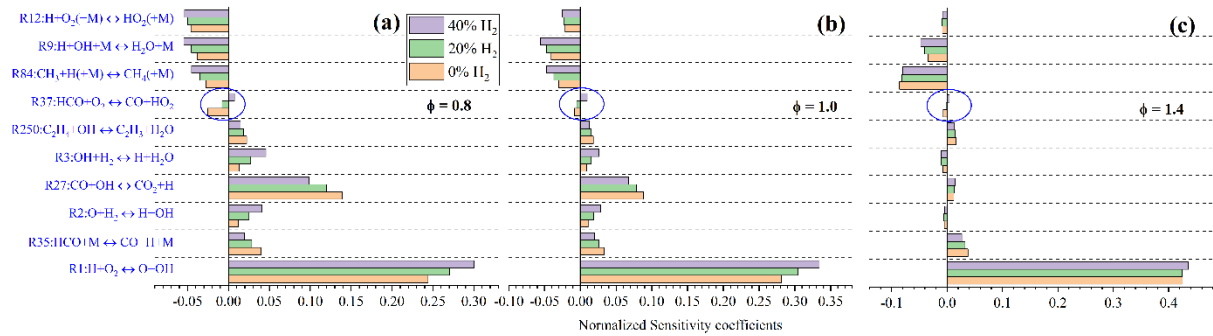


Figure 8.11. The normalized sensitivity coefficient for the laminar burning velocity of  $\{(1-z) n\text{-C}_{12}\text{H}_{26}+z\% \text{H}_2\}$ /air flames,  $z$  varies 0-40% at 425 K and 1 bar (a) lean:  $\phi = 0.8$  (b) stoichiometric:  $\phi = 1.0$  and (c) rich:  $\phi = 1.4$

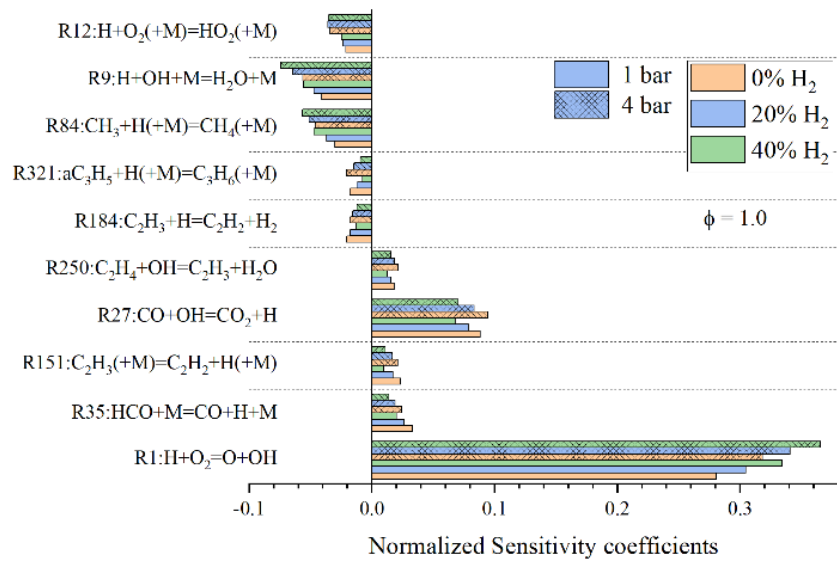


Figure 8.12. Normalized sensitivity coefficient of  $\{(1-z) n\text{-C}_{12}\text{H}_{26} + z\% \text{H}_2\}$ /air flames,  $z$  varies 0-40% at 425 K, 2-4 bar, and  $\phi = 1.0$

As expected in the high-temperature flame chemistry, the chain branching/ termination reactions associated with H radicals were the most sensitive ones. It can be observed that the reactions involving H radical consumption have slightly increased sensitivity coefficient values with pressure increment. Figure 8.12 reports the effect of initial pressure on the sensitivities of elementary reactions at a different mole fraction of H<sub>2</sub> in n-dodecane. At a given mole fraction of H<sub>2</sub> in n-dodecane, with an increase in initial pressure from 1 to 4 bar, it was found that the

three-body termination reaction  $\text{H}+\text{OH}+\text{M} = \text{H}_2\text{O}+\text{M}$  (R9) takes over the reaction  $\text{H}+\text{O}_2(+\text{M}) = \text{HO}_2(+\text{M})$  (R12) and became the most sensitive reaction in suppressing LBV.

## 8.9 Reaction pathways

The reaction pathway diagram is the graphical representation of the production/ consumption rate of major/ minor species involved in a complex reaction mechanism. Figure 8.13 shows the reaction pathway diagram of n-dodecane/ $\text{H}_2$ /air with (a)  $X_{\text{H}_2} = 0\%$  and (b)  $X_{\text{H}_2} = 40\%$  mixtures at  $\phi = 1.4$ , respectively, at 450 K and 1 bar. The thickness of the arrow lines indicated the strength of elemental flux. From the pathways, it was observed that the combustion chemistry of n-dodecane mainly depends on smaller sub-species like  $\text{C}_1$ - $\text{C}_4$ . The major reaction pathways for carbon consumption observed were:

Pathway – 1:  $\text{C}_2\text{H}_4 \rightarrow \text{C}_2\text{H}_3 \rightarrow \text{C}_2\text{H}_2 \rightarrow \text{HCCO} \rightarrow \text{CO} \rightarrow \text{CO}_2$

Pathway – 2:  $\text{C}_2\text{H}_6 \rightarrow \text{C}_2\text{H}_5 \rightarrow \text{C}_2\text{H}_4 \rightarrow \text{C}_2\text{H}_3 \rightarrow \text{C}_2\text{H}_2 \rightarrow \text{C}_2\text{H}_2 \rightarrow \text{HCCO} \rightarrow \text{CO} \rightarrow \text{CO}_2$

The addition of 40%  $\text{H}_2$  to n-dodecane had significantly altered the major pathways. The dominant pathway for this mixture was  $\text{CH}_4 \rightarrow \text{CH}_3 \rightarrow \text{CH}_2\text{O} \rightarrow \text{HCO} \rightarrow \text{CO} \rightarrow \text{CO}_2$ . The elemental flux through the above pathway was significantly higher as compared to that of n-dodecane-air mixture. Similarly,  $\text{CH}_3 \rightarrow \text{CH}_2^* \rightarrow \text{CH}_2 \rightarrow \text{HCO} \rightarrow \text{CO} \rightarrow \text{CO}_2$  pathway also becomes prominent. Most of the reaction paths lead to the formation of HCO and then  $\text{CO}_2$ . Conversion of HCO to CO element flux increased from 0.592 to 0.867 (46%), and CO to  $\text{CO}_2$  decreased from 0.233 to 0.177 (24%), indicated that hydrogen combustion takes over the HC combustion chemistry.

## 8.10 Emission analysis

Hydrogen addition was aimed to bring down greenhouse gases and pollutant emissions. Hence, a simulation was performed using a freely propagating flame model to estimate the possible emissions from n-dodecane-air mixture without and with  $\text{H}_2$  blending. For this purpose, Naik et al. [40] kinetic mechanism was used. It had 597 species and 3854 reactions with the  $\text{NO}_x$  subsets from GRI- $\text{NO}_x$  mechanism, HCN reaction chemistry, and  $\text{NO}_x$  -HC sensitization chemistry. Figure 8.14 (a) & (b) shows the effect of  $\text{H}_2$  addition on the important pollutant species, such as  $\text{CO}_2$ , CO, and  $\text{NO}_x$  of premixed n-dodecane/ $\text{H}_2$  reacting with air at 1 bar, 425 K, and  $X_{\text{H}_2} = 0$  to 40%. As expected, Figure 8.14 (a) depicts that both the mole fractions of  $\text{CO}_2$  and CO decreased with the addition of  $\text{H}_2$ . Typically, the mole fraction of green-house species,  $\text{CO}_2$ , decreased by 55% with the addition of 40% of  $\text{H}_2$  in the fuel. The

mole fraction of pollutant species, CO, also considerably decreased at an average of 30% due to the larger availability of OH, which facilitated the oxidation of CO to CO<sub>2</sub>.

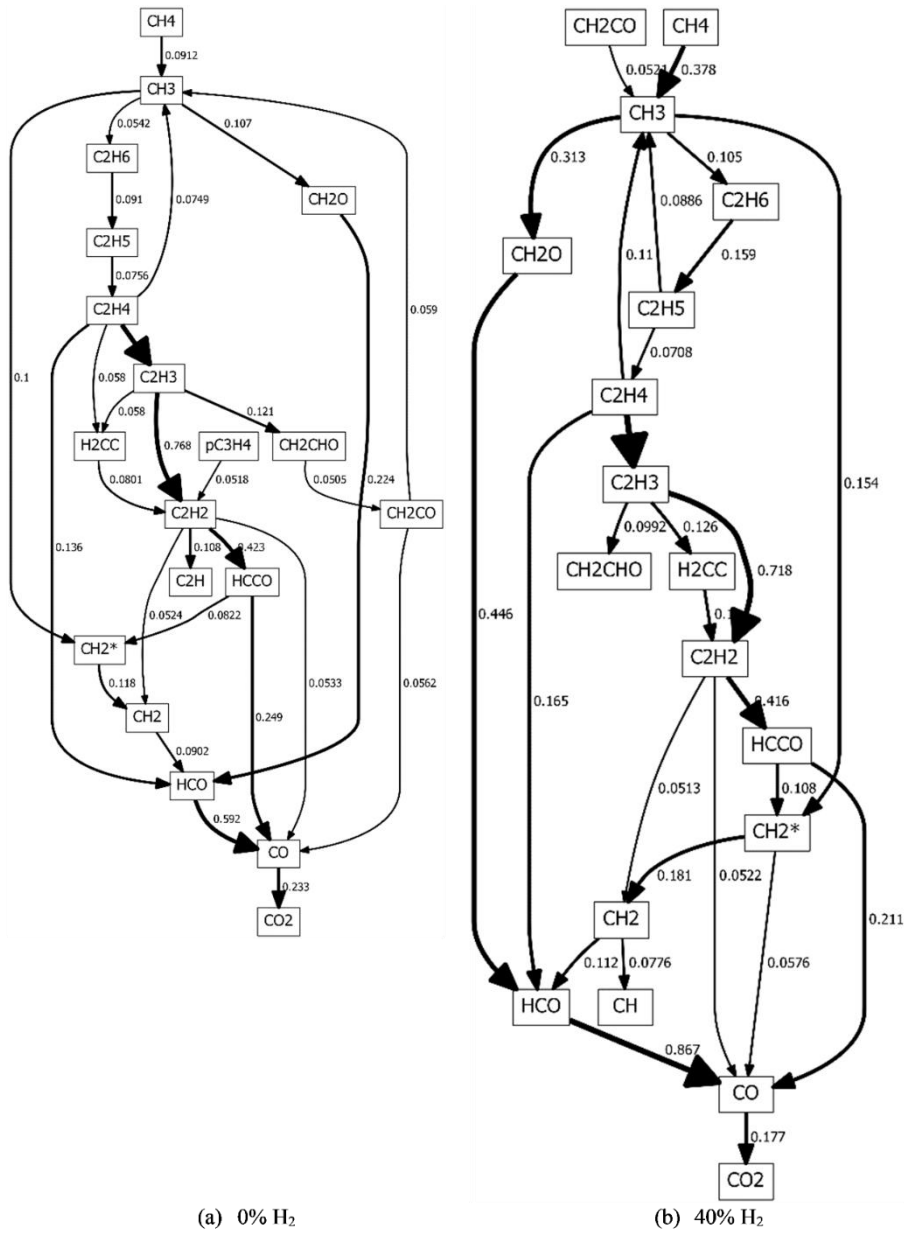


Figure 8.13. Reaction pathway diagram showing the carbon elemental flux change of n-dodecane/H<sub>2</sub>/air with (a) X<sub>H<sub>2</sub></sub> = 0% and (b) X<sub>H<sub>2</sub></sub> = 40% mixtures at  $\phi = 1.4$ , at 450 K and 1 bar

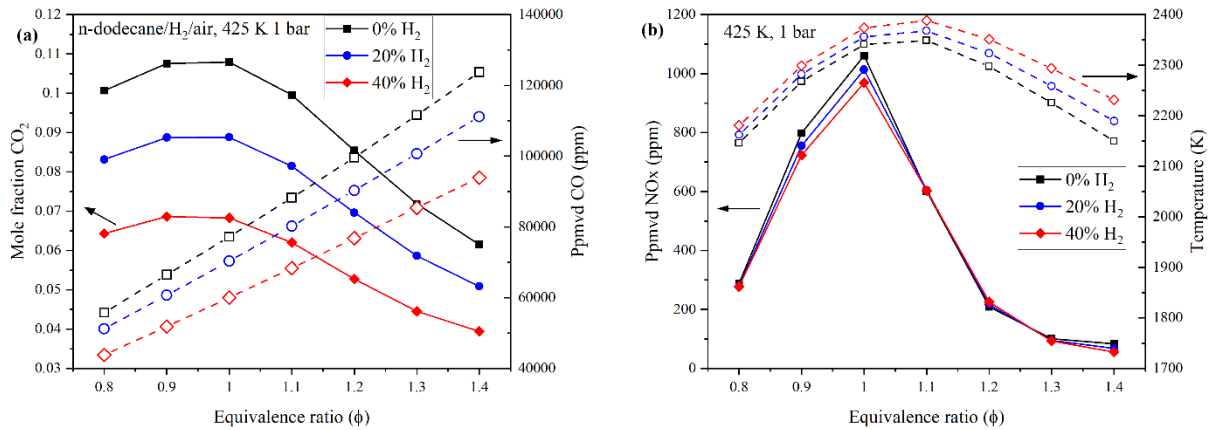


Figure 8.14. Effect of H<sub>2</sub> addition of n-dodecane/H<sub>2</sub>/air mixtures on emissions (a) CO<sub>2</sub> and CO (b) NO<sub>x</sub> at 1 bar 425 K

Figure 8.14 (b) shows the variation of (a) mole fraction of NO<sub>x</sub> and (b) equilibrium flame temperature (EFT) with equivalence ratio at 1 bar, 425 K, X<sub>H<sub>2</sub></sub>=0-40%. As expected, the peak NO<sub>x</sub> emission occurred in a stoichiometric mixture due to the occurrence of high flame temperature. The mole fraction of NO<sub>x</sub> slightly decreased with the addition of H<sub>2</sub>, as the variation in the EFT was quite less. Thermal NO<sub>x</sub> variation was insignificant. The slight reduction in X<sub>NO<sub>x</sub></sub> was essentially due to the shorter residence time of H<sub>2</sub> blended fuel as compared to n-dodecane, which was consistent with the literature [67,138].

## 8.11 Summary

An experimental and numerical study was carried out to understand the effect of H<sub>2</sub> on LBV, flame stability, and emissions of liquid hydrocarbon fuel n-dodecane/air flames with different hydrogen blending levels and a wide range of equivalence ratios at elevated pressures using Spherically expanding flame method. The main conclusions are as follows:

1. Unstretched LBV of the binary mixture increased with an increase in the mole fraction of H<sub>2</sub> at all the investigated operating conditions. The increment in LBV was higher up to a factor of two for stoichiometric mixtures. The addition of H<sub>2</sub> improved the flame propagation rate essentially through a significant improvement in the kinetic effect than an increase in the equilibrium flame temperature, i.e., thermal effect.
2. H<sub>2</sub> blending decreased the magnitude of burned gas Markstein length, which indicated that the flame's response to stretch effects declined. At rich mixtures, the H<sub>2</sub> blending in n-dodecane avoided the transition of a stable flame to an unstable flame due to thermo-diffusive effects at all the studied pressures because of an increase in the

transport properties of the mixture and the associated effective Lewis number ( $Le_{eff} > 1$  also above critical Lewis number).

3. At both elevated pressures and higher  $H_2$  fractions, the on-set instabilities occur earlier due to the effective reduction of flame thickness and the decrement of the effect of flame stretch on burning velocity.
4. Hydrogen blending in n-dodecane increases the OH radical concentration and reduces the  $CO_2$  and CO emission significantly up to more than 55% and 30 respectively. Peak  $NO_x$  emission of 40%  $H_2$  blended n-dodecane mixture produced 8% lower  $NO_x$  than the unblended mixture.

# CHAPTER 9

## ABSOLUTE EGR GAS DILUTION EFFECTS ON OXY-METHANE MIXTURES

Exhaust or Flue Gas Recirculation (EGR) is one of the most efficient ways to reduce pollutant emissions such as  $\text{NO}_x$  and CO in internal combustion engines and other combustion applications. Oxy-fuel combustion with exhaust gas recirculation receives special attention for its potential use for  $\text{CO}_2$  capture and storage. But, the addition of EGR to the combustible mixture alters its thermophysical properties and the reaction rate of the mixtures [43]. Hence, it is essential to understand the effect of adding a single or a mixture of diluents like EGR on combustible properties such as laminar burning velocity. Recently, oxy/ oxy-rich combustion drew a larger interest in industrial furnaces and power generation [139]. Traditionally, oxy-fuel combustion is used in rocket thrust chambers. One of the important advantages of oxy-fuel combustion is its rapid burning rate and better flame stability towards thermo-diffusive effects [84]. Diluted oxygen-enriched combustion results in lesser pollutant emissions due to the lower flame temperatures. The addition of a diluent to a fuel affects its consumption rate due to the: (i) reduction in the chemical energy, flame temperature, and transport properties and it is addressed as a thermal effect, and (ii) participation of diluent in the reaction kinetics may change the reaction paths and also the reaction rate, and it is addressed as a chemical effect [43].

### Operating conditions

Table 9.1. Summary of operating conditions of diluted oxy-methane mixtures

Mixture	Dilution, Z (%)	p (bar)	T (K)	$\phi$	#
(100-Z) % ( $\text{CH}_4 + (2\text{O}_2/\phi)$ ) +Z% $\text{H}_2\text{O}$	40, 50, 60	1	393, 423, 453	0.6-1.4	45
	50	2, 4	423	0.6-1.4	10
(100-Z) % ( $\text{CH}_4 + (2\text{O}_2/\phi)$ ) +Z% $\text{N}_2$	50	1, 2, 4	423	0.6-1.4	15
(100-Z) % ( $\text{CH}_4 + (2\text{O}_2/\phi)$ ) +Z% $\text{CO}_2$	50	1, 2, 4	423	0.6-1.4	15
(100-Z) % ( $\text{CH}_4 + (2\text{O}_2/\phi)$ ) +Z% $\text{N}_2/\text{CO}_2$	50	1	393	0.6-1.4	10
Total number of experiments					95

## Chemical Kinetic mechanism

Table 9.2. List of chemical kinetic mechanisms used for diluted oxy-methane mixtures

Name of the mechanism	Number of Species	Number of reactions
GRIMech 3.0 [113]	53	325
FFCM-1 [114]	36	291

## 9.1 Effects of Steam dilution on flame instability

As mentioned in the introduction, exclusive studies on steam dilution with methane-oxygen mixtures were not available, and hence, the following few sections discuss results on steam dilution. An important strength of the SPF method was the estimation of the burned gas Markstein length,  $L_b$ , which provides the necessary information on the response of the flame towards the real-time effects such as unsteadiness, curvature, and preferential diffusional effects.  $L_b$  was estimated from both NE (Eq. 3.6) and NQ (Eq. 3.7) schemes. Both the schemes predicted very close to each other. Hence, for better readability, only the values obtained using the NE were reported in Figure 9.1. The burned gas Markstein length of diluted methane-oxygen mixtures with steam at 1bar, 393 K, 423 K,  $\phi=0.6-1.4$  and 40-60% steam.

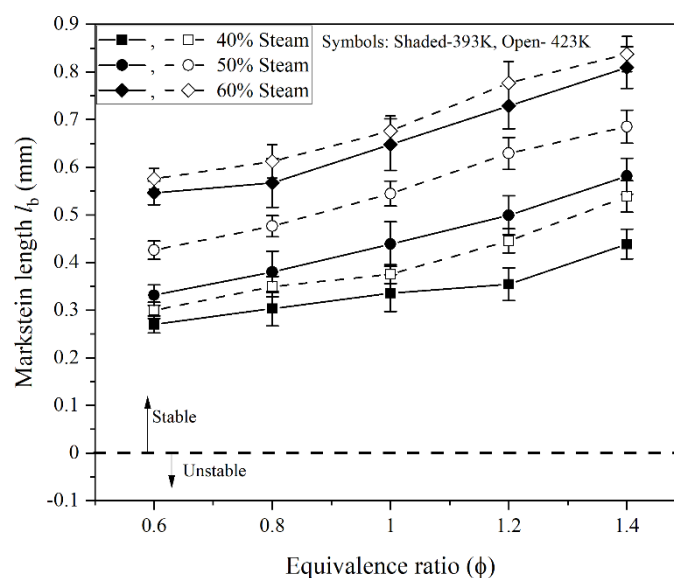


Figure 9.1. Variation of burned gas Markstein length with equivalence ratio for different percentages of steam addition in the mixture at 1bar and 393 K (shaded symbols) 423 K (open symbols) obtained through nonlinear extrapolation method

Figure 9.1 shows that either the dilution fraction of steam increased from 40% to 60% at a given equivalence ratio or a change in equivalence ratio from 0.6-1.4 at a given dilution fraction, and the  $L_b$  remained positive. Its positive value increased in both scenarios indicating that the sensitivity of the flame towards the stretch and the thermo-diffusive effects got enhanced. With an increase in the steam mole fraction, the flame got thicker, and LBV reduced, and as a result, the flame response time to stretch increased, leading to larger values of  $L_b$ . An encouraging observation was that an increase in the positive value of  $L_b$  indicated that the addition of steam had indeed made the mixtures more stable towards the thermo-diffusive instabilities at all the equivalence ratios. The values of effective Lewis number [105] estimated for all the conditions were well greater than their respective critical Lewis numbers, mentioning that the present mixtures were stable to the thermo-diffusive effects and corroborated well with the Markstein length analysis. Figure 9.1 also exhibited an increase in initial temperature from 393 K to 423 K at all the mole fractions of steam and equivalence ratios.  $L_b$  also increased, mentioning that the preheated and diluted flames were more stable even though their sensitivity was raised to stretch effects due to an increase in the Lewis number.

## 9.2 Suppression effects of steam on LBV

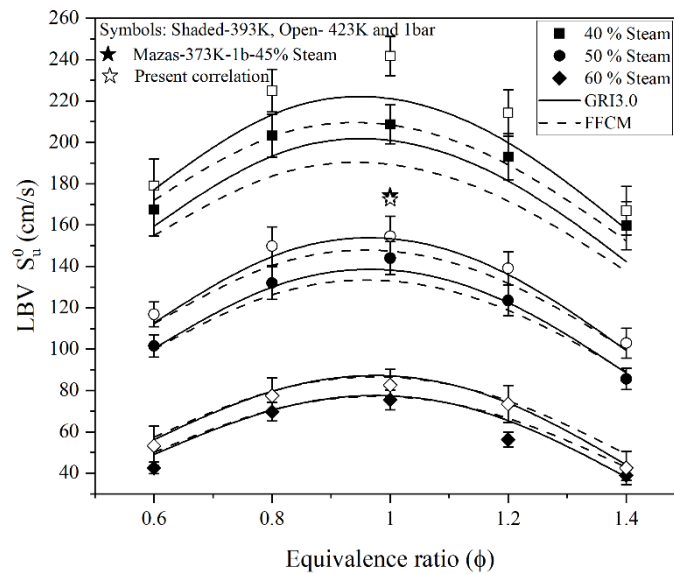


Figure 9.2. Experimental (symbols) and computed (Solid and dotted lines) laminar burning velocities of  $\text{CH}_4/\text{O}_2/\%$  Steam mixtures as a function of the equivalence ratio with various steam percentages at 1 bar 393 K (filled symbols) and 1bar 423 K (Open symbols). Dash lines represent laminar burning velocity data using the FFCM-1 mechanism, and the filled star symbol represents [43] data. The open star symbol indicates the present correlation prediction at the same operating condition

Figure 9.2 displays the unstretched LBV as a function of equivalence ratio at 1 bar, 393–423 K and  $X_{steam} = 40\text{-}60\%$ . The trend of variation in LBV with equivalence ratio at all studied steam dilution fractions and the initial temperature was identical. The steam addition decreased the LBV due to a reduction in flame temperature and kinetic effect [43]. At 40% steam, the predicted values deviated ( $\pm 1.5\%$  to  $\pm 10.8\%$ ) significantly with the measurements. An increase in the preheating temperature raised LBV due to an increase in the flame temperature and other transport properties. Figure 9.2 also shows the LBV of premixed methane-oxygen diluted with 45% steam at 373 K and 1 bar reported by [43] as a shaded star symbol. To compare with their data, a correlation was developed (provided in 9.7) to estimate the LBV for the measured conditions of [43] and reported in Figure 9.2 (unshaded star symbol), and it showed an excellent agreement with their data as the deviation was less than 2 cm/s. Due to the presence of H<sub>2</sub>O in the mixture, the thermal radiation effects may become important. Present mixtures have LBV in the range of 37cm/s – 237 cm/s. Following the similar discussion presented in section 7.8, the effects of radiation on LBV is neglected, and the same discussion was applicable for the mixtures presented in section 9.3 too.

### 9.3 Steam suppression effects on LBV at elevated pressures and temperatures

The variation of unstretched LBV with an equivalence ratio of 50% ( $\text{CH}_4 + (2\text{O}_2 / \phi) + 50\% \text{H}_2\text{O}$ ) at 423 K and  $p=1\text{-}4$  bar is depicted in Figure 9.3.

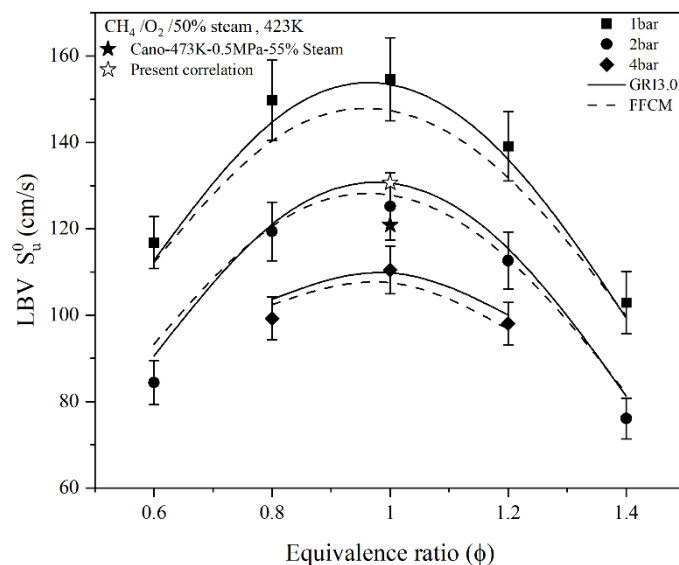


Figure 9.3. Experimental (symbols) and predicted (solid lines) laminar burning velocities of 50% ( $\text{CH}_4 + (2\text{O}_2 / \phi) + 50\% \text{H}_2\text{O}$ ) mixtures at different equivalence ratios, 1-4 bar and 423 K. Continuous line –

GRIMech3.0 dashed line- FFCM-1 and dark shaded star symbol represent [85] data. The open star symbol indicates the prediction using the present correlation at the same operating condition

With an increment in the initial pressure, the LBV decreased due to an increase in the mixture density and dominance of third-body reactions. Figure 9.3 clearly shows that the measured values of LBV showed good agreement with GRIMech3.0 than FFCM-1 at all initial pressures. It also shows the LBV data measured by [85] as an unshaded star symbol at 55% steam, 473 K, and 5 bar, and the estimated LBV from the present correlation as a shaded star symbol, and the deviation between them was 7.48%.

To find out the key elementary reactions that influence the LBV at different pressures, a normalized A-factor sensitivity was analyzed and reported in Figure 9.4.

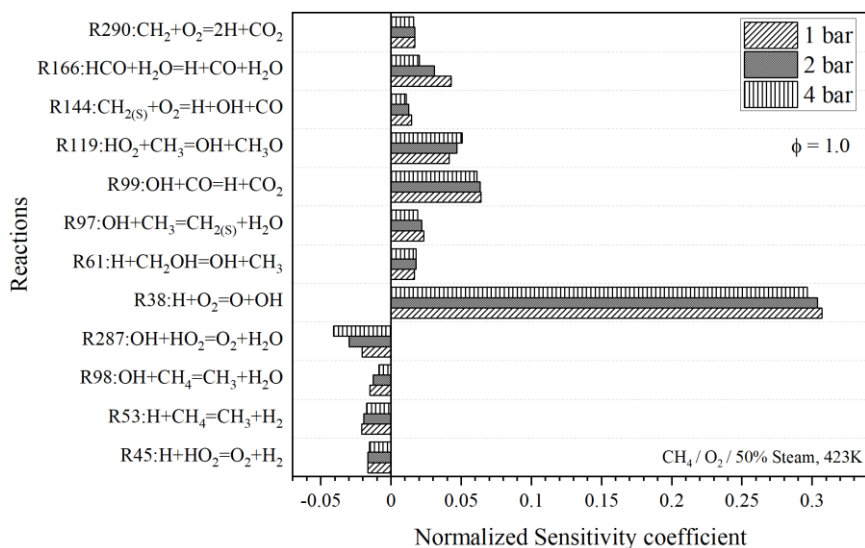


Figure 9.4. Normalized sensitivity coefficients of top ten contributing elementary reactions of Stoichiometric 50% (CH<sub>4</sub> + (2O<sub>2</sub> / $\phi$ )) +50% H<sub>2</sub>O mixtures at initial pressures 1-4 bar and 423 K.

Figure 9.4 depicts that with an increase in the pressure, the positive sensitivity of important chain branching reaction R38 (H+O<sub>2</sub>  $\leftrightarrow$  OH+H), R99, and R166 decreased, whereas the negative sensitivity of recombination reaction R287 (OH+HO<sub>2</sub>  $\leftrightarrow$  O<sub>2</sub>+H<sub>2</sub>O) increased, which indicated that the recombination reactions dominate at higher pressure resulted in the decrement of LBV.

Figure 9.5 shows the effects of equivalence ratio and initial temperature on the LBV of 50% (CH<sub>4</sub> + (2O<sub>2</sub> / $\phi$ )) +50% H<sub>2</sub>O mixtures at 1 bar. As the initial temperature hiked, the LBV also raised due to the increase in the flame temperature and reaction rates. The peak value of LBV was observed at the stoichiometric condition for all levels of steam dilution. At 453 K, the

predicted LBV from both the kinetic schemes was well-off than the measurements. Again, the values of LBV predicted by GRIMEch3.0 showed less deviation than FFCM-1.

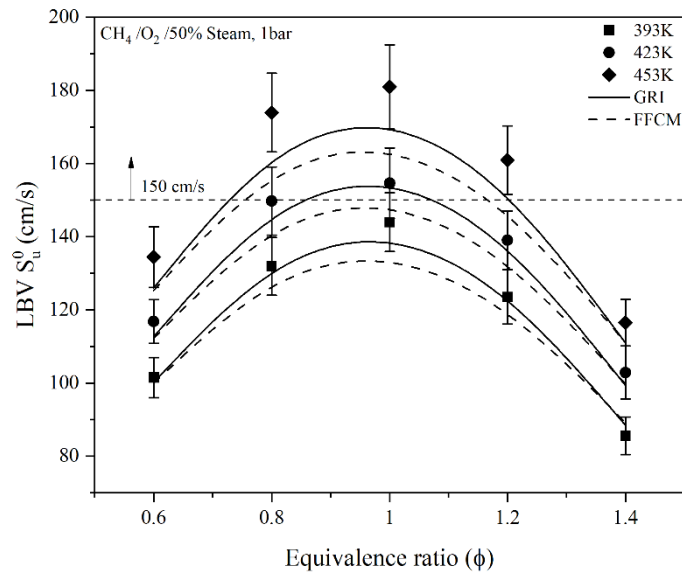


Figure 9.5. Experimental (symbols) and predicted (solid lines) laminar burning velocities of 50% ( $\text{CH}_4 + (2\text{O}_2/\phi) + 50\%$   $\text{H}_2\text{O}$ ) mixtures at different equivalence ratios, 1 bar and 393, 423, and 453 K. Continuous line – GRIMEch3.0, dashed line- FFCM-1

## 9.4 Effects of EGR diluents on flame stability

Figure 9.6 shows the measured values of burned gas Markstein length estimated using NE (Eq. 3.6) for 50% ( $\text{CH}_4 + (2\text{O}_2/\phi) + 50\%$   $\text{H}_2\text{O}/\text{N}_2/\text{CO}_2$ ) at  $\phi = 0.6-1.4$  1 bar, and 423K. All the studied mixtures had positive  $L_b$  indicating that they were stable towards thermos-diffusive effects.

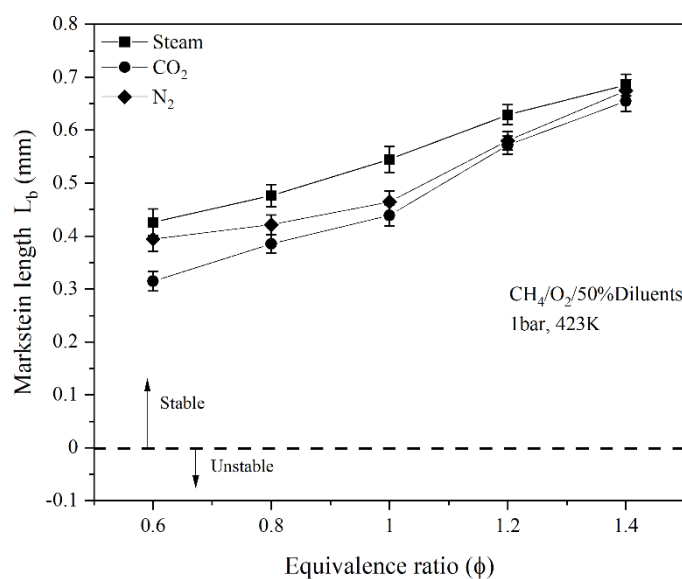


Figure 9.6. Variation in the burned gas Markstein length with an equivalence ratio of 50% ( $\text{CH}_4 + (2\text{O}_2/\phi) + 50\%$  diluents) at 1 bar and 423K

The steam addition increased the flame stability more than N<sub>2</sub> and CO<sub>2</sub> due to the higher values of the effective Lewis number, as reported in Figure 9.7. The CO<sub>2</sub> has the least positive values of  $L_b$ , indicating that it is less sensitive to preferential diffusion effects, but it is also in danger that the mixture may turn unstable with a further increase in the mole fraction of CO<sub>2</sub>. At rich mixture conditions, all the values of Markstein length obtained with all the diluents were close to each other, indicating that the choice of diluent did not have a significant effect on the flame stability, which is good information for EGR mixtures as they would have all these three diluents in tandem. Figure 9.7 shows the comparison of effective (Eq. 3.19)/ critical (Eq. 3.22) Lewis numbers of 50% (CH<sub>4</sub> + (2O<sub>2</sub> / $\phi$ )) +50% H<sub>2</sub>O/N<sub>2</sub>/CO<sub>2</sub> mixtures. All  $Le_{eff} > Le^*$ , indicating stable mixtures and corroborated well with the positive values of  $L_b$  as illustrated in Figure 9.7.

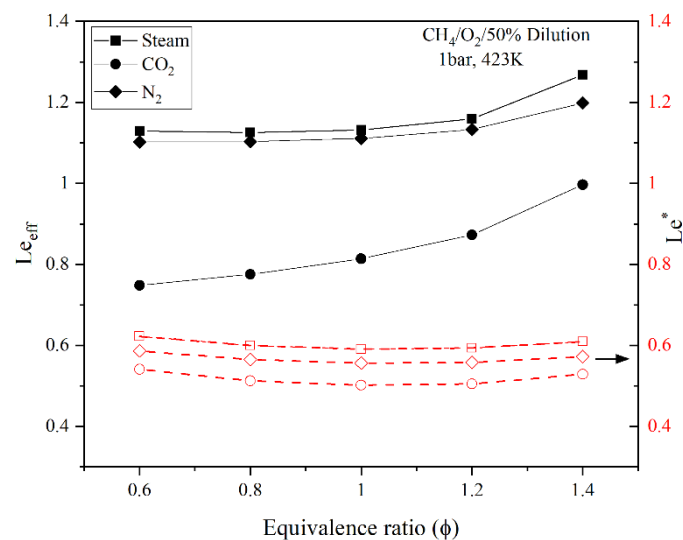


Figure 9.7. Variation in the effective/ critical Lewis number with an equivalence ratio of 50% (CH<sub>4</sub> + (2O<sub>2</sub> / $\phi$ )) +50% diluents at 1 bar and 423K

## 9.5 Effects of different diluents on LBV at a range of equivalence ratios

Figure 9.8 depicts the effect of different diluents on the flame propagation rate of the methane-oxygen mixtures. Maybe for the first time, the suppression effect of all three major diluents, which are part of the exhaust gases on the combustion characteristics of methane, was investigated at an identical mixture and thermodynamic conditions. The addition of 50% diluents to the oxy-methane mixture at all equivalence ratios decreased the LBV substantially: (a) CO<sub>2</sub> – 87% (averaged across all equivalence ratios) as compared to the no diluents, (b) steam-69% and (c) N<sub>2</sub>-61% due to thermal and kinetic effects. To quantify the thermal/ kinetic

effects of each diluent was analysed in CHEMKIN by replacing the original diluent with a fictitious diluent [133]. The thermal effect  $\left(\frac{LBV_{No\ diluent}-LBV_{fictitious\ diluent}}{LBV_{No\ diluent}}\right)$  of methane-oxygen diluted with steam/ N<sub>2</sub>/ CO<sub>2</sub> were 98.51%/ 98.50%/ 90.51% (averaged across all equivalence ratios), respectively. Similarly, the kinetic effect  $\left(\frac{LBV_{fictitious\ diluent}-LBV_{diluent}}{LBV_{No\ diluent}}\right)$  of steam [133] / N<sub>2</sub>/ CO<sub>2</sub> were 1.49%/ 1.50%/ 9.49% respectively at 1 bar and 423 K, and a similar observation was reported by [82] and [140]. The measured LBV data with steam and CO<sub>2</sub> dilution showed an excellent agreement with GRIMech3.0 and FFCM-1, whereas, for N<sub>2</sub>, the matching was relatively poor. Hence, the LBV was also predicted using the modified version of GRIMech3.0 reported in [44], and the simulated values matched well with the 50%N<sub>2</sub> than other diluents. Modified GRI-Mech3.0 predicted well for the faster mixtures. Due to the presence of 50%H<sub>2</sub>O, and 50%CO<sub>2</sub> in the mixture, the thermal radiation effects may become important. Present mixtures have LBV in the range of 50cm/s – 223 cm/s. Following the similar discussion presented in section 7.8, the effects of radiation on LBV is neglected.

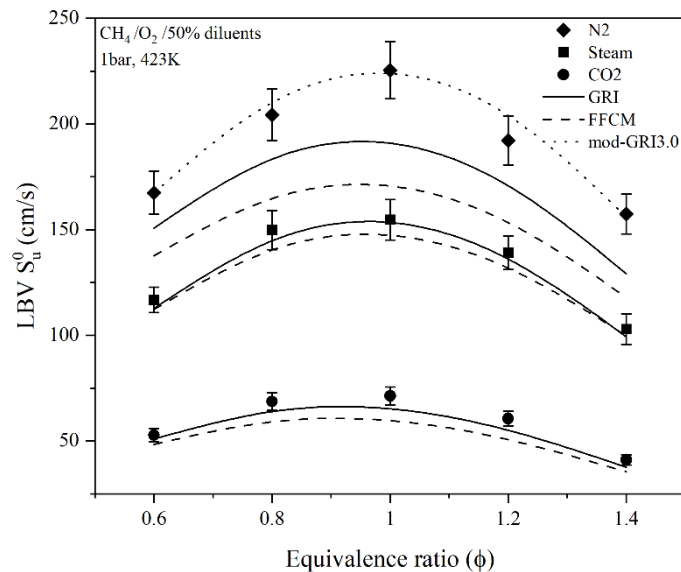


Figure 9.8. Experimental (symbols) and predicted (solid lines) unstretched LBV of 50% (CH<sub>4</sub> + (2O<sub>2</sub> /φ)) +50% diluents mixtures at different equivalence ratios at 1 bar and 423 K Continuous line – GRIMech3.0, dashed line- FFCM-1 and dotted line-modified GRIMech3.0

## 9.6 Effect of different diluents on LBV at elevated thermodynamic conditions

Figure 9.9 (a) shows the unstretched LBV of 50% (CH<sub>4</sub> + (2O<sub>2</sub> /φ)) +50% H<sub>2</sub>O/N<sub>2</sub>/CO<sub>2</sub> as a function of initial temperature and different equivalence ratios. As the initial temperature

increased, the values of LBV increased due to the respective increase in the flame temperature for all diluents. Dilution with  $N_2$  has the least effect on LBV, followed by the moderate effect of steam, and the severe effect of  $CO_2$  matched quite identical to the results of 1 bar & 423 K. Figure 9.9 (a) also shows LBV predicted with GRIMech3.0 and FFCM-1 only at  $\phi=1$  for better readability, and the deviation between the measurements and the simulations was quite higher for the  $N_2$  cases.

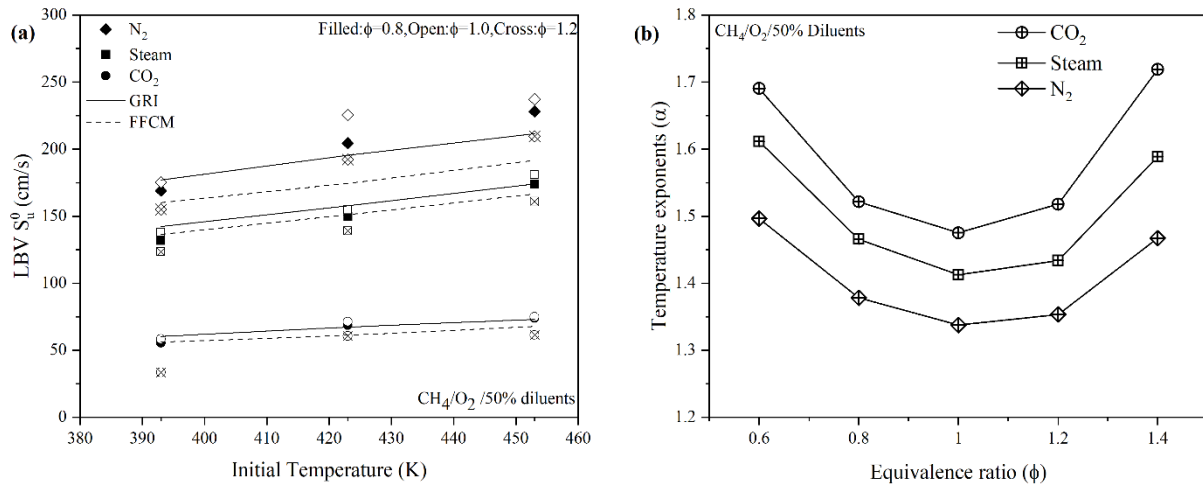


Figure 9.9. (a) Variation in laminar burning velocities of 50% ( $CH_4 + (2O_2/\phi)$ ) + 50% diluents mixtures with initial temperatures and equivalence ratios at 1 bar. (b) Temperature exponent as a function of equivalence ratio. Continuous line – GRIMech3.0, dashed line- FFCM-1

The LBV data presented in Figure 9.9 (a) was fitted with the power-law  $S_{u, T_u, 1bar}^0 = S_{u, 0}^0 \left( \frac{T_u}{T_{u0}} \right)^\alpha$  where  $T_u$  is the initial temperature,  $T_{u0}$  is 300 K,  $S_{u, T_u, 1bar}^0$  is the unstretched LBV at  $T_u$  & 1 bar,  $S_{u, 0}^0$  is the unstretched LBV at 300 K & 1 bar, and  $\alpha$  is the temperature exponent. The temperature coefficients ( $\alpha$ ) are plotted in Figure 9.9 (b). The temperature exponent of  $CO_2$  was the highest, and the  $N_2$  was the lowest. To understand the reason, the Boltzmann energy factor  $exp\left(\frac{-E_A}{R_u T}\right)$  where  $E_A/R_u$  is the activation Temperature and  $T$  is the equilibrium flame temperature was estimated, and it followed the identical nonlinear trend displayed in Figure 9.9 (b) and hence, the variation in  $\alpha$  is primarily due to an exponential dependence of reaction rate on the flame temperature. As FFCM-1 was consistently predicting lower than GRIMech3.0, the predicted flame temperature from them showed a  $\pm 0.14\%$  deviation between them. Later, sensitivity analysis was performed, and it showed that there was a considerable difference (7.79%) observed between GRIMech3.0 and FFCM-1 in some of the key elementary reactions, and that was the reason for the deviation between them.

Figure 9.10 (a) shows the effect of equivalence ratio and pressure (2 bar, 4 bar) on the unstretched LBV for 50%  $(\text{CH}_4 + (2\text{O}_2 / \phi)) + 50\%$   $\text{H}_2\text{O}/\text{N}_2/\text{CO}_2$  at 423K. Mixtures with (a)  $\phi=0.6-1.4$  at 2 bar and (b)  $\phi=0.8-1.2$  at 4 bar were studied. At all elevated pressures, the peak LBV was observed in a stoichiometric mixture. As the pressure raised, the LBV decreased for all the diluents, and the reason was the increase in the mixture density and also the domination of recombination reactions, as discussed in the earlier section, 9.3. Figure 9.10 (b) shows the pressure exponent ( $\beta$ ) obtained from  $S_{u, 300K,p}^o = S_{u,o}^o \left(\frac{p}{p_o}\right)^\beta$  where  $p$  is initial pressure,  $p_o = 1$  bar,  $S_{u, 300K,p}^o$  is the unstretched LBV measured at 300K and  $p$ , and its variation with equivalence

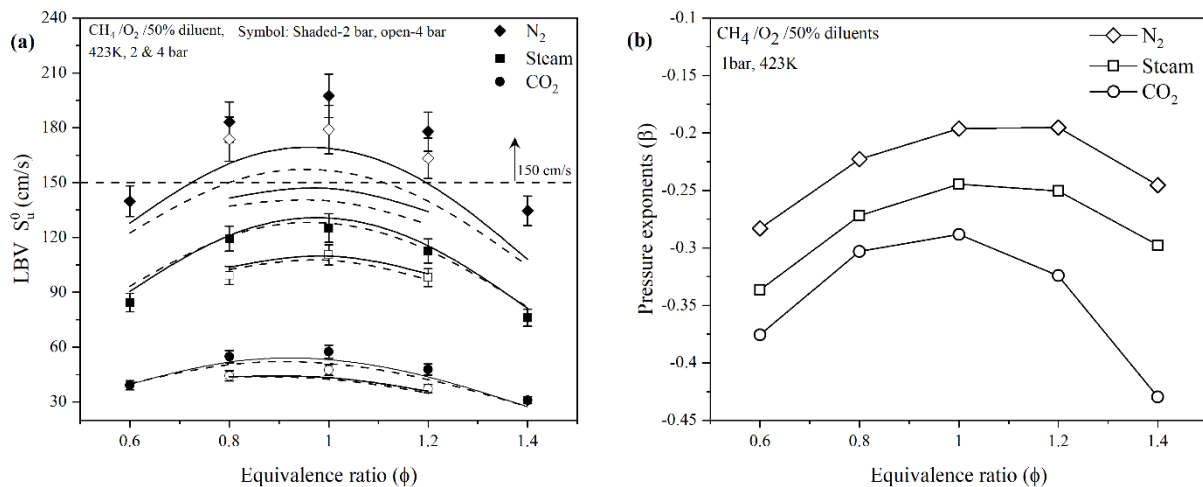


Figure 9.10. (a) Variation in laminar burning velocities of 50%  $(\text{CH}_4 + (2\text{O}_2 / \phi)) + 50\%$  diluents" mixtures with an equivalence ratio at 423 K and 2 bar & 4 bar. (b): Pressure exponent as a function of equivalence ratio. Continuous line – GRIMech3.0, dashed line- FFCM-1

ratio. The mixture with a larger kinetic effect and slower flames was more sensitive to pressure. Section 9.5 mentioned that the kinetic effect of  $\text{N}_2$  & steam were nearly the same, but the steam diluted flames were slower than the  $\text{N}_2$  dilution due to low values of flame temperature and diffusional properties. In all aspects, the presence of  $\text{CO}_2$  in the mixture made it more sensitive towards pressure and temperature.

## 9.7 LBV correlation oxy-methane-steam mixtures

From the range present elevated pressure, temperature, and equivalence ratio of methane-oxygen-steam mixtures laminar burning velocity measurements, a correlation was developed by using the [30] method. The proposed correlation includes the equivalence ratio and steam diluent terms to generalize the fit equation.

$$S_u^0 = b_1 \times \left( \frac{T_u}{T_{u,0}} \right)^\alpha \times \left( \frac{P}{P_0} \right)^\beta \times (b_2 + b_3\phi + b_4\phi^2) \times (b_5 + b_6X + b_7X^2)$$

Where,  $b_1 - b_7$  are the nonlinear regression model coefficients,  $\alpha$  temperature exponent,  $\beta$  pressure exponent,  $\phi$  equivalence ratio, and  $X$  is the dilution molar fraction. For steam conditions, the reference conditions are  $T_{u,0} = 373 \text{ K}$  and  $P_0 = 1 \text{ bar}$ . Coefficients  $b_1 - b_7$  were adjusted to minimize the root mean square error (RMSE). The RMSE was defined as the standard deviation of the residuals, which is the difference between the experimental data and the  $S_u^0$  values predicted by the correlation. The model coefficients were optimized with the `fmincon` function (an optimization function in MATLAB). In the present work, the objective function was set as the RMSE of the residuals. The convergence criteria

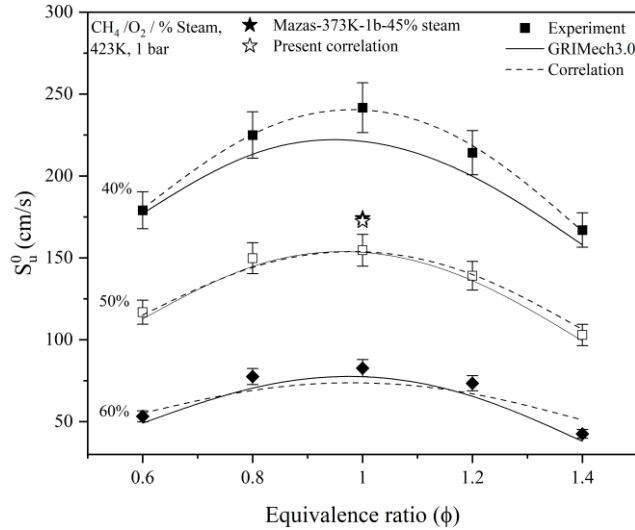


Figure 9.11. Experimental (symbols) and computed (Solid and dotted lines) laminar burning velocities of  $(100-z) \% (\text{CH}_4+2\text{O}_2/\phi) + z\% \text{H}_2\text{O}$  where  $z$  was varied from 40-60% steam at different equivalence ratios, 1bar and 423 K. Continuous/dashed lines correspond to GRIMech3.0, and present correlation fits and filled star symbol represents [43] data. The open star symbol indicates the present correlation prediction at referred operating condition

was defined as a change in the objective variable less than  $1e^{-6}$  between two consecutive iterations. The optimized correlation coefficients are  $b_1 = 118.55$ ,  $\alpha = 1.67$ ,  $\beta = -0.26$ ,  $b_2 = -1.28$ ,  $b_3 = 5.92$ ,  $b_4 = -3.02$ ,  $b_5 = 2.81$ ,  $b_6 = -5.01$  and  $b_7 = 1.41$ . with an RMSE of 5.75 cm/s. The maximum deviation between the experimental and correlation results was detected as 8.44 cm/s at 1 bar, 423 K,  $\phi = 1.4$ , and  $X = 60\% \text{ Steam}$ .  $S_u^0$  values provided by the correlation were plotted in Figure 9.11.  $S_u^0$  predictions of the correlation are highly consistent with the experimental

data. However, the little discrepancy can be observed at very rich equivalence ratios and extreme dilution conditions.

## 9.8 Summary

The present work investigated the effects of the addition of steam/ N<sub>2</sub>/ CO<sub>2</sub> on the laminar burning velocity and the burned gas Markstein length of methane-oxygen mixtures at  $T_u=393$ -453 K,  $p=1$ -4 bar, and  $\phi =0.6$  to 1.4. Important conclusions were:

- (1) The addition of the steam decreased the unstretched LBV due to the predominant thermal effect than the kinetic effect.
- (2) Burned gas Markstein length remained positive, and it increased with an increment in the steam dilution fraction due to the respective increase in the effective Lewis number
- (3) The addition of steam/ N<sub>2</sub>/ CO<sub>2</sub> to the premixed CH<sub>4</sub>-O<sub>2</sub> mixture led to a reduction in the LBV. The suppression effects were the highest for CO<sub>2</sub> and followed by steam and nitrogen at a given set of initial conditions due to both thermal and kinetic effects.
- (4) The flame was stable to all the diluents in the presently studied conditions. Markstein lengths were the highest for steam and followed by N<sub>2</sub> and CO<sub>2</sub> due to higher effective Lewis number.
- (5) The temperature/ pressure exponents of steam/ N<sub>2</sub>/ CO<sub>2</sub> showed that slower flames were more sensitive to both pressure and temperature.
- (6) From the entire study, it can be concluded that predictions with GRIMech3.0 closely matched with that of the experiments if the magnitude of LBV was less than 150 cm/s than the FFCM-1 kinetic scheme. For mixtures having LBV higher than 150 cm/s, the modified GRIMech3.0 worked fine.

# CHAPTER 10

## CONCLUSIONS

The objective of the present work was to investigate in detail the unstretched LBV and flame stability characteristics of n-dodecane, an important species of surrogate fuels, under various mixture ratios and operating conditions using a freely expanding spherical flame method based on an extensive literature review. A new rig comprising a cuboidal combustor with optical access, heating system, fuel injection system, and high-speed shadowgraph system was used to generate freely expanding spherical flames and also to record it. The post-processing was achieved using in-house MATLAB programs to find the unstretched LBV and burned gas Markstein length.

The following four combustible mixtures (a)  $nC_{12}H_{26} + 4.76$  air (b) 35% ( $nC_{12}H_{26} + O_2$ ) + 65%  $N_2 / CO_2 / H_2O$ , (c) (1-Z) %  $nC_{12}H_{26} + Z$  %  $H_2$  reacting in air, Z=0 to 40 %, and (d) (100-X) % ( $CH_4 + (2O_2/\phi)$ ) + X%  $H_2O / CO_2 / N_2$ ;  $X_{H_2O} = 40-60\%$ ,  $X_{CO_2} = 50\%$ ,  $X_{N_2} = 50\%$ , were investigated at normal/ elevated, initial pressures and initial temperatures. The unstretched LBV and burned gas Markstein length were measured, and the effects of all major EGR diluents such as  $N_2$ ,  $CO_2$ , and steam, on LBV and flame stability were examined for the first time at an identical operating condition. The main conclusions of all the four mixtures are summarised below:

### 10.1 n-dodecane-air mixtures

**Study-1:** This study investigated the LBV and stability aspects of premixed n-dodecane-air mixtures at  $p=1-4$  bar,  $T = 400-450$  K, and equivalence ratio = 0.8-1.4 using freely expanding spherical flame method and 1D planar flame simulations.

- The unstretched LBV of premixed n-dodecane-air estimated by the linear extrapolation scheme showed a maximum deviation of 7.42% at  $\phi=1.4$  as compared to that of a non-linear stretch extrapolation due to the non-unity Lewis number,
- Unstretched LBV of premixed n-dodecane-air mixtures increased with an increase in the initial temperature due to a hike in flame temperature and mixture diffusivity. It decreased with a hike in initial pressure due to higher mixture density and dominance of third-body reactions.
- The predicted LBV using Jetsurf2.0 and You et al. mechanisms agreed well with the experimental values well within the experimental uncertainties, whereas LBV

estimated by Polimi-1410 showed a significant deviation with the measurements to a tune of 28%, especially at elevated operating conditions.

- The thermo-diffusive instability parameter burned gas Markstein length  $L_b$  showed destabilization for rich mixtures at  $\phi=1.4$  when (a)  $T < 450$  K and independent of pressures, due to thicker & slower flames, and longer stretch duration, (b)  $p \geq 1$  bar and  $T=425$  K, due to a significant reduction in the flame thickness. The comparison of kinetic and stretch response times of all the unstable mixtures indicated that a thinner flame having smaller Karlovitz number was affected by thermo-diffusive instability.
- The presence of preferential diffusion of  $O_2$  from the preheat zone to the reaction zone was demonstrated by analysing the predicted flame structure of premixed n-dodecane-air mixture at  $\phi=1.4$ . It showed that the deficient reactant,  $O_2$  diffused faster into the reaction zone than n-dodecane resulting in an accumulation of n-dodecane in the preheat zone, and hence, the local equivalence ratio at the preheat zone was 1.63 against the global equivalence ratio of 1.4.
- The effective and critical Lewis numbers estimated through the BM model only predicted the flame transition from stable to unstable at rich equivalence ratio accurately and corroborated well with the measurements.
- The onset of hydrodynamic instability (small cells appeared uniformly on the flame surface) was delayed/ preponed for a stable/ unstable mixture having positive/ negative  $L_b$ . It depends strongly on the flame thickness. A thicker flame delayed the onset of hydrodynamic instability for a longer duration as compared to that of a thinner flame.

## 10.2 Oxy-n-dodecane mixtures

**Study-2:** The mixture considered in this work was  $(100-Z)\%$   $(n-C_{12}H_{26}+(18.5 O_2/\phi)) + Z\%$   $(N_2/CO_2/H_2O)$  mixtures at 400-450 K, 1-4 bar,  $\phi=0.6-1.4$ , and Z varied for (a)  $N_2=55-75\%$ , (b)  $CO_2/ H_2O = 65\%$  to address the effect of dilution on LBV and flame stability with different diluents independently at identical operating conditions. The equilibrium flame temperatures of the above mixtures were in the range of 2100K to 2800K. This is also the first time where the LBV was measured for mixtures having such high-flame temperatures. The major outcomes of this study were listed below:

- The highest LBV of 233 cm/s was measured for stoichiometric 45% $(n-C_{12}H_{26}+(18.5O_2/\phi)) + 55\%N_2$  mixture at 1 bar and 450 K. The LBV increased by nearly

three times, as the  $X_{N_2}$  reduced from 75%-55%, due to an increase in the chemical energy, equilibrium flame temperature, and reaction rates.

- The normalized net heat release rate and mole fractions  $X_{(H+O+OH)}$  varied exponentially with equilibrium flame temperature whereas LBV followed the power law for different nitrogen fractions due to the non-monotonic increment of thermal diffusivity of the added nitrogen.
- Only You et al. chemistry predicted LBV that matched with experimental data. JetsurF2.0 / PoliMi-1410 mechanisms under / over predicted the LBV, which indicated that the mechanism validated with conventional air combustion measurements needed a revision for oxy-fuel mixtures.
- Dilution of oxy-n-dodecane mixtures with  $N_2$ /  $CO_2$ / steam decreased the unstretched LBV significantly due to a decrease in the heating value of the mixture and subsequent reduction in the temperature and the kinetic activities. The predicted LBV with the contemporary kinetic schemes of mixtures having higher magnitudes of LBV significantly deviated with the measurements.
- The flame stability of mixtures having high flame temperatures increased significantly against the thermo-diffusive effects due to an increase in heat diffusivities. In addition, unlike n-dodecane-air mixtures, the n-dodecane- $O_2$  mixtures were quite stable at rich equivalence ratios, even at elevated initial pressure conditions.
- The contribution of thermal and kinetic effects of different diluents were estimated through simulations, and the overall decrease in the LBV due to the addition of  $N_2$ /  $H_2O$ /  $CO_2$  as compared to an undiluted mixture was 60%/ 68%/ 87%, which was due to thermal effect: 96%/ 93%/ 67%, and chemical effect: 4%/ 7%/ 33%.
- Among different diluents, n-dodecane- $O_2$ -steam mixtures were highly stable than  $N_2$  and  $CO_2$  owing to higher thermal diffusivity and the associated  $Le$  number. The pressure exponents of diluted oxy-n-dodecane mixtures were insensitive to initial pressure than n-dodecane-air mixtures.

### 10.3 Hydrogen blended n-dodecane-air mixtures

**Study-3:** The effect of addition of hydrogen on the LBV of a binary mixture of n-dodecane- $H_2$  was also studied. The binary fuel was  $\{(1-Z) \% nC_{12}H_{26} + Z\% H_2\}$ , and it reacted with air at 1-4 bar and 425 K, where the hydrogen fraction was varied from 0 – 40% (by volume) in n-dodecane. The key observations are listed below:

- An interesting aspect was that the stretched flame speed of n-dodecane-H<sub>2</sub> mixture showed a linear variation with the stretch rate, and the unstretched flame speed estimated by the linear/ nonlinear extrapolation schemes, were same which contradicted with that of n-dodecane mixture which showed a strong non-linear behaviour between flame speed and stretch rate.
- LBV increased with the addition of H<sub>2</sub> at all the studied operating conditions up to a factor of two at stoichiometric condition. The addition of H<sub>2</sub> tremendously increased the reaction rates of the binary fuel whereas only a minor increase in the equilibrium flame temperature was observed.
- H<sub>2</sub> addition decreased the magnitude of Markstein length, which indicated that the response of flame to stretch effects got reduced. Importantly, H<sub>2</sub> blending makes the flame stable at rich equivalence ratio at all the studied pressures due to its high mobility, and hence,  $Le_{eff}$  was always greater than the critical Lewis number.
- At both elevated pressures and higher H<sub>2</sub> fractions, the on-set instabilities occur earlier due to the effective reduction of flame thickness and the decrement of the effect of flame stretch on burning velocity.

## 10.4 Oxy-methane mixtures

**Study-4:** The absolute dilution effect of various exhaust recirculation gases were studied on (100-X) % (CH<sub>4</sub> + (2O<sub>2</sub>/φ)) + X% H<sub>2</sub>O/CO<sub>2</sub>/N<sub>2</sub>; X<sub>H<sub>2</sub>O</sub> = 40–60%, X<sub>CO<sub>2</sub></sub> = 50%, X<sub>N<sub>2</sub></sub> = 50%, mixtures at 1 -4 bar and 393 – 453 K. The major conclusion obtained from this work are presented below:

- ✓ The addition of steam/ N<sub>2</sub>/ CO<sub>2</sub> to the premixed CH<sub>4</sub>-O<sub>2</sub> mixture led to the reduction in unstretched LBV, and the suppression effects were highest for CO<sub>2</sub>, and it was followed by steam and nitrogen due to both thermal and kinetic effects at a given set of initial conditions.
- ✓ Burned gas Markstein length remained positive for oxy-methane diluted mixtures, and it increased with an increment of steam dilution fraction due to the respective increase in the effective Lewis number and flame thickness.
- ✓ The widely recognized GRIMech3.0 mechanism was not efficient in predicting the LBV of oxy-fuel diluted mixtures if the magnitude of the burning velocity of the mixture was higher than 150 cm/s. FFCM-1 was consistently under-predicted at all conditions. Therefore, chemical mechanisms developed for the oxidation of CH<sub>4</sub>/ air

mixtures failed to predict accurately the LBV of oxy-fuel mixtures. The temperature/pressure exponents of steam/ N<sub>2</sub>/ CO<sub>2</sub> showed that slower flames were more sensitive to both pressure and temperature.

## 10.5 The overall contribution of present work

- The present work published a large volume of accurate, unstretched LBV and burned gas Markstein length data of n-dodecane and methane measured using a freely expanding spherical flame method under various categories and at elevated thermodynamic conditions. The reported large dataset, especially at elevated thermodynamic conditions, will be useful to kinetic scheme developers working in long-chain liquid fuels.
- Absolute dilution effects of all major EGR components (steam, CO<sub>2</sub>, N<sub>2</sub>) at identical thermodynamic and mixture conditions were published for the first time in the literature for lower alkane-methane and heavy hydrocarbon: n-dodecane.
- Thermo-diffusive instability effects of n-dodecane/air, n-dodecane/O<sub>2</sub>, and n-dodecane/H<sub>2</sub>/air mixtures were newly reported.
- A compact correlation was developed for finding LBV of oxy-methane mixtures as a function of equivalence ratio and dilution fraction for different diluents and successfully validated with existing literature and simulation predictions of up to 50 bar pressures with a deviation of less than 7%.

## 10.6 Application potential of the present work

- With the presented large range of accurate LBV data, one can optimize the existing chemical kinetic mechanisms in order to improve its accuracy in predicting LBV at different mixture compositions.
- The wide range of EGR diluted LBV data, and the presented LBV correlation as a function of equivalence ratio and dilution fraction will be useful for industrial gas turbine operations.
- LBV is used in the design of new fuels to suit a particular application. This data shall help in designing new fuels too.

## **10.7 Future scope of the present work**

- Development of a compact and reliable surrogate fuel for kerosene and Jet fuels.
- With the successful execution of primary experiments of various classes of liquid fuels (Alcohol-ethanol, Ether-DEE, Alkane-methane, ethane, propane, n-decane, dodecane, MCH, Ester-methyl formate, Aromatics-Propyl benzene, and Hydrogen blended studies), the government policy of ethanol blended petrol (EBP) liquids and its combustion characteristics can be estimated. The combustion characteristics of upcoming methanol blended transport fuels need to be studied.
- To increase the energy density, various particles in smaller concentrations were added to various liquid fuels. The impact of suspended particles on the combustion characteristics of the liquid fuel has to be analysed.

## References

- [1] OPEC Monthly Oil Market Report. Organ Pet Export Ctries 2021;1:1–93.
- [2] Dagaut P, Cathonnet M. The ignition, oxidation, and combustion of kerosene: A review of experimental and kinetic modeling. *Prog Energy Combust Sci* 2006;32:48–92.
- [3] Battin-Leclerc F. Detailed chemical kinetic models for the low-temperature combustion of hydrocarbons with application to gasoline and diesel fuel surrogates. *Prog Energy Combust Sci* 2008;34:440–98.
- [4] Pitz WJ, Cernansky NP, Dryer FL, Egolfopoulos FN, Farrell JT, Friend DG, et al. Development of an experimental database and chemical kinetic models for surrogate gasoline fuels. SAE Tech Pap 2007.
- [5] Chen C, Yang S. The energy demand and environmental impacts of oxy-fuel combustion vs. post-combustion capture in China. *Energy Strateg Rev* 2021;38:100701.
- [6] Si J, Wang G, Shu Z, Liu X, Wu M, Zhu R, et al. Experimental and Numerical Study on Moderate or Intense Low-Oxygen Dilution Oxy-Combustion of Methane in a Laboratory-Scale Furnace under N<sub>2</sub>, CO<sub>2</sub>, and H<sub>2</sub>O Dilutions. *Energy and Fuels* 2021;35:12403–15.
- [7] Chen Q, Wang X, Gong J, Xu S. Numerical investigation of the combustion characteristics of hydrogen and oxygen in a microthruster. *Int J Hydrogen Energy* 2022;47:5627–37.
- [8] Allam R, Martin S, Forrest B, Fetvedt J, Lu X, Freed D, et al. Demonstration of the Allam Cycle: An Update on the Development Status of a High Efficiency Supercritical Carbon Dioxide Power Process Employing Full Carbon Capture. *Energy Procedia* 2017;114:5948–66.
- [9] Tan Q, Hu Y, Tan Z. Study on diesel low-nitrogen or nitrogen-free combustion performance in constant volume combustion vessels and contributory. *Atmosphere (Basel)* 2021;12.
- [10] Wu ZJ, Yu X, Fu LZ, Deng J, Hu ZJ, Li LG. A high efficiency oxyfuel internal combustion engine cycle with water direct injection for waste heat recovery. *Energy* 2014;70:110–20.

- [11] Yi F, Axelbaum RL. Oxy-combustion of low-volatility liquid fuel with high water content. *Energy and Fuels* 2015;29:1137–42.
- [12] India Energy Outlook 2021. *India Energy Outlook 2021* 2021.
- [13] Mazloomi K, Gomes C. Hydrogen as an energy carrier: Prospects and challenges. *Renew Sustain Energy Rev* 2012;16:3024–33.
- [14] Tang C, Zhang Y, Huang Z. Progress in combustion investigations of hydrogen enriched hydrocarbons. *Renew Sustain Energy Rev* 2014;30:195–216.
- [15] Violi A, Yan S, Eddings EG, Sarofim AF, Granata S, Faravelli T, et al. Experimental formulation and kinetic model for JP-8 surrogate mixtures. *Combust Sci Technol* 2002;174:399–417.
- [16] Stephen Turns. *An Introduction to Combustion: Concepts and Applications*. McGraw-Hill Education; 2013.
- [17] ANSYS CHEMKIN R1 ANSYS reaction design, San Diego, 2020.
- [18] Law CK, Faeth GM. Opportunities and challenges of combustion in microgravity. *Prog Energy Combust Sci* 1994;20:65–113.
- [19] Law CK, Sung CJ. Structure, aerodynamics, and geometry of premixed flamelets. *Prog Energy Combust Sci* 2000;26:459–505.
- [20] Natarajan J, Lieuwen T, Seitzman J. Laminar flame speeds of H<sub>2</sub>/CO mixtures: Effect of CO<sub>2</sub> dilution, preheat temperature, and pressure. *Combust Flame* 2007;151:104–19.
- [21] Egolfopoulos FN, Cho P, Law CK. Laminar flame speeds of methane-air mixtures under reduced and elevated pressures. *Combust Flame* 1989;76:375–91.
- [22] Goswami M, Derks SCR, Coumans K, Slikker WJ, de Andrade Oliveira MH, Bastiaans RJM, et al. The effect of elevated pressures on the laminar burning velocity of methane+air mixtures. *Combust Flame* 2013;160:1627–35.
- [23] Akram M, Kumar S. Experimental studies on dynamics of methane-air premixed flame in meso-scale diverging channels. *Combust Flame* 2011;158:915–24.
- [24] Keshavamurthy. *Combustion Characteristics of Multicomponent Fuel-air Mixtures*. Indian Institute of Technology, Delhi, 2005.

- [25] Egolfopoulos FN, Hansen N, Ju Y, Kohse-Höinghaus K, Law CK, Qi F. Advances and challenges in laminar flame experiments and implications for combustion chemistry. *Prog Energy Combust Sci* 2014;43:36–67.
- [26] Konnov AA, Mohammad A, Kishore VR, Kim N II, Prathap C, Kumar S. A comprehensive review of measurements and data analysis of laminar burning velocities for various fuel+air mixtures. *Prog Energy Combust Sci* 2018;68:197–267.
- [27] Gerstein M, Levine O, Wong EL. Flame Propagation. II. The Determination of Fundamental Burning Velocities of Hydrocarbons by a Revised Tube Method. *J Am Chem Soc* 1951;73:418–22.
- [28] Lewis B, von Elbe G, LEWIS B, VON ELBE G. *Combustion, Flames and Explosions of Gases*. 1987.
- [29] Prathap C, Ray A, Ravi MR. Investigation of nitrogen dilution effects on the laminar burning velocity and flame stability of syngas fuel at atmospheric condition. *Combust Flame* 2008;155:145–60.
- [30] Duva BC, Wang YC, Chance LE, Toulson E. Correlations for the laminar burning velocity and burned gas Markstein length of methane-air mixtures diluted with flue gases at high temperatures and pressures. *Fuel* 2020;281:118721.
- [31] Johnston RJ, Farrell JT. Laminar burning velocities and Markstein lengths of aromatics at elevated temperature and pressure. *Proc Combust Inst* 2005;30:217–24.
- [32] Far KE, Parsinejad F, Metghalchi H. Flame structure and laminar burning speeds of JP-8/air premixed mixtures at high temperatures and pressures. *Fuel* 2010;89:1041–9.
- [33] Singh D, Nishiie T, Qiao L. Experimental and kinetic modeling study of the combustion of n-decane, Jet-A, and S-8 in laminar premixed flames. *Combust Sci Technol* 2011;183:1002–26.
- [34] Kumar K, Sung CJ. Laminar flame speeds and extinction limits of preheated n-decane/O<sub>2</sub>/N<sub>2</sub> and n-dodecane/O<sub>2</sub>/N<sub>2</sub> mixtures. *Combust Flame* 2007;151:209–24.
- [35] Ji C, You X, Holley AT, Wang YL, Egolfopoulos FN, Wang H. Propagation and extinction of mixtures of air with n-Dodecane, JP-7, and JP-8 jet fuels. 46th AIAA Aerosp Sci Meet Exhib 2008:1–13.

- [36] Ji C, Dames E, Wang YL, Wang H, Egolfopoulos FN. Propagation and extinction of premixed C5-C12 n-alkane flames. *Combust Flame* 2010;157:277–87.
- [37] Hui X, Sung CJ. Laminar flame speeds of transportation-relevant hydrocarbons and jet fuels at elevated temperatures and pressures. *Fuel* 2013;109:191–200.
- [38] Richter S, Raida MB, Naumann C, Riedel U. Measurement of the Laminar Burning Velocity of Neat Jet Fuel Components. *Proc World Congr Momentum, Heat Mass Transf* 2016:3–7.
- [39] Le Dortz R, Strozzi C, Sotton J, Bellenoue M. Evaluation of the surrogates capacity to reproduce the laminar burning velocities and the sensitivity to stretching of a commercial kerosene under constant volume combustion conditions. *Fuel* 2021;287:119426.
- [40] Naik C V., Puduppakkam K V., Modak A, Meeks E, Wang YL, Feng Q, et al. Detailed chemical kinetic mechanism for surrogates of alternative jet fuels. *Combust Flame* 2011;158:434–45.
- [41] JetSurF, version2.0.
- [42] Cai X, Wang J, Zhang W, Xie Y, Zhang M, Huang Z. Effects of oxygen enrichment on laminar burning velocities and Markstein lengths of CH<sub>4</sub>/O<sub>2</sub>/N<sub>2</sub> flames at elevated pressures. *Fuel* 2016;184:466–73.
- [43] Mazas AN, Fiorina B, Lacoste DA, Schuller T. Effects of water vapor addition on the laminar burning velocity of oxygen-enriched methane flames. *Combust Flame* 2011;158:2428–40.
- [44] Khan AR, Anbusaravanan S, Kalathi L, Velamati R, Prathap C. Investigation of dilution effect with N<sub>2</sub>/CO<sub>2</sub> on laminar burning velocity of premixed methane/oxygen mixtures using freely expanding spherical flames. *Fuel* 2017;196:225–32.
- [45] Prathap C, Ray A, Ravi MR. Effects of dilution with carbon dioxide on the laminar burning velocity and flame stability of H<sub>2</sub>-CO mixtures at atmospheric condition. *Combust Flame* 2012;159:482–92.
- [46] Tang CL, Huang ZH, Law CK. Determination, correlation, and mechanistic interpretation of effects of hydrogen addition on laminar flame speeds of hydrocarbon-air mixtures. *Proc Combust Inst* 2011;33:921–8.

- [47] Okafor EC, Nagano Y, Kitagawa T. Experimental and theoretical analysis of cellular instability in lean H<sub>2</sub>-CH<sub>4</sub>-air flames at elevated pressures. *Int J Hydrogen Energy* 2016;41:6581–92.
- [48] Jiang X, Zhang R, Deng F. Effects of equivalence ratio and blending ratio on the ignition delays of n-pentane/hydrogen mixtures under engine relevant pressure. *Fuel* 2021;288:119669.
- [49] Eckart S, Pizzuti L, Fritsche C, Krause H. Experimental study and proposed power correlation for laminar burning velocity of hydrogen-diluted methane with respect to pressure and temperature variation. *Int J Hydrogen Energy* 2022;47:6334–48.
- [50] Berwal P, Solagar S, Kumar S. Experimental investigations on laminar burning velocity variation of CH<sub>4</sub>+H<sub>2</sub>+air mixtures at elevated temperatures. *Int J Hydrogen Energy* 2022;47:16686–97.
- [51] Xiao P, Wu H, Wang Z, Zhang S, Lee C fon, Wang Z, et al. Experimental and kinetic investigation on the effects of hydrogen additive on laminar premixed methanol–air flames. *Int J Hydrogen Energy* 2019;44:22263–81.
- [52] Zhou J, Lu C, Xu C, Yu Z. Experimental and Numerical Study on the Effect of Hydrogen Addition on Laminar Burning Velocity of Ethanol–Air Mixtures. *Energies* 2022;15.
- [53] Yu H, Hu E, Cheng Y, Yang K, Zhang X, Huang Z. Effects of hydrogen addition on the laminar flame speed and markstein length of premixed dimethyl ether-air flames. *Energy and Fuels* 2015;29:4567–75.
- [54] Zhang P, Kang Y, Huang X, Peng S. Study on effect of hydrogen addition on extinction dynamics of dimethyl ether spherical diffusion flame. *Int J Hydrogen Energy* 2020;45:11350–67.
- [55] Ravi S, Petersen EL. Laminar flame speed correlations for pure-hydrogen and high-hydrogen content syngas blends with various diluents. *Int J Hydrogen Energy* 2012;37:19177–89.
- [56] Yao SR, Shih HY. Dilution effects analysis on NO<sub>x</sub> emissions of opposed-jet H<sub>2</sub>/CO syngas diffusion flames. *Int J Hydrogen Energy* 2022;47:15896–908.
- [57] Zhang GP, Li GX, Li HM, Lv JC. Effect of diluent gas on propagation and explosion characteristics of hydrogen-rich syngas laminar premixed flame. *Energy*

- 2022;246:123370.
- [58] Shrestha KP, Lhuillier C, Barbosa AA, Brequigny P, Contino F, Mounaïm-Rousselle C, et al. An experimental and modeling study of ammonia with enriched oxygen content and ammonia/hydrogen laminar flame speed at elevated pressure and temperature. *Proc Combust Inst* 2021;38:2163–74.
- [59] Chen X, Liu Q, Jing Q, Mou Z, Shen Y, Huang J, et al. Flame front evolution and laminar flame parameter evaluation of buoyancy-affected ammonia/air flames. *Int J Hydrogen Energy* 2021;46:38504–18.
- [60] Osipova KN, Korobeinichev OP, Shmakov AG. Chemical structure and laminar burning velocity of atmospheric pressure premixed ammonia/hydrogen flames. *Int J Hydrogen Energy* 2021;46:39942–54.
- [61] Pessina V, Berni F, Fontanesi S, Stagni A, Mehl M. Laminar flame speed correlations of ammonia/hydrogen mixtures at high pressure and temperature for combustion modeling applications. *Int J Hydrogen Energy* 2022;47:25780–94.
- [62] Li H, Xiao H, Sun J. Laminar burning velocity, Markstein length, and cellular instability of spherically propagating NH<sub>3</sub>/H<sub>2</sub>/Air premixed flames at moderate pressures. *Combust Flame* 2022;241:112079.
- [63] Zeng W, Liu J, Liu Y, Chen B, Liu A. The effect of hydrogen addition on the combustion characteristics of RP-3 kerosene/air premixed flames. *Energies* 2017;10.
- [64] Xu C, Wang Q, Li X, Liu K, Liu W, Oppong F, et al. Effect of hydrogen addition on the laminar burning velocity of n-decane/air mixtures: Experimental and numerical study. *Int J Hydrogen Energy* 2022;47:19263–74.
- [65] Tahtouh T, Halter F, Mounaïm-Rousselle C. Laminar premixed flame characteristics of hydrogen blended iso-octane-air-nitrogen mixtures. *Int J Hydrogen Energy* 2011;36:985–91.
- [66] Comandini A, Chaumeix N, Maclean JD, Ciccarelli G. Combustion properties of n-heptane/hydrogen mixtures. *Int J Hydrogen Energy* 2019;44:2039–52.
- [67] Akram MZ, Ma F, Waqar Akram M. A numerical approach to elucidate the combustion and emission characteristics of n-dodecane under hydrogen enrichment. *Energy Convers Manag* 2022;255:115294.

- [68] Zhang L, Ma H, Pan J, Shen Z, Wang L, Liu R, et al. Effects of hydrogen addition on the explosion characteristics of n-hexane/air mixtures. *Int J Hydrogen Energy* 2019;44:2029–38.
- [69] Wang Y, Gu M, Zhu Y, Cao L, Zhu B, Wu J, et al. A review of the effects of hydrogen, carbon dioxide, and water vapor addition on soot formation in hydrocarbon flames. *Int J Hydrogen Energy* 2021;46:31400–27.
- [70] Karimi M, Wang X, Hamilton J, Negnevitsky M, Lyden S. Status, challenges and opportunities of dual fuel hybrid approaches-a review. *Int J Hydrogen Energy* 2021;46:34924–57.
- [71] Faye O, Szpunar J, Eduok U. A critical review on the current technologies for the generation, storage, and transportation of hydrogen. *Int J Hydrogen Energy* 2022;47:13771–802.
- [72] Wu X, Zhang H, Yang M, Jia W, Qiu Y, Lan L. From the perspective of new technology of blending hydrogen into natural gas pipelines transmission: Mechanism, experimental study, and suggestions for further work of hydrogen embrittlement in high-strength pipeline steels. *Int J Hydrogen Energy* 2022;47:8071–90.
- [73] Zhunqing H, Nannan S, Yi J, Xin Z. Experimental research on a blended hydrogen-fuel engine. *Int J Hydrogen Energy* 2022.
- [74] Tsujimura T, Suzuki Y. The utilization of hydrogen in hydrogen/diesel dual fuel engine. *Int J Hydrogen Energy* 2017;42:14019–29.
- [75] Tian Z, Wang Y, Zhen X, Liu D. Numerical comparative analysis on performance and emission characteristics of methanol/hydrogen, ethanol/hydrogen and butanol/hydrogen blends fuels under lean burn conditions in SI engine. *Fuel* 2022;313:123012.
- [76] Zareei J, Rohani A, Nuñez Alvarez JR. The effect of EGR and hydrogen addition to natural gas on performance and exhaust emissions in a diesel engine by AVL fire multi-domain simulation, GPR model, and multi-objective genetic algorithm. *Int J Hydrogen Energy* 2022;47:21565–81.
- [77] Das S, Kanth S, Das B, Debbarma S. Experimental evaluation of hydrogen enrichment in a dual-fueled CRDI diesel engine. *Int J Hydrogen Energy* 2022;47:11039–51.
- [78] Luo H, Chang F, Jin Y, Ogata Y, Matsumura Y, Ichikawa T, et al. Experimental

- investigation on performance of hydrogen additions in natural gas combustion combined with CO<sub>2</sub>. *Int J Hydrogen Energy* 2021;46:34958–69.
- [79] Koroll GW, Mulpuru SR. The effect of dilution with steam on the burning velocity and structure of premixed hydrogen flames. *Symp Combust* 1988;21:1811–9.
- [80] Singh D, Nishiie T, Tanvir S, Qiao L. An experimental and kinetic study of syngas/air combustion at elevated temperatures and the effect of water addition. *Fuel* 2012;94:448–56.
- [81] Schmitt S, Wick M, Wouters C, Ruwe L, Graf I, Andert J, et al. Effects of water addition on the combustion of iso-octane investigated in laminar flames, low-temperature reactors, and an HCCI engine. *Combust Flame* 2020;212:433–47.
- [82] Galmiche B, Halter F, Foucher F, Dagaut P. Effects of dilution on laminar burning velocity of premixed methane/air flames. *Energy and Fuels* 2011;25:948–54.
- [83] Boushaki T, Dhu?? Y, Selle L, Ferret B, Poinso T. Effects of hydrogen and steam addition on laminar burning velocity of methane-air premixed flame: Experimental and numerical analysis. *Int J Hydrogen Energy* 2012;37:9412–22.
- [84] Albin E, Nawroth H, Göke S, D'Angelo Y, Paschereit CO. Experimental investigation of burning velocities of ultra-wet methane-air-steam mixtures. *Fuel Process Technol* 2013;107:27–35.
- [85] Chica Cano JP, Cabot G, Foucher F, de Persis S. Effects of oxygen enrichment and water dilution on laminar methane flames at high pressure. *Fuel* 2018;225:499–508.
- [86] Xiang L, Chu H, Ren F, Gu M. Numerical analysis of the effect of CO<sub>2</sub> on combustion characteristics of laminar premixed methane/air flames. *J Energy Inst* 2019;92:1487–501.
- [87] Ren F, Xiang L, Chu H, Jiang H, Ya Y. Modeling Study of the Impact of Blending N<sub>2</sub>, CO<sub>2</sub>, and H<sub>2</sub>O on Characteristics of CH<sub>4</sub> Laminar Premixed Combustion. *Energy and Fuels* 2020;34:1184–92.
- [88] Xiang L, Dong W, Hu J, Nie X, Ren F, Chu H. Numerical study on CH<sub>4</sub> laminar premixed flames for combustion characteristics in the oxidant atmospheres of N<sub>2</sub>/CO<sub>2</sub>/H<sub>2</sub>O/Ar-O<sub>2</sub>. *J Energy Inst* 2020;93:1278–87.

- [89] Ren F, Xiang L kai, Chu H qiang, Ya Y chen, Han W wei, Nie X kang. Numerical investigation on the effect of CO<sub>2</sub> and steam for the H<sub>2</sub> intermediate formation and NO<sub>x</sub> emission in laminar premixed methane/air flames. *Int J Hydrogen Energy* 2020;45:3785–94.
- [90] Taylor SC. *Burning Velocity and the Influence of flame stretch*, PhD Thesis. University of Leeds, 1991.
- [91] Burke MP, Chen Z, Ju Y, Dryer FL. Effect of cylindrical confinement on the determination of laminar flame speeds using outwardly propagating flames. *Combust Flame* 2009;156:771–9.
- [92] Zeng M, Yuan W, Li W, Zhang Y, Wang Y. Investigation of n-dodecane pyrolysis at various pressures and the development of a comprehensive combustion model. *Energy* 2018;155:152–61.
- [93] Lee TW, Jain V, Kozola S. Measurements of minimum ignition energy by using laser sparks for hydrocarbon fuels in air: Propane, dodecane, and jet-A fuel. *Combust Flame* 2001;125:1320–8.
- [94] Balusamy S, Cessou A, Lecordier B. Direct measurement of local instantaneous laminar burning velocity by a new PIV algorithm. *Exp Fluids* 2011;50:1109–21.
- [95] Rozenchan G, Zhu DL, Law CK, Tse SD. Outward propagation, burning velocities, and chemical effects of methane flames up to 60 ATM. *Proc Combust Inst* 2002;29:1461–70.
- [96] Jayachandran J, Zhao R, Egolfopoulos FN. Determination of laminar flame speeds using stagnation and spherically expanding flames: Molecular transport and radiation effects. *Combust Flame* 2014;161:2305–16.
- [97] Hassan MI, Aung KT, Kwon OC, Faeth GM. Properties of laminar premixed hydrocarbon/air flames at various pressures. *J Propuls Power* 1998;14:479–88.
- [98] MATLAB®, version 6.5, The Math Works, Inc.
- [99] Kelley AP, Bechtold JK, Law CK. Premixed flame propagation in a confining vessel with weak pressure rise. *J Fluid Mech* 2012;691:26–51.
- [100] Kelley AP, Law CK. Nonlinear effects in the extraction of laminar flame speeds from

- expanding spherical flames. *Combust Flame* 2009;156:1844–51.
- [101] Jomaas G, Law CK, Bechtold JK. On transition to cellularity in expanding spherical flames. *J Fluid Mech* 2007;583:1–26.
- [102] Bechtold JK, Matalon M. The dependence of the Markstein length on stoichiometry. *Combust Flame* 2001;127:1906–13..
- [103] Bouvet N, Halter F, Chauveau C, Yoon Y. On the effective Lewis number formulations for lean hydrogen/hydrocarbon/ air mixtures. *Int J Hydrogen Energy* 2013;38:5949–60.
- [104] Lapalme D, Lemaire R, Seers P. Assessment of the method for calculating the Lewis number of H<sub>2</sub>/CO/CH<sub>4</sub> mixtures and comparison with experimental results. *Int J Hydrogen Energy* 2017;42:8314–28.
- [105] Addabbo R, Bechtold JK, Matalon M. Wrinkling of spherically expanding flames. *Proc Combust Inst* 2002;29:1527–35.
- [106] Dinkelacker F, Manickam B, Muppala SPR. Modelling and simulation of lean premixed turbulent methane/hydrogen/air flames with an effective Lewis number approach. *Combust Flame* 2011;158:1742–9.
- [107] Chen Z. On the extraction of laminar flame speed and Markstein length from outwardly propagating spherical flames. *Combust Flame* 2011;158:291–300.
- [108] Law CK, Jomaas G, Bechtold JK. Cellular instabilities of expanding hydrogen/propane spherical flames at elevated pressures: Theory and experiment. *Proc Combust Inst* 2005;30:159–67. <https://doi.org/10.1016/j.proci.2004.08.266>.
- [109] Clarke A. Calculation and consideration of the Lewis number for explosion studies. *Process Saf Environ Prot Trans Inst Chem Eng Part B* 2002;80:135–40.
- [110] Xiouris C, Ye T, Jayachandran J, Egolfopoulos FN. Laminar flame speeds under engine-relevant conditions: Uncertainty quantification and minimization in spherically expanding flame experiments. *Combust Flame* 2016;163:270–83.
- [111] Reaction Design. CHEMKIN Theory Manual CHEMKIN ® Software 2013:1–402.
- [112] Kee R, Grcar J, Smooke M, Miller J, Meeks E. PREMIX : A FORTRAN Program for Modeling Steady Laminar One-Dimensional. SANDIA Natl Lab, 1985:1–87.
- [113] Smith GP, Golden DM, Frenklach M, Moriarty NW, Eiteneer B, Goldenberg M, et al.

- GRI- Mech 3.0 n.d. [http://www.me.berkeley.edu/gri\\_mech/](http://www.me.berkeley.edu/gri_mech/).
- [114] Smith GP, Tao Y, Wang H. Foundational fuel chemistry model version 1.0 (FFCM-1).
- [115] You X, Egolfopoulos FN, Wang H. Detailed and simplified kinetic models of n-dodecane oxidation: The role of fuel cracking in aliphatic hydrocarbon combustion. *Proc Combust Inst* 2009;32 I:403–10.
- [116] Ranzi E, Frassoldati A, Stagni A, Pelucchi M, Cuoci A, Faravelli T. Reduced kinetic schemes of complex reaction systems: Fossil and biomass-derived transportation fuels. vol. 46. 2014.
- [117] Narayanaswamy K, Pepiot P, Pitsch H. A chemical mechanism for low to high temperature oxidation of n-dodecane as a component of transportation fuel surrogates. *Combust.Flame* 2014;161:866–84.
- [118] Lapointe S, Zhang K, McNenly MJ. Reduced chemical model for low and high-temperature oxidation of fuel blends relevant to internal combustion engines. *Proc Combust Inst* 2019;37:789–96.
- [119] DG Goodwin HK Moffat RS. Cantera: An object-oriented software toolkit for chemical kinetics, thermodynamics, and transport properties 2009:2009.
- [120] Anaconda Software Distribution. Anaconda documentation. Anaconda Inc; 2020. Retrieved from, <https://docs.anaconda.com/>. 2020:2020.
- [121] Ellson J, Gansner E, Koutsofios L, North SC, Woodhull G. Graphviz - Open source graph drawing tools. *Int Symp Graph Draw Springer* 2002;2265 LNCS:483–4.
- [122] Lowry, William Jaap de Vries, Michael Krejci EP. Laminar Flame Speed Measurements and Modeling of Pure Alkanes and Alkane Blends at elevated Pressures. *ASMETurbo Expo* 2010;2:855–73.
- [123] Dirrenberger P, Le Gall H, Bounaceur R, Glaude PA, Battin-Leclerc F. Measurements of laminar burning velocities above atmospheric pressure using the heat flux method-application to the case of n- pentane. *Energy and Fuels* 2015;29:398–404.
- [124] Kim HH, Won SH, Santner J, Chen Z, Ju Y. Measurements of the critical initiation radius and unsteady propagation of n-decane/air premixed flames. *Proc Combust Inst* 2013;34:929–36.

- [125] Munzar JD, Akih-Kumgeh B, Denman BM, Zia A, Bergthorson JM. An experimental and reduced modeling study of the laminar flame speed of jet fuel surrogate components. *Fuel* 2013;113:586–97.
- [126] Wu F, Liang W, Chen Z, Ju Y, Law CK. Uncertainty in stretch extrapolation of laminar flame speed from expanding spherical flames. *Proc Combust Inst* 2015;35:663–70.
- [127] Wu X, Huang Z, Wang X, Jin C, Tang C, Wei L, et al. Laminar burning velocities and flame instabilities of 2,5-dimethylfuran-air mixtures at elevated pressures. *Combust Flame* 2011;158:539–46.
- [128] Moghaddas A, Bennett C, Eisazadeh-Far K, Metghalchi H. Measurement of Laminar Burning Speeds and Determination of Onset of Auto-Ignition of Jet-A/Air and Jet Propellant-8/Air Mixtures in a Constant Volume Spherical Chamber. *J Energy Resour Technol* 2012;134:4–9.
- [129] Rajesh N, Prathap C. Investigation on the laminar burning velocity and flame stability of premixed n-dodecane-air mixtures at elevated pressures and temperatures. *Fuel* 2022;318.
- [130] Yu H, Han W, Santner J, Gou X, Sohn CH, Ju Y, et al. Radiation-induced uncertainty in laminar flame speed measured from propagating spherical flames. *Combust Flame* 2014;161:2815–24.
- [131] Xie Y, Wang J, Zhang M, Gong J, Jin W, Huang Z. Experimental and numerical study on laminar flame characteristics of methane oxy-fuel mixtures highly diluted with CO<sub>2</sub>. *Energy and Fuels* 2013;27:6231–7.
- [132] Chen Z, Qin X, Xu B, Ju Y, Liu F. Studies of radiation absorption on flame speed and flammability limit of CO<sub>2</sub> diluted methane flames at elevated pressures. *Proc Combust Inst* 2007;31 II:2693–700.
- [133] Zhang W, Gou X, Chen Z. Effects of water vapor dilution on the minimum ignition energy of methane, n-butane and n-decane at normal and reduced pressures. *Fuel* 2017;187:111–6.
- [134] Ranzi E, Frassoldati A, Grana R, Cuoci A, Faravelli T, Kelley AP, et al. Hierarchical and comparative kinetic modeling of laminar flame speeds of hydrocarbon and oxygenated fuels. *Prog Energy Combust Sci* 2012;38:468–501.

- [135] Wu F, Law CK. An experimental and mechanistic study on the laminar flame speed, Markstein length and flame chemistry of the butanol isomers. *Combust Flame* 2013;160:2744–56.
- [136] Bradley D, Harper CM. The development of instabilities in laminar explosion flames. *Combust Flame* 1994;99:562–72.
- [137] Gu XJ, Haq MZ, Lawes M, Woolley R. Laminar burning velocity and Markstein lengths of methane-air mixtures. *Combust Flame* 2000;121:41–58.
- [138] Titova NS, Torokhov SA, Favorskii ON, Starik AM. Analysis of the mechanisms of ignition and combustion of i-C<sub>8</sub>H<sub>18</sub>-H<sub>2</sub> and n-C<sub>10</sub>H<sub>22</sub>-H<sub>2</sub> fuel blends in air. *Combust Explos Shock Waves* 2016;52:631–42.
- [139] Oh J, Noh D. Laminar burning velocity of oxy-methane flames in atmospheric condition. *Energy* 2012;45:669–75.
- [140] Anderlohr JM, Pires Da Cruz A, Bounaceur R, Battin-Leclerc F. Thermal and kinetic impact of CO, CO<sub>2</sub>, and H<sub>2</sub>O on the postoxidation of IC-engine exhaust gases. *Combust Sci Technol* 2010;182:39–59.

## Appendix -A: Ignition Discharge Energy Measurement

In the freely expanding spherical flame method, a spherical flame is initiated by means of a spark kernel provided by a spark ignition system. It comprised of extended electrodes which were vertically positioned inside the chamber. The pointed tips of the electrodes were assembled at the center of the chamber with a short gap of 1-3 mm. A spark with a short duration is discharged in this gap. The strength of this spark strongly depends on the primary voltage and the current of the spark ignition coil. The flame kernel generated by this spark was highly unsteady and non-spherical in shape. Then, the flame kernel develops or grows into a smooth spherical flame and the ignition effects disappear. Hence, the smallest radius of a smooth spherical flame chosen for the estimation of LBV quite strongly dependent on the spark energy. Hence, the spark should have the minimum possible energy only to initiate a self-sustainable flame. The smallest ignition energy needed to initiate a self-sustainable flame is called minimum ignition energy (MIE). The energy deposited through the spark should be close enough to the MIE. Each fuel has its respective MIE, and it depends on the structure of the fuel. For example, the MIE of Propane/ n-Pentane/ n-Heptane/ Isooctane are 5.5/7.8/14.5/27.0 mJ at and 298 K [1]. Also, MIE depends on the equivalence ratio too. At a given equivalence ratio, MIE increased with an increase in the carbon number of the fuel. The equivalence ratio at which the lower limit of MIE shifted towards richer condition with increase in the carbon number of a fuel, for methane ( $\phi = 0.9$ ), propane ( $\phi = 1.25$ ), heptane ( $\phi = 1.8$ ), and n-dodecane ( $\phi = 3.5$ ) [2]. The reason was that the heavier molecules diffused slowly which affected the replenishing of fuel molecules at the ignition point. This clearly indicates the requirement of a higher ignition energy under lean fuel conditions for heavier liquid fuels than lighter hydrocarbons. Furthermore, the MIE decreased with an increase in the initial pressure and initial temperature [1].

The discharge energy between electrodes can be varied by adjusting (a) the primary current and voltage, and (b) the electrode gap itself. In the current test facility, the electrode gap was adjustable from 1mm to 5mm. For both the fuels, methane and n-dodecane, the electrode gap was kept constant at 1 mm based on the recommendation by Ferguson et al. [3] and Friedman et al. [4]. Only for the lean mixtures of premixed n-dodecane-air mixtures at 1 bar and 400 – 450 K, the primary voltage was increased from 12 V to 14 V, as stated above, that the lean combustible mixtures required higher MIE to ignite a self-sustainable flame. If a combustible mixture was ignited with a spark having insufficient ignition energy, it leads to a weak flame kernel which got extinguished immediately due to the strong transient effects and the energy

losses to the electrodes [5] as shown in Figure A.1. In the following section, the methodology followed to find the energy of the spark generated in between the electrodes is discussed.

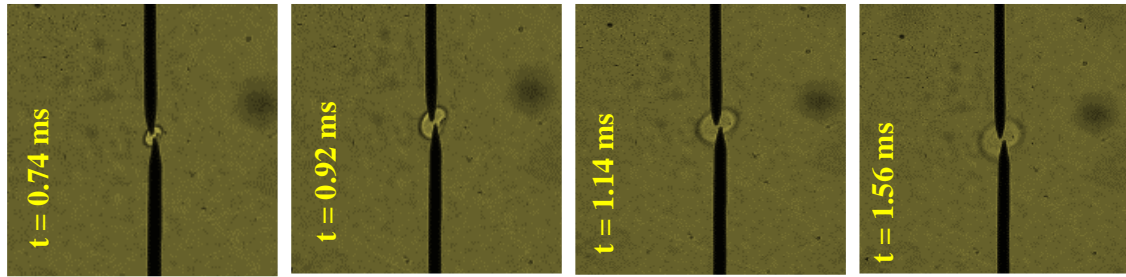


Figure A.1 The sequence of flame strong kernel emerges and extinguish a weak kernel of lean n-dodecane-air mixture at 1 bar 400 K,  $\phi = 0.8$ .

### Experimental procedure

Table A1 lists the important technical properties of the ignition coil used in this study. It has two primary power inputs and one signal input to trigger it. The minimum secondary voltage attainable was 30 kV in order to ionize the molecules between the electrode gaps to generate a spark. Figure A.2 shows the fundamental circuit diagram of the coil. The electronic control unit (ECU) was connected to a pulse generator. Figure A.3 shows the wiring connection arrangement of various instruments. Current and voltage probes were connected across the coil to measure the primary current and voltage drawn by the coil while generating the spark. An oscilloscope was used to record the transient profiles of current, and voltage.

Table A1. Summary of ignition coil technical data.

Technical data	
Supply voltage	12 -14 V
Operating Temperature	-30 to 180 °C
Primary resistance	$0.98 \pm 5\% \Omega$
Secondary resistance	$7.2 \pm 10\% K\Omega$
Secondary voltage with 35 PF Load	30 KV min
Energy (into 1000V Zener)	30 mJ

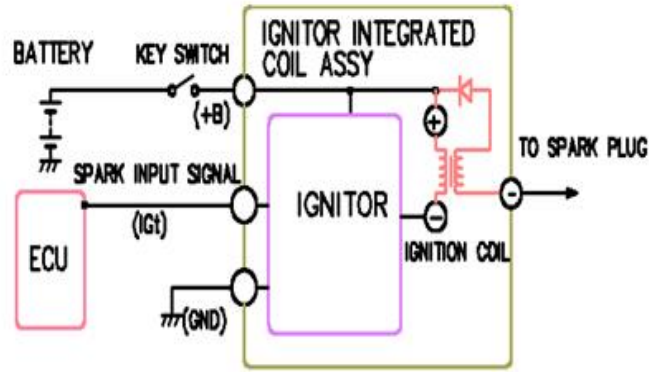


Figure A.2. Circuit diagram of ignition coil

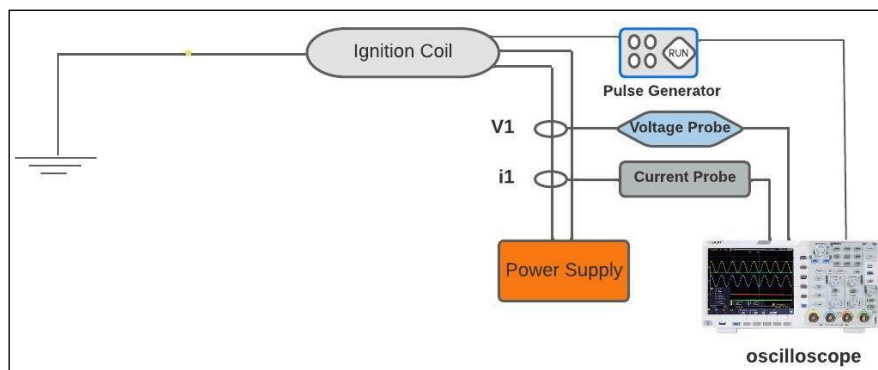


Figure A.3. The wiring diagram of the experimental arrangement.

The measured time-dependent parameters are used in Equation (A-1) to measure the maximum possible ignition energy that can be stored in the coil.

$$E = \int_0^t v(t)i(t)dt \quad \text{A-1}$$

where  $E$ -minimum ignition energy,  $v(t)$ , the primary voltage-time curve;  $i(t)$  the primary current-time curve;  $t$ , spark duration (1 ms). The ignition energy discharged by means of an electrical arc between the electrodes is approximated (with transmission loss, and custom spark plug efficiency) to be the same as that of the stored in coil.

Two methodologies were adapted to measure the discharge ignition energy (1) by varying the primary voltage, and (2) by varying the electrode gap. For a given constant electrode gap of 1 mm and a fixed spark duration of 1 ms, the primary voltage was increased from 10, 12, and 14 V by keeping the primary current constant at 20 mA. The variations in the primary current flow and voltage during the actual spark were measured using a current probe (Pintech AC/DC

Probe-PT2710:0.4-60 A) and a voltage probe (Keysight - N2791A:70 to 700 V), as shown in Figure A.4.

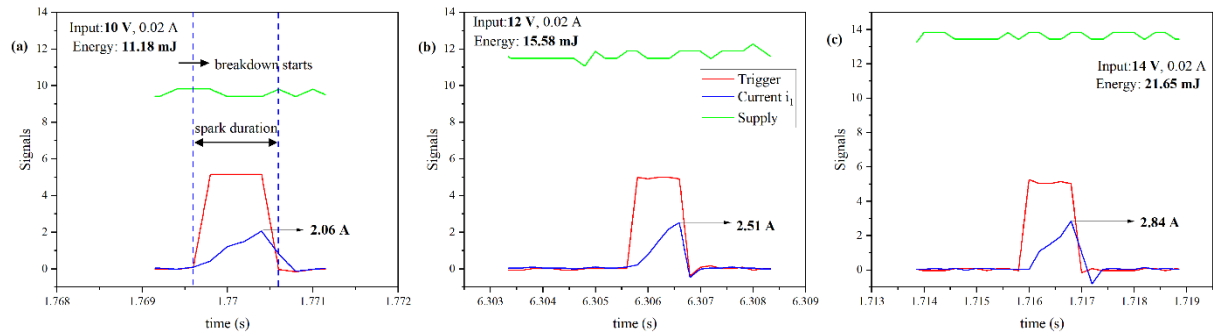


Figure A.4. The variation of primary current with different input voltage (a) 10 V, (b) 12 V, and (c) 14 V in given constant 1 ms pulse width

Figure A.4 clearly shows that an increase in the primary voltage from 10 to 14V for a fixed spark gap of 1mm, the spark energy also simultaneously increased from 11.18 to 21.65 mJ as the primary current consumed also increased. The measured spark energy was in the general MIE range of 10-30 mJ meant for hydrocarbons for  $\phi=0.8-1.4$ . Although the present work does not involve any changes in the electrode gap, due to the uncertainty in smaller gap measurements, the ignition energy measurements were carried out for different electrode gaps (1-3 mm) by keeping the primary voltage as constant at 12V. Figure A.5 shows that the ignition energy increased with an increase in the electrode gap, and then remained constant at 3 mm. For a maximum gap of 3 mm, the energy drawn by the coil went up to 19.44 mJ, which was also within the hydrocarbons range for a constant spark duration (trigger pulse width) of 1 ms.

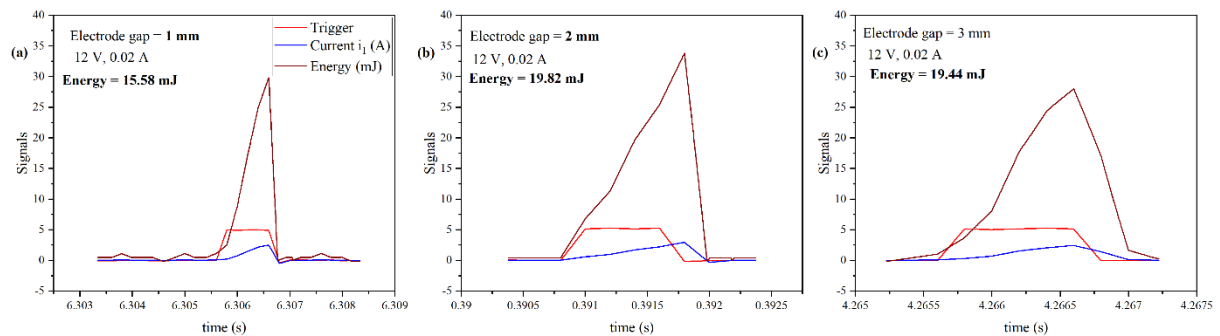


Figure A.5. The variation of primary current and spar energy with different spark gaps (a) 1 mm, (b) 2 mm, and (c) 3 mm for constant pulse width of 1 ms

Therefore, these measurements confirm that the coil discharge energy falls within the recommended range, and hence, ignition effects are negligible or minimal in the flame propagation at a smaller radius.

## References

- [1] Stephen Turns. *An Introduction to Combustion: Concepts and Applications*. McGraw-Hill Education; 2013.
- [2] Lee TW, Jain V, Kozola S. Measurements of minimum ignition energy by using laser sparks for hydrocarbon fuels in air: Propane, dodecane, and jet-A fuel. *Combust Flame* 2001; 125:1320–8. [https://doi.org/10.1016/S0010-2180\(01\)00248-6](https://doi.org/10.1016/S0010-2180(01)00248-6).
- [3] Ferguson CR, Keck JC. On laminar flame quenching and its application to spark ignition engines. *Combust Flame* 1977; 28:197–205. [https://doi.org/10.1016/0010-2180\(77\)90025-6](https://doi.org/10.1016/0010-2180(77)90025-6).
- [4] Friedman R, Johnston WC. Pressure dependence of quenching distance of normal heptane, iso-octane, benzene, and ethyl ether flames. *J Chem Phys* 1952; 20:919–20. <https://doi.org/10.1063/1.1700600>.
- [5] Essmann S, Markus D, Grosshans H, Maas U. Experimental investigation of the stochastic early flame propagation after ignition by a low-energy electrical discharge. *Combust Flame* 2020; 211:44–53. <https://doi.org/10.1016/j.combustflame.2019.09.021>.

## Appendix-B: Uncertainty Quantification

The uncertainties associated in the present measurements of unstretched laminar burning velocity and burned gas Markstein length using the outwardly propagating spherical flame method, and their quantification are discussed in this chapter. The uncertainties depend on number of factors such as: unburned gas mixture composition, initial temperature, initial pressure, estimation of radius through image processing, extrapolation schemes, thermal radiation and the density ratio of burned to unburned gases. Uncertainty was estimated by following the procedure reported by Xiouris et al. [110]. The total uncertainty involved in the measurement of LBV ( $a_{S_u^0}$ ) was categorized into three stages, (i) mixture preparation, (ii) data acquisition, and (iii) post processing. The uncertainty of each stage was estimated independently, and subsequently combined to provide an accurate estimate of the total uncertainty in the unstretched LBV and burned gas Markstein length. Table B.1 shows the list of sensors used for measuring absolute partial pressure and temperature of unburned gas mixtures.

Table B.1 Pressure and temperature sensors range and accuracy.

Instruments	Range	Accuracy
Absolute Pressure Transducer (Druck:PTX 5072-TA-A1-CA-H0-PF)	0 – 0.5 bar	$\pm 0.25$ % FS
	0 – 1 bar	$\pm 0.25$ % FS
Keller Druck -Leo 3	0 – 4 bar	$\pm 0.1$ % FS
K type Sheathed Thermocouple (Tempsens Pvt Ltd)	70 to 1500 K	$\pm 3$ % FS

### (i) Uncertainty in the Mixture Preparation

The uncertainty involved in the mixture preparation process is mainly due to the system errors associated with the instruments. In present experiments, gas components were filled by measuring respective partial pressures and total mixture pressure by piezo resistive pressure transducer and mixture initial temperature measured by thermocouple. Therefore, the uncertainties of all the factors related to the mixture preparation  $a_{S_u^0,MP}$ , that affect  $S_u^0$  were defined as follows:

$$\begin{aligned}
a_{S_u^0, MP^2} = & \sum \left( \frac{\partial S_u^0}{\partial R_i} \right)^2 a_{R_i}^2 + \sum_{i=1}^M 1 \sum_{j=1, j \neq i}^M 1 \left| \frac{\partial S_u^0}{\partial R_i} \right| \left| \frac{\partial S_u^0}{\partial R_j} \right| a_{R_i} a_{R_j} + \left( \frac{\partial S_u^0}{\partial T_{u,0}} \right)^2 a_{T_{u,0}}^2 \\
& + \left( \frac{\partial S_u^0}{\partial P_0} \right)^2 a_{P_0}^2
\end{aligned} \tag{B.1}$$

To determine overall uncertainty associated with the LBV measurements, the above factors were assumed to be uncorrelated. Therefore, the above expression was deduced as,

$$a_{S_u^0, MP^2} = \sum \left( \frac{\partial S_u^0}{\partial R_i} \right)^2 a_{R_i}^2 + \left( \frac{\partial S_u^0}{\partial T_{u,0}} \right)^2 a_{T_{u,0}}^2 + \left( \frac{\partial S_u^0}{\partial P_0} \right)^2 a_{P_0}^2 \tag{B.2}$$

where  $a_{R_i}^2$ ,  $a_{T_{u,0}}^2$  and  $a_{P_0}^2$  are the uncertainty of partial pressure measurement of gas filling process, mixture initial temperature and mixture initial pressure measurement. The uncertainty in the value of  $R_i$  is caused by error in the pressure transducer  $a_p = 0.00125$  and  $0.0025$  bar for 0.5 and 1 bar range pressure transducers with a least count of 0.001 bar, because  $R_i = \frac{P_{s_i}}{P_{s_{i+1}}}$  and therefore any change in the partial pressure value corresponding change in the value  $R_i$ .

After obtaining the partial pressure values through perturbation based on the instrument error at a given pressure, their respective mole fraction and equivalence ratios were estimated. Then, for all the mixture conditions, the LBV was predicted using CHEMKIN. Similar exercise was repeated for four different perturbations to fetch data in the upper and lower limit of the operating condition, to find its sensitivity to LBV.

For calculating the uncertainty on LBV due to the uncertainty in the initial pressure, initial temperature measurements, again, based on instruments accuracy range, a few operating conditions were populated with respect to the experimental value of initial pressure and temperature. For all the newly populated operating conditions, where experimental values were not there, the LBV was simulated, and the respective derivatives were estimated, and it was followed by the calculation of uncertainty with respect to the perturbed initial parameter. The obtained values were substituted in the above equation and the uncertainty in the mixture preparation was calculated.

## (ii) Uncertainty in data acquisition

Uncertainty involved in the data acquisition was mainly due to real-time image capturing method. The present shadowgraph system was carefully arranged to minimize the aberrations and the image distortion to reduce the error in the flame radius estimation. Since the

shadowgraph system has non-negligible error less than 1% and its uncertainty is insensitive to  $S_u^0$ , therefore error due to data acquisition was neglected.

### (iii) Post processing uncertainty

The flame radius as a function of time was obtained through a circle fit procedure applied on flame images by minimizing the following objective function and the error associated in the estimation of this function was considered as the uncertainty in the calculation of flame radius.

$$a_{R_f} = \sqrt{\frac{\sum_i^k (R_i - R_{fit})^2}{k - 1}} \quad \text{B.3}$$

Where  $R_i$  and  $R_{fit}$  are flame radius of instantaneous image and corresponding circle fit,  $k$  is number of points used for fitting. Therefore, two fits are possible,

$$a_{R_f} = f_1(t) \quad \text{B.4}$$

$$a_{R_{fit}} = f_2(t) \quad \text{B.5}$$

While post processing data to obtain the unstretched LBV and Markstein length ( $L_b$ ), the range of radius used was 8-20mm. In addition to that, the estimated flame speed-time plot had minor fluctuations or noise essentially due to the usage of numerical differentiation to find the flame speed from the consequent two flame radii. To remove the same, the flame speed data was conditioned using a smoothing algorithm, and the uncertainty arising due to the smoothing is explained in the present work.

The flame speed is defined as  $S_b = \frac{dR}{dt}$  but due to finite data collecting rate, the flame speed has to be calculated numerically as:

$$S_b(t_i) = \frac{-R(t_{i+2}) + 8R(t_{i+1}) - 8R(t_{i-1}) + R(t_{i-2})}{12\Delta t} \quad \text{B.6}$$

Where  $\Delta t = 1/FPS$ , FPS is frame rate at which imaging of the flame is done. Therefore, the uncertainty in the flame speed is given as:

$$a_{S_b}(t_i) = S_b(t_i) \left( \frac{a_{R_{i+2}} + 8a_{R_{i+1}} + 8a_{R_{i-1}} + a_{R_{i-2}}}{12} \right) \quad \text{B.7}$$

The uncertainty in stretch, defined as  $K = \frac{2S_b}{R}$  can be written:

$$a_K(t_i) = K(t_i) \sqrt{\left(\frac{a_{R_i}}{R_i}\right)^2 + \left(\frac{a_{S_{b_i}}}{S_{b_i}}\right)^2} \quad \text{B.8}$$

Now consider  $R_{f,1}$  and  $R_{f,n}$  from the radius data, such that  $R_{f,1} < R_{f,n}$  and these two radius range are free of any ignition or confine effects. Then any radius lying between these two bounds, its corresponding stretch, flame speed and respective uncertainties can be used for either a linear or a nonlinear fitting to obtain the unstretched flame speed and burned gas Markstein length. Also the uncertainties in these quantities can be calculated.

Let,

$$R_{fit} = [R_{f,1}, R_{f,2}, \dots, R_{f,n}]; a_{R_{fit}} = [a_{R_{f,1}}, a_{R_{f,2}} \dots a_{R_{f,n}}] \quad \text{B.9}$$

$$S_{b_{fit}} = [S_{b_{f,1}}, S_{b_{f,2}}, \dots, S_{b_{f,n}}]; a_{S_{b_{fit}}} = [a_{S_{b_{f,1}}}, a_{S_{b_{f,2}}} \dots a_{S_{b_{f,n}}}] \quad \text{B.10}$$

$$K_{fit} = [K_{f,1}, K_{f,2}, \dots, K_{f,n}]; a_{K_{fit}} = [a_{K_{f,1}}, a_{K_{f,2}} \dots a_{K_{f,n}}] \quad \text{B.11}$$

Then

$$\frac{\partial S_b^0}{\partial K_{f,i}} = \frac{\Delta S_b^0}{\Delta K_{f,i}} = \frac{S_b^0|_{K_{f,i+aK_{f,i}}} - S_b^0|_{K_{f,i-aK_{f,i}}}}{2a_{K_{f,i}}} \quad \text{B.12}$$

$$\frac{\partial S_b^0}{\partial S_{b_{f,i}}} = \frac{\Delta S_b^0}{\Delta S_{b_{f,i}}} = \frac{S_b^0|_{S_{b_{f,i}+aS_{b_{f,i}}}} - S_b^0|_{S_{b_{f,i}-aS_{b_{f,i}}}}}{2a_{S_{b_{f,i}}}} \quad \text{B.13}$$

$$\frac{\partial L_b}{\partial K_{f,i}} = \frac{\Delta L_b}{\Delta K_{f,i}} = \frac{L_b|_{K_{f,i+aK_{f,i}}} - L_b|_{K_{f,i-aK_{f,i}}}}{2a_{K_{f,i}}} \quad \text{B.14}$$

$$\frac{\partial L_b}{\partial S_{b_{f,i}}} = \frac{\Delta L_b}{\Delta S_{b_{f,i}}} = \frac{L_b|_{S_{b_{f,i}+aS_{b_{f,i}}}} - L_b|_{S_{b_{f,i}-aS_{b_{f,i}}}}}{2a_{S_{b_{f,i}}}} \quad \text{B.15}$$

The values  $S_b^0|_{S_{b_{f,i}+aS_{b_{f,i}}}}$ ,  $S_b^0|_{K_{f,i+aK_{f,i}}}$ ,  $L_b|_{S_{b_{f,i}+aS_{b_{f,i}}}}$ , and  $L_b|_{K_{f,i+aK_{f,i}}}$  are obtained by varying one element at a time and then performing the fit. Once the derivatives are calculated the uncertainty in the data is obtained as:

$$a_{S_b^0, no\ smooth} = \sqrt{\sum_{i=1}^n \left(\frac{\partial S_b^0}{\partial S_{b_i}}\right)^2 a_{S_{b_i}}^2 + \sum_{i=1}^n \left(\frac{\partial S_b^0}{\partial K_i}\right)^2 a_{K_i}^2} \quad \text{B.16}$$

$$a_{L_b, no\ smooth} = \sqrt{\sum_{i=1}^n \left(\frac{\partial L_b}{\partial S_{b_i}}\right)^2 a_{S_{b_i}}^2 + \sum_{i=1}^n \left(\frac{\partial L_b}{\partial K_i}\right)^2 a_{K_i}^2} \quad \text{B.17}$$

The subscript ‘no smooth’ implies that the uncertainty associated with a non-smoothed data. As mentioned earlier smoothing is required to minimise the noise raised due to numerical differentiation of consecutive radius points, which also contribute to the LBV. This uncertainty was quantified by smoothing the flame speed data and using this data to calculate the stretch. Then a fitting was carried out using the radius data, smoothed flame data and the corresponding smooth stretch data, which provided a value of unstretched flame speed and Markstein length. Now,

$$a_{S_{b_0}, smoothing} = ||S_{b_0}|_{smoothed\ data} - |S_{b_0}|_{non\ smoothed\ data} || \quad \text{B.18}$$

$$a_{L_b, smoothing} = ||L_b|_{smoothed\ data} - |L_b|_{non\ smoothed\ data} || \quad \text{B.19}$$

Therefore, uncertainty of LBV and  $L_b$  are estimated by the following expression,

$$a_{S_{b_0}} = \sqrt{a_{S_{b_0}smoothed}^2 + a_{S_{b_0}non\ smoothed}^2} \quad \text{B.20}$$

$$a_{L_b} = \sqrt{a_{L_bsmoothed}^2 + a_{L_bnon\ smoothed}^2} \quad \text{B.21}$$

The calculated data processing uncertainty will be added with uncertainty in mixture preparation, initial temperature, initial pressure and radiation, final experimental uncertainty is the summation of all these individual uncertainties and reported in the plots.

### Sample calculation (study -3)

Mixture: 35% ( $C_{12}H_{26} + (18.5O_2)/\phi$ ) + 65%  $N_2$ , 1 bar, 450 K,  $\phi = 0.6 - 1.4$ , least count = 0.001, error = 0.00125 bar, frame rate = 17000 FPS, smoothing factor = 0.35.

## Mixture preparation uncertainty

Uncertainty in the mixture preparation can impact the laminar burning velocity through equivalence ratio, for 35% ( $C_{12}H_{26} + (18.5O_2)/\phi$ ) + 65%  $N_2$  flame experiments, the absolute partial pressure measurements of each component was treated as independent, uncorrelated variables. The mole fractions of the mixtures were slightly perturbed by its instrument uncertainty and hence, the equivalence ratios. You et al. mechanism was used to quantify the uncertainty effect on laminar burning velocity. The procedure needed to populate two different equivalence ratios on the lower and upper regimes of the studied equivalence ratio by a small perturbation as shown in Table B.2. This perturbation provided the partial pressures of each species for the additional cases which takes care of the instrument accuracy too needed to estimate the contribution of uncertainty in the equivalence ratio. To be in line with the measurements, the estimated partial pressures and the associated mole fraction values were corrected to three decimal points, and the respective equivalence ratios were estimated.

Table B.2 Populated equivalence ratios for uncertainty quantification.

Phi	Populated mole fractions			Stoichiometric Mole fractions			Perturbed variables		
	X_ele 1	X_ele2	X_ele 3	X-DD	X-O <sub>2</sub>	X-N <sub>2</sub>	X-O <sub>2</sub>	X-N <sub>2</sub>	$\phi_{var}$
0.6	0.010	0.339	0.651	0.018	0.332	0.650	0.342	0.658	0.553
0.6	0.011	0.338	0.651	0.018	0.332	0.650	0.342	0.658	0.609
0.6	0.012	0.339	0.649	0.018	0.332	0.650	0.343	0.657	0.665
0.6	0.011	0.340	0.649	0.018	0.332	0.650	0.344	0.656	0.609
1	0.017	0.332	0.651	0.018	0.332	0.650	0.338	0.662	0.946
1	0.018	0.331	0.651	0.018	0.332	0.650	0.337	0.663	1.003
1	0.019	0.332	0.649	0.018	0.332	0.650	0.338	0.662	1.060
1	0.018	0.333	0.649	0.018	0.332	0.650	0.339	0.661	1.003
1.4	0.023	0.326	0.651	0.018	0.332	0.650	0.334	0.666	1.288
1.4	0.025	0.324	0.651	0.018	0.332	0.650	0.332	0.668	1.403
1.4	0.026	0.325	0.649	0.018	0.332	0.650	0.334	0.666	1.461
1.4	0.025	0.327	0.648	0.018	0.332	0.650	0.335	0.665	1.401

Table B.3 Mixture preparation uncertainty

$\phi$	LSC	$a_{S_{u,MP}}^0$ (cm/s)
0.6	1.33	13.41
0.8	0.65	11.61
1	0.02	1.09
1.2	-0.82	7.24
1.4	-2.23	12.38

Figure B.3 shows the computed Logarithmic Sensitivity Coefficients  $LSC = \frac{d \ln(S_u^0)}{d(\phi)}$  for 35%  $(C_{12}H_{26} + (18.5O_2)/\phi) + 65\%$   $N_2$  mixtures at 450 K, and 1 bar. Off-stoichiometric mixtures exhibit larger LSC, similar trend is reported in literature [110]. All the calculated values are attached in the excel sheet of the supplementary files.

Independent perturbation for the unburned mixture temperature and pressure values by their associated uncertainties ( $\pm 3$  K / temperature and 0.00125 bar / pressure) were designed and You et al. mechanism was used to quantify the uncertainty impact of each initial conditions on LBV estimated.

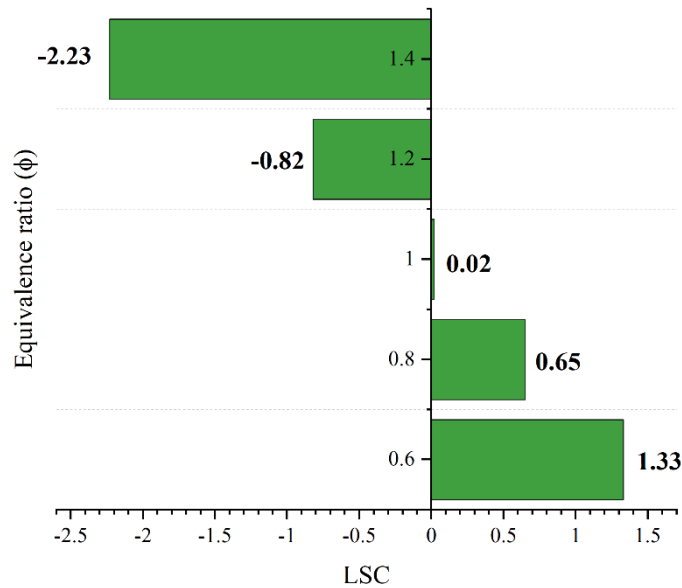


Figure B.1 Logarithmic sensitivity coefficients of  $S_u^0$  for 35%  $(C_{12}H_{26} + (18.5O_2)/\phi) + 65\%$   $N_2$  mixtures at 450 K and 1bar

Table B.4 Initial temperature uncertainty

$\phi$	$S_{uo,+}$	$S_{uo,-}$	T1 (K)	T2 (K)	$dS_{uo}/dT$	$a_{S_{uo,T}^0}$
0.6	112	110	453	447	0.33	1.00
0.8	149	146	453	447	0.50	2.25
1	162	159	453	447	0.50	2.25
1.2	152	149	453	447	0.50	2.25
1.4	122	120	453	447	0.33	1.00

Table B.5 Initial pressure uncertainty

$\phi$	Suo_+	Suo_-	P1 (bar)	P2 (bar)	dS <sub>uo</sub> /dP	$a_{S_{u,P}^0}$
0.6	110.94	111	1.00125	0.99875	24.00	0.0009
0.8	147.75	148	1.00125	0.99875	100.00	0.015625
1	160.07	160	1.00125	0.99875	28.00	0.001225
1.2	150.34	150	1.00125	0.99875	136.00	0.0289
1.4	120.81	121	1.00125	0.99875	76.00	0.009025

Table A.6 Mixture preparation uncertainty

$\phi$	$a_{S_{u,MP\phi}^0}$	$a_{S_{u,T}^0}$	$a_{S_{u,P}^0}$	$a_{S_{u,MP}^0}$ (cm/s)
0.6	13.41	1.00	0.0009	13.75
0.8	11.61	2.25	0.0156	13.43
1	1.09	2.25	0.0012	6.84
1.2	7.24	2.25	0.0289	9.90
1.4	12.38	1.00	0.0090	12.74

## Post processing uncertainty

The uncertainty in the radius measurement due to pixel to physical conversion, propagates in the flame speed and Markstein length, and hence in the reported laminar burning velocity. The error profile in the image processing was used to estimate the error involved in flame speed with nonlinear expansion extrapolation scheme to calculate the post processing uncertainty on LBV and Markstein length. Figure B.2 shows the uncertainty in the calculation of radius for different images of stoichiometric n-dodecane/O<sub>2</sub>/65%N<sub>2</sub> mixtures at 1 bar 450 K.

Finally, the post processing uncertainty calculated by,

$$a_{S_{u,pp}^0} = S_{u, sim}^0 \times \frac{a_{S_b^0, pp}}{S_b^0, NE} \quad \text{B.22}$$

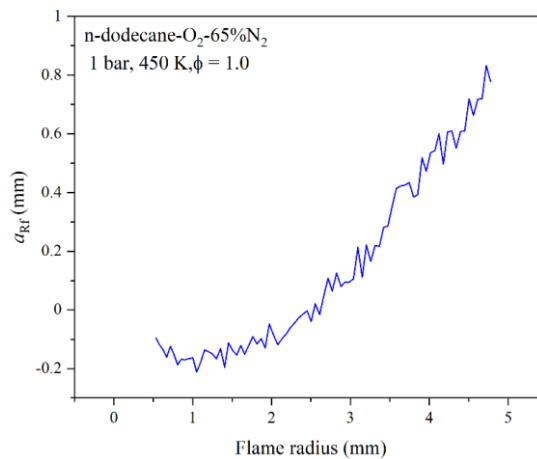


Figure B.2 Variation of flame radius uncertainty with flame growth.

where  $S_{u_{sim}}^0$  is LBV obtained through simulation by using You et al.,  $a_{S_{b,pp}}^0$  is uncertainty of experimental flame speed due to radius error, and  $S_{b_{NE}}^0$  is corresponding experimental unstretched flame speed. Table B.6 shows the post processing uncertainty on LBV and Markstein length for different equivalence ratios.

Table B.7 Post processing uncertainty of LBV and Markstein length.

$\phi$	$a_{S_{b,pp}}^0$	$S_{b_{NE}}^0$	$S_{u_{sim}}^0$	$a_{S_{u,pp}}^0$	$a_{L_b}$ (cm)
0.6	5.51	550.23	111.10	1.11	0.0079
0.8	10.43	858.47	149.22	1.81	0.0080
1	10.28	952.44	161.83	1.75	0.0073
1.2	10.46	936.77	151.60	1.69	0.0076
1.4	8.70	869.20	120.81	1.21	0.0067

The overall uncertainty was quantified by root-of-sum-of-squares method, by following expression.

$$a_{S_u^0} = \sqrt{a_{S_{u,MP}}^2 + a_{S_{u,PP}}^2} \quad \text{B.23}$$

Table B.8 Mixture preparation, post processing, and total uncertainty on LBV

$\phi$	$a_{S_{u,MP}}^0$	$a_{S_{u,PP}}^0$	$a_{S_u^0}$ (cm/s)
0.6	13.75	1.11	13.79
0.8	13.43	1.81	13.55
1	6.84	1.75	7.06
1.2	9.90	1.69	10.04
1.4	12.74	1.21	12.80

## Minimization of extrapolation uncertainty

In the present work, the uncertainty of LBV and burned gas Markstein length was estimated by following the procedure reported by Xiouris et al. [141] and a non-linear extrapolation (NE) [99] model was fitted to a radius range of 8-20mm which falls in the weak stretched regime. Further, Wu et al [126] provided a correlation to minimize the extrapolation uncertainty. For the present mixtures, all the chosen data range were within the limits of  $-0.05 < Ma_{linear} Ka_{mid} < 0.15$ , except two lean mixtures, as plotted in Figure B.3. Hence, the present radius range and extrapolation scheme had a high value of goodness of fit in the range of 96% and above for the

investigated diluted, oxy-n-dodecane mixtures and meets the recommended criteria to minimize the extrapolation uncertainty.

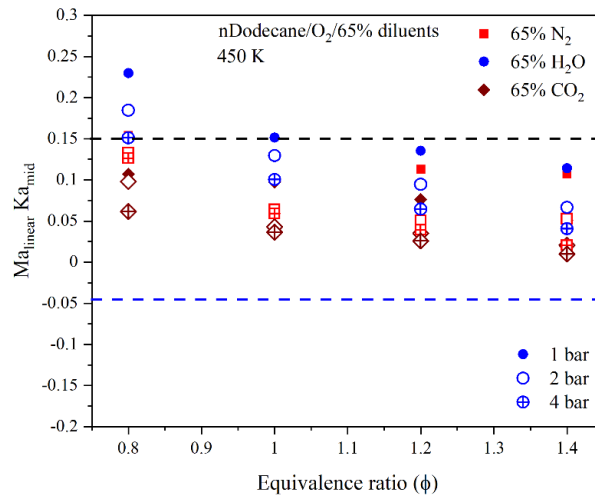


Figure B.3 Extrapolation uncertainty parameter as a function of equivalence ratio of 35% ( $n\text{-C}_{12}\text{H}_{26} + (18.5\text{O}_2/\phi) + 65\%$  diluent) at 1 and 4 bar 450 K.

## Density ratio

The unburned to burned gas densities at equilibrium can be calculated using standard thermodynamic properties with EQUIL model in CHEMKIN. Three kinetic models (JetsurF2.0, You et al., and PoliMI-1410) were used to simulate the n-dodecane/air and n-dodecane/ $\text{O}_2/65\%\text{N}_2$  flames at 1 bar, 450 K, and  $\phi = 0.8 - 1.4$ . The average relative average deviation seen in the modelled density ratio results was found to be 0.062% and 0.088% respectively, indicating that the species-specific thermodynamic properties used in each model have a negligible impact on the overall LBV results. Therefore, uncertainty in the density ratio calculation is relatively insignificant compared to the other sources of uncertainty.

Table B.9 Reported average uncertainties of LBV and Lb for various mixtures.

Study	Mixtures	Uncertainty range (%)	
		LBV	Markstein length
Study-1	n-dodecane-air	$\pm 5.87 - 6.03$	$\pm 6.27 - 9.28$
Study-2	n-dodecane- $\text{O}_2$ -diluent	$\pm 5.81 - 6.45$	$\pm 7.64 - 8.95$
Study-3	(n-dodecane+ $\text{H}_2$ )-air	$\pm 4.8 - 8.69$	$\pm 7.8 - 13.2$
Study-4	Methane- $\text{O}_2$ -diluent	$\pm 4.83 - 6.93$	$\pm 6.48 - 9.42$

## List of Publications

### Peer-Reviewed Journals:

1. **Natarajan Rajesh**, Shu Zheng, and Chockalingam Prathap, "A Study on the effect of different diluents on Laminar Burning Velocity and Flame Stability of Oxy-Dodecane mixtures at elevated pressures and Temperatures", **Combustion and Flame**, Volume 255, 112875, 2023. (IF:5.8)
2. **Natarajan Rajesh**, and Chockalingam Prathap, "Investigation on the Laminar Burning Velocity and Flame Stability of premixed n-Dodecane-Air mixtures at elevated pressures and temperatures", **Fuel**, Volume 318, 123347, 2022. (IF:8.1)
3. **Natarajan Rajesh**, M. Akash and Chockalingam Prathap, "Investigation on the effect of steam/CO<sub>2</sub>/N<sub>2</sub> on the flame suppression and flame stability of methane-oxygen mixtures at elevated thermodynamic conditions", **Fuel**, Volume 309, 121987, 2021. (IF:8.1)
4. **Natarajan Rajesh**, and Chockalingam Prathap, "Effect of Hydrogen addition on laminar burning velocity and flame stability of n-dodecane/H<sub>2</sub>/air mixtures at elevated operating conditions", **International Journal of Hydrogen Energy** (In Press). (IF:7.2)

### International and National Conferences:

1. **Rajesh Natarajan**, and Chockalingam Prathap, Investigation on the effects of pressure and Hydrogen addition on laminar burning velocity and flame stability of n-Dodecane-Hydrogen-air mixtures, Proceedings of the 26<sup>th</sup> National and 4<sup>th</sup> International ISHMT-ASTFE Heat and Mass Transfer Conference December 17-20, 2021, IIT Madras DOI: 10.1615/IHMTC-2021.3520.
2. **Rajesh Natarajan**, and Chockalingam Prathap, Impact of Hydrogen blending on Laminar burning velocity and flame stability of Methylcyclohexane/air mixtures, Proceedings of the 27<sup>th</sup> National Conference on IC engines and Combustion November 5-7, 2022, VIT Vellore NCICEC0446.
3. Thulaseedharan Krishnadath, Chockalingam Prathap, **Rajesh Natarajan**, Tippa Muniraja and S Senthilmurugan. Measurement of laminar burning velocity of premixed mixtures of ethane/propane reacting in air and oxygen enriched air using freely

expanding spherical flames. Proceedings of the 26<sup>th</sup> National and 4<sup>th</sup> International ISHMT ASTFE Heat and Mass Transfer Conference December 17-20, 2021, IIT Madras, DOI:10.1615/IHMTC-2021.2780.

4. M.S. Krishnanunni, **Rajesh Natarajan**, J.P. Madhav, Subodh Purohit, Neeraj Mathur, Senthil Murugan S, Chockalingam Prathap ‘Effect of hydrogen addition on the Thermal performance of self-aspirating LPG/ Natural gas domestic burners’ 15<sup>th</sup> International Symposium on Experimental and Computational Aerothermodynamics of Internal Flows. 24-27<sup>th</sup> October 2023, IIT-Madras, India.

#### **Poster Presentation**

- **Natarajan Rajesh**, Chockalingam Prathap, Effect of Hydrogen addition on laminar flame characteristics of n-Dodecane-Hydrogen-air mixtures at different thermodynamic conditions, Indo- German International Conference on “Metrology for the deployment of green hydrogen and renewable fuels in India”. April 4-6 (2022). PTB – Germany (Received Third Position).